Synthèse et caractérisation de nanomatériaux pour la délivrance contrôlée de médicaments en réponse à des stimuli externes

Fernando Espinola Portilla

To cite this version:

Fernando Espinola Portilla. Synthèse et caractérisation de nanomatériaux pour la délivrance contrôlée de médicaments en réponse à des stimuli externes. Autre. Université Paris sciences et lettres; Universidad de Guanajuato, 2022. Français. NNT : 2022UPSLC015 . tel-04835689

HAL Id: tel-04835689
https://pastel.hal.science/tel-04835689v1

Submitted on 13 Dec 2024

PSL UNIVERSITÉ PARIS

UNIVERSIDAD DE GUANAJUATO

THÈSE DE DOCTORAT
DE L'UNIVERSITÉ PSL

Préparée à Chimie ParisTech
Dans lecadre d'une cotutelle avec Universidad de Guanajuato

Synthèse et caractérisation de nanomatériaux pour la délivrance contrôlée de médicaments en réponse à des stimuli externes

Synthesis and characterisation of nanomaterials for controlled drug delivery in response to external stimuli

Soutenue par
Fernando Enrique ESPINOLA PORTILLA
Le 12 Decembre 2022

Ecole doctorale n° 406
Chimie moléculaire Paris Centre

Spécialité
Chimie Moléculaire

Composition du jury :

Christine, MÉNAGER Professeure, Sorbonne Université	*Présidente*
Katarzyna, WROBEL Professeure, Universidad de Guanajuato	*Examinatrice*
Jan, PETR Professeur, University Olomouc	*Rapporteur*
Andrés, DE LUNA BUGALLO Professeur, UNAM	*Rapporteur*
Thomas, PONS Chargé de recherche, ESPCI - PSL	*Examinateur*
Mario, ÁVILA RODRIGUEZ Professeur, Universidad de Guanajuato	*Examinateur*

Chimie Paris ParisTech | PSL

Synthesis and characterisation of nanomaterials for controlled drug delivery in response to external stimuli

A doctoral thesis submitted to

Universidad de Guanajuato
División de Ciencias Naturales y Exactas

and

Université Paris Sciences et Lettres
École NationaleSsupérieure de Chimie de Paris (Chimie ParisTech)
École Doctorale Chimie Moléculaire de Paris Centre (ED406)

for the degree of Doctor en Química de la Universidad de Guanajuato and Docteur de Université Paris Sciences et Lettres

Author
Fernando Enrique Espinola Portilla

Supervised by

Prof. Silvia Gutiérrez Granados
Prof. Anne Varenne

Prof. Gonzalo Ramírez García

CERTIFICATE OF APPROVAL

This manuscript has been read and approved by the Examining Committee constituted by:

Dr. Katarzyna Wrobel
President of the jury
(UGTO)

Dr. Christine Ménager
President of the jury
(Sorbonne Université)

Dr. Andrés De Luna Bugallo
Rapporteur
(UNAM)

Dr. Jan Petr
Rapporteur
(University Olomouc)

Dr. Mario Ávila Rodríguez
Examiner
(UGTO)

Dr. Thomas Pons
Examiner
(Université PSL)

STATEMENT OF ORIGINALITY

This is to certify the originality of this thesis, and that its content is the product of my own work. This thesis has not been submitted for any degree or other purposes.

M.Sc. ESPINOLA-PORTILLA Fernando Enrique

ACKNOWLEDGEMENTS

To the Institutions who give me technical, scientific, and financial support to realize this thesis:

Mexican National Council for Science and Technology (CONACYT) for their support through the doctoral fellowship.

Campus France for their support through the doctoral fellowship.

Dirección de Apoyo a la Investigación y al Posgrado of the University of Guanajuato (DAIP) for the complementary financial support during the different stays during the doctoral program.

To my « ***Universidad de Guanajuato*** » and my ***« École Nationale Supérieure de Chimie de Paris - Université PSL*** »

To the "***Administración del Posgrado en Química***" as well as to "***Dirección de Relaciones Internacionales y Colaboración Académica en el área de Convenio***s" of the University of Guanajuato or all the support received in administrative matters.

National Laboratory for the Characterization of Physicochemical Properties and Molecular Structure of the University of Guanajuato for permit us to use their installations and equipments.

To the ***Centro de Investigaciones en Óptica – Centro CONACYT*** for permit us to use their installations and equipments.

To the ***Centro de Física Aplicada y Tecnología Avanzada – UNAM*** for permit us to use their installations and equipments.

To the project **UNAM – PAPIIT No. IA204422** for the financial support.

Merci à " ***La Maison du Mexique*** " à Paris pour toutes les dispositions prises en matière d'hébergement et pour les personnes formidables qu'elle m'a permis de rencontrer.

Paulina Lozano Sotomayor (UG), and Lourdes Palma Tirado (UNAM), for her technical assistance during electron microscopy observations.

Je remercie Gregory LEFEVRE pour nous avoir permis d'utiliser son équipement de zetasizer.

My most sincere regards and acknowledgements to the examining committee professors for reading and reviewing this complex manuscript of doctoral work, for sharing his vision and observations towards it, providing an enrichment to the work.: ***Dra. Katarzyna Wrobel, Dr. Christine Menager, Dr. Andrés De Luna Bugallode, Dr. Jan Petr, Dr. Mario Ávila Rodríguez and Dr. Thomas Pons.***

Gracias al gran equipo de profesores y alumnos de “**Electroquimica Ambiental**”, *Dra. Silvia, Dr. Alatorre, Dr. Peralta, Cristina, Rosy, Emmanuel, Josué, Jasmín, Cecilia, Deborah, Oscar, Nelson y Martin* por todo el apoyo y acompañamiento recibido dentro del ámbito personal y profesional. En especial agradezco al ***Dr. Oracio*** por su gigantesco apoyo en la formación de precursores poliméricos esenciales para este trabajo doctoral, así por su amistad y consejos personales y profesionales en esta aventura. Siempre estarán en mi mente y corazón.

Un grand merci à l'ensemble des professeurs et copains de L’École nationale supérieure de chimie de Paris: *Fethi BEDIOUI, Sophie GRIVEAU, Cyrine SLIM, Bich-thuy DOAN, Camille LESCOT, Laura TRAPIELLA, Fanny d’ORLYE, Anne VARENNE, Cristina, Menel, Gethnet, Sarah, Amina, Brenda Maria, Amal, Karen, Alice, Sun-Jie, Tahani, Robin, Namdi, Gerson, Geovanna, Elahe* ; pour les discussions scientifiques, le soutien technique et administratif, la camaraderie, l'hospitalité et pour tous les grands moments, ainsi que les moments difficiles, que nous avons vécus ensemble. Vous serez toujours dans mon esprit et mon cœur.

My greatest thanks to all my advisors for guiding me in my professional growth as a researcher and personal growth as a human being:

Dra. Silvia Gutiérrez Granados: mi amiga desde la licenciatura y asesora desde la maestría hasta el doctorado, gracias por aconsejarme tanto de la vida y por presentarme a las personas correctas en mi proyecto de doctorado. Gracias también por todas las aventuras, fiestas y viajes en todas partes de México y del mundo. Sin usted, sin duda no estaría hasta donde he llegado. También llegaré muy lejos gracias a todo lo que me ha enseñado. No tengo más palabras que “Gracias“.

Prof. Anne Varenne: Merci d'avoir renforcé ma critique scientifique et mon attachement à mon travail de doctorat, mais surtout merci de m'avoir fait aimer le métier de chercheur et d'avoir été un excellent exemple de directeur de thèse et d'être humain. Merci de m'avoir fait confiance. Merci de m'avoir accueilli avec tant de gentillesse et d'amitié dans un pays nouveau et étrange, pour l'amitié, les fêtes et les aventures que nous avons vécues ensemble à Paris. Je vais aller loin grâce à ton soutien et à ton exemple.

Dr. Gonzalo Ramírez Gracia: Antes que mi asesor, un gran amigo que me has apoyado en todo mi crecimiento profesional, así como en el personal. Gracias por todas las idas al FBI y demás aventuras que compartimos juntos. Gracias también por recibirme en todos los lugares en los que has trabajado y haberme permitido trabajar de la mano contigo. Como asesor, infinitas gracias por todo el seguimiento constante, paciencia y enseñanzas en todos los aspectos que un buen investigador deben de tener, tu siendo ese gran ejemplo. Aprendí y crecí profesionalmente demasiado gracias a ti. Sin duda, también no estaría hasta donde estoy sin tu apoyo y estoy seguro de que llegaré tan lejos como tú. Muchas muchas gracias el Gonzi.

Prof. Fanny d’Orlyé: Merci d'être le meilleur professeur d'électrophorèse capillaire au monde, pour ta patience et ton soutien dans tous les aspects de la vie en laboratoire. Merci pour les bonnes discussions scientifiques et pour tout ce que tu m'as appris sur le terrain scientifique. Merci de m'avoir remonté le moral dans les moments difficiles du projet. Merci d'être un excellent exemple de directeur de thèse. Merci beaucoup par tout.

Prof. Laura Trapiella: Muchas gracias, Lau por el gran recibimiento que me diste al llegar a París, por todo el gran apoyo administrativo y técnico en la escuela, por todos los ánimos que me dabas en los momentos difíciles del doctorado, por todas las discusiones científicas y por el gran ser humana que eres tanto dentro como fuera del laboratorio. Aunque en el papel no seas mi asesora, para mi fuiste mucho más que eso y la única forma que tengo para reconocerte es agradecerte todo lo que hiciste por mí.

Sin duda nada de esto hubiera sido posible sin el gran apoyo de aquellos viejos y nuevos amigos que me acompañaron en esta aventura del doctorado. Gracias **Debi** por todo lo que me has ayudado a crecer a nivel personal y profesional más allá del ámbito científico; llegaremos lejísimos en todos nuestros proyectos juntos. Gracias **Cris** por ser mi compañera de trabajo y amiga; por crecer juntos como profesionistas y por compartir experiencias increíbles en todas partes de Francia y México. Gracias **Katy** por ser la mejor amiga en los momentos más difíciles y extraños en Francia, por todas las aventuras y por permitirme conocerte; gracias a ti, la experiencia en Francia fue la más increíble. Merci **Amina**, d'avoir été une personne si incroyable avec tout le monde, de m'avoir intégré en France dans tous les aspects, mais de m'avoir aimé et d'avoir été là dans chaque moment de bonheur et de tristesse que j'ai vécu loin de chez moi. Merci **Alice AM** pour l'incroyable amitié que nous avons forgée, pour tous les rires, les aventures, les danses et les câlins ; merci d'avoir été le meilleur professeur de français ; merci de m'avoir aimé et de m'avoir écouté et d'avoir été l'ami que je n'ai jamais demandé et qui est entré dans ma vie pour y rester à jamais. Obrigado **Brrrrenda Marria** por ser um amiga tão incrível dentro e fora do laboratório, pelas incríveis viagens e experiências na Europa, por me acompanhar nos momentos mais tensos e incríveis da pandemia, mas acima de tudo, por me acompanhar no momento mais difícil da minha vida; se você e Tiago não tivessem estado lá, aquele episódio sombrio na minha vida teria sido um inferno; verdadeiramente, muito obrigado por tudo e por você. Gracias **Karen y Solecito** por todo el increíble ambiente fuera y dentro del lab. Gracias **Emmanuel** por todas las aventuras y experiencias en Francia y México.

Finalmente, esta tesis está dedicada con todo el cariño del mundo a mi familia hermosa porque gracias a ustedes soy la increíble persona que soy y llegaré tan lejos como la vida me permita. A mi **Viejo** que se me fue en el camino pero nunca dejo de apoyarme, confiar en mi y darme la confianza y fuerza que se necesitaba en este camino; a mi **Mamá** increíble por acompañarme y nunca dejarme solo en ningún momento y circunstancia, por confiar tanto en mi y brindarme confianza, por todo su amor e impulso y por ser la mejor; a mi **Hermanita** querida por su gran apoyo, escucharme e impulsarme a vencer mis miedos y por nunca dejarme solo; a mi cuñado **Gon y sobrinos** por darme fuerza en esta aventura; y a ti mi **Kari** hermosa por ser la mejor amiga, novia, esposa y amante; la mejor persona que conozco, por acompañarme en todo mi proceso de crecimiento profesional y personal en esta aventura del doctorado, por acompañarme a la distancia en París, por la gran experiencia de ser y estar contigo, por permitirme compartirme a nivel personal y profesional, por cuidarme siempre; y pero ser la mejor persona en esta experiencia que se llama mi vida; Te amo.

PREFACE

This doctoral thesis manuscript represents the work carried out and directed jointly between L'École Nationale Supérieure de Chimie de Paris, (Chimie ParisTech PS) and Universidad de Guanajuato, in accordance with the terms and conditions applicable in the co-supervision agreement for the elaboration of this thesis project established by the mentioned universities. The experimental research has been performed in the laboratories of Synthesis, Electrochemistry, Imaging and Analytical Systems for Diagnosis (SEISA) from the Institute of Chemistry for Life and Health Sciences (i-CLeHS) (Paris, France), the Biofunctional Nanomaterials Laboratory at the Centro de Física Aplicada y Tecnología Avanzada – UNAM (Queretaro, Mexico), and the laboratory of Environmental Electrochemistry at the División de Ciencias Naturales y Exactas of the University of Guanajuato (Guanajuato, Mexico).

This doctoral thesis project has been supervised and directed by a multidisciplinary group composed by Anne Varenne, Silvia Gutiérrez Granados and Gonzalo Ramírez Garcia. Dr. Fanny d'Orlyé and Dr. Laura Trapiella Alfonso have also supervised and participated fruitfully in the discussion of the entire work.

This manuscript is presented in English, and it includes an extended summary in French according to the agreement for International Joint Doctorate Supervision.

The overall purpose of this work has been to design and synthesize a smart drug delivery system based on stimuli-responsive polymers able to self-assembly into micelle-like aggregates, combined with Janus-like nanoparticles. These nanohybrids integrate the magnetic and upconverting photoluminescence responses of the inorganic moieties with the drug loading and release ability of the light- and pH- sensitive polymers.

Therefore, this work sequentially describes the different stages required to achieve this objective. In Chapter II, the synthesis of the random co-polymers and the optimization of their self-assembling into micelle-like aggregates is first described. Then, the physicochemical characterization with classical methodologies along with fine-tuned electrokinetic strategies in a capillary electrophoresis format were implemented for a deep understanding of the equilibria conditions and species involved in the formation and stability of the micelle-like aggregates; In Chapter III, capillary electrophoresis and other complementary techniques were also implemented to elucidate the integration and interactions of the anticancer drug Doxorubicin in the micelle-like aggregates. Furthermore, these techniques were also used to determine the drug loading and release parameters upon UV-light exposition and pH variation; the synthesis and characterisation of new hybrid Janus-like nanoparticles with magnetic and upconverting sections is presented in Chapter IV. Finally, those nanoparticles were integrated with the micelle-like aggregates to get a near infrared-activated multifunctional system for magnetically-guided optical imaging and stimuli-responsive release of drugs.

Some general conclusions are presented in the last section of this manuscript, together with some proposals for continuing the development and application of this promising theranostic tool.

As a result of this collaborative PhD work, the next papers have been published in JCR indexed journals:

Espinola-Portilla, F., d'Orlyé, F., Trapiella-Alfonso, L., Gutiérrez-Granados, S., Ramírez-García, G., & Varenne, A. (2022). A deep understanding of the self-assembly and colloidal stability of light and pH dual-responsive spiropyran random copolymer micelle-like nano-aggregates. Materials Today Communications, 2022, 31, 103499. Doi: https://doi.org/10.1016/j.mtcomm.2022.103499 (February). Chapter II of this manuscript

Espinola-Portilla, F., d'Orlyé, F., Trapiella-Alfonso, L., Gutiérrez-Granados, S., Ramírez-García, G., & Varenne, A. (2022). Rational understanding of entrapment loading and release of doxorubicin by UV-light and pH responsive Poly(NIPAM-co-SPMA) micelle-like aggregates. Submitted 2022, 31 (Ago). (Under revision). Chapter III of this manuscript.

NIR-light and pH- responsive nanocomposite based in upconverting-magnetic Janus-like nanoparticles integrated in Poly(NIPAM-co-SPMA) micelle-like aggregates for optical imaging and controlled release of drugs. (In preparation). Chapter IV of this manuscript.

LIST OF CONTENTS

ACRONYMS

Acronyms	Details
ACP	Amphiphilic copolymers
AFM	Atomic force microscopy
AZO	Azobenzene
BBB	Blood brain barrier
BCP	Block copolymer
BET	Brunauer–Emmett–Teller
BGE	Background electrolyte
CAC	Critical aggregation concentration
CE	Capillary electrophoresis
CNTs	Carbon nanotubes
CoPo	Copolymer
CZE	Capillary zone electrophoresis
DDS	Drug delivery systems
DEX	Dextran
DLC	Drug loading capacity
DLS	Dynamic light scattering
DMF	N,N-dimethyl-formamide
DMSO	Dimethyl sulfoxide
Dox	Doxorubicin
DoxHCl	Doxorubicin Hydrochloride
DTD	DT-diaphorase
DTXL	Docetaxel
EDX	Energy dispersive X-ray
EOF	Electroosmotic flow
EPR	Enhanced permeability and retention
FA	Folic acid
FDA	Food and Drug Administration
FT-IR	Fourier-transform infrared spectroscopy
GNPs	Gold nanoparticles
GPC	Gel permeation chromatography
GSH	Glutathione
HNPs	Hybrid nanoparticles
HPLC	High-performance liquid chromatography
JNPs	Janus nanoparticles
LCST	Lower critical solution temperature
LDE	Laser doppler electrophoresis
LIF	Laser induced fluorescence

Acronyms	Details
LUV	Large uni-lamellar vesicles
MAA	Maleic acid amides
MC	Merocyanine
Mic	Micelle-like aggregate
MicDoxHCl	Doxorubicine loaded in micelle-like aggregate
MicJNP	Janus nanoparticles loaded in micelle-like aggregate
MicJNPDox	Janus nanoparticles and Doxorubicine loaded in micelle-like aggregate
MNPs	Magnetic nanoparticles
MOF	Metal organic framework
MRI	Magnetic resonance imaging
MSNs	Meso-porous silica nanoparticles
MWCNTs	Multi-walled carbon nanotubes
NADPH	Nicotinamide adenine dinucleotide phosphate
NGs	Nanogels
NIPAM	N-isopropyl acrylamide
NIR	Near-infrared light
NMR	Nuclear magnetic resonance
NPs	Nanoparticles
OA	Oleic acid
ODE	Octadecene
OM	Oleylamine
oNB	o-Nitrobenzyl
P4VP	Poly(4-vinyl pyridine)
PBS	Phosphate-buffered saline
PDI	Polydispersity index
PDT	Photodynamic therapy
PEG	Polyethylene glycol
PNIPAM	Poly(Nisopropylacrylamide)
PTT	Photothermal therapy
PTX	Paclitaxel
PVP	Polyvinyl pyrrolidine
QDs	Quantum dots
RES	Reticuloendothelial system
ROS	Reactive oxidative species
SEM	Scanning electron microscopy
SNS	Stimuli-responsive nanocarrier systems
SP	Spiropyran
SPIONs	Super paramagnetic iron oxide nanoparticles

Acronyms	Details
SPMA	1′-(2-methacryloxyethyl)-3′,3′-dimethyl-6-nitrospiro-(2H- 1-benzopyran-2,2′-indoline)
SPR	Surface plasmon resonance
STEM	Scanning transmission electron microscopy
SUV	Small uni-lamellar vesicles
SWCNTs	Single walled carbon nanotubes
TEM	Transmission electron microscopy
TGA	Thermal gravimetric analysis
THF	Tetrahydrofuran
TPA	Two-photon absorption
TR	Transferrin
UC	Upconversion
UCNPs	Upconverting nanoparticles
UCST	Upper critical solution temperature
UV	Ultraviolet
XRD	X-ray diffraction

INDEX OF FIGURES

Chapter I

Chapter II

Chapter III

Chapter IV

ANEXE I

GENERAL INTRODUCTION

Nowadays nanomaterials have led to many day-to-day applications in different domains. Their unique properties have broken some barriers in research areas including biomedical, material, physics, and chemistry sciences, thereby providing high impacting-tools for society. Nevertheless, those properties can be tuned, amplified and optimized by the nature, size, shape, surface chemistry and chemical environment of these nanomaterials. Hence, the use of nanoparticles for biomedical applications as a theranostic tool, serving as drug carriers as well as probes for imaging, implies their synthesis improvement and deep knowledge of their physicochemical behaviour in relevant media. Particularly, in the context of chemotherapy, this treatment mostly used for curing cancer diseases provokes various side effects due to the uncontrolled reaction of the drugs acting indiscriminately in normal and cancerous cells. To avoid those concerns, drug delivery systems (DDS) have been developed for new therapy strategies helped by nanotechnology, which could allow a controlled release of drugs overcoming the disadvantages of standard therapies.1,2

The development of efficient theranostic nano-objects is therefore still a challenge. Some strategies employ different nanostructure configurations like nanoparticles (NPs) for the transport of agents like vaccines, drugs, genes, proteins, and enzymes.3 These nanocarriers (1 to 100 nm) can be designed from a variety of materials in different shapes and sizes for drug delivery systems (DDS). They should provide good biocompatibility, long-term blood circulation period, and overcome the endosome–lysosome mechanism, thus having unique features such as enhanced biodistribution, pharmacokinetics, stability, solubility and reduction in toxicity.4,5 These nanoparticles (NPs) could be of organic, inorganic and hybrid (combination of materials) nature. Organic nanocarriers including liposomes, dendrimers, polymeric micelle-like nanoagregates, and carbon nanotubes (CNTs) polymers, can conjugate a variety of drugs as well as ligands for appropriate drug delivery. Inorganic nanocarriers, formed by noble metals, semiconductors, metal oxides, or lanthanides such as gold NPs (GNPs), quantum dots (QDs), magnetic NPs (SPIONs), mesoporous silica (MSNPs), and upconverting NPs (UCNPs), possess synergetic therapeutic effect apart from DDS, such as photodynamic or photothermal therapies. Hybrid nanoparticles (HNPs) combine two or more organic and inorganic moieties with additive or synergistic activity, having configurations like organic–inorganic, inorganic–inorganic, or multi-components. Some examples of these nanosystems are lipid-polymer, ceramic-polymer, magnetic-polymer, luminescent UCNPs-polymer micelles, etc.6

These HNPs integrated into a single nanosystem could provide simultaneous diagnostic and therapeutic functions in a single dose, denominated as "theranostic tools".7 They should allow to follow their biodistribution when injected, control the drug delivery and determine the efficiency of the therapy by in-vivo imaging. There are two general approaches to forming HNPs, either by bonding the surface of solid NPs to another NP, or by encapsulation of one nanostructure into the other one.8 Since it is vital to avoid side effects, nanotheranostic tools need to be site-specific and smart imaging-DDS. For this, two elements should be considered: (i) these smart stimuli-responsive nanomaterials should enable efficient anticancer drug transport and delivery to control their loading and release, and (ii) targeting properties for efficient vectorization to the cancerous site for therapeutic action.6 Some strategies to design smart NPs include functionalization for specific targeting of cancer cells, incorporation of stimuli-responsive moieties, and incorporation of other substances to be co-delivered.5

Micelle-like nanoaggregates are polymeric NPs for DDS that can provide good stimuli-responsive properties. They are formed by internal hydrophobic core and an external hydrophilic shell. A block copolymer is formed from two homopolymers linked to form a single polymer chain, while random copolymers consist of monomers linked in each polymer backbone without a sequential order or pattern. When they are diluted in an aqueous solution, amphiphilic molecules exist separately as unimers (single polymer chain). By increasing the unimer concentration till the critical aggregation concentration (CAC), unimers undergo self-folding or -assembly thanks to the presence of hydrophobic pendants in the polymeric chain being stabilized by the hydrophilic pendants.9,10 The most common synthesis method consists in the copolymer dissolution in an organic solvent such as N,N-dimethyl-formamide (DMF), dimethyl sulfoxide (DMSO) or Tetrahydrofuran (THF), followed by the drop by drop addition of aqueous solutions, normally deionized water and finally a dialysis purification process. These self-assembled micelle-like nanostructures can incorporate poorly soluble drugs thanks to the hydrophobic micelle core. For this, the drug is dissolved with the copolymer in the organic solvent and the process as described above is followed.11,12

From the literature review, some challenges remain for the biomedical application of micelle-like aggregates. For example, premature or inadequate drug release into the circulation or target tissue.6 A very effective way to achieve proper drug load and delivery is the development of smart stimulus-responsive polymers as precursors for micelle-like aggregates.13–16 Exploiting internal stimuli associated with cancerous tumours (pH, enzymes, hypoxia, etc.) as well as external stimuli (light, magnetic, temperature, etc.) would allow destabilisation of the micelle-like aggregates in response to these stimuli, achieving a temporally and spatially controlled release.6 The pH difference in most solid tumour's acidic medium (pH 6.5-7.2) has been widely exploited to activate pH-sensitive micelle-like aggregates at the tumour site or in a specific organelle upon their decomposition or destabilisation for the drug release. In this process, pendant acidic or basic groups such as carboxylate, sulfonate and amino groups in polymeric chains are gradually ionised as a function of pH, inducing alterations of the structure, solubility, surface activity, and/or polymeric chain conformation, whereby specific polymer groups switch between a neutral and charged state.17,18 Some pH-responsive polymeric micelles are poly(2-(diisopropylamino)ethyl methacrylate) (PDPAEMA), poly(4-vinylpyridine) (P4VP), poly(histidine) (PHis) and poly(β-amino ester).19 In light-responsive polymers, the UV-light irradiation source is the most used due to the high number of polymers that respond to this wavelength.20 Photochemical reaction processes consist of the photocleavage of light-responsive units of the polymers, ii) photoisomerization, and iii) photo-cross-linking.21 Reversible photo-isomerized compounds like azobenzene (AZO) and spiropyran (SP), are usually used as hydrophobic moieties in the synthesis of light-responsive amphiphilic copolymers, which self-assembly into micelle-like aggregates in aqueous medium. Upon UV light irradiation, they will isomerized into their polar structure form, causing NPs disassembly and subsequently efficient and controlled drug release.22

Spiropyran (SP) is a photoreactive non-polar organic compound that experiences a cis-trans isomerisation under UV light (200–400 nm), via the ring-opening on the spiro-carbon forming a stable polar compound called merocyanine (MC). This zwitterionic MC compound, after C-O bond cleavage, contains a phenolate anion and a positively charged indolium, which provide a much larger dipole moment in contrast to the hydrophobic non-polar SP form.23 In the visible spectrum (500–600 nm), MC returns to SP isomer in a reversible process. Furthermore, SP isomerisation into MC could also show acido-chromism, thermo-chromism and solvato-chromism, by complexation with metal cations that can stabilise MC.24 For example Zhi-Min Dang and co-workers reported a micelle formed in water from an amphiphilic random copolymer which comprises a photo- and pH-sensitive spiropyran (SP) core and a thermo-sensitive N-isopropyl acrylamide (NIPAM) shell. Under UV light irradiation, the self-assembled nanoparticles dissociate due to photoisomerization and thus the loaded molecules can be released. In acidic condition, the NPs swells, releasing also the drug.25

Although UV light-responsive micelle-like nanoaggregates present many advantages, their development still faces some challenges including i) poor penetration depth that makes inefficient drug release in deep body regions, and ii) high tissue damage derived from phototoxicity. However, NIR and Vis wavelengths (600–1000 nm), conversely, allow higher tissue penetration depth because of the optically transparent tissue window in that region due to a very low absorption by the blood, water, and melanin molecules.20 Hence, nanomaterials with the capacity to convert the NIR light to UV-Vis light, such as upconverting NPs (UCNPs) seem promising for biomedical applications.

UCNPs have the property of converting low-energy NIR radiation into high-energy radiation, in the UV-Vis-NIR spectral range, through a phenomenon known as photon upconversion.26 With a host matrix, an activator and a sensitiser ion, the up-converting process is generated by the photo absorption of identical energy from its ground state to a metastable E1 state of the sensitiser. Subsequently, the sensitiser transfers its non-radiative energy to the activator, shifting to its E2 emission level, followed by the sensitiser relaxation to the ground state. Finally, the activator ion relaxes and emits its light of higher energy.27 UCNPs are classically composed of a hexagonal phase NaYF4 as the host matrix, a Yb3+ sensitizer ion stimulated by NIR light of (980 - 800 nm) and Tm3+used as activator ion28,29. Those materials are excited by NIR light and emitting UV-Vis light and can be synthesised through thermal decomposition or hydrothermal/solvothermal process28,29.30 For example, Xin Zhao and co-workers prepared an up-conversion nanosystem composed of an encapsulated UCNP in the core of a light- and pH- polyspiropyran micelle-like nanoaggregate to liberate doxorubicin when the environment is at pH 4.5 and/or under NIR irradiation to provide spiropyran hydrophobic-hydrophilic shifting processes thanks to the up-converting phenomena of the UCNPs. The irradiation of NIR light is absorbed by the UCNP emitting UV light for its subsequent absorption by the SP compound to start photo-isomerization.31

To this date, the drug loading and release capacity of nanocarriers has been evaluated through classic methodologies based on UV-Vis, fluorescence spectroscopy, and HPLC. However, capillary electrophoresis (CE) has emerged as a powerful analytical method to physiochemically characterize nano-objects and is known as an efficient method for interaction studies, that can be transposed for the study of drug loading and release in the NPs including micelle-like aggregates. An iterative synthesis/characterization study should allow us to quickly optimize the design of the NPs.

On the other hand, nanotheranostic tools for simultaneous cell labeling, in vivo cancer targeting, and drug delivery have gathered large interest in their combination of magnetic and luminescent nanostructures forming hybrid NPs using SiO2, Au, Fe2O3, TiO2 and UCNPs.32 In most cases, core-shell structured magnetic-luminescent NPs33–36 are synthesised but they face several challenges that limit their applications because the luminescent and magnetic properties can be highly reduced. For example, a magnetic shell could absorb and block the exciting light and up-conversion luminescence, reducing quantum yields of the UCNPs,37 and inversely, the up-conversion luminescence shell could interfere with the interaction between the magnetic core and an incident magnetic field. Consequently, the major challenge in this field is not only to develop reproducible and easy methods to obtain magnetic-luminescent nanostructures, but also to efficiently fabricate HNPs with good either magnetic efficiency or/and high luminescence properties. Thus, owing to the combination of magnetic and luminescence properties, Janus-like NPs (JNPs), having an asymmetric structure, will probably be a better structure applicable as theranostic tool. Janus nanoparticles are so named in reference to Janus, the Roman god of doorways, typically depicted as having two faces. Like the ancient deity, JNPs also have two faces, consisting each of them of different chemistry, size, morphology, material, etc.38 A general method for their preparation is the phase separation with a homogeneous—heterogeneous nucleation mechanism39 that consists in the epitaxial growth of one particle from the surface of the other one, usually the first NP working as a seed in which the lattice incompatibility makes it difficult for the second material to form a stable core-shell structure.40 Therefore, HNPs combining inorganic nanoparticles with micelle-like nanoaggregates are being estimated as excellent potential theranostic tools through the synergistic objectives of imaging, drug vectorization and delivery, and therapies such as photothermal or photodynamic. To convert these nanocomposites into smart nanocarriers, they must be directed to a specific target.5 For this purpose, adding magnetic fractions (MNPs) for external guidance to the decoration of the nanocomposites has to be considered.41

According to the previous literature, the improvement of the design of theranostic tools for their use for smart drug delivery and imaging via site-directed magnetic transport should integrate the synthesis of new smart hybrid nanosystems like JNPs, combining properties of luminescent and magnetic, as well as the synthesis of polymers that that react to stimuli such as pH and light, and that can encapsulate the JNPs. Also, a good understanding of the physicochemical characterization of the NPs and of the interaction between the drug to load and the nanosystems, will help to understand the equilibria involved in drug loading and release, the loading and release capacity. For this purpose, capillary electrophoresis seems a very interesting methodology to deep characterize and quantify these objects and the involved interactions to design efficient theranostic NPs.

Therefore, the objective of this PhD project is to synthesise and characterise magneto-luminescent Janus-type inorganic hybrid nanomaterials coated with a light- and pH-sensitive copolymer for disease monitoring along with smart delivery and controlled release of active ingredients in a site-directed manner.

In the first step, we aim at synthesizing micelle-like nano-aggregates that can load a drug and to be able to deliver the drug at a specific site, through external or internal stimuli. Therefore, the synthesis of pH- light-responsive random amphiphilic spiropyran-based copolymer poly(NIPAM-co-SPMA) micelle nano-aggregates was performed and optimized through the determination of their physico-chemical characterizations by combining different methodologies. Several classical characterization methods such as dynamic light scattering (DLS), laser doppler electrophoresis (LDE), and transmission electron microscopy (TEM) where employed for this purpose. To go deeper into the composition of the synthetic batch and in understanding of its colloidal stability, capillary electrophoresis (CE) coupled to a fluorescence detector (LIF) was also developed. The objective was to reveal and control the crucial influence of copolymer concentrations, stirring time, pH and ionic strength gradients on the formation, equilibrium, and stability of functional micelle-like aggregates.

In the second step, a deep understanding of the interactions between the micelle-like aggregates (Mic) and antineoplastic drugs, such as doxorubicin, has to be provided thanks to the combination of capillary electrophoresis, DLS and TEM. This would allow connecting the drug loading and release capacity to the NPs synthesis parameters and to regulate the type of interactions involved in the loading and release processes.

Finally, the synthesis and characterisation of Janus-type magneto-luminescent hybrid inorganic nanoparticles with magnetic and up-conversion fractions were performed. They were then encapsulated, along with active ingredients, in the micelle-like aggregate previously synthesized. for characterisation and perform drug release tests using light irradiation stimuli and/or pH change. The drug loading and release process have then to be understood and quantified with this smart hybrid magneto-luminescent Janus-type NPs, decorated with a pH and UV-light responsive polymer.

CHAPTER I

Nanomaterials for controlled drug delivery in response to external stimuli: State of the art

1.1 Drug Delivery

Cancer is a disease in which cells in the body multiply out of control and spread to other parts of the body. Under normal conditions, human cells form and multiply to form new cells as the body needs them. As cells age or become damaged, they die and are replaced by new cells. When the process does not follow this order and abnormal or damaged cells form and multiply when they should not, tumours, which are lumps of tissue, form. In addition, tumours are either malignant (cancerous) or benign (non-cancerous). Cancerous cells cause blood vessels to grow in the direction of the tumours carrying oxygen and nutrients, reducing these in adjacent normal cells, causing their death. On the other hand, cancerous tumours can spread and/or invade nearby tissues. They may also travel further to other parts of the body and form other tumours, in a process called metastasis.[42] Worldwide, it is the second most common cause of death, while in Mexico and France, it is the third and fourth most common cause respectively.[43–45]

Chemotherapy, being the treatment mostly used for curing cancer disease, provokes various side effects due to the uncontrolled reaction of the drugs in normal and cancerous cells. To avoid those concerns, drug delivery has been developed, so as to transport therapeutic agents into a specific region of the body with adequate pharmacokinetics. The delivering strategies consist of enteral and parenteral paths in which the first strategy involves the gastrointestinal tract, including oral, rectal, or sublingual approaches, while the second strategy comprises intravenous, intramuscular or subcutaneous administrations. Even though it is non-invasive, the enteral path reduces drug bioavailability due to metabolic transformations or incomplete absorption.[1] Hence, the development of new therapies which could allow a controlled release of drugs overcoming the disadvantages of first-pass metabolism and side effects has been a central issue for the scientific community.[2]

The first section of the chapter defines the drug delivery nanostructures and how their unique physicochemical properties are being harnessed for the treatment of different diseases, among which cancer. Some important parameters involved in the smart releasing of drugs and proper vectorization towards targets of interest are also described, as well as some important parameters regarding their biocompatibility. A special emphasis is made on the intelligent polymers, which release the effective cargo upon appropriated stimuli.

1.1.1 Nanostructures for drug delivery

Since the discovery of the enhanced permeability and retention (EPR) effect three decades ago and impaired lymphatic drainage of tumours, nanotechnology has been identified as a promising tool for the formation of drug delivery vehicles for cancer treatment or therapy. The EPR effect is based on the hyperpermeability of the tumour vessels, which allows particles to enter the tumour interstitial space, as well as on the absence of functional lymphatics in the tumour interior, which enables them to stay there for a long time. The hyperpermeability of tumour vasculature is mainly due to the large intercellular openings between endothelial cells that comprise the neoplastic tumour vessel wall.[46] These openings might be hundreds of nanometers in size, contrary to the openings of the normal vessel wall, whose size is less than 10 nm. Therefore, the rationale for employing the EPR effect to treat cancer is that therapeutic nanoparticles with sizes larger than 10 nm will not be able to extravasate to normal tissues, reducing adverse effects, and would selectively pass through the openings of the tumour vessels.[47]

For these, there are different nanostructure configurations like nanofibers, nanocomposites, nanoparticles (NPs), and nanotubes that have been employed for transporting agents like vaccines, drugs, genes, proteins, and enzymes.[3] Nanocarriers can be designed from a variety of materials in different shapes and sizes for drug delivery systems (DDS) described in Figure 1.1. They should provide good biocompatibility and are generally inactive in normal physiological environments. These nanocarriers most have a long-term blood circulation period with the sustained release of drug overcoming the endosome–lysosome mechanism.[4] The modification of the physiochemical properties of nanocarriers such as surface, composition as well as shape can enhance their activity with decreased secondary effects.[4] Thus, some of the unique features of nanocarriers include: enhanced biodistribution, pharmacokinetics, stability, solubility and reduction in toxicity.

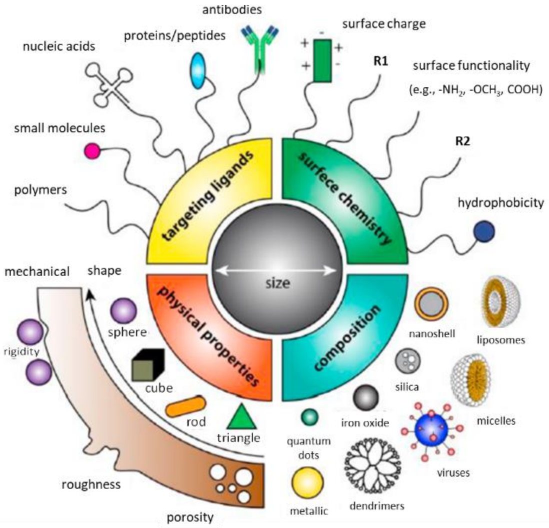

Figure 1.1. Schematic representation of some general parameters considered during the design of nanocarriers for drug delivery applications.[4]

Nanocarriers are colloidal nanoparticles which size should lie between 1 and 100 nanometer (nm) in diameter, as the microcapillaries of the body are 200 nm.[5] These nanoparticles (NPs) could be of organic, inorganic and hybrid (combination of materials) nature. Organic nanocarriers include NPs such as liposomes, dendrimers, polymers, micelles and viral capsids. They are very versatile and can conjugate a variety of drugs as well as ligands for appropriate drug delivery.[48] Inorganic nanocarriers are based on noble metal, semiconductor, metal oxide and lanthanides. Some remarkable examples include gold NPs, quantum dots, magnetic NPs, mesoporous silica, and upconverting NPs. These inorganic nanocarriers also possess synergetic therapeutic effect in their implementation such as photodynamic o photothermal therapies, in addition to drug delivery.[49] Furthermore, altering the composition or size of the inorganic nanocarriers enables remarkable magnetic, plasmonic or optical properties. Hybrid nanocarriers combine two or more organic and inorganic moieties with additive or synergistic activity, and some representative configurations are organic–inorganic, inorganic–inorganic, or multi components.[6]

Since it is vital to avoid side effects, nanocarriers need to be site-specific, and smart drug delivery systems have been developed. These limitations in nanocarriers synthesis have led to the development of smart nanocarrier-based drug delivery systems, which are also known as Smart Drug Delivery System (SDDS).

1.1.2 Smart drug delivery systems

A smart drug delivery system consists of three main elements: (i) smart nanomaterials that enable efficient anticancer drug transport, (ii) targeting properties for efficient delivery at the cancerous site for therapeutic action, and (iii) stimulus strategies to control the loading and release of the payloads at the pre-located cancer cell site.[6] In addition, they should avoid the clearance process by the immune system, should be accumulated for cargo release at the target site and at the right concentration under external or internal stimulation. Some methods to convert conventional nanomaterials into smart nanocarriers cand be found, including functionalization for specific targeting of cancer cells, incorporation of stimuli-responsive moieties, and incorporation of other substances to be co-delivered.[5]

Here, the most reported nanocarriers in smart DDS are presented (Figure 1.2): (i) liposomes, (ii) dendrimers, (iii) carbon nanotubes (CNTs), (iv) polymeric micelle-like nanoparticles, (v) meso-porous silica nanoparticles (MSNs), (vi) gold nanoparticles (GNPs), (vii) super paramagnetic iron oxide nanoparticles (SPIONs), (viii) quantum dots (QDs), and (ix) upconverting nanoparticles (UCNPs).[6] Each of these nanocarriers will be briefly described below, and special attention will be paid to micelle-like aggregates (Section 1.2) and upconverting nanoparticles (Section 1.3), both of which are object of further studies in this work.

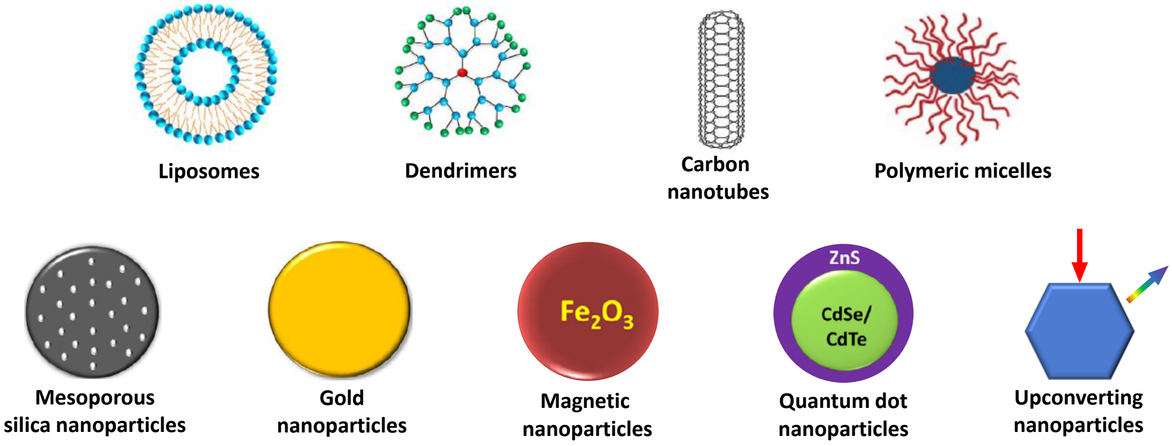

Figure 1.2. Schematic representation of the nanocarriers more used in smart drug delivery systems.[6]

Liposomes are natural amphipathic phospholipid-based nanocarriers consisting of a fatty acid-based hydrophobic tail and a phosphate-based hydrophilic head phospholipids. Liposomes are formed when these phospholipids self-assemble in an aqueous medium into bi-layer vesicles with polar ends facing the water and non-polar ends forming liposome core with the property of entrapping water or water-soluble drugs. Based on the number of bilayers and the size of the liposome, they can be classified into large/small uni- or multi-lamellar vesicles. Smart liposomes can be responsive to various external and internal stimuli, including pH variations, enzyme transformation, redox reaction, light, ultrasound, and microwaves, thus allowing for the release of the drugs. Functionalization of conventional liposomes with molecules such as polyethylene glycol helps liposomes escape the reticuloendothelial system (RES), while the grafting with specific biomolecules like peptides, antibodies, or proteins, allows to actively target the cancer cells.[50]

Dendrimers are branched polymers nanoscale size, monodisperse, water soluble and biocompatible. They composed a core, some branching dendrons and surface-active groups, which will determinate dendrimers physiochemical hydrophobic or hydrophilic properties. In addition, these surface-active groups are oriented outwards, allowing drug encapsulation inside the dendrimer by drug – surface-active groups. Dendritic surface modifications can be realized to directly attack cancer cells by peptides, proteins, carbohydrates, aptamers, antibodies, etc. and it can also be modified by various stimuli responsive agents for a controlled drug released.[51]

Meso-porous silica nanoparticles (MSN) are nanomaterials formed by ordered or hollow/rattle-type meso-porous silica (SiO_2) structures, having high surface areas of the internal (honeycomb-like porous) and external surface. The adjustable pore size is suitable for drug loading and for grafting different functional groups. By grafting the surface with stimulus-responsive copolymers, including endogenous (pH, redox, enzyme, etc.) or exogenous (temperature, light, magnetic field, etc.) stimuli, they can work as gatekeepers to control the pore opening-closed mechanism for drugs loading and release processes. For targeting the delivery of MSNs to the cancerous zone, it is possible to modify their surface with the use of small molecules folate, mannose), transferrin, peptides and antibodies.[52]

Gold nanoparticles (GNPs) are metal nanocarriers with different shapes and sizes, that can deliver payloads (drug molecules, proteins, DNA and RNA). By grafting their surface with polymers, drug release can be achieved under external (ultrasound, X-ray, light, etc.) or internal stimulus. In addition, due to the surface plasmon resonance (SPR) phenomenon, GNPs are also able to convert light irradiation to heat, dispersing it to kill the cancer cells. To show enhanced solubility and stability under physiological conditions, PEGylation of their surface can be realized. Their surface grafting with suitable ligands (peptides or antibodies)[53] can allow their penetration through the blood brain barrier. Also, using various simple ligands, like transferrin (TF) or folic acid, GNPs surface modification can be done to direct them to tumours.[54]

Super paramagnetic iron oxide nanoparticles (SPIONs) are magnetized nanoparticles under the application of a magnetic field that presents no residual magnetism after magnetic field is retired. Examples of this kind of NPs include iron oxides maghemite/magnetite (Fe_3O_4), and their mixtures with other transition metals like copper, cobalt, and nickel. Those nanoparticles are usually functionalized to reduce their aggregation, protect their surfaces from oxidation, avoid their capture by the RES, and get adequate affinity to conjugate drugs and targeting ligands. Cationic lipids and polymers, for example, can modify SPIONs for drugs and genetic materials delivery. In another strategy, stimuli-responsive polymer can coat SPIONs also for drug delivery. As a main advantage, the vectorization of these nanocarriers can be controlled by an external magnetic field.[55]

Carbon nanotubes (CNTs) are graphene sheet carbon allotropes rolled up to achieve a cylindrical tube structure. Depending on the graphene sheets, they can be classified in single walled (SWCNT) and multi-walled (MWCNT) CNTs. Even though they can pass through various cellular barrier, it is possible to functionalize them in a chemical or physical manner to increase solubility, avoid the RES, and increase their biocompatibility. Furthermore, CNTs have been modified with DNA, siRNA, antisense and aptamers and have been employed for drug loading and releasing by stimuli responsive polymeric functionalization. In addition, functionalized CNTs can be used as a diagnostic tools via photothermal ablation due to the strong optical absorption at the NIR region.[56]

Quantum dots (QDs) are fluorescent and phosphorescent semiconducting NPs with photophysical properties, often made of atoms from II and VI groups in the periodic table, as well as transition-metal dichalcogenides, perovskites, and carbon, among others. These NPs have applications not only in drug delivery, but also as contrast agents in tumours for optical imaging. They essentially consist of a core, a shell, and a capping material. As an example, a composition of a small (2–10 nm) core CdSe and a shell ZnS. Due to their position of a versatile surface chemistry, QDs are allowed to modify their photophysical properties and surface to enhance the applicability by capping the QDs double layer. Also, tumour site targeting is possible by using ligands like peptides, folate, or proteins to graft QD surface.[57]

Furthermore, the use of multiple nanostructures integrated into a single nanosystem that can provide simultaneous diagnostic and therapeutic functions in a single dose, are called “theranostic tools”.[7] It is then possible to follow their biodistribution, monitor the progress and efficacy of a therapy, by an in vivo imaging. In general there are two approaches to form these theranostic tools, either by bonding the surface of a solid NPs to another NP, or by encapsulating one nanostructure into another, forming hybrid nanoparticles.[8] **Hybrid nanomaterials** are mixtures of two or more inorganic and/or organic components, having either core-shell or Janus-like structure. The resulting nanomaterial will have a synergistic mix of their own physicochemical properties.[58] Organic hybrid nanosystems are commonly composed of polymer-protein, polymer-lipid, or polymer-polymer. For example, *Chen Tang et al.* produced submicrometric-sized polymeric polyacrylonitrile/polystyrene hybrid polymeric nanoparticles by seeded emulsion polymerisation.[59] Inorganic hybrid nanoparticles such as magnetic-mesoporous silica, gold-iron, mesoporous silica-upconverting nanoparticles, etc. are some commonly use examples. *Chen Xiangjun et al.* reported PEGylated branched gold-iron oxide (Au-Fe_3O_4) NPs, synthesized via a simple hydrogen reduction and providing a photothermal effect due to the irradiation of near-infrared (NIR) light.[60] Organic-inorganic hybrid NPs, on the other hand, are the most used nanosystems for DDS, normally mixing metal NPs with polymeric micelles in a core-shell structure. Although the core-shell structures are most common, Janus-like hybrid nanoparticles (JNPs) have been also obtained. Some clear advantages lie on their asymmetric structure, as it allows (i) the reduction of signal attenuation or interference,(ii) independent release of multiple drugs, (III) possible photothermal properties, and (iii) a motion of JNPs thanks to a potential gradient for different therapies or DDS.[61]

However, for a smart drug delivery nanosystem, the drug-controlled release at the sites of interest must be achieved. Accordingly, stimuli responsive agents decorating nanocarriers have been described in the last recent years as potential effective strategies to enhance this process. Therefore, stimuli-responsive nanocarriers will be described in the following section, with a subsequent focus on smart polymers.

1.1.3 Stimuli responsive agents

Reacting to an external or internal stimulus, drugs and genes have been efficiently delivered by stimuli-responsive nanosystems, based on lipidic and polymeric compounds such as liposomes, micellar assemblies, micelle-like nanoagregates, dendrimers, and others similar nanoparticles. Furthermore, these stimuli-responsive nanosystems can be actively (specific affinity to receptors) or passively (based on the EPR effect) adapted for targeting approach.[62]

Inside the body, there are significant differences between cancerous tissues with respect to healthy tissues, such as pH difference, highly oxidative conditions, abnormal enzyme gradients, among others. These differences have helped to developed endogenous stimuli-responsive nanocarriers corresponding to pH, redox, enzymes and hypoxia stimuli. On the other hand, the use of various external sources like light, magnetic field, temperature or ultrasound, have also brought advancements in the development of these responsive-nanocarriers.[63] Figure 1.3 schematize some endogenous and exogenous stimuli properties.

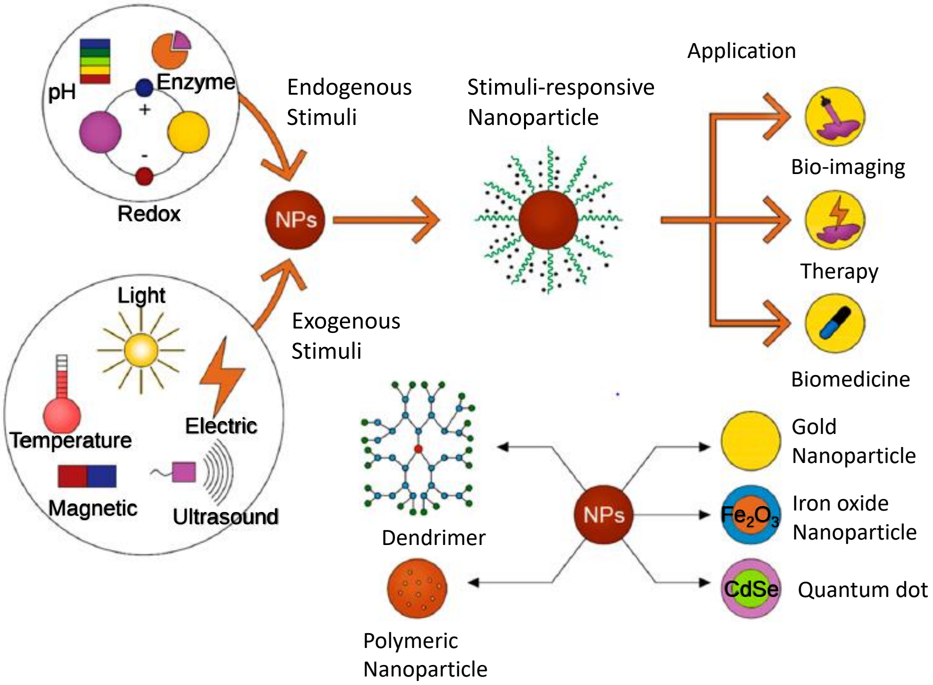

Figure 1.3. Schematic diagram of stimuli-responsive nanomaterials.[63]

INTERNAL OR ENDOGENEOUS STIMULI

pH is a common stimulus in drug delivery, employed either in conventional treatments via gastrointestinal track or in nanocarriers delivery at cells organelles such as lysosomes, golgi, and endosomes.[64] Interestingly, in healthy tissues and blood, extracellular pH is generally conserved at 7.4 (physiological pH). In tumours however, extracellular pH is more acidic, ranging between 5.5–7.2 due to the high glycolysis.[65] The shift towards a glycolytic metabolism is due to the production of acidic metabolites, consequence of irregular angiogenesis in fast-growing tumours, which causes a rapid shortage of both nutrients and oxygen.[66] In the anticancer drug-delivery systems, stimuli-responsive polymers are mainly used, employing two principal strategies: (i) the use of polyacids or polybases which experience changes, either in their solubility or in their conformation thanks to their ionisable groups; and (ii) the incorporation of molecules with acidification-sensitive bonds into the polymer chain, which are broken (releasing the anchored molecules), or can modify the polymeric electrical charge.[67] Nowadays, several types of pH-sensitive nanocarriers, including mesoporous silica-polymeric nanoparticles[68], magnetic-polymeric nanosystems[69], polymer-drug nanoassemblies[70], polymeric micelles[71], liposomes[72], polymersomes[73], nanogels[74], and dendrimers[75], etc., have been explored.

Redox stimuli are present in cancerous cells due to highly oxidant conditions resulting from oxidative stress. Reactive oxidative species (ROS) levels in inflamed tissues is 10–100 times greater than in healthy ones. Furthermore, glutathione (GSH) concentration in cancerous tissues is 100–1000 times greater than that in blood, and about 100 times more than that in healthy physiological tissue.[76] This molecule is a strong reducing agent due to the presence of the thiol group which inhibits ROS accumulation. This biomarker has been also used as an interesting stimulus for drug delivery because disulphide bonds are susceptible to rapid cleavage by GSH, attaining redox sensitivity.[77] Diselenide bonds (Se-Se) are also sensitive to redox potential variations, but with lower bond energy than that of the disulphide analogous.[78] Moreover, the H_2O_2-responsive nanocarriers have been also developed for tumour therapy, including for treating hypoxic and multidrug resistant tumours.[79] The redox-responsive method could also be applied to separate the surface shell[80] cross-linking the core to increase stability.[81] Various redox-sensitive nanocarriers have been designed such as nanocapsules[82], mesoporous silica nanoparticles[83], polymer-drug conjugates[84], polymersomes[85], polymeric vesicles, polymeric micelles[86], nanogels[87], inorganic nanoparticles, etc.[88–90]

Enzymes play a fundamental role in most physiological processes, such as angiogenesis, cell proliferation, migration, autophagy, and apoptosis. It has been found a group of enzymes whose expression is increased or reduced in tumoral tissues, including Proteases, Phospholipases, Glycosidases, Azobenzene reductase, and Glutathione reductase.[91] Thus, nanosystems for drug delivery take advantage of the presence of these enzymes in the cancerous extracellular medium to provoke the release. The enzyme-sensitive nanocarriers work on the basis of the following mechanisms[92]: (i) cleavage of enzyme-sensitive bonds between bioactive compounds and protecting groups for activating prodrugs, probes and ligands; (ii) cleavage of enzyme-activated polymer chain leading to disassembly of nanomaterials; (iii) direct cleavage of the conjugation between nanocarriers and drugs. Several enzyme-sensitive nanocarriers have been designed such as polymeric assemblies[93], nanoparticles[94], and hydrogels[95], mesoporous silica nanoparticles[96], dendrimers[97], magnetic nanoparticles[98], polymeric micelles[99] and liposomes[100], etc.

Hypoxia is the absence of sufficient oxygen in the tissues and is one of the main characteristics observed in cancerous tumours (more than 60%), where the oxygen partial pressure is less than 10 mmHg (13 µmol/L) compared to the 40–60 mmHg (50–80 µmol/L) in normal tissues.[101,102] This insufficient oxygen supply from the blood is due to (i) abnormally fast metabolism, (ii) disorganised vasculature and (iii) the short oxygen diffusion distance (< 200 µm) between vessels, generated by the uncontrolled growth of the cancerous tumour.[103] In this pathological environment, enzymes (nitroreductase, azoreductase, inducible nitric synthase, methionine synthase reductase, DT-diaphorase (DTD) and nicotinamide adenine dinucleotide phosphate (NADPH)) that are involved in electron reducing or electron donating reactions are upregulated by aerobic glycolysis in hypoxic cells.[104] Additionally, this same hypoxic environment generates increased resistance to common therapies (radiotherapy, chemotherapy, photodynamic therapy and sonodynamic therapy). Based on these findings, researchers have designed and developed some hypoxia-activated nanocarriers, including liposomes[105], MSNPs[106], UCNPs[107], layer-by-layer nanoparticles[108], nanovesicles[109], polymeric micelles[110], polymersomes[111], albumin nanoparticles[112], cell membrane coated metal organic framework (MOF)[113], etc.

EXTERNAL OR EXOGENOUS STIMULI

Light irradiation, such as UV-Vis and near-infrared light (NIR), could remotely activate the light-sensitive nanocarriers in biological systems (e.g., cancer cells, or tumors).[21] Meanwhile, light-activated tumour treatment could be carried out in a very specific way by controlling the precise wavelength range of irradiation to avoid or minimise damage to normal organs and tissues as do short UV-Vis wavelengths.[114] Thereby, studies applying NIR light-sensitive nanocarriers have been prioritised.[115] [116] Nanocarriers could response to light for drug delivery and light-activated tumour therapy by: (i) changing the structural conformation of various molecules like azobenzene, spiropyran, dithienylethene and diazonaphthoquinone etc.[21] (ii) cleaving the light-sensitive chemical bonds for the dissociation of the nanocarriers such as o-nitrobenzyl (ONB) alcohol, truxillic acid derivatives, etc.;[21] (iii) generating reactive oxygen species (ROS) like singlet oxygen ($^1O_2$) for photodynamic therapy (PDT) by porphyrins, chlorins, bacteriochlorins, phthalocyanines, naphthalocyanines, corroles, etc.,[117] and (iv) inducing a photothermal effect for tumour ablation by photothermal therapy (PTT) using photo-thermal agents (PAs) such as carbon, gold, silver and germanium nanomaterials.[118] Several light-responsive nanocarriers have been exploited, including polyion complex vesicles (PICsomes)[119], polyplexes[120], polymeric micelles[121], polymersomes[122], liposomes[123], nanogels[124], nanorods[125], nanorattles[126], upconverting nanoparticles (UCNPs)[127], gold nanoparticles (GNps)[128], graphene[129], and carbon nanotubes[130], etc.

Magneto-responsive nanocarriers have a natural movement intrinsic to the magnetic field applied to the tumours, while they could also generate local hyperthermia to simultaneously trigger drug release and tumour ablation. Nanocarriers incorporate magnetic materials such as iron oxide nanoparticles (Fe_3O_4)[131] or iron oxide hybrid nanoparticles (graphene/Au/Fe_3O_4, $ZnFe_2O_4$, etc.).[132,133] Also, for tumour detections, analysis and imaging, the incorporation of MNP by magnetic resonance imaging (MRI) could be performed.[134] The magnetic-guided accumulation of nanocarriers in tumours can be induced by locating a permanent magnetic field in malignant tissues after administration.[135] In addition, the hyperthermia phenomenon could induce apoptosis of cancer cells, or release of drug-biomolecules from magnetically sensitive nanocarriers in the specific affected regions.[136,137] Considering the combination of these applications, magnetic-sensitive nanocarriers are usually considered as theranostic agents.[138]. Until now, several magnetic-responsive nanocarriers have been formulated, including magnetic nanoparticles[139], liposomes[140], superparamagnetic iron-oxide nanoparticles (SPIONs)[141], polymeric micelles[142], and magnetic nanogels[143], etc.

Thermo-responsive nanocarriers have been widely used where thermo-responsiveness is observed by an abrupt change in the properties of at least one component of the nanocarrier that may undergo physico-chemical variations, such as solubility, associated with the surrounding temperature, triggering drug release.[144] For biomedical applications, nanocarriers are typically designed to be stable at physiological temperatures (37°C) and sensitive at higher temperatures (> 40°C).[92] Some thermo-responsive polymers include poly(Nisopropylacrylamide) (PNIPAM)[145], poly(N-inyl isobutyramide) (PAMAM)[146], poly(2-oxazoline) (POxs)[147], and poly [2-(2-methoxyethoxy) ethyl methacrylate] [PMEOMA][148], among others.[149] Another thermo-responsive strategy is to produce a slight decrease in temperature such as cryotherapy where a swelling or deflation of the nanocarrier allows drug diffusion due to increased porosity.[150] Some thermosensitive nanocarriers that have been analyzed are liposomes[151], polymeric micelles[152], nanocapsules[153], nanogels[154] and vesicles[155], etc.

Ultrasound is a transducer-generated sound wave that, when propagating through body tissues, produces various physical effects such as pressure variation, acoustic fluid flow, cavitation and local hyperthermia.[156,157] Thus, by adjusting the frequency to high (> 20 kHz) or low (< 20 kHz), the strategy could enable both controlled drug release by nanocarriers and monitoring imaging, respectively.[92] For example, compressible objects such as microbubbles contract and expand as they experience the passage of acoustic waves. These cavitation-induced changes in volume lead to the capture and release of drugs, and the scattered "echoes" can be used for imaging.[158] Interestingly, radiation forces generated by the ultrasonic field can lead to the direction of movement of fluid currents (acoustic flow), which allows the controlled and localised displacement of NPs.[159] In addition, acoustic waves generate thermal energy that can propagate through tissues and generate friction that can be used as a hyperthermia strategy in cancer treatment. Focused ultrasound can lead to localized tissue heating, and thus for tissue hyperthermia and drug release from thermo-sensitive carriers.[160] Several size switchable nanocarriers have been engineered, such as nanobubbles[161], calcium carbonate ($CaCO_3$) nanoparticles[162], liposome[163], nanodroplets[164], and nanoparticles[165], etc.

Stimuli-sensitive NPs could therefore control the dosing frequency, generally including the participation of polymeric systems that act like "molecular gatepeekers". Thus, a compilation of the most commonly used stimuli-responsive polymers is presented in the next section.

1.1.4 Stimuli-responsive polymers for smart drug delivery systems

Stimuli-responsive polymers are materials that can display remarkable changes in their properties with slight change in environmental conditions. These systems may be formed by either amphiphilic polymers which spontaneously aggregate into core–shell self-assemblies, encapsulating the drug; or physical conjugation of the drug onto the responsive-polymer backbone creating an amphiphile for further self-assembly or surface functionalisation of a preformed polymer nanoparticle. The most frequently used polymers for pH-, thermo-, and light- stimuli are presented below.

pH-responsive polymers with pKa values between 3 and 10 are formed by weakly acidic or basic ionisable groups.[166] These groups either accept or donate protons in response to changes in environmental pH. The pendant acidic or basic groups such as carboxylate, sulfonate and amino groups are gradually ionised as a function of pH, inducing alterations of the structure, solubility, surface activity, and/or polymeric chain conformation, whereby specific polymer groups switch between a neutral and charged state.[17] pH-responsive polymers can be catalogued according to their chemical composition as homopolymers or copolymers; according to their structure like linear, grafted, brushed, star-like and dendritic structures; or according to their polarity like amphiphilic, hydrophobic or hydrophilic molecules. Some functional presentations of these materials include solid spheres, micelles, micelle-like aggregates, vesicles or hydrogels. [167] Two main strategies have been employed to design such stimuli-sensitive polymers. One consists of polymers which undergo modification of their charge, either through (i) weakly acidic functions that lead to swelling at basic pH or (ii) alkaline functions that lead to swelling at acidic pH. This contributes to an electrostatic repulsion between polymeric charged groups, conformational and/or solubility changes, which leads to the drug release.[64] The second approach is the addition of an acid-cleavable bond into the polymeric chain, resulting in the polymeric detachment causing the drugs- biomolecules release.[18] Those strategies are schematized in Figure 1.4.[19]

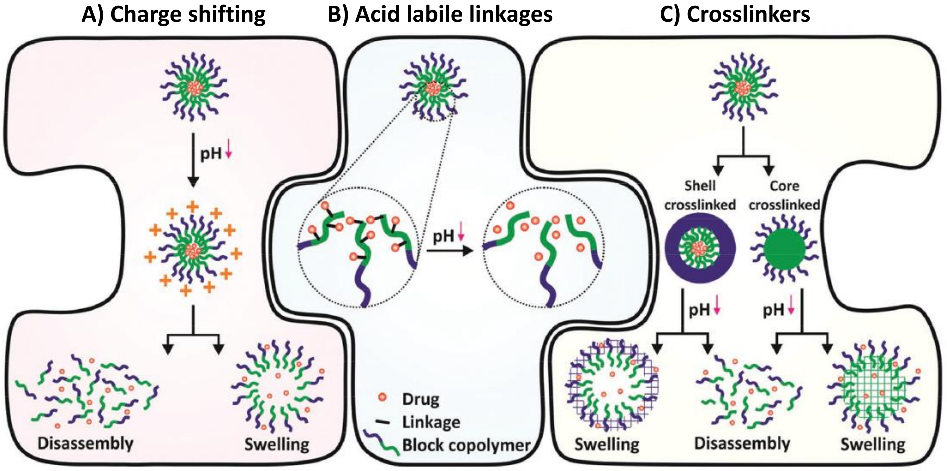

Figure 1.4. Schematic representation of strategies in pH-responsive polymers nanosystems.[19]

The change from hydrophobic to hydrophilic properties is one of the most commonly used processes for pH-sensitive polymers when they are in an acidic environment. Molecular groups such as amines are part of these polymers as in the case of poly(2-(diisopropylamino)ethyl methacrylate) (PDPAEMA), poly(4-vinylpyridine) (P4VP), poly(histidine) (PHis) and poly(β-amino ester).[19]When the pH of the polymer is lower than the pKa, the protonation phenomenon of the amino group changes the polarity (from hydrophobic to hydrophilic), simultaneously sensing an electrostatic repulsion when the ambient pH drops below its pKa (Figure 1.5). Amphiphilic copolymers are used to introduce hydrophobic pH-sensitive moieties into the synthesis of DDS, thus forming self-assembling structures. It is necessary that the sensitive fractions maintain their hydrophobicity at physiological pH (7.4) and switch to their hydrophilic properties in the acidic environment of the tumour medium.[19]

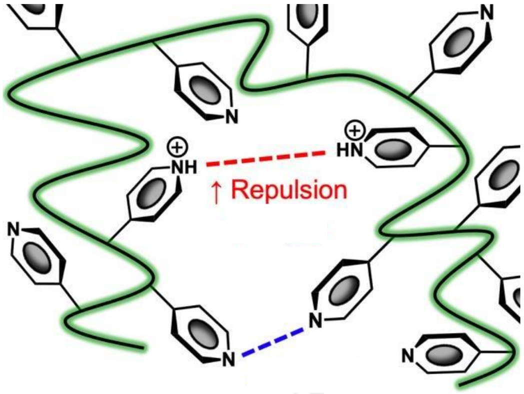

Figure 1.5. Schematic representation of an amino group protonation experimenting electrostatic repulsion.[168]

For example, *Thi Lien Nguyen et al.* reported the self-assembly of pH-responsive random and block copolymers composed of poly(2-(diisopropylamino)ethyl methacrylate) and poly(2-methacryloyloxyethyl phosphorylcholine) in aqueous media showing that in acidic pH, these copolymers disaggregate to single polymer chains. In contrast, separated micelles were formed in the mixture upon increasing the pH of the solution above the critical value of 8.[169] In our previous work, a covalent functionalization of Fe_2O_3 SPIONPs with a triblock copolymer including a alkoxysilane array, APTES-3TMPM, and the pH-responsive P4VP was formed. P4VP polymeric chains underwent hydrophobic-hydrophilic reversibility in acidic conditions induced by protonated pyridine repulsive forces between chains, thus allowing the capture and release of a drug.[170] Also, *Penghui Wang et al.* used poly(L-histidine) as a pH-responsive hydrophobic block to synthesize a block copolymer (PEG-PCL-PHis) combined with hydrophilic poly (ethylene glycol) for DDS. After a slightly acidic pH changed conditions, it experienced a hydrophobic-hydrophilic transition that control DOX loading-release process.[171] Thus, charge-changing nanomaterials produced by pH differences, which also have a fast response as they do not require polymer bond breaking, have great potential in DDS with the capacity the endosomal escape.

In the context of pH smart polymers, another strategy implies the incorporation of covalent pH-responsive linkages that are stable at neutral pH, but labile at acidic pH. The pH-responsive linkages most commonly discussed include hydrazone, imine, acetal/ ketal, cis-aconityl group, and β-thiopropionate moieties (Figure 1.6). The hydrazone linkage (Figure 1.6A) is one of the most used linkages in pH-responsive DDS. Hydrazone hydrolyses very slowly at pH 7.4, in contrast to acidic pH

(5-6) where the rate of hydrolysis is higher. Also, the hydrophilic biocompatible polymer poly(N-(2-hydroxypropyl)methacrylamide) (HPMA) has been widely used as hydrazone linked polymer–drug conjugates for delivery systems.[172] For example, *Yamini Bobde et al.* worked on the self-assembled polymer-drug conjugate-nanoparticle (p(HPMA)-p(HPMA-NH-N-DOX)-b-mPEG(P6)) which shows a faster release of doxorubicin (DOX) from the nano conjugate at the intra-tumoral environment (pH 6.5) and intracellular pH (pH 5.5) compared to the release at physiological pH (pH 7.4).[173] Hydrazone can also be used to engineer pH-responsive NPs. For example, *Zhijian Chang et a*l. synthesised a combined self-assembly polymeric platform for drug release and photodynamic therapy. The MPEG-Hyd-Br2-BODIPY structure was based on 2,6-diBr-BODIPY as the photosensitizer core, and on MPEG as the hydrophilic side chain which exhibited an accelerated release rate when pH was decreased from 7.4 to 5.0.[174] Hydrazone linkages have also been used to conjugate drugs onto hyperbranched NPs. For example, *Guoping Li et al*. designed a hydrophobic pH- triggered carbon dot –hydrazine-drug conjugate (CDs-Hy-DOX) with covalently conjugated DOX onto the carbon dots (CDs) via acid-labile linkage with hydrazine (Hy) as bridge. Then the fluorescent traceable hybrid prodrug nanoparticles were fabricated via co-self-assembly with the CDs-Hy-DOX as pH-sensitive prodrug and a pH/reduction dual-triggered degradable hyper- branched polymer PEG-PO-Cy as polyethylene glycol (PEG)-based surfactant, as well as gatekeeper for pH/reduction dual-triggered DOX release.[175]

Because of their weak bonds under acidic conditions, imine groups (Figure 1.6B) have also been studied to design pH-responsive NPs in DDS. For example, *Ding et al.* developed dextran-doxorubicin NPs conjugates based on imine linkages (DEX-Dox), where the hydroxyl groups of dextran are oxidised to aldehydes for conjugation to Dox by forming imines.[176] Likewise, the cis-aconityl group (Figure 1.6C), derived from the maleic acid amide (MAA) family, has been used in polymeric NPs for DDS. For example, *Jingyi Zhu et al.* developed a hybrid nanosystem of dendrimers with GNPs (Au DENPs) for DOX transport release at acidic pH, where the drug is covalently bond to the folic acid-functionalised acetylated poly(amidoamine) dendrimer via linkages with the pH-sensitive cis-aconityl group for subsequent integration of the GNPs.[177]

Another pH-responsive linker is acetal (Figure 1.6D), taking as an example the work reported by *Emily T. et al.* modifying polysaccharide NPs with acetal and finding their degradation upon acidic pH change.[178] In the case of the β-thiopropionate linker (Figure 1.6E), *Chao-Ran Xu et al.*, as an example, developed an amphiphilic polymer consisting of poly(2-(2-hydroethoxy) ethyl methacrylate) (PHEO2MA) and dihydrolipoic acid (DHLA) functionalised with acrylate-tetractocin

(ACPT) to form nano-aggregates in aqueous solution. At pH 6, the β-thiopropionate linkers released the drug camptothecin (CPT) .[179]

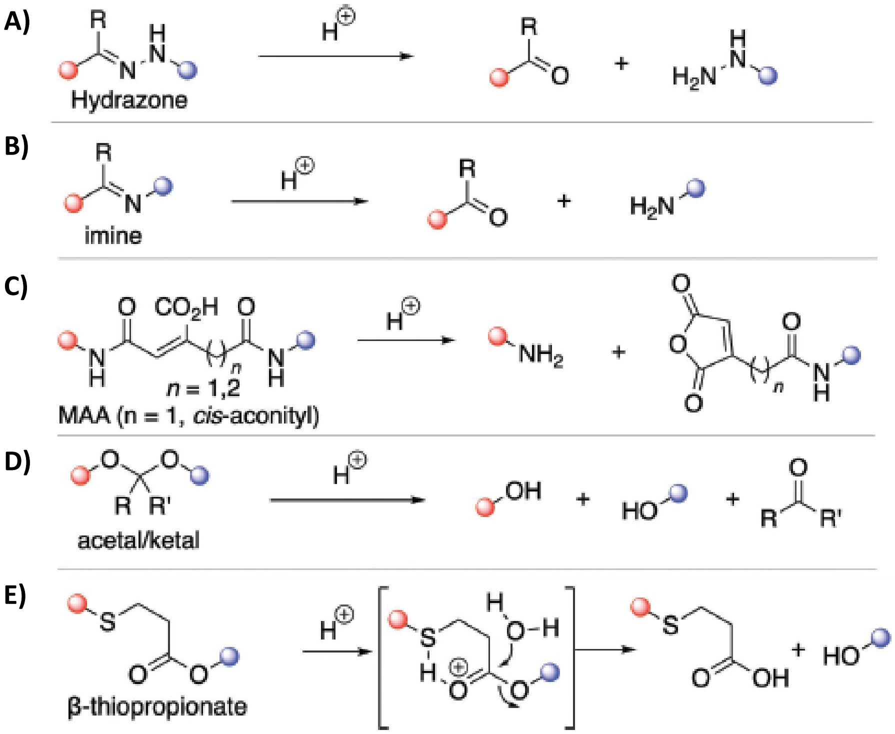

Figure 1.6. pH-responsive moieties with their respectively hydrolyzed subproducts. A) Hydrazone linkages; B) imine linkages; C) maleic acid amide (MAA) linkages as cis-aconityl linkages); D) acetal/ketal linkages; E) β-thiopropionate linkages.[19]

One challenge in NPs DDS is to maintain appropriate colloidal stability once they are dispersed in biological environments. Crosslinking as strategy could enhance the NPs stability.[19] Crosslinking is the general term for the process of forming covalent or non-covalent interactions to join two polymer chains together. Ideally, the cross-linking should be reversible, allowing the NPs to decompose upon reaching the target site. Examples of degradable crosslinkers are disulphurised or pH-sensitive derivatives.[180] For example, polymeric nanogels (NGs) are cross-linked NPs that form a structure network. When these are held together by molecular entanglements and/or secondary forces (ionic, H-bonding or hydrophobic), they are called physical or reversible nanogels, as opposed to permanent or chemical gels that use covalent bonds. There is also the combination of physical and chemical networks called semi-interpenetrating networks. When undergoing a shift to a more acidic pH, NGs generate porosity by electrostatic repulsions. For example, with acidic groups such as carboxylic or sulphonic ones present in the NGs, a swelling and increase in hydrophilicity of the NP will be observed due to these repulsions, generated by the negative charge on the inner groups in the polymer chains. On the other hand, if basic groups, such as amines, are used, they also exhibit polymeric repulsions when ionised. The degree of ionisation will depend on the number of pendant groups.[167] In a recent study, *Taehoon Sim et al.* (Figure 1.7) synthesised pH-sensitive NGs based on poly(aspartic acid-graft-imidazole)-poly(ethylene glycol) using PEG as linear crosslinkers. By trapping the drug irinotecan (IRI), it was shown that at acidic pH it changes its size due to the swelling process it undergoes, thereby triggering release.[181]

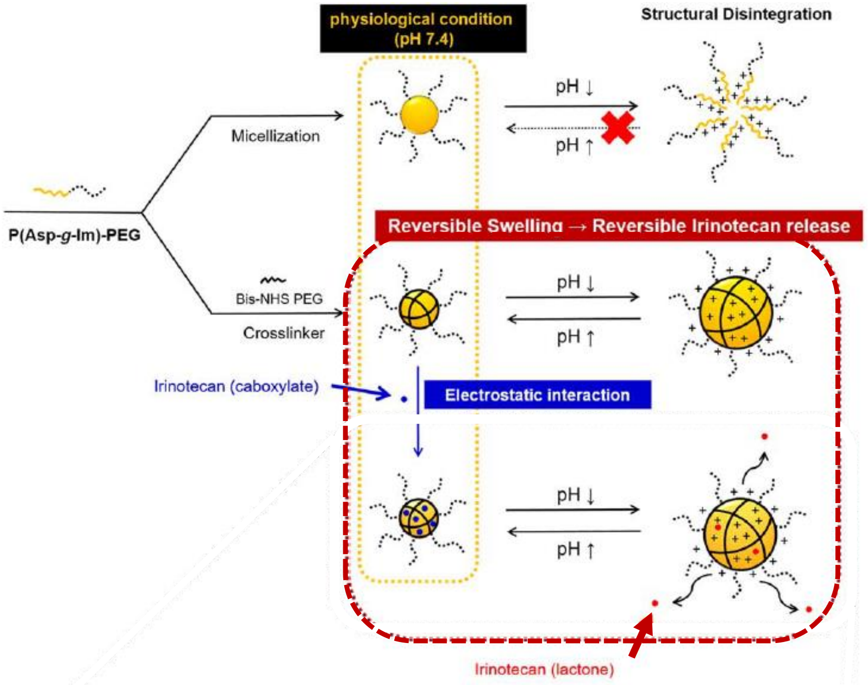

Figure 1.7. Crosslinking strategy representation in pH-responsive polymers nanosystems.[181]

Thermo-responsive polymers have a temperature parameter called the critical solution temperature in which the polymer exhibits a temperature transition phase in a correspondence drastic solubility change. In a binary polymer/solvent mixture phase diagram, due to a miscibility gap, two different limits are observed, the lower critical solution temperature (LCST), and the upper critical solution temperature (UCST). For LCST, as long as the temperature is kept below the critical solution temperature, the polymer is completely miscible. Above this temperature two immiscible phases are reached, a diluted polymer phase and a concentrated polymer phase.[182] On the contrary, by decreasing the temperature below the phase transition temperature at the UCST, the polymer is present in these two dual phases.[182] Hence, thermo-responsive polymers will change their hydrophilicity property to their hydrophobicity by heating the system above LCST, and by cooling below the UCST. In both cases, the change towards hydrophobicity is due to polymer dehydration as the polymer-polymer interactions are thermodynamically favoured. Physically, this process is observed as a collapse of the polymer chains from elongated structures to collapsed lumps. Finally, the phase separation process takes place in a miscibility gap represented by a bimodal curve; below the LCST and above the UCST, there is only one phase independent of polymer concentration (Figure 1.8).

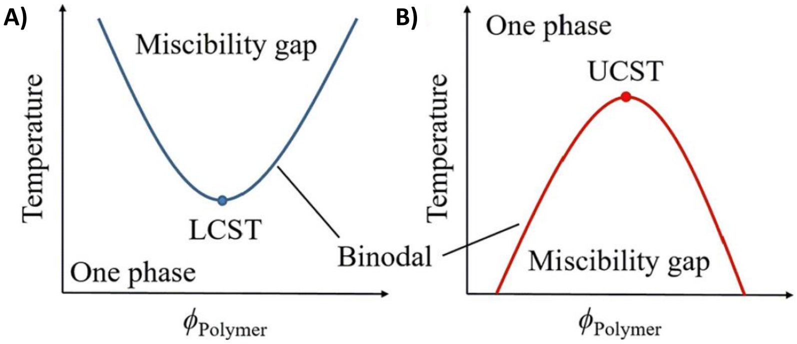

Figure 1.8. Phase diagram for polymer/solvent mixtures exhibiting: (a) LCST, and (b) UCST.

Thermo-responsive polymers experiencing a LCST are the most common ones. Poly(N-alkyl-substituted acrylamides) polymers were the first analysed showing this phenomenon in water. Poly(N-isopropylacrylamide) (PNIPAM) is particularly well suited for biomedical applications.[183] This is due to a low phase transition sensitivity to ambient conditions at 32°C, close to human body temperature, where slight gradients in pH or ambient concentration changes will cause a very small variation in the transition temperature.[183] *Fatemeh Farjadian et al.*, presented an example were, derived from a random copolymer of poly(N-isopropylacrylamide-co-acrylamide). Thermo-responsive polymeric NPs were produced to analysed DOX release in response to the temperature increment from 37 to 42 °C (Figure 1.9).[184] In most cases, thermo-responsive polymeric micelles or hydrogels includes PVCL, poly(2-alkyl-2-oxazoline)s, poly(ether)s, and poly(N,N-dimethylaminoethyl methacrylate).[185]

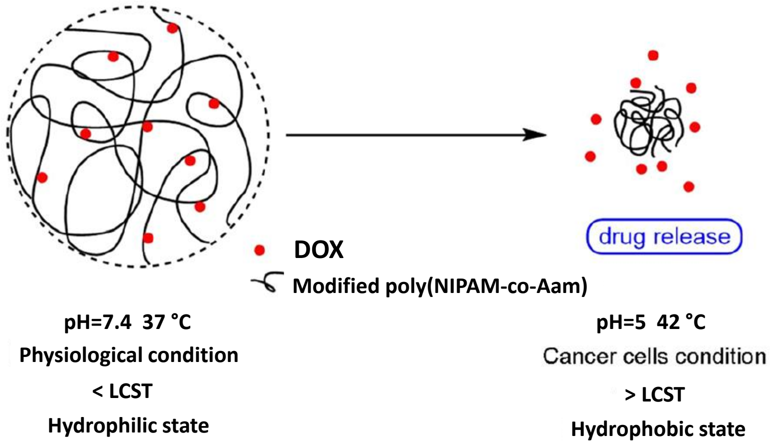

Figure 1.9. Drug release representation of LCST of PNIPAM copolymer.[184]

Conversely, because of their increased sensitivity to gradient changes in pH, ionic strength, or concentration, UCST thermo-responsive polymers are less frequent (Figure 1.10).[186] In the NPs formation for this polymers, they can be assembled between polymer chains by either hydrogen bonding or ionic interactions. Via hydrogen bond interactions, thermo-responsive polymers such as poly(N-acryloyl glycinamide) (PNAGA) or poly(acrylamide-co-acrylonitrile) copolymers, are placed as side groups.[187] Via ionic interactions, cationic and anionic groups dual charged polymers (neutral overall charge) self-assemble by intermolecular and intramolecular dipole-dipole interaction. For both cases, above the UCST, hydrogen or dipolar interactions are broken, disassociating the polymeric chains.[188]

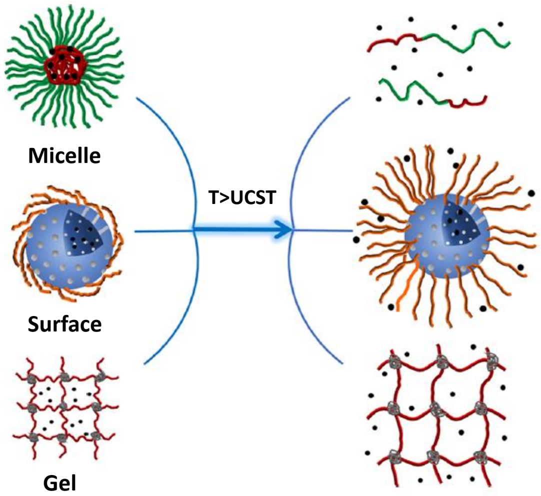

Figure 1.10. Drug release representation of UCST polymeric micelle, surface and gel.[187]

Light-responsive polymers can be classified into 200– 400 nm ultraviolet (UV), 400–700 nm visible (Vis), and 700–1000 nm near infrared (NIR) wavelengths regions, according to the light irradiation required for excitation.[20] UV light irradiation source is the most used because the majority of light-responsive polymers are sensitive in this wavelength region, providing the necessary energy to photo-cleavage, photo-isomerisation, photo-rearrangement or photo-cross-linking. With these photoreactions, release of therapeutic drugs can be achieved. However, it presents relevant challenges, including i) poor penetration depth that makes inefficient drug release in deeply body regions, and ii) high tissue damage derived from phototoxicity. Therefore, limited biomedical applications are supplied by UV-light irradiation in DDS normally. NIR and Vis wavelengths (600–1000 nm) conversely allow higher tissue penetration depth because an optically transparent tissue window is defined in that region of the electromagnetic spectra due to a very low absorption by the blood, water, and melanin molecules, compared to UV irradiation (Figure 1.11A). In addition, the tissue penetration depth is 7.5 ± 0.5 mm, 6.3 ± 0.5 mm, and only 1.0 ± 0.02 mm, for NIR, Vis and UV light irradiations respectively (Figure 1.11b).[20]

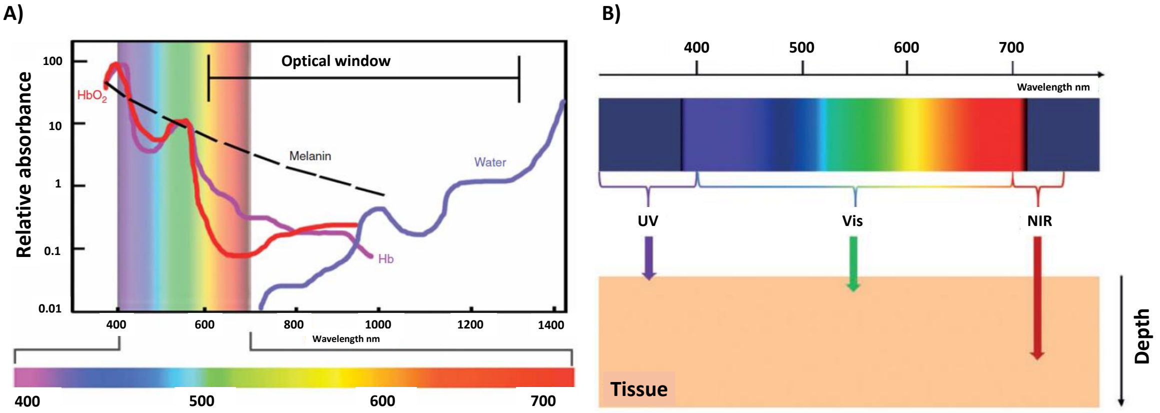

Figure 1.11 A) tissues-transparent window and B) tissue depth penetration for NIR, Vis, and UV lights.[189]

As a result of photochemical reaction process, light-responsive polymers can be divided qccording to three different light irradiation mechanisms: i) photocleavage of light-responsive unit, ii) photoisomerization, and iii) photo-cross/decross-linking.[21]

Photocleavable polymers exhibit a chemical bond rupture in the polymeric chain upon light irradiation and drug release is governed by this chemical bond rupture in DDS. Some mostly uses cleavage- compounds are o-nitrobenzyl (oNB) and coumarin derivates. In response to 300–365 nm UV light, oNB group is photocleaved, forming o-nitrosobenzaldehyde as byproduct, and leads the release of organic acids simultaneously (Figure 1.12A).[190] On the other hand, coumarin derivates as a photocleavable moiety under UV light exposure, decomposes its carbonyl group into an ionic intermediate and forms organic acids by a hydrolysis process (Figure 1.12B). Additionally, coumarin can anchor groups such as amines, alcohols, phenols, phosphates, and carboxylic acids leading to a toxicity diminution, providing high stability, and port bright fluorescence emission properties.[191]

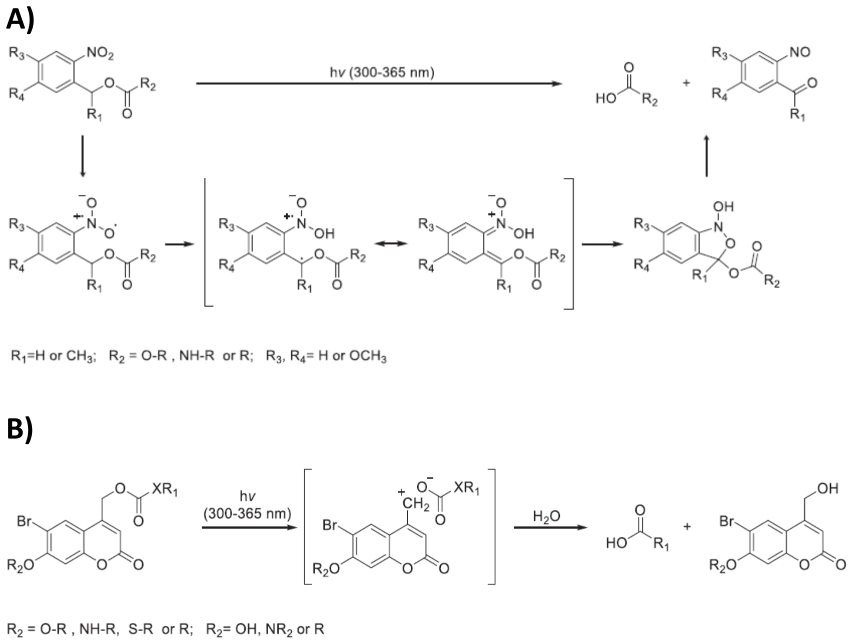

R_1=H or CH_3; R_2 = O-R , NH-R or R; R_3, R_4= H or OCH_3

R_2 = O-R , NH-R, S-R or R; R_2= OH, NR_2 or R

Figure 1.12 Schematic representation of A) Photocleavage mechanism of oNB derivatives and B) Photocleavage mechanism of coumarin derivate.[190,191]

Also, there are four types of photocleavable polymer systems depending on the photocleavage group location within the polymer chain and the mechanism of structural change (Figure 1.13): i) light-degradable polymers with photocleavable end-capped terminal groups ; ii) side chains photocleavable light-degradable polymers; iii) photocleavable side chains by light-induced hydrophobic to hydrophilic transition; and iv) degradable polymers with multi-photocleavable linker main-chain.[192]

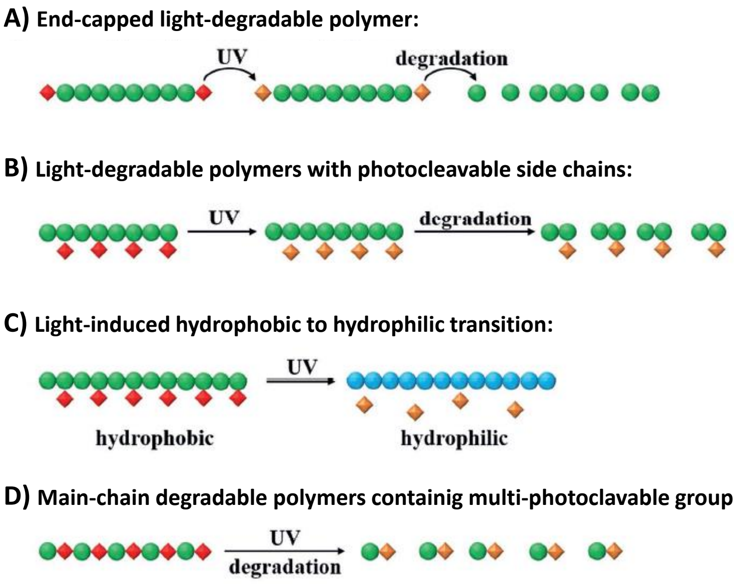

A) End-capped light-degradable polymer:

B) Light-degradable polymers with photocleavable side chains:

C) Light-induced hydrophobic to hydrophilic transition:

D) Main-chain degradable polymers containig multi-photoclavable groups:

Figure 1.13 Illustration of various strategies for light-cleavable polymer systems.[21]

In the first group, polymers are end-capped with photocleavable protecting groups, which have the potential to trigger a rapid depolymerization into small molecules via a cascade of self-immolative reactions in response to irradiation. In one representative example, *Shasha Li et al.* synthesized novel light-responsive polyhedral oligomeric silsesquioxane (POSS) end-capped poly(o-nitrobenzyl methacrylate) (POSS–PNBMA) in which the o -nitrobenzyl-based amphiphilic hybrid polymer self-assembled into spherical micelles (POSS–P(NBMA- co -MAA)), which are responsible to UV irradiation and lead to the transformation of P(NBMA-co-MAA) into PMAA, and to the reorganization of the assemblies, inducing the release of the encapsulated molecule Nile Red.[193]

In the second group, photocleavable species that are conjugated to the polymer side chains lead to the deprotection of functional groups upon light irradiation, triggering a consecutive degradation process of the polymer main-chains, and thus, releasing the payload. Based on this strategy, Chen Ma and co-workers synthesised a block copolymer consisting of a crystalline oligo(p-phenylenevinylene) (OPV_5) segment, a hydrophilic poly(N-isopropylacrylamide) ($PNIPAM_{40}$) block, and a photocleavable o-nitrobenzyl (ONB) junction (OPV_5-ONB-b- $PNIPAM_{40}$). By employing these fiber-like micelles as a model, the influence of PNIPAM chains density on the resistance toward fragmentation of micelles in water was investigated.[194] Unlike photoinduced self-immolative polymers, the light-triggered hydrophobic-to-hydrophilic transitions observed after removal of photo-responsive protecting groups lead to the nanoparticle degradation, and thus, to a drug release.[195] By virtue of this unique approach, *Cheng Wang and co-workers* synthesised thermo- and photo-responsive hydrogels based on amphiphilic triblock copolymers, poly(N-isopropylacrylamide)-b-poly(4-acryloylmorpholine)-b-poly(2-((((2-nitrobenzyl)oxy)carbonyl) amino)ethyl methacrylate) (PNIPAM-b-PNAM-b-PNBOC) as new DOX carriers in which the hydrophobic PNBOC cores within hydrogels undergo amidation-induced cross-linking and hydrophobic-to-hydrophilic transitions under UV irradiation.[196] Finally, more photocleavable groups in a polymer chain can lead to a more complete polymer decomposition. When incorporating multiple photocleavable units on polymeric chain responding to UV-light irradiation, high degradation is achieved without further reactions. Their synthesis is easily performed by functional monomers polycondensation. As an example of this strategy, the pioneering work of *Lei Li et al.* reported the synthesis of three polymers able to photodegrade by UV and Vis light via the Passerini multicomponent polymerization of 1,6-hexanedioic acid and 1,6-diisocyanohexane with 5-methoxy-2-nitrobenzaldehyde (M2), 4,5-dimethoxy-2-nitrobenzaldehyde (M3) or 7-(N,N-diethylamino)-4-formylcoumarin (M4) respectively.[197]

Another pertinent strategy concerns the use of photo-isomerized compounds by the incidence of UV light, which allows to exploite their Vis irradiation reversibility feature to develop light-responsive drugs nanocarries in a more controlled manner. In the formation of these nanocarriers, amphiphilic polymeric nanocarriers will change their nonpolar part into a more polar one upon UV light irradiation, due to the photoisomerization reaction causing NPs disassembly and subsequently efficient drug release. Azobenzene (AZO) and spiropyran (SP) polymeric based derivatives are usually used in the synthesis of this kind of photoisomerization nanosystem. For a stable nonpolar trans AZO isomer submitted to 300–400 nm UV irradiation, an isomerization occurs forming its metastable polar cis isomer. In a reversible photoreaction, this cis-to-trans isomerization can be accomplished by > 400 nm Vis light irradiation or by heating (Figure 1.14A).[22] On the other hand, by UV irradiation, nonpolar SP moiety can be able to isomerize to its polar trans conformation so called merocyanine (MC).[198] Under Vis light or heating, similar to AZO, cis-to-trans reversibility isomerization of SP can be induced (Figure 1.14B).

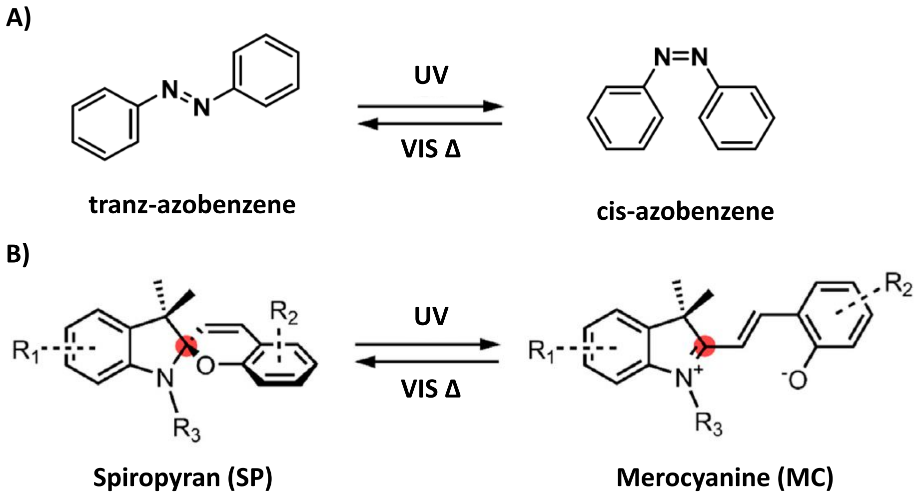

Figure 1.14 Photoinduced isomerization of based derivates a) trans-Azobenzene to cis-azobenzene and b) SPiropyran (SP) to Merocyanine (MC).[22,198]

Spiropyran (SP) is a photoreactive colourless neutral non-polar organic compound structurally formed by a benzopyran fraction attached via an sp^3 C (spiro-carbon) to an indoline heterocycle in an orthogonal orientation due to the sp^3 hybridisation of the spiro-carbon.[24] By the irradiation with UV light (200–400 nm), SP is photoexcited and experiences a cis-trans isomerisation via the ring-opening on the spiro-carbon, forming a stable and coloured open intermediate benzopyran double bonded called merocyanine (MC) (Figure 1.14B). This zwitterionic MC compound, after C-O bond cleavage at the SP, contains a phenolate anion and a positively charged indolium, which provides a much larger dipole moment increasing hydrophilicity, in contrast to the hydrophobic non-polar SP form.[23] In the MC form, the spiro-carbon is sp^2 hybridised with a co-planar structure between the indoline and benzopyran moieties that provides a π-electron conjugation allowing absorption in the visible spectrum (500–600 nm) due to a significant absorption spectrum shift of the molecule. Hence, the MC isomer returns to the SP isomer (more stable in standard conditions) in a reversible process. Furthermore, SP isomerisation into MC could also show acido-chromism, thermo-chromism and solvato-chromism, by complexation with metal cations that can stabilise MC.[24]

SP is an amphiphilic copolymer that can form micelle-like aggregates presenting a hydrophobic core surrounded by a hydrophilic shell. Polyethylene glycol (PEG) is commonly used to make the block copolymer backbone.[199] During the micelle-like formation, hydrophobic drugs could be loaded in the hydrophobic core. These drugs could subsequently be released upon a ring-opening MC isomerization process derived from its high hydrophilicity. In a recent example, *Wang et al.*

synthesised a pH- light-responsive methyl ether polyethylene glycol-poly (β-amino ester) (MPEG-PAE) copolymer with fluorescent naphthalimide (NAPH) and SP fractions introduced along the polymer chain. This copolymer was then used to form polymeric nanoparticles that exhibited both dual-colour fluorescence and controlled drug loading and release activity. The photo-conversion of the hydrophobic SP to the hydrophilic MC form under 365 nm UV irradiation, caused the NPs disruption as a consequence of both swelling and aggregation. After 520 nm irradiation, partial reformation of NPs indicated reversibility from MC to SP.[200] In another example, *Bahareh Razavi et al*. developed another copolymer composed by a hydrophilic temperature-responsive poly (N-isopropylacrylamide) (PNIPAM) block, and a hydrophobic poly (methyl methacrylate) (PMMA) block containing SP. It was observed that the amphiphilic block copolymers have the ability of self-assembly to micelle-like structures. DOX capture and release behaviours were evaluated.[201]

Responsive lipid-based nanocarriers bearing SP have also been studied. *Tong, Kohane et al.* synthesised hybrid SP/lipid-PEG nanoparticles (SP NPHs), composed by a hydrophobic C9 alkyl chain SP derivative (SP-C9), a hydrophilic 1,2-distearoyl-sn-glycero-3-phosphoethanolamine-N-carboxy (polyethylene glycol)-5,000 (DPSE-PEG), and lecithin. Due to the conversion of SP NPHs to MC NPHs under UV-light irradiation, the NPs experienced a reduction in size. Under darkness or Vis light irradiation, NPs return to their original size and morphology. Different compounds such as rhodamine B, coumarin 6, cyanine 5, paclitaxel, docetaxel, proparacaine, and DOX have been used as model molecules for analysis of the drug delivery behaviour.[202]

Another photo-activated strategy is the reversible cross-linking or decross-linking of polymeric NPs. Coumarin and cinnamoyl are commonly used to prepare these photoinduced crosslinked polymeric NPs through UV-light irradiation. If the nanocarriers are irradiated with more energetic photons, decross-linking processes are observed to occur spontaneously.[203] As an example, the photochemical reactions involving cross-linking, decross-linking as well as photocleavage of coumarin derivate were studied by *Hui Wang et al.* Using the dendrimer assembly, they cross-linked coumarin into the dendrimers were via its introduction under hydrophobic interactions. Upon exposition to 365 nm UV irradiation, the coumarin was decross-linked and assemblies were degraded, hence releasing the drug cargo.[204]

As noted, all past examples require UV-Vis photons to be activated. However, molecules such as haemoglobin and water within our tissues and blood could strongly absorbed that kind of light, decreasing tissue penetration and causing severe side effects such as phototoxicity and mutations.[205] On the other hand, NIR light has a much greater tissue penetrating ability, slightly cellular damage, isomerization, or crosslinking photoreactions.[206] This photoreactive process can be achieved by using nanomaterials with the capacity to convert the NIR light to UV-Vis light and two strategies are commonly reported: i) the two-photon absorption (TPA) process and ii) the NIR-to-UV upconversion (UC) process.

As described before, the use of stimuli-responsive polymers is of vital importance for an efficient drug delivery process. Micelle-like nanoaggregates or NPs functionalised with polymers are the most used nanocarriers due to their multiple advantages which will be described in the next section. Polymeric micelles will be discussed extensively, with more emphasis on those that are sensitive to stimuli such as light, pH and temperature.

1.2 Micelle-like nanoaggregates

Micelle-like nanoaggregates are drug delivery systems with an internal hydrophobic core and an external hydrophilic shell. A block copolymer is formed from two homopolymers linked to form a single polymer chain, while random copolymers consist of monomers linked in a given polymer backbone without a sequential order or pattern. When they are diluted in an aqueous solution, amphiphilic molecules exist separately as unimers (single polymer chain). However, when unimer chains concentration increase, aggregation occurs.[9] In the case of amphiphilic block copolymers, self-assembly is induced by hydrophobic chain aggregations, then forming the micelle-like nanoaggregates (Figure 1.15A). In contrast, self-folding or -assembly of amphiphilic random copolymers is achieved by interactions of the hydrophobic moieties in the polymeric chain, while hydrophilic moieties stabilize the global structure (Figure 1.15B). As a consequence, smaller micelle-like aggregates are obtained with random copolymers when compared to block copolymers.[10]

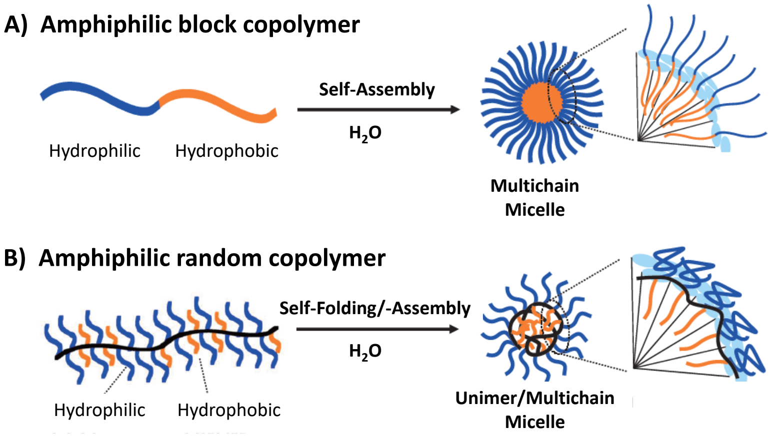

Figure 1.15 Schematic representation of self- assembly of A) amphiphilic block and B) amphiphilic random copolymer micelle-like aggregates.[10]

Some improved characteristics of micelle-like nanoaggregates compared to other DDS NPs are i) smaller NPs size that allows a more passive arrival into solid tumours and a more efficient cell internalisation; and ii) the ability to carry hydrophobic compounds by internalising them into the hydrophobic core. This results in extended blood circulation time due to the stabilisation provided by the hydrophilic shell. In addition, micelle-like aggregates are easily prepared through simpler self-assembly approaches compared to other types of polymeric nanoparticles.[199]

1.2.1 Synthesis and characterization of Micelle-like aggregates and Drug Loading

For micelle-like aggregates formation, the concentration of polymers must reach the critical aggregation concentration (CAC), which is a key parameter dependant on the molar fractions and hydrophilic-hydrophobic equilibrium of both copolymer sections. Below the CAC, the copolymers are found as unimers in suspension. The attractive forces between the hydrophobic groups drive the formation of the core, while the repulsion forces between the hydrophilic groups modulates the formation of the shell, finding a colloidal stabilisation. The CAC value is usually a thousand times lower in micelle-like aggregates (10^{-6}–10^{-7} M) than in micellar surfactants (10^{-3}–10^{-4} M). On the other hand, increasing hydrophobic chain lengths conduce to CAC decreasing, improving the stability of the micelle.[207] Therefore, the concept of CAC is very critical in drug delivery applications with micelle-like aggregates, discussed later in this section. When the formulation is inadequate, rapid dilution in intravenous administration could disintegrate the micelles, releasing the drug in non-specific environments. The general methods for preparation and drug-loading of micelle-like aggregates are dialysis, oil-in-water emulsion, solid dispersion, and freeze-drying (Figure 1.16). Those methods are described in the next paragraphs.

Dialysis is the most common method employed for micelle-like aggregates preparation. It consists in the copolymer dissolution in an organic solvent such as N,N-dimethyl-formamide (DMF), dimethyl sulfoxide (DMSO) or Tetrahydrofuran (THF), followed by the drop by drop addition of aqueous solutions or pure water. The aqueous solutions will control de copolymer concentration, while the organic solvent will gradually be displaced by a dialysis purification process. Thereby, poorly soluble drugs are incorporated in the organic solvent to be entrapped at the hydrophobic micelle core.[11,12]

In the **Oil-in-water emulsion method**, the polymer is dissolved in a volatile nonpolar solvent such as acetone or chloroform (combined or not with ethanol). To form an oil-in-water type emulsion, the initial solution is added to water followed by a sonication process. The formation of the micelle-like aggregate is completed once organic solvent is completely evaporated. The drug is co-dissolved with the copolymer for the loading process.[11,12]

For the **solid dispersion method**, the polymer and the hydrophobic drug are dissolved in an organic solvent which is removed under decreased pressure to form a polymer/drug solid dispersion. The polymer/drug layer is heated and then hot water is added to induce the micelle-like aggregation.[11,12]

In the **freeze-drying method**, the polymer and drugs are dispersed in a combination of water and tert-butanol to subsequently apply a freeze-dried process. Upon rehydration of this freeze-dried mixture, the drug-loaded micelle-like nanoaggregates are spontaneously formed.[11,12]

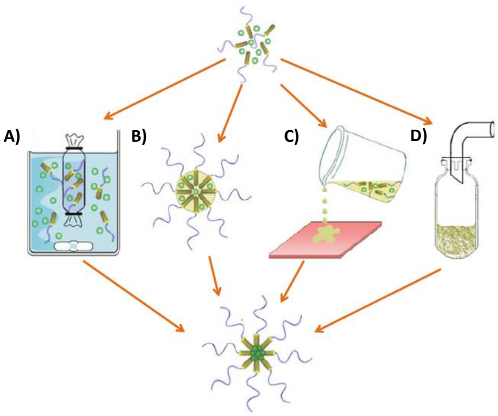

Figure 1.16 Schematic representation of micelle-like aggregates preparation.[12]

An essential parameter to understanding the formation and properties of the micelle-like aggregates is the critical aggregation concentration (CAC). This value can be correlated to other properties such as the surface tension, absorbance or fluorescence of dyes or fluorophores, and hydrodynamic size.[208] The interfacial free energy of the polymer-water system is reduced due to the minimisation of the contact surface between the hydrophobic chains and the aqueous solution, thus reducing the surface tension until a minimum value which is reached at polymer concentrations corresponding to the CAC. When no further change in surface tension is observed, the copolymer concentration will be higher than the CAC.[9] This parameter can be calculated via the Wilhelmy plate or Du Noüy ring. Considering the second approach, absorbance or fluorescence intensities are gradually increased increased upon rising the polymer concentrations due to the incorporation of a probe molecule into the core of aggregates. When no further increase in the absorbance or fluorescence signals are noted, the CAC value is found. Agents such as Sudan III, coumarin-6, Nile red, 1,6-diphenyl-1,3,5-hexatriene (DPH) and pyrene are suitable hydrophobic fluorophores for this technique.[209] Finally, dynamic light scattering can be used for CAC determination because monomers have smaller size and lower contribution to the scattered light intensity than the micellar aggregates, thus indicating the CAC.[210]

1.2.2 Stimuli-responsive micelle-like nanoaggregates

Despite the concepts and progress described above, some concerns such as the premature or inadequate drug release into the general circulation or target tissues restrict the successful application of micelle-like aggregates as DDS.[6] An effective way to achieve proper vectorization and drug delivery is the implementation of stimulus-responsive polymers as precursors for micelle-like aggregates.[13–16] Some recent examples of pH-, temperature- and light-responsive micelle-like aggregates will be discussed below.

The most acid character of the solid tumour environments (pH 6.5-7.2) compared to general physiologic pH value has been widely exploited to activate **pH-sensitive** micelle-like aggregates. Upon destabilisation of the micelles by the pH variations, the drug is released at specific sites in the organism (Figure 1.17). For example, *Huanhuan Liu et al.* prepared micelle-like nanoaggregates based in the poly(acrylic acid)-b-polycaprolactone (PAA-b-PCL) amphiphilic copolymer. They found a 15 wt% drug loading capacity when gambogenic acid (GNA) was used as model drug, and the *in vitro* tests showed improved cytotoxicity and cellular uptake compared to studies in which the drug was dosed in the free form.[211] In other example, *Jingjie Feng et al.* designed a complex pH-responsive micelle-like nanoaggregate formed by a tri-block copolymer poly(N,N-diethyl-aminoethyl-methacrylate)-b-poly(poly(ethylene-glycol)methyl-ether-methacrylate)-b-poly(ε-caprolactone), functionalized with cholic acid-based CA-(PCL-b-PDEAEMA-b-PPEGMA)$_3$. Paclitaxel (PTX) was encapsulated with a drug loading efficiency of 30 wt %. This aggregate was stable in pH 7.4 PBS, but 55% of the load was released 80 h after shifting to pH 5.0.[212] In a more recent example, *Ching-Wei Hsu et al* developed an amphiphilic structure based in PEGylated chitosan/4-(dodecyloxy) benzaldehyde for capture an and photo-damage protection of indocyanine green (ICG). In this case, the acid cleavage of benzoic-imine bonds and the chitosan protonation promoted the ICG release once the pH was reduced to 5.0.[213]

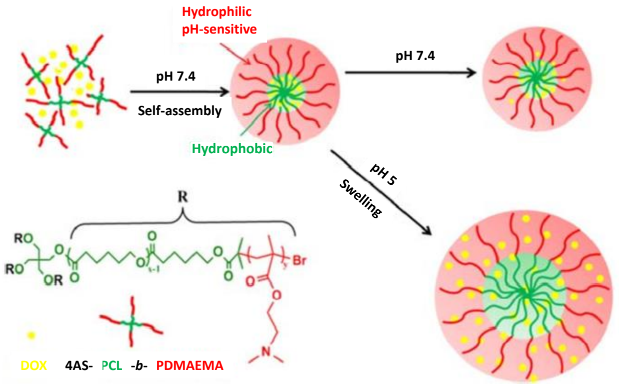

Figure 1.17 Schematic representation for self-assembly of a copolymer and the pH-responsive drug release.[214]

The **thermo-sensitive** micelle-like aggregates are conformed by copolymers with thermo-responsive sections that experience a physio-chemical change at their phase transition temperature (Figure 1.18). For example, *Benzhi Ju et al*. synthesised a thermo-responsive carrier based in 2-hydroxy-3-butoxypropyl starch (HBPS), in which the hydrophobic–hydrophilic balance of starch was modulated using butyl glycidyl ether as hydrophobic reagent. The LCST of HBPS were adjusted in the 4.5–32.5 ◦C range by varying the molar proportion of hydrophobic groups. In water, HBPS could self-assemble into micelles below the LCST, while more polar and larger objects were formed above the LCST.[215] In another example *A. Pietrangelo and co-workers* examined the effect of different core segments on micellar physicochemical properties and the capture and release efficiency of doxorubicin (DOX) upon exposition to thermal stimuli. Those structures consisted in an A–B block copolymers of PNP (poly(N-acryloyl-2-pyrrolidone)), PMNP (poly(Nacryloyl-5-methoxy-2-pyrrolidone)), or PBNP (poly(N-acryloyl-5-butoxy-2-pyrrolidone)) as hydrophobic cores and PNIPAM (poly(Nisopropylacrylamide)) as a thermo-responsive hydrophilic shell. When heated above the LCST, the DOX release efficiency decreased in the following order: PNIPAM–PNP > PNIPAM–PMNP > PNIPAM–PBNP.[216] *Chuanzhuang Zhao et al.* demonstrated a new strategy to copolymerize a thermo-responsive poly(acrylic acid) with acrylonitrile in aqueous media and room temperature conditions. This approach resulted from the contribution of numerous hydrogen bonds between the carboxylic acid groups and the hydrophobic interactions of the acrylonitrile fractions.[217] In another interesting example, *Xing Liang et al*. presented the synthesis of a double thermo-sensible amphiphilic triblock copolymer. The copolymerization of hydrophobic monomer N-vinylcaprolactam (LCST1) and 3-methyl-N-vinylcaprolactam (LCST2) showed a first temperature transition from 19 to 27 °C, and a second one at 41−42 °C, respectively. Also, hydrophilic N-vinylpyrrolidone was copolymerized to form the micelle shell. The first LCST enabled the micelle formation and DOX loading, while the second one induced the micelle core collapse to release the drug.[218]

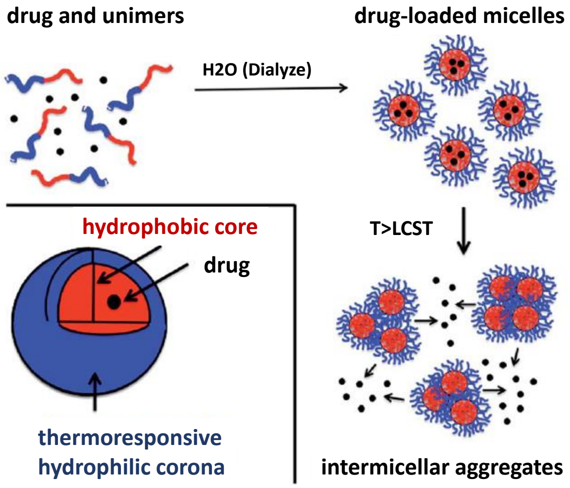

Figure 1.18 Schematic representation of the release mechanism using thermoresponsive micelle-like aggregates.[216]

The **light-responsive** micelle-like aggregates are typically obtained by integrating photo-sensible molecules into the copolymer structure, such as azobenzene, pyrene, cinnamoyl, spiropyran, or nitrobenzyl groups. *Jiayi Chen et al.* synthesized a doxorubicin-conjugated polymer (Poly-Dox) with 4-(4-acetyl-2-methoxy-5-nitro-phenoxy)-butyric acid which can self-assemble to form polymeric micelle-like aggregates (Poly-Dox-M) in water. Furthermore, polyethylene glycol (PEG) was incorporated to shield the adsorption of proteins in the blood circulation, improving the tumour targeting of drugs and reducing the cardiotoxicity of doxorubicin. After ultraviolet irradiation, the amide bond connecting doxorubicin was broken, thus inducing its detachment from PEG and its enhanced cellular uptake.[219] *Kyoung Nan Kim et al*. developed diazonaphthoquinone-conjugated micelle-like nanoparticles with poly(ethylene glycol)-block-poly(l-lysine trifluoroacetate) (PEG-PLL-DNQ) that showed hydrophobic to hydrophilic transitions under UV-light, releasing the encapsulated anticancer drug doxetaxel (DTX).[121] In another recent example, Samuel Pearson et al. produced a light-responsive glycopolymer micelle-like aggregate by the self-assembly of amphiphilic block copolymers containing azobenzene and b-galactose units. The azobenzene units isomerised very rapidly to their more polar cis isomers under UV irradiation, reaching the photo-stationary state within 2 min, with reversion to the trans state taking several hours in the dark. Unloaded micelles showed low *in vitro* cytotoxicity, while micelles loaded with the model hydrophobic compound Nile red demonstrated better cellular uptake in human melanoma A375 cells.[220]

Spiropyran is a very relevant light-responsive moiety implemented in various nanocarriers. For instance, *Hanjian Shen et al*. reported an amphiphilic light-responsive block copolymer spiropyran-poly(2-methacryloyloxyethyl phosphorylcholine) (SP-PMPC) that self-assemble to micelle-like aggregates encapsulating DOX. The *in vitro* studies showed that the release of DOX was accelerated under UV-irradiation (λ=365 nm) when compared to similar systems in darkness.[221] In a more recent example, *Zhouxiaoshuang Yang et al.* carried out the synthesis and drug-release evaluation of random and block copolymers of oligo(ethylene glycol)methyl ether methacrylate (OEGMA) and 1′-(2-methacryloxyethyl)-3′,3′-dimethyl-6-nitrospiro-(2H- 1-benzopyran-2,2′-indoline) (SPMA) systems. When copolymers self-assembled in water, block copolymer micelles showed more regular morphology than those formed by the random copolymer, and both copolymers exhibited the hydrophilic/hydrophobic transitions under UV light irradiation, controlling the drug release of DOX.[222]

Multi-stimulus-responsive micelle-like aggregates have been also reported (Figure 1.19). As a recent example, *Zhi-Min Dang and co-worker*s reported a triple-responsive amphiphilic random copolymer conformed by the photo- pH-sensitive spiropyran (SP) and the thermo-sensitive N-isopropyl acrylamide (NIPAM). The amphiphilic copolymer self-assembled in aqueous media to produce micelle-like nanoaggregates in which the SP sections formed the core, and the NIPAM segments formed the shell. The self-assembled nanoparticles were dissociated under UV light irradiation, and swollen in acid media, thus releasing the loaded molecules. Conversely, above the LCST or in an alkaline condition, no significant release occurred despite nanoparticles shrunken.[25] Interestingly, simultaneous acid or heating stimuli with UV-light irradiation induced a more efficient release compared with single stimuli.

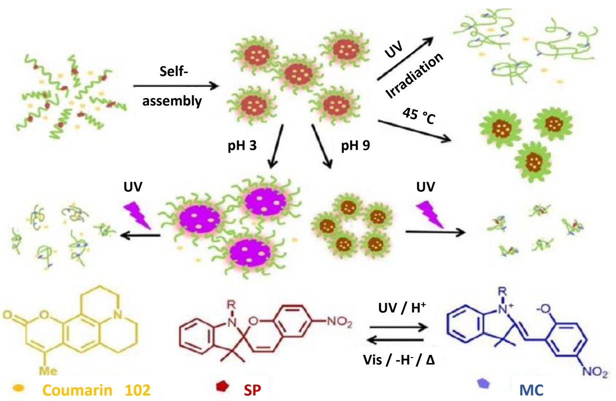

Figure 1.19 Schematic representation of multi-stimulus-responsive micelle-like aggregates under UV light, pH and temperature stimulation.[25]

Most of the photoreactive compounds are sensitive to highly-energetic UV-light, thus limiting their implementation in clinical trials. An interesting alternative to avoid this limitation is the integration of up-converting compounds and micelle-like aggregates. As an example, *Guojie Wang and co-workers* prepared a hybrid nanosystem conformed by UCNPs encapsulated by spiropyran amphiphilic copolymer micelle-like nanoaggregates. UCNPs are able to convert the NIR-light into UV or visible emissions whose energy was transferred to the SP moiety to form the MC isomer. This transition induces the disaggregation of the nanosystem, thus releasing the model molecule Coumarin 102. Furthermore, those systems swollen in acid media, contributing to the drug release efficiency.[223]

This pioneering strategy inspired the present PhD work. Thereby, the up-conversion materials and mechanism will be discussed in detail in the next section.

1.3 Upconverting Nanoparticles

Upconversion nanoparticles (UCNPs) convert low-energy NIR photons into high-energy emissions in the UV-Vis-NIR spectral range.[26] Thereby, they are emerging as a components of novel tools for diagnosis or therapy. The fundamentals of this phenomenon, the synthesis of UCNPs, and their use for drug delivery applications are explained in this section, with emphasis in their combination with smart photo-responsive micelle-like aggregates.

1.3.1 Up-conversion Mechanism

According to the Stokes law, in a photoluminescence mechanism the excitation photons are more energetic (lower wavelength) than emitted ones. Conversely, the emitted photons are more energetic in an anti-Stokes process. This phenomenon is also called the upconversion (UC) process, and requires the successive absorption of two or more photons to provide enough energy for the upconverted emission.[29] Lanthanide-doped materials can achieve this process owing to the 4f-4f orbital transitions, and the protection of the 4f electrons by the external 5s and 5p shells. Likewise, these orbital transitions allow energy transfer among neighbouring lanthanide ions.[224]

The UC phenomenon is related to different mechanisms as shown in Figure 1.20.[225] Excited state absorption (ESA) is the most simple process of UC because it involves a single ion. Upon absorption of a photon, this ion is first excited from its ground state to a more energetic level E1. The same ion is subsequently excited by another photon, thus reaching the level state E2. Thereafter, the electron decays from the level E2 to the ground state, allowing the upconversion emission. Lanthanides such as Er^{3+}, Ho^{3+}, Tm^{3+}, and Nd^{3+}, are highly efficient for this process because of their stepwise energy levels. The energy transfer upconversion (ETU) process requires the presence of two neighbouring lanthanide ions. The ion 1 is known as the "sensitiser" and the ion 2 as the "activator". The sensitiser is excited from the ground state to an excited level upon absorption of a photon, whose energy is transferred to the level E1 in the activator. With a second photon absorption, the activator is excited to the E2 level to finally decay to its ground state and emit upconversion light. The concentration of the dopants plays an important role in the efficiency of UC due to the distance between the sensitising and activating ions. Also, this is the most common and efficient process in upconversion nanoparticles (UCNPs). For the cooperative sensitisation upconversion (CSU) process, the participation of three ions is necessary, with 1 and 3 being the same ion. Those ions are excited to their level E1 to simultaneously transfer their energy to the ion 2, thus reaching the energy level E2. Upon relaxation, ion 2 generates the UC phenomenon. This process is usually less efficient than the two previous ones. In the photon avalanche (PA) UC process, the pumping of photons above a certain excitation threshold is necessary because, below this threshold, the photoluminescence is very low. This two-ion process works in a loop involving both the ESA process for light excitation and an efficient cross-relaxation (CR) process. The E1 level of ion 2 is initially populated by a non-resonant low-energy absorption. The loop process starts by exciting ion 2 from E1 to the E2 level (ESA process) to decay and emit UC light. It continues simultaneously with the absorption of a second photon and a CR process between ion 2 and ion 1, transferring the energy from ion 2 to ion 1. Thereafter, ion 1 transfers its energy to ion 2 to maintain its E1 level, completing the loop.

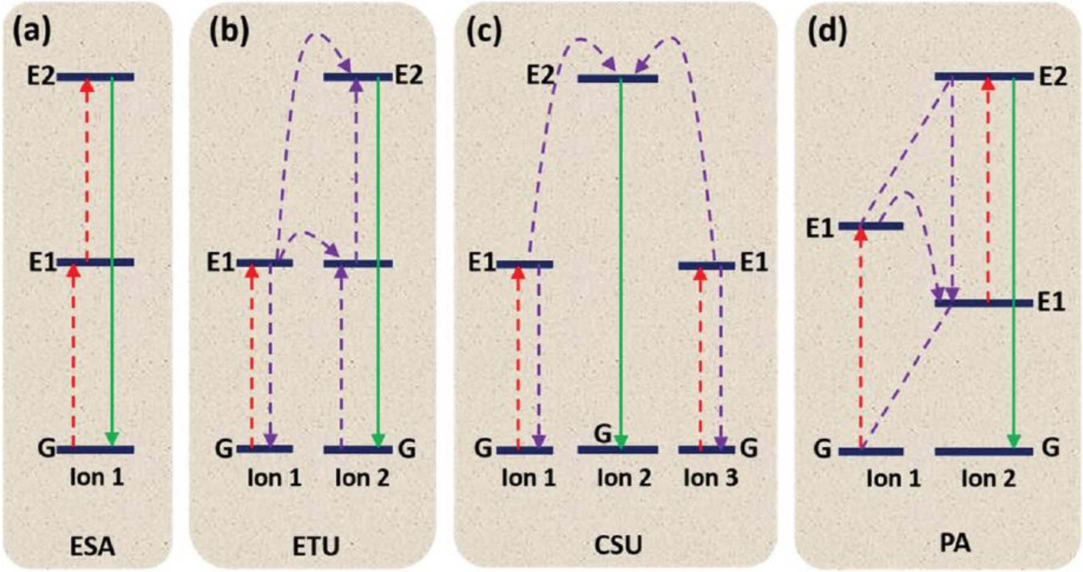

Figure 1.20 Schematic representation of the up-conversion processes: (a) excited-state absorption (ESA), (b) energy transfer up-conversion (ETU), (c) cooperative sensitization up-conversion (CSU), and (d) photon avalanche (PA). Photon excitation, energy transfer, and emission processes are represented by the red, violet, and green lines, respectively.[225]

1.3.2 Up-converting nanoparticles (UCNPs)

Lanthanide-doped UCNPs consist of a host matrix, an activator and a sensitiser.[29] The choice of a crystalline host matrix is essential due to its influence on the performance of the luminescence process. Also, the host matrix needs to accommodate the lanthanide dopants ions in a homogeneous manner, showing minimal lattice stress and conserving de chemical stability with non-radiative energy losses.[27] Crystal lattices such as LaF_4, YF_4, $NaYF_4$ and $BaYF_4$, have been used to meet most of the mentioned parameters. Up to day, the hexagonal phase of $NaYF_4$ (β-$NaYF_4$) is the most efficient matrix.[28]

Yb^{3+} and Nd^{3+} are the most used sensitizers with a doping percentage of 20 - 30 %. They have absorption bands centred around 980 and 810 nm, providing sufficient energy to their neighbouring activating ions. On the other hand, lanthanides such as Er^{3+}, Tm^{3+}, and Ho^{3+} are the most used activators ions because of their slightly different energy levels concerning the sensitizers ions, and also because they have a ladder-like arrangement of their energy levels. Different configurations of UCNPs and their related emissions are summarized in Figure 1.21.[29]

Some synthetic routes such as combustion, thermal decomposition, hydrothermal/solvothermal method and ionic liquids-based synthesis have been developed for UCNPs preparation. Among them, thermal decomposition and hydrothermal/solvothermal are the most used strategies for theranostic applications due to the narrow size distribution and high dispersibility of the UCNPs produced. In the thermal decomposition synthesis, lanthanides are dissolved in high-boiling-point solvents such as octadecene (ODE), together with ligands such as oleic acid (OA) and oleylamine before to be heated at temperatures around 280 °C to achieve highly monodispersed UCNPs. In the hydrothermal/solvothermal method, the precursors are heated in an autoclave above a critical temperature, accelerating solid reactions. The inner pressure is controlled by the temperature and the boiling point of the solvents, their chemical nature, and their volume or ratio. This strategy brings highly crystalline nanocrystals with modulable physicochemical properties.[30]

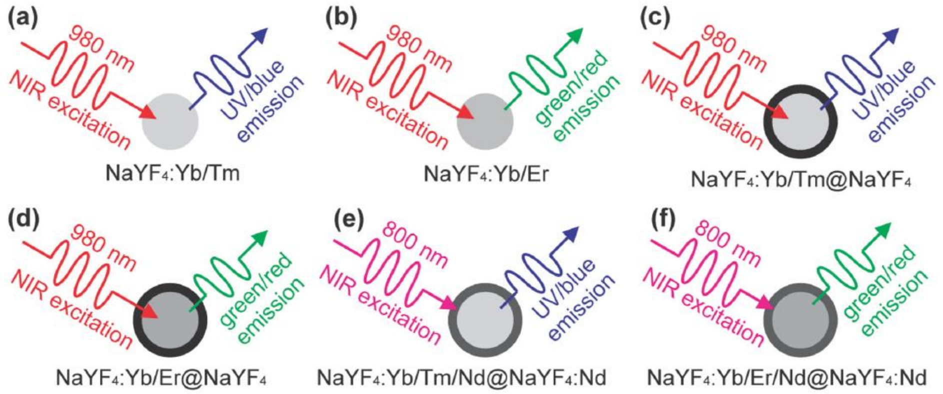

Figure 1.21 Schematic illustration of various configurations of UCNPs[226]

Different methods to incorporate other functional fractions or compounds during or after the UCNPs synthesis have been tested. Two relevant configurations for drug delivery applications are presented below: (i) UCNP-silica, and (ii) UCNPs-polymer nanocomposites.

1.3.3 UCNPs – silica nanocomposites in drug delivery applications

Silica shells on UCNPs have various applications such as improving colloidal stability in an aqueous medium and providing a surface for anchoring distinct chemical groups (amines, carboxyl, thiols) that can be used to attach targeting agents, polymers, or photosensitive molecules. Additionally, the silica surface is usually porous, which can provide a large surface area for bioactive compounds loading.[227] Silica presents low cytotoxicity, biocompatibility and excellent chemical stability.[228] Functionalization is usually achieved by condensation of functional alkoxysilanes. The Stöber method is the most common technique to incorporate a silica coating.[229] In this method, the tetraethyl orthosilicate starts a series of condensation reactions that convert this precursor molecule into a kind of mineral-like deposit through the formation of Si-O-Si bonds on the surface of UCNPs.[230] Another coating route is the water-in-oil reverse microemulsion method, which takes advantage of chemical reactions in hydrophilic cavities generated by a homogeneous mixture of ammonia, cyclohexane, surfactants and tetraethyl orthosilicate. These hydrophobic ligands promote uniform and monodisperse silica deposition on UCNPs.[231]

For these reasons, important studies have recently been carried out on the integration of silica and/or mesoporous silica with UCNPs for the development of new theranostic tools. For example, *Shi's group* demonstrated the first doxorubicin release controllable by NIR-light irradiation based on the silica coated of an UCNPs ($NaYF_4$:TmYb@$NaYF_4$). After UCNPs silica coated, the nanosystem was functionalized by photo-switchable azobenzene molecules as gatekeepers for drug release, and by a transcriptional activator (TAT) peptide to enhance the cellular uptake ($NaYF_4$:Tm,Yb@$NaYF_4$@$mSiO_2$-azo). The upconverted UV and visible light emissions induced the reversible photoisomerization of azobenzene molecules, thus controlling the DOX release. It was also determined that the negatively charged silica surface promotes strong interactions of the surface with the DOX through hydrogen bonds and electrostatic forces (Figure 1.22).[232]

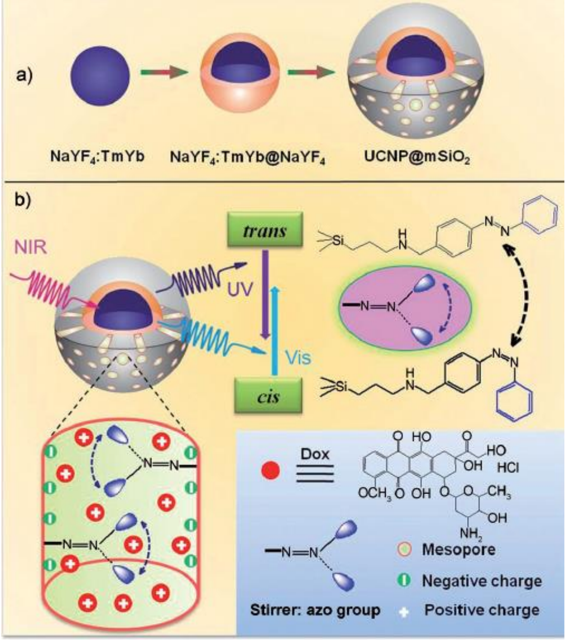

Figure 1.22 a) Schematic representation for UCNPs coated with an outer mesoporous silica layer and b) NIR light DOX release of $NaYF_4$:Tm,Yb@$NaYF_4$@mSiO 2-azo

1.3.4 UCNPs – polymer nanocomposites in drug delivery applications

Polymeric functionalization or entrapment is an interesting approach leading to more stable UCNPs in aqueous suspensions. Indeed, UCNPs are usually hydrophobic due to the use of capping ligands like oleic acid (OA). For example, PAA polymer was incorporated through a ligand-exchange reaction at the $NaGdF_4$:Ho^{3+}/Yb^{3+} UCNPs to allow their suspension in aqueous media.[233] Polymeric capping can also enlarge the bloodstream circulation time by reducing the nonspecific uptake by macromolecules or cells. Different polymers such as polyvinyl pyrrolidine (PVP), poly(amidoamine) (PAMAM), polymers containing ending carboxylic groups (–COOH), polyethylenimine (PEI), polyacrylic acid (PAA), and thiolate-grafting (–SH) polymers have been incorporated at the surface of UCNPs, thus allowing their biomedical applications.[234] Another surface-functionalisation method is the ligand attraction polymer attachment, in which the hydrophobic ligands on the UCNP surface interact with the hydrophobic segment of an amphiphilic polymer via Van Der Waals forces. This results in the exposition of the hydrophilic segment of the amphiphilic polymer, which allows adequate suspension in aqueous media.[235] Polyethylene glycol (PEG)-lipid, poly((ethylene glycol)-block -lactic acid) (PEG-b-PLA), octylamine-block-poly(acrylic acid) (OA-PAA), octylamine-block-poly(acrylic acid)-block-polyethylene glycol (OA–PAA–PEG), poly(styrene)- block -(allyl alcohol) (PS-b-PAA), and poly(ethylene glycol)- block -poly(carprolactone) (PEG-b-PCL), are amphiphilic polymers frequently used in this method.[236] As an example, *Liu's group* has implemented amphiphilic-PEG coatings on $NaYF_4$:Yb,Er for drug delivery and cell imaging applications.[237]

1.3.5 UCNPs – micelle-like aggregates in drug delivery applications

Photo-responsive polymer chains can be anchored on the surface of UCNPs by chemical conjugation, or by self-assembly of copolymers. In the latter, drug molecules can be physically trapped via electrostatic interactions with the functional groups from the polymeric shell. By NIR light irradiation into the nanosystem, emitted UV light induces photoreactions, which changes the physicochemical structure of the polymers and results in trapped drugs release. Next, examples of micelle-like aggregates combined with UCNPs for smart drug delivery are described.

Yue Zhao and co-workers were the first to work on this type of nano-systems. They encapsulated $NaYF_4$:TmYb UCNPs into micelle-like nanoaggregates formed by the amphiphilic block copolymer poly(ethylene oxide)-block-poly(4,5-dimethoxy-2-nitrobenzyl methacrylate). Upon 980 nm excitation, the UV-light energy derived from the up-converting phenomena photocleaved the o-nitrobenzyl groups, thus dissociating the micelles and releasing the model drug (Figure 1.23).[238] In another example, *Jinqiang Jiang et al*. prepared $NaLuF_4$:Gd,Yb,Tm UCNPs encapsulated by an amphiphilic random copolymer of P(NVP-co-NHPSS). Upon 980 nm -light incidence and consequent 365 nm emission, the N−O bond was photocleaved, inducing the release of the drug.[239] More recently, *Yue Zhao and co-workers* prepared a near-infrared (NIR) light-responsive UCNPs-based nanocarrier for the controlled drug release using an amphiphilic diblock copolymer. There, the inner block is the hydrophobic UV-sensitive poly(4,5-dimethoxy-2-nitrobenzyl methacrylate) (PNB), and the outer block is the hydrophilic poly(methoxy polyethylene glycol monomethacrylate) (POEG). In aqueous solution, the copolymer self-assembled into a “micelle-like” aggregate which allowed the encapsulation of UCNP and doxorubicin (DOX). Under 980 nm laser exposure, UV light was emitted by the UCNP and then absorbed by the PNB inner layer, resulting in the o-nitrobenzyl groups cleavage. This reaction increases the hydrophilicity of the copolymer, disrupting the structure of the nanocarrier and thus leading to the DOX releasing. This approach based on the self-assembly of copolymers to build NIR light-sensitive nanocarriers with well-defined structures becomes a universal platform offering possibilities for photo-controlled drug delivery.[240]

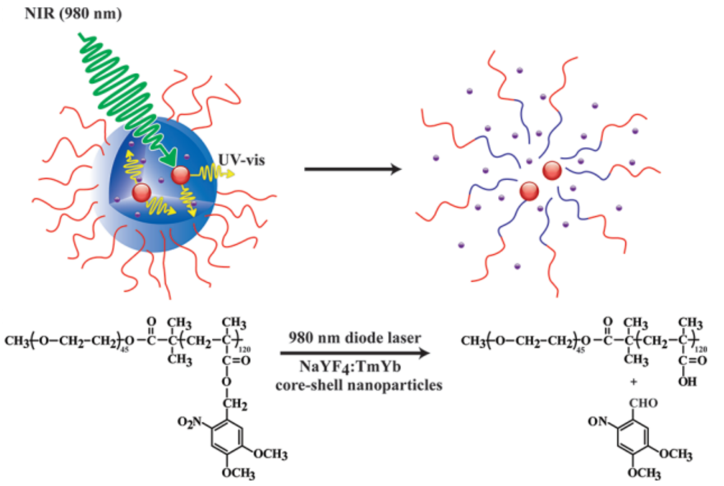

Figure 1.23 Schematic representation of a near-infrared (NIR) light-responsive photocleavage reaction with a UCNP.[238]

Using photo-isomerisation of azobenzene, *Xiaotao Wang et al.* prepared NIR light- pH-responsive yolk−shell nanocapsules as DDS. UCNP were modified with a porous silica shell, and then with poly(methacrylic acid) (PMAA). A second stimului-responsive PMAA coating was incorporated. Silica nanocavities allowed the drug loading, while PMAA azobenzene isomerization triggered the release of up to 17 wt% of the loaded DOX.[241] In another example showed by *Kai Yan et al.,*[242] smart temperature-, UV-Vis light-, and ion- responsive micelles were synthesised. This composite consisted of the amphiphilic copolymer composed by a hydrophilic core of oligo ethylene glycol methyl ether methacrylate and a hydrophobic shell of azobenzene-containing methacrylate. With this multi-responsive nanoaggregate, drugs could be transported and released upon exposition to near infrared light- and heating- stimuli.

Xin Zhao and co-workers also prepared a light- and pH-responsive micelle-like micelle-like nanoaggregate bearing UCNPs to liberate DOX (Figure 1.25). In this case, both pH 4.5 and/or NIR irradiation trigger the spiropyran hydrophobic-hydrophilic shifting thanks to the up-converting phenomena. The polymeric section was formed by thea 1´-(2-methacryloxyethyl)-3´,3´-dimethyl-6-nitrospiro-(2H-1benzopyran-2,2-indoline) monomer and methacrylic acid (MAA). DOX loading and release capacities of 10 wt% and 54 wt % were respectively verified.[31] *Jianmei Lu et al.* fabricated a nanosystem by the self-assembly of the photo-responsive spiropyran copolymer with silica-coated UCNPs in the micelle core. Firstly, Yb^{3+} and Tm^{3+} UCNPs doped were encapsulated with a mesoporous silica core (MUCNPs). Subsequently, the light-responsive copolymer poly(ethylene glycol)-co-poly(1´-(2-methacryloxyethyl)-3´,3´-dimethyl-6-nitrospiro-(2H-1benzopyran-2,2-indoline)) (PSMN-FA) was synthesised. Drug loading was achieved through MUCNP silica mesopores for a further coating via copolymer self-assembly. For the drug releasing process, the exposition to 980 nm light induced the micelle-like disaggregation.[243] As a final example (Figure 1.24), *Guojie Wang and co-workers* reported the NIR light- pH-responsive nanosystem formed by the incorporation of UCNPs into the spiropyran-functionalized amphiphilic polymers described in figure 1.19.[223] This doctoral project was inspired by these works, and they will be addressed in detail in the following chapters.

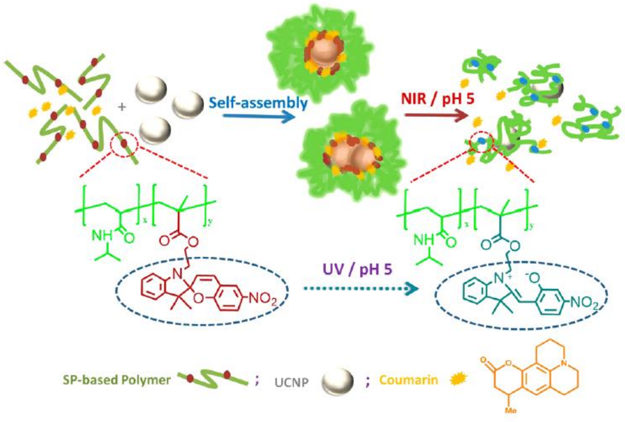

Figure 1.24 Schematic representation for the fabrication of UCNP spiropyran nanocomposites and NIR Light and pH controlled release of the loaded drug.[223]

1.4 Physicochemical characterization of smart drug delivery systems

Some NPs properties such as crystal structure, chemical composition, surface charge, area, and chemistry, size distribution, shape, degree of aggregation, etc., are parameters that are directly related to NPs applications and need to be determined. Thus, physicochemical characterizations are necessary and investigated for the optimization of the nanomaterial's synthesis and for the adequate choice of batches for biomedical applications. In the following sections, the most employed methods to characterise those parameters are first described in a general way, including a more in-depth description of the capillary electrophoresis methodology as an alternative high-powerful method for NP characterization.

1.4.1 Conventional methods for nanoparticle physicochemical characterisation

X-ray diffraction (XRD) is a widely used techniques for the characterization of inorganic NPs in a powder form giving statistically representative results. This technique provides nanomaterial print marks regarding the crystalline structure, nature of the phase, lattice parameters and crystalline grain size (using the broadening of the most intense peak and Scherrer equation). For the characterization of new hybrid NPs, an advantage of using the XRD technique is that NPs composition can be determined by comparing the position and intensity of the peaks with reference patterns reference available from the International Center for Diffraction Data (ICDD, previously known as Joint Committee on Powder Diffraction Standards, JCPDS) database. However, for amorphous materials or materials with crystal size below 3 nm, XDR technique is not suitable as it would provide too broad peaks. [244]

Fourier transform infrared spectroscopy (FTIR) is a technique that provides information concerning molecular structures and NPs surface interactions. The resulted spectrum shows the position of bands which is related to the strength and nature of bonds and specific functional groups, providing thus chemical surface details. The measurement records the mid-infrared (4000–400 cm^{-1})

electromagnetic radiation absorption of a molecule, based on the modified dipole moment of the IR active molecule.[245]

Nuclear magnetic resonance (NMR) spectroscopy is another important technique used to understand interactions or coordination between a ligand and the surface of diamagnetic or antiferromagnetic NPs. This technique is based on the phenomenon of nuclear magnetic resonance that occurs in the nuclei of atoms with non-zero spin when they are exposed to a strong magnetic field. Small difference in electromagnetic radiation energy (radio wave range) can be measured and is causes when transitions between the "spin up" and "spin down" are generated.[246] It can also be applied to monitor diffusion of gases adsorbed onto the surface of metal NPs and measure the hydrodynamic diameter of well-dispersed metal NPs in solution by analysing particle diffusion coefficient according to Brownian motion and calculation of the Stokes– Einstein equation. However, NMR is not suitable to characterize ferri- or ferro- magnetic NPs.

The **Brunauer–Emmett–Teller (BET)** technique is an accurate, rapid, and simple method mainly used for the determination of the surface area of nanoscale materials. The basis of the technique lies on the physical adsorption of a gas on the NPs surface.[247]

Thermal gravimetric analysis (TGA) gives information on the surface coating and mass-to-mass ratio of the NPs. In this technique, nanomaterial sample mass is measured in a temperature increase in which components with different degradation temperatures decompose and vaporise, changing the recorded mass. These mass loss is recorded in function of the temperature so as to determine the type and quantity of organic ligands that interact with NPs.[248]

UV-Vis spectroscopy (UV-Vis) is an important technique to identify optical properties of NPs, that are related to size, shape, concentration, NP surface refractive index, colloidal stability and agglomeration state in solutions. This technique measures the light reflected intensity of NPs and compares it to the light reflected intensity of a reference material (polar or no-polar medium). It is therefore a relatively facile and low-cost characterization method accessible for the study of nanoscale materials.[245]

Mass spectrometry (MS) and **inductively coupled plasma- MS (ICP-MS)** have drawn interest as a strong tool for the analytical characterisation of NPs through the information provided in terms of elemental and molecular information on the composition, structure and chemical state of the NPs, also helping in the determination of impurities and bioconjugation to target biomolecules in NPs surface. They are highly sensitive and usually require simple calibration protocols.[249,250] Molecular MS techniques can also provide information on protecting ligands surrounding NPs correlating the entire nanosystem with their chemical composition.

Gel permeation chromatography (GPC) gives information such as molecular weight (Mw) distribution, average molecular mass, and degree of branching for polymers. Size exclusion chromatography, can be an interesting tool to separate nanoparticles based on their hydrodynamic volume or size.[251]

Dynamic light scattering (DLS) is a useful employed technique to find NPs size in colloidal suspensions. By a continuous Brownian motion, NPs are dispersed in a colloidal solution and DLS measures the light scattering which, combined with the Stokes– Einstein equation, is used to determine the NP hydrodynamic diameter. Importantly, a relatively low NP concentration is needed in DLS, to avoid multiple scattering effects.[252]

The **Zeta potential (ζ-potential)** parameter is an indicator that determines the stability of NPs sample in colloidal dispersions. NPs could be positively or negatively charged and will tend to repel each other when they are highly charged, thus forming stable colloidal solutions. This surface charge can be modulated via pH modifications. At the 'isoelectric point' the zeta potential of the NPs is zero. At low ζ-potential values, NPs flocculation can occur; while at ζ-potential values in the range of ±20–30 mV or higher, NPs suspensions are considered to be stable. It is also possible to tune ζ-potential value through the modification of the NP surface chemistry to stabilise the NPs colloidal suspension via electrostatic repulsion, or by varying the ionic strength, the nature of solvents or the medium composition.[252]

Transmission electron microscopy (TEM) is the most common microscopy technique in the examination, in solid satete, of NPs size and shape, as it offers direct imaging of the sample, which allows for a more accurate physical homogeneity estimation. However, some limitations have to be taken into consideration, such as the difficulty to quantify a large number of particles or deceptive images due to orientation factors. In this microscopy technique a uniform current density electron beam (usually between a range of 60 to 150 keV) is irradiated to the NPs sample in which part of the electrons are transmitted, building the final image, while the remaining electrons are elastically or inelastically scattered. This electron-NPs interaction will depend on their size, sample density and elemental composition.[253] **Cryo-electron microscopy (cryo-TEM)** is a type of TEM at cryogenic temperatures that allows the visualisation of nearly unaltered samples in a frozen environment, commonly used for NPs that are stable in a solution medium.[254] **Scanning electron microscopy (SEM)** uses electrons for imaging NPs samples employing the scattered or reflected electrons in NPs surface.[255] In **scanning transmission electron microscopy (STEM)**, in contrast to TEM, the electron beam is focused to a fine spot that is then scanned over the NPs sample. The use of the electron beam across the sample makes it appropriate to couple techniques such as **energy dispersive X-ray (EDX)** spectroscopy or **electron energy loss spectroscopy (EELS),** which use energy dispersive x-ray or electron energy loss detection respectively to obtain elemental maps in an atomic scale.[256] Finally, **Atomic force microscopy (AFM)** is another microscopy technique capable of creating 3D images of surfaces at high magnification. AFM is based on the measurement of the interaction forces between the sample and a sharp tip (silicon or silicon nitride) attached to the end of a cantilever that functions as a fine probe. When the measurement process starts, the cantilever moves as a result of the attractive or repulsive forces between the tip and the sample surface, quantifying the bending of the cantilever by means of a reflected laser beam. The image is formed by the "atomic forces" calculated by the variation of the laser and the known stiffness of the cantilever.[255]

1.4.2 Capillary Electrophoresis for nanoparticles physicochemical characterization

Electrophoresis is the process in which molecules or particles migrate in a liquid medium (background electrolyte, BGE), under an electric field, according to their size, charge and the BGE nature. The apparent electrophoretic velocity (μ^{app}) is the sum (in vectors) of i) the electroosmotic velocity (μ_{eof}), which depends on the BGE nature (pH, ionic strength, viscosity, dielectric constant, nature of the buffer ions) and ii) the electrophoretic velocity (μ_e) of the analyte of interest. In the case of NPs, the electrophoretic velocity depends on the size and zeta potential of the NPs, as well as the colloidal suspension concentration (collective effect).[257–260] The electrophoretic mobility of a analyte ($cm^2V^{-1}s^{-1}$) is then calculated according to the equation:

$$\mu_c = \mu^{app} - \mu_{eof} = \frac{L_d L_t}{V}\left(\frac{1}{t_c} - \frac{1}{t_{eof}}\right)$$

where L_d and L_t (cm) are the effective length and total length of capillary relative to the detector, respectively, V (Volt) is the applied separation voltage, t_c and t_{eof} are the migration time of the analyte and the neutral molecule (DMF).[260]

When the BGE is at a pH higher than 3, the surface of the silica capillary, containing SiOH, undergoes a deprotonation, leading to a negatively charged surface which originate a double layer of cations. The inner cation layer is dense and stationary, while the outer layer is free to move toward the cathode by applying a high-voltage, thus creating an intrinsic electroosmotic flow (EOF). Under an electric field in a positive polarity, the cations and neutral compounds migrate till the end of the capillary (where the cathode is placed), with a velocity that is the sum of the electroosmotic and electrophoretic mobilities. On the other hand, the anions can reach the detector if their electrophoretic velocity is lower than the electroosmotic velocity, ; or else they do not enter the capillary.[261]

Electrokinetic separations can be developed in six different types of systems: capillary zone electrophoresis (CZE), capillary gel electrophoresis (CGE), micellar electrokinetic capillary chromatography (MEKC), capillary electrochromatography (CEC), capillary isoelectric focusing (CIEF), and capillary isotachophoresis (CITP).[261] Between them, capillary zone electrophoresis is the most used methodology (Figure 1.25). The ending sides of the capillary are immersed in a vial containing both the electrode and the BGE, and the detector is either positioned at the outer end of the capillary or coupled to the capillary end [262] Generally, a UV-Vis detector is integrated in the electrophoretic system, and different other detectors can be coupled, such as fluorescence (laser induced fluorescence – LIF), electrochemical, mass spectroscopy or optical spectroscopy detectors.[263]

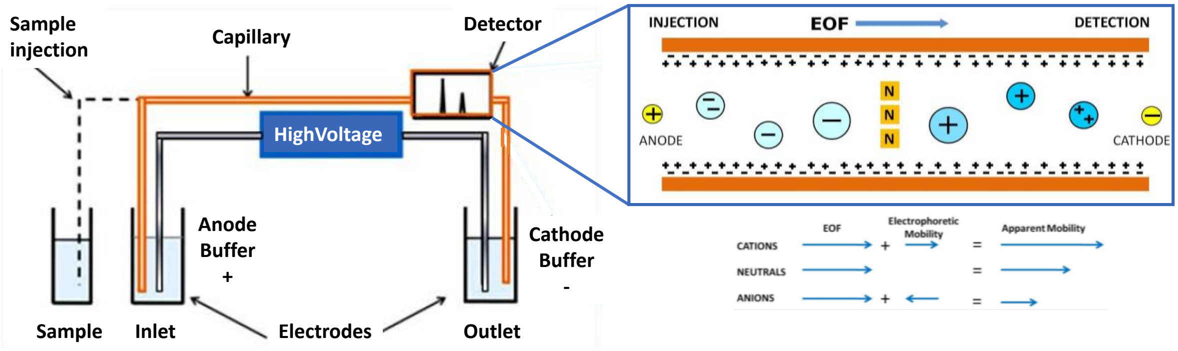

Figure 1.25 Schematic representations of CE mechanism of separations and standard setup.[264]

Except for CE, electrokinetic methodologies do not imply a a stationary phase, which allows to study and characterize dynamic systems and interactions in free medium. It is therefore a powerful methodology for studying deeply biomedical NPs interactions and applications for DDS, with the possibility to use a BGE mimicking the physiological. This methodology presents other advantages such as high separation efficiency in aqueous, hydro-organic, or organic medium, low sample and chemical consumption, easy sample preparation, and short analysis time, compared to others separation methods.[262]

As indicated before, NPs stability and interactions in their surrounding environment are important to be well understood. Thus, CE is now considered to be a powerful method for NPs characterization, in terms of physico-chemical properties and interactions various molecules.[265] It allows NPS size and surface charge determination.[257,258,258,259,266–269] It furthermore allows to quantify and optimize surface functionalization, so as to improve their stability, enhance their bio compatibility, and to prevent aggregation[259,268,270]

Metallic NPs, generally those consisting of gold and silver, have been the most analysed for the determination of their electrophoretic mobility, a key parameter to estimate, by means of different mathematical approaches, the characteristic factors of the NPs population.[268] By combining CE and Taylor dispersion analysis methodologies (TDA - method to determine the diffusion coefficient and thus the equivalent hydrodynamic radius and size distribution of a given particle population). *Ute Pyell et al.* [259] designed a new method to adequately describe the electrophoretic behaviour of GNPs by simplifying Oshsima's model. Experiments were carried out by performing different hydrophilic polymer coatings on GNPs to estimate their ζ-potential, surface charge density, effective charge number and size distribution (single-modal, bimodal or multimodal). In another approach, *Ángela I. López-Lorente and co-workers*[271] achieved a ligand exchange by simultaneously influencing the formation of self-assembled monolayers of thiolated ligands on the surface of gold and silver NPs. The NPs were separated in a capillary containing a background electrolyte (BGE) with thiolated ligands (thioctic acid or thiomatic acid). By analysing electrophoretic mobility changes of the NPs, the mechanism of ligand exchange due to the modification of their surface charge was observed. Furthermore, mixtures of NPs with different thiolated ligands, with the same sizes and shapes were separated based on the different affinity between the ligands and each type of NPs.

For **QDs**, CE has been also used to control and validate their synthesis, and their functionalization.[272] *Gonzalo Ramírez-Garcia et al.*[273] for example, characterized the stability, ζ-potential, and size of core/shell/shell QDs with different metallic phthalocyanines cores (Zn, Al, or In) and functionalized groups (carboxyphenoxy- or sulfonated-) by varying pH and ionic strengths. Briefly, they showed that stability could be achieved by adding more functionalized groups to the QDs. With zinc mono-carboxyphenoxyphtalocyanine (ZnMCPPc-QDs), aggregation was observed under any pH and low ionic strength, whereas QDs capped with zinc tetracarboxyphenoxy phtalocyanine (ZnTPPc-QDs) demonstrated good colloidal stability at a pH equal or higher than 7.4. Again, due to the presence of functional groups, aluminum tetrasulfonated phthalocyanine (AlTSPPc-QDs) and indium tetracarboxyphenoxy phthalocyanines (InTCPPc-QDs) QDs found stability at pH higher than 9.0. Furthermore, they showed that when ionic strength increased, the ζ-potential correlated with low stability and aggregation.

Metal oxide NPs like TiO_2, SiO_2, Fe_2O_3 have been also characterized by CE. For example, *Gonzalo Ramírez-Garcia et al*.[274] evaluated, optimized and controlled the synthesis, functionalization and colloidal stability of persistent luminescent NPs (aluminium-doped zinc) modified with neutral, negatively and positively -charged functional groups in different buffer medias regarding the application of these NPs for biomedical approaches. In the study negatively charged NPs were well dispersed in phosphate buffers, while zwitterionic buffers were more adequate for positive NPs, and both types of buffers were shown to well stabilize neutral NPs.

Also **Carbon-based** nanomaterials going from the fullerenes to the carbon dots have been characterized by CE. For example, *Lisa A. Holland and co-workers*[275] used CE to characterize the oxidation of multi-walled carbon nanotubes by adding to the BGE a polytryptophan peptide containing a single arginine residue that works as a receptor to evaluate the CNT degree of carboxylation by forming a peptide nanotube receptor-ligand complex. Using a UV detector to observe the migration shift of the WRWWWW peptide, the apparent dissociation constants were obtained by the increment of the multi-walled CNT concentrations.

Finally, for **Polymeric NPs**, challenges in their characterizations are a daily issue due to many variables affecting their stability like chemical composition, hydrophilic/hydrophobic balance, surface effective charge, etc. In this sense, CE methodologies have emerged to be a complete characterization method for this NPs. As an example *Tao Liu et al.*[276], used CE to monitor the progress and kinetics of the click chemistry reaction, so as to decorate dendrigraft poly-l-lysines (derivatized with acetylenic groups) with tryptophan-PEG-azide arms via triazole ring formation.

1.4.3 Drug loading and release quantitation by capillary electrophoresis for SDDS.

To this day, the drug-loading and release capacity of nanocarriers has been evaluated through classic methodologies based on UV-Vis, fluorescence spectroscopy, and HPLC. However, CE can be and excellent analytical method to reveal information about interactions between the model drugs and the nanoparticles. The few examples of the use of CE for the determination of drug uptake and release are shown below.

In 2008 *Susanne K. Wiedmer and co-workers* used CE methods to study interaction and entrapment, employing salbutamol sulphate (SS), sodium cromoglycate (SCG) and beclomethasone dipropionate (BDP) as model drugs in poly(d,l-lactic acid) (PLA) nanoparticles. The results show clear interaction between PLA and SS and SCG, compared to the low level of interaction that exists between PLA and BDP. However, although the detection of the drugs was acceptable, the results showed that the drugs were outside the particles, indicating poor encapsulation. Nevertheless, it was demonstrated the possible quantification of drugs located inside the polymeric nanoparticles.[273] *Ulrik Franzen et al.* (2011) developed a coupling method with CE/ICP-MS spectrometry to characterize the PEGylated liposomal oxaliplatin capture and release. Free and total oxaliplatin concentrations were calculated to obtain encapsulation efficiency and by subsequent liposome sonication, the drug release was calculated. Interestingly, the results obtained suggested CE as a useful tool for liposomal DDS characterization.[274] In another example, employing also CE/ICP-MS methodology, *Tam.T.T.N. Nguyen et al.* (2013) detected and quantified liposomal-cisplatin interactions, to better understand drug encapsulation and human plasma stability. The method also helped to analysed liposomal disintegration under sonication to quantify drug release. Using alternative phospholipid compositions, oxaliplatin as a model drug was also analysed, so as to mimic an in vivo drug release into patients.[275] In the use of nanostructured lipid carriers (NLCs) DDS, in 2015 *Jessica Otarola et al*. implemented an easy and rapid CE methodology to detect piroxicam loading efficiency by the measured free drug concentration in NLC sample. By varying different BGE buffer solutions, pH and applied voltage, was optimized for higher piroxicam detection efficiency. The BGE (pH9) providing the best results was composed of 50 mM ammonium acetate and 13.75 mM ammonia.[276] More recently (2018) *Marta Kepinska et al.* designed and studied complexes of fullerene with DOX. After physicochemical characterization of the fullerene size (280 nm) and the ζ potential of fullerene, DOX and fullerene-DOX complex (-30, -8 and -24, respectively), DOX release at different pHs was quantified by CE with LIF detector was determined showing 43 wt% at pH 7.4 and 100 wt% at pH 5.25 free DOX release.[277] *Siyam M. Ansar et al*. in 2018 developed a CE methodology with UV-vis detector to separate and quantify unloaded DOX from a liposomal DDS (Figure 1.27) in a BGE optimized as 20 mM PBS buffer (pH 6.5) containing 10% sucrose.[278] In a 2019 previous study, the same authors designed and tested a CE/ICP-MS/ MS method to determined external and intra-liposomal ammonium sulphate $(NH_4)_2SO_4$ in liposomal DDS carrying DOX. $(NH_4)_2SO_4$ helped to maintain drugs in the intra-liposomal space and by the compilation technique, the molecule quantification was achieved without the need of liposomal disintegration showing the importance of this molecule.[279] Definitely these all methodologies were proved powerful for fast and direct DDS separation and should be used as a standard characterisation.

Project Objectives

Synthesise and characterise magneto-luminescent Janus-type inorganic hybrid nanomaterials coated with a light- and pH-sensitive copolymer for disease monitoring along with smart delivery and controlled release of active ingredients in a site-directed manner.

Specific objectives

- Perform studies for the optimisation in formation and characterisation of micelle-like aggregates composed of light- and pH-responsive amphiphilic copolymers.

- Develop analytical methodologies to quantify and monitor drug concentrations captured and released by nanomaterials in response to stimuli.

- Test drug loading and drug release by light irradiation and/or pH change in micelle-like aggregates.
- Synthesise and characterise Janus-type hybrid inorganic nanoparticles with magnetic and upconversion fractions.

- Coat the hybrid nanoparticles with active ingredients embedded in the micelle-like aggregate for characterisation.

- Perform drug release tests using light irradiation stimuli and/or pH change.

CHAPTER II

A deep understanding of the self-assembly and colloidal stability of light and pH dual-responsive spiropyran random copolymer micelle-like nano-aggregates

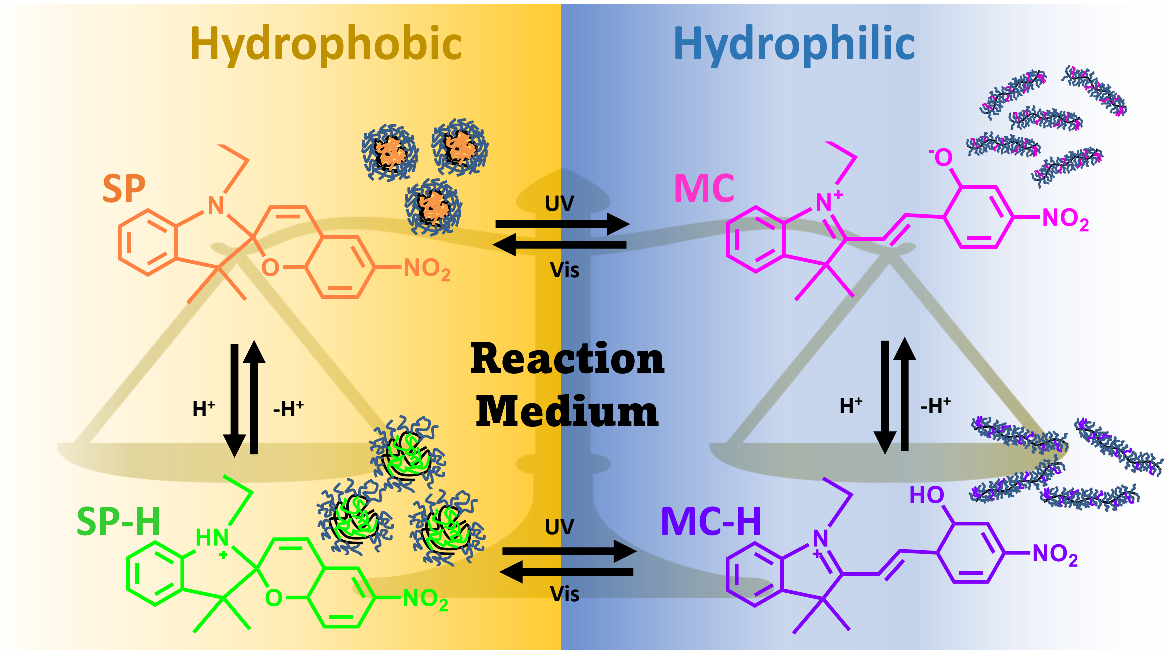

This work has been valorised by a scientific publication in a peer reviewed journal (Materials Today Commun. 2022, 10.1016/j.mtcomm.2022.103499)

2.1 Introduction

As shown in the Chapter I (sections 1.1.4 & 1.2), Polymeric micelles formed of amphiphilic copolymers (ACP) have been recognized as promising tools for pharmaceutical and biomedical applications as bioactive compounds (drugs, proteins, genes, nucleic acids, etc.) smart delivery systems. To generate such efficient ACP-based structures for biomedical applications, it is therefore crucial to: i) control their formation in terms of size and surface charge density, ii) determine the behaviour and colloidal stability of these micelle-like aggregates in different pH and ionic strength solubilization media, and iii) study two delivery strategies (i.e. pH- and UV light-induced) and their combination, to improve the control of site-specific drug release. Until the moment the assembly of the multi-responsive poly(NIPAM-co-SPMA) copolymer has only been studied in deionized water medium, resulting in varied morphologies and micelle-like aggregates sizes ranging from 100 nm to 500 nm.[201,280–282] This lack of structural control could limit the potential translation of the micelle-like aggregates towards clinical applications. Therefore, the focus of this chapter is the rational study of the formation of this micelle-like nanoaggregates and the implications of the medium to better control the final structure and size. Either deionized water or phosphate buffer solution (PBS) at physiological pH (pH= 7.4) and different ionic strengths (25, 50, and 100 mM) were employed here to study the formation of micelle-like aggregates. Their characterization in all media were systematically performed with different methods to determine their morphology, stability, and physicochemical properties, as well as to evaluate induced changes in response to different stimuli such as pH (pH 6.0 and 4.0) and UV-light.

For this purpose, a deep physicochemical characterization was performed through the combination of capillary electrophoresis (CE), dynamic light scattering (DLS), transmission electron microscopy (TEM), and laser doppler electrophoresis (LDE). Whereas DLS and TEM provide global information on the micelle’s sizes in liquid and solid states, respectively, LDE provides information of the effective surface charge density in solution. CE is a powerful separation methodology to characterize distinct structuration’s of nano-objects and associated intrinsic polydispersity in free separation medium (no stationary phase) , leading to low sample consumption, and fast analysis times at low operating costs.[283–286] This method also allows a deep study of interactions (such as copolymer aggregations) in suspensions, and go into the fundamental comprehension of the structural and chemical behaviour of complex systems in different media.[257,258,269] Furthermore, it also enables to perform *in vitro* studies related to drug entrapment and release in physiological-like media with controlled ionic strength, pH, and temperature. CE was therefore employed here for the separation of the synthesis products in batch thanks to differences in electrophoretic velocities of the mixture components to go deeper in the characterization of the resulting self-assembled structures. This electrokinetic approach is intending to design more appropriate and performant micelle-like aggregates for multi-task applications.

2.2 Materials and methods

2.2.1 Materials and reagents

Methacryloyl chloride, triethylamine (Et_3N), tetrahydrofuran (THF), methylene chloride, N-isopropylacrylamide (NIPAM), azobisisobutyronitrile (AIBN), mono basic and dibasic sodium phosphate were purchased from Sigma-Aldrich (Paris, France). Spiropyran (SP) was purchased from TCI (Paris, France). Sodium bicarbonate ($NaHCO_3$), sodium hydroxide (NaOH), and magnesium sulfate ($MgSO_4$) were supplied by Karal (Guanajuato, Mexico). Solvents such tert-butanol, diethyl ether, methyl alcohol, and ethyl alcohol were purchased from J.T. Baker (Mexico City, Mexico). Dialysis bags were obtained from Spectrum Labs (Breda, The Netherlands).

2.2.2 Synthesis of Poly(NIPAM-co-SPMA) random copolymer

The spiropyran functionalized PNIPAM was synthesized according to a previously reported methodology.[280] Briefly, spiropyran monomer (SPMA) was formed by mixing SP (0.3 g), methacryloyl chloride (240 µL), and Et_3N (230 µL) into 30 mL THF at 0 °C. Then the mixture was stirred for 28 hours. The resulting solution was filtered and extracted with $NaHCO_3$ solution and methylene chloride (1:1). The organic layer was washed three times with water, dried with $MgSO_4$, and then concentrated by evaporation. The product was recrystallized with 95% ethyl alcohol. Subsequently, NIPAM (1.53 g), SPMA (0.094 g) and AIBN (0.037 g) were dissolved in 3 ml tert-butanol. After three times freeze-pump-thaw cycles, the mixture was stirred under 70 °C for 15 hours. The copolymer was precipitated in diethyl ether (100 ml) and methyl alcohol (1 ml) mixture solution to remove the unreacted small molecule compounds. After filtering and drying at 40 °C under vacuum for 48 hours, the polymer poly(NIPAM-co-SPMA) was obtained. Schematic representation of Poly(NIPAM-co-SPMA) synthesis is represented in Figure 2.1 A). The synthesis of the copolymer was confirmed by H-NMR Figure 2.1 B) The number-average molecular weight (Mn) and polydispersity index (PDI) of the copolymer determined through gel permeation chromatography (GPC) were 2.05 x 104 g.mol^{-1} and 1.07, respectively. The molar ratio between NIPAM and SP was in 18:1.[280]

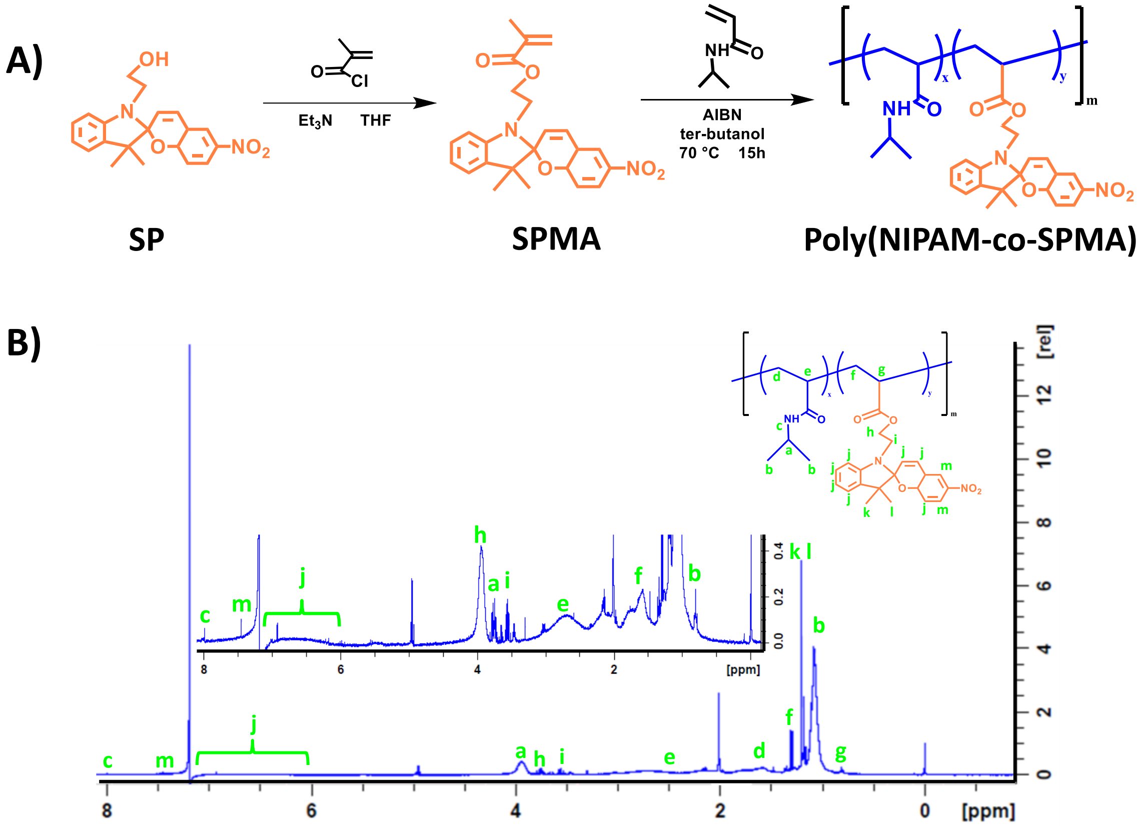

Figure 2.1 A) Schematic representation of Poly(NIPAM-co-SP) random copolymer synthesis, and B) Corresponding H-NMR.

2.2.3 Formation of Poly(NIPAM-co-SPMA) random copolymer micelle-like aggregates in water and buffer solutions

The formation of the micelle-like aggregates using the Poly(NIPAM-co-SP) was first performed in water by varying stirring time (2, 5, 7, and 15 hours) and concentration of the copolymer (0.1, 0.2, 0.3, and 0.5 g.L^{-1}), so as to optimize the process. Poly(NIPAM-co-SP) (2 mg) was dissolved in 1 mL of THF. 1 mL deionized water was added at a rate of 1 µL.s^{-1} with a quick stirring rate (1100 r.p.m.). Then, 9 mL of deionized water were added to the previous solution to ensure the formation of the micelle-like aggregates. After the stirring step, THF was removed by dialysis (10 kDa cut-off) with water at room temperature for 24 h. Samples were stored in amber vials at 8 °C. Also, the formation of micelle-like aggregates was performed in pH 7.4 PBS at different ionic strengths (25, 50, and 100 mM), with the same protocol, by replacing deionized water with PBS.

2.2.4 Poly(NIPAM-co-SPMA) random copolymer micelle-like aggregates characterization

The hydrodynamic diameter of self-assembled micelle-like aggregates as well as their ζ-potential were measured through dynamic light scattering (DLS) and laser Doppler electrophoresis (LDS) at room temperature (25 °C) using a Malvern Zetasizer Nano Men3600 (ville, pays) in the same medium as for formation unless otherwise stated. For the morphology of the micelle-like aggregates TEM images were obtained using a JEOL JEM-1010 microscope equipped with an ORIUS digital camera, by GATAN. The samples were prepared by immersing lacey carbon coated copper grids into the micelle-like aggregate suspensions and allowed to dry at room temperature. Lacey-carbon, 300 mesh copper grids and were purchased from Ted Pella, Inc. (CA, USA)

Capillary electrophoresis experiments were performed on an Agilent 7100 capillary electrophoresis instrument with an UV-diode array detector and coupled to a Zetalif LED induced fluorescence detector. Fused silica capillaries of 75/363 µm I.D./O.D. with polyimide outer coating (cat. no. TSP075375) were purchased from Polymicro Technologies (Phoenix, AZ, USA). Capillary dimensions were 35 cm long, with 12 and 26.5 cm to fluorescence and UV detection windows, respectively. New capillaries were conditioned by performing successive washing under 950 mbar of 0.1 M NaOH (5 min), 0.01 M NaOH (5 min), water (5 min), and BGE (11 min). Unless otherwise specified, 25 mM

PBS at pH 7.4 was used as BGE. 25 mM PBS pH 6 and acetate buffer solution (ABS) 25 mM pH 4 were used to test the pH response of the micelle-like aggregates. Samples were introduced hydrodynamically (20mbar for 3 s) on the inlet side of the capillaries. Separations were carried out by applying a +8 kV voltage. The temperature of the capillary cartridge was set at 36 °C to emulate that of the body.

2.3 Results and discussion

2.3.1 Micelle-like aggregate formation in water: influence of stirring time and copolymer concentration

The formation of stimuli-responsive micelle-like aggregates is classically performed in water, which limits the control over the final size of the carrier (100 – 500 nm).[201,280–282] Furthermore, the assembly of hydrophobic chains into polymeric micelles with controlled size and appropriate colloidal stability has been shown to be highly dependent on specific parameters such as stirring time and speed, temperature, and solvents.[287] To control the micelle-like aggregate size and stability, their formation was first performed in water while varying the stirring time in the 2 to 15 h range, and the copolymer concentration in the 0.1 to 0.5 g.L^{-1} range. For the copolymer employed in this study, it is known that micelle formation must be performed at a fast-stirring speed (above 800 r.p.m.)[288] and a temperature below 40°C (lower than the lower critical solution temperature of the copolymer[280]). Therefore, the stirring and temperature were set as 1000 r.p.m. and 36°C, respectively for all experiments. The different batches were characterized by DLS in the same solubilization medium to estimate the mean micelle-like aggregates size. The hydrodynamic diameter, polydispersity index (PDI), peak width and standard deviation are presented in Table 2.1.

First, the influence of copolymer concentration (0.1, 0.2, 0.3 and 0.5 g.L^{-1}) on the aggregate formation was studied with a stirring time of 7h, which is a common time found in literature. A polymeric membrane was visually observed only at a copolymer concentration of 0.5 g.L^{-1} (see Figure 2.2). This phenomenon could be expected considering such concentration vastly higher than the CAC of the copolymer knowing that a higher CAC micelle-like aggregates in water turns into membranes.[289] Therefore, batches at 0.5 g.L^{-1} polymer concentration were discarded from the study. Subsequently, at polymer concentrations of 0.1 and 0.2 g.L^{-1}, a single aggregate population was evidenced (see Figure 2.3 A) with equivalent hydrodynamic diameter 125 ± 3 and 124 ± 2 nm, respectively, with a narrow size distribution, evidencing that the working concentration is above the CAC. On the other hand, when working at 0.3 g.L^{-1}, two populations were evidenced, at 193 ± 8 and 25 ± 5 nm, probably due to a restructuration of aggregated structures at this concentration as a transition toward membranous structures observed at and 0.5 g.L^{-1}. For the subsequent synthesis experiments, the concentration selected was 0.2 g.L^{-1}.

Figure 2.2 Polymeric membrane formation using 0.5 mg/ml Poly(NIPAM-co-SPMA) in water.

Then, the stirring time was explored as a synthesis parameter working at 0.2 g.L^{-1} (Figure 2.3 B). The resulting batches presented either one or two populations, with hydrodynamic diameters ranging from 36 ± 3 to 718 ± 14 nm, with a PDI between 0.3 and 0.6. It is worth noting that one of the limitations of DLS in colloidal objects characterization is its narrow resolution, preventing the possibility to recognize particle populations differing in size from each other of a factor lower than 3 (particles of 90 and 110 nm are not distinguished) resulting in an apparent monomodal distribution with a high polydispersity index (PDI)[9].

For 2h and 15h stirring times. two populations were evidenced when measuring the peak intensities (36/294 nm and 110/718 nm hydrodynamic diameters, respectively). Only one population (the smallest one) was evidenced when measuring the number of particles, which is coherent with the fact that plotting the number privileges the visualization of the smallest objects. On the other hand, the intensity graph shows all populations found in the solution giving a higher weight to the biggest objects. This result indicates the formation of two different size structures. For 5 and 7 h stirring time, a single signal was evidenced, with hydrodynamic diameters of 358 ± 33 and 126 ± 2 nm, respectively. Furthermore, except for 7 hours stirring, the size distribution of the aggregates is not monodispersed, having large peak widths due to the poor thermodynamic stability control on the aggregate formation, breaking up or agglomerating (micellar associations).[290] A stirring time of 7 hours allowed for the smallest aggregate population modal size and PDI. This stirring time was selected for further studies.

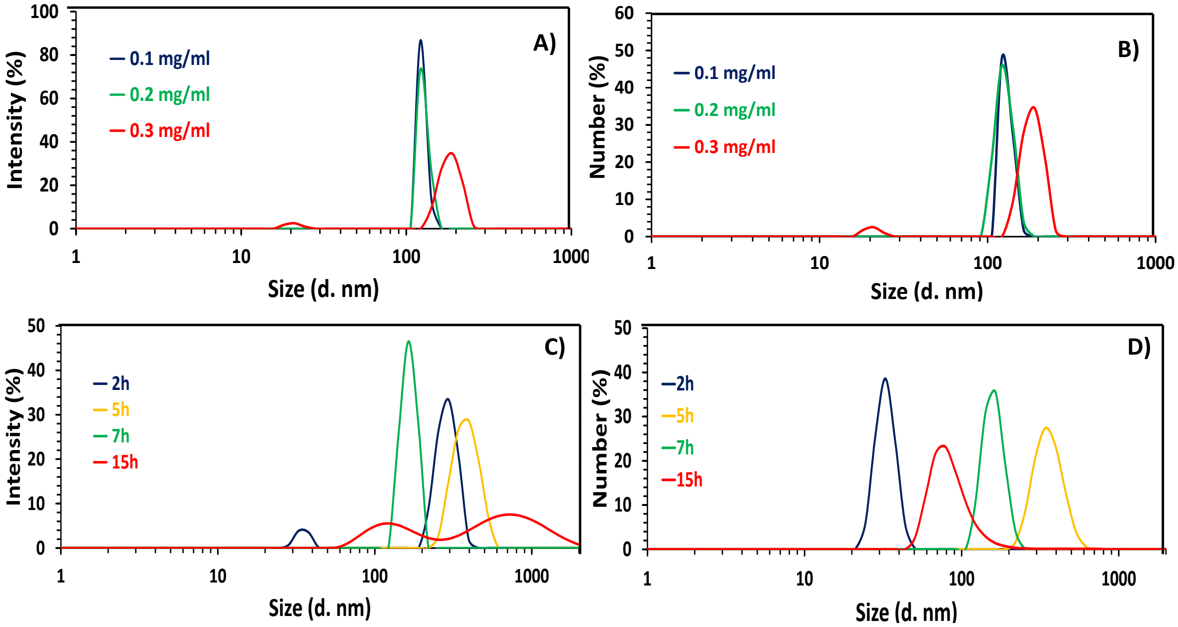

Figure 2.3 Copolymer concentration (A and B) and Stirring time (C and D) effects on the DLS hydrodynamic diameter of micelle like aggregates. Experimental results are presented on intensity and number values

Table 2.1 DLS results for optimization of micelle-like aggregates formation according to polymer concentration (at a 7h stirring time) and stirring time (at a 0.2 mg.mL-1 concentration).

Concentration (mg.mL-1)	D_H [a] (nm)	PDI [b]	Std Dev (n=3) [c]	Peak with (nm)
0.1	125	0.302	3	20
0.2	124	0.361	3	20
0.3	193	0.547	8	6.2
	25		5	92
Stirring Time (h)	**D_H [a] (nm)**	**PDI [b]**	**Std Dev (n=3) [c]**	**Peak with (nm)**
2	36	0.557	3	5
	294		4	141
5	358	0.598	33	236
7	126	0.361	2	78
15	110	0.552	28	111
	718		14	884

[a] Hydrodynamic Diameter

[b] Polydispersity Index

[c] Standard Deviation (3 repetitions)

Thus, a standard protocol for the formation of different ACP-based self-assembled structures was optimized in water. It was observed that the stirring time and the polymer concentration are key parameters to control the final structure of the micelle-like aggregates. Aggregated structures, thermodynamically stable and showing smaller modal size and reduced PDI values were obtained with 0.2 g.L^{-1} concentration and stirring time of 7h. These experimental conditions were fixed for subsequent experiments.

2.3.2 Micelle-like aggregates formation in PBS: influence of ionic strength

Since the pH and ionic strength seem to play an important role in the micelle-like aggregate formation and stability, their influence on the self-assembly of the random Poly(NIPAM-co-SPMA) amphiphilic copolymer was investigated for the first time in this work. As these parameters are inherently regulated in the internal fluids of the cells[291], the study of micelle-like aggregate formation was carried out using pH 7.4 phosphate buffers at different ionic strengths 100mM (Mic100), 50mM (Mic50), and 25mM (Mic25), and the results compared with those obtained in deionized water (MicH_2O). Capillary zone electrophoresis, DLS and TEM observations were studied in parallel to deeply understand their physicochemical properties and to optimize the formation of these structures (Figure 2.4).

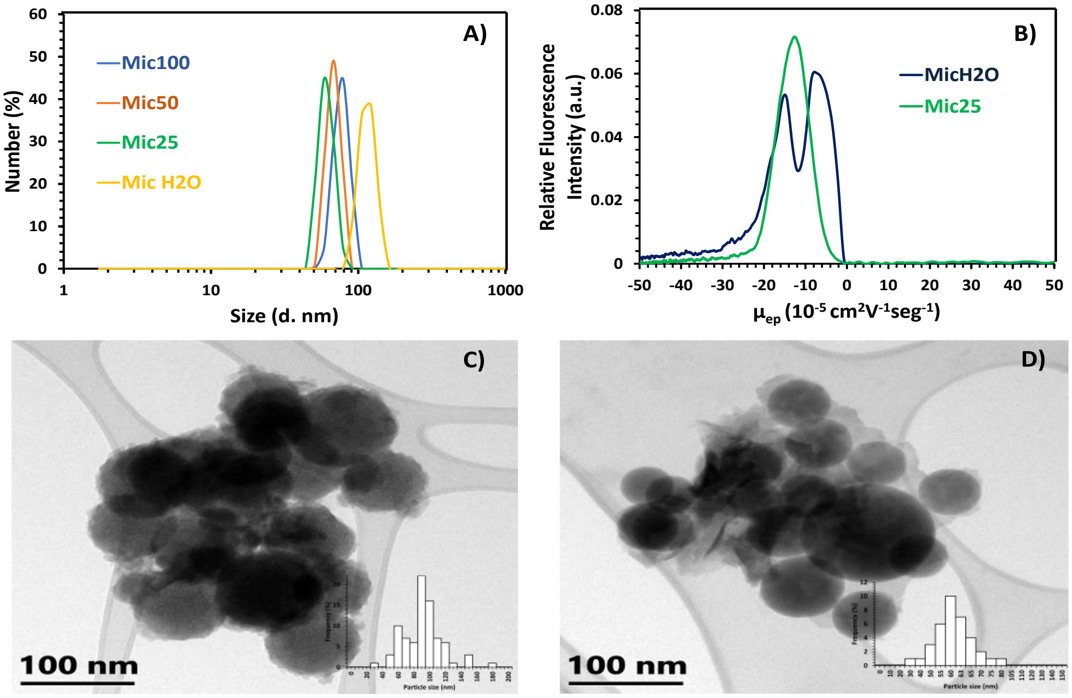

Figure 2.4 Ionic strength effect on the DLS hydrodynamic diameter (A) electrophoretic profiles (B) of micelle-like aggregates, in 25 mM PBS (pH 7.4). TEM images (size distribution histograms insets) of MicH2O (C) and Mic25 (D).

It should be noted that the main difference between water and phosphate buffer, regardless of the ionic strength, is the pH control. When deionized water meets atmospheric carbon dioxide, its absorption produces carbonic acid, which can reduce the water's pH to weakly acid values around pH 5.6.[292] This is a considerable factor regarding the formation of pH-sensitive structures. Indeed, when these micelle-like aggregates are in an acidic aqueous medium, they swell.[293] In addition, the pH-sensitive SPMA blocks (pKa 6-7)[291] tend to stretch towards the solvent after protonation.[294]

The DLS measurements (performed in the same medium used for the synthesis) of the micelle-like aggregates formed in water (MicH_2O) compared to those formed in PBS buffers pH 7.4, are presented in Figure 2.4 A. The MicH_2O hydrodynamic diameter is higher (126 nm ± 2, PDI 0.361) than those of Mic100 (91 ± 9 nm, PDI 0.565), Mic50 (67 ± 1 nm, PDI 0.414) and Mic25 (61 ± 2 nm, PDI 0.365) obtained in pH 7.4 PBS buffer (Table 2.2). Briefly, the increase in ionic strength of PBS generates an increase in hydrodynamic diameter. A schematic representation of micelle formation in deionised water and PBS at pH 7.4 is proposed in Figure 2.5. Since the NIPAM blocks are electrostatically neutral, electrostatic shielding in the shell is not responsible for the ion-dependent behaviour. When ions are added in the formation medium the solubility of precursor polymer is reduced promoting aggregated structures integrating a greater number of copolymers to the core resulting in larger objects.[295,296] Eventually, the lowest modal population size (61 nm) and PDI (0.365) value is found for Mic 25 indicating a higher control formation equilibrium of aggregated structures.

Table 2.2 Different I.S. DLS results for micelle-like aggregates formation

I.S. (mM)	D_H [a] (nm)	PDI [b]	Std Dev [c]	Peak width (nm)
100	91	0,565	9	23
50	67	0,414	1	20
25	61	0,365	2	20
H_2O *	124	0,361	3	36

[a] Hydrodynamic Diameter

[b] Polydispersity Index

[c] Standard Deviation (3 repetitions)

* Deionized water

Therefore, smaller objects with lower size distribution were produced in 25 mM PBS. It is shown in the literature that these characteristics[199] extend their permanency in the systemic circulation, allow a better control over their biodistribution and transport across barriers, improve their targeting efficiency, and reduce their toxicity.[297] This solubilization medium was then selected for subsequent studies.

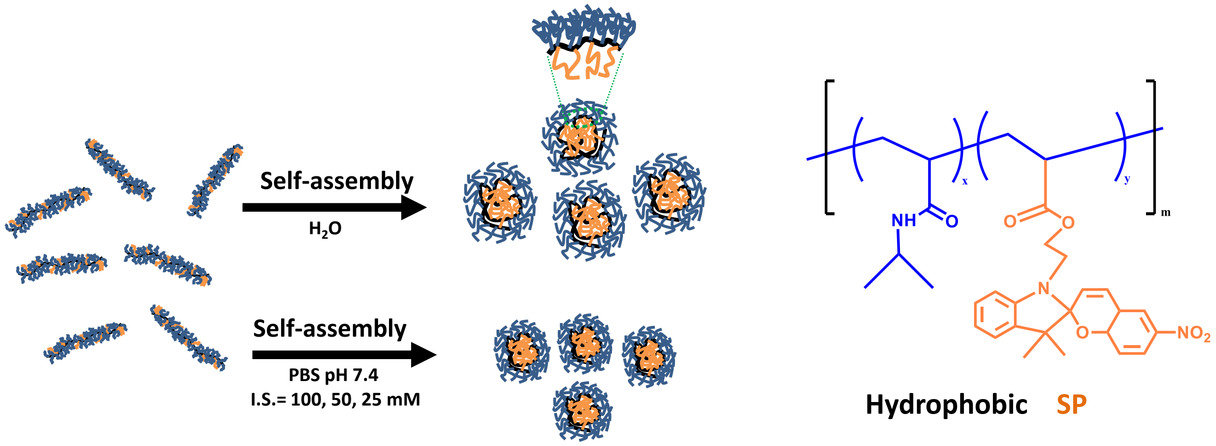

Figure 2.5 Schematic representation of Poly(NIPAM-co-SP) random copolymer micelle-like aggregates self-assembly in water and buffered solutions.

When employing CE for the separation of the micelle-like aggregates batches, a buffered background electrolyte (BGE) is mandatory for efficient and repeatable separations. Therefore, CE characterization was performed on MicH$_2$O and Mic25 (Figure 2.4 B) by employing a 25 mM PBS (pH 7.4) BGE, with UV-visible and fluorescence detection. As the SP compound is fluorescent, fluorescent detection allowed to be more specific than UV-visible detection. MicH$_2$0 presents a structured electrokinetic profile showing two non-resolved peaks at an electrophoretic mobility of $-16 \times 10^{-5} \pm 2$ and $-7 \times 10^{-5} \pm 3$ $cm^2V^{-1}s^{-1}$ here as Mic25 presents one peak at -13×10^{-5} $cm^2V^{-1}s^{-1} \pm 0.5$. The identified peaks were proved not to arise from the precursor's copolymer (see Figure 2.6). It must be reminded that MicH20 was synthesized in water, analysed in water by DLS, providing global information on hydrodynamic diameter, and then separated by CE in the 25 mM PBS BGE, according to their charge density over hydrodynamic radius ratio. The dual peaks for MicH$_2$0 on Figure 2.4 B) could be due to the micelle–like aggregate transfer from water to 25 mM PBS, related to a conductivity difference between the sample area (water) and the 25 mM PBS separation medium. The electrophoretic mobilities of MicH$_2$0 and Mic25 are similar, whereas the hydrodynamic diameter of MiCH$_2$O (measured by DLS in their medium formation) is twice the one of Mic25, which should indicate different structures according to the solubilization medium, as previously described (Figure 2.5).

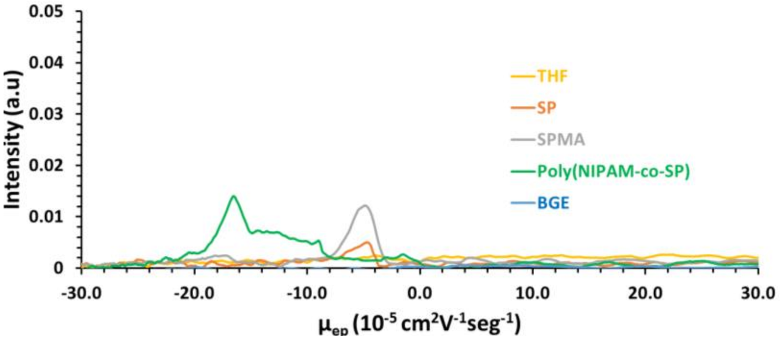

Figure 2.6 C.E. Fluorescence detection of micelle-like aggregates precursors in a concentration of 0.2 mg/ml using as BGE PBS pH 7.4 I.S. 25mM.

Moreover, morphology and size of the formed aggregates MicH$_2$O (80 – 100 nm) and Mic25 (55 – 60 nm) determined by TEM in Figure 2.4 C) and Figure 2.4 D) respectively, shows spherical morphologies as well as a trend of decreasing diameter when the aggregate formation take place in PBS.

Therefore, Mic25 demonstrated a better control of the aggregated structures in terms of size, polydispersity, and thermodynamic stability. These results highlight the strong interest of CE for the physicochemical characterization and understanding of micelle-like aggregate structuration. This simple methodology can mimic physiological environments and help foreseeing the impact of the medium on the *in vivo* behaviour of such polymeric aggregates.

2.3.3 Mic25 micelle-like aggregate stability in physiological-like PBS: influence of the ionic strength

The influence of the analytical conditions for the Mic25 (Figure 2.7) was then studied through DLS and CE in PBS pH 7.4 with different ionic strengths (25, 50, and 100 mM). Mic25 diameters measured by DLS were 64 ± 2 nm (PDI 0.365), 60 ± 3 nm (PDI 0.536) and 58 ± 5 nm (PDI 0.475) for 25mM, 50mM and 100mM ionic strengths respectively. Significant differences in hydrodynamic diameters were not observed upon variation of the I.S. of the analysis medium. On the other hand, electrophoretic mobilities decreased in absolute value while increasing the I.S. of the BGE (-13×10^{-5} cm^{2}V^{-1}s^{-1}, -8×10^{-5} cm^{2}V^{-1}s^{-1} and -6.5×10^{-5} cm^{2}V^{-1}s^{-1} for I.S. of 25, 50 and 100 mM, respectively). This evolution in conjunction with the fluorescence intensity decrease is possibly related to a modification of the core auto-assembled structure. A parallel study for MicH20 shows similar trends on the electrophoretic mobility and fluorescence intensity behaviors (Figure 2.8). These results evidence the influence of the ionic strength on the self-assembly of Mic25. As they provide similar sizes whatever the I.S., Mic25 were further studied regarding the influence of micelle stimulation by pH and UV light on their structure and behavior in physiological buffers.

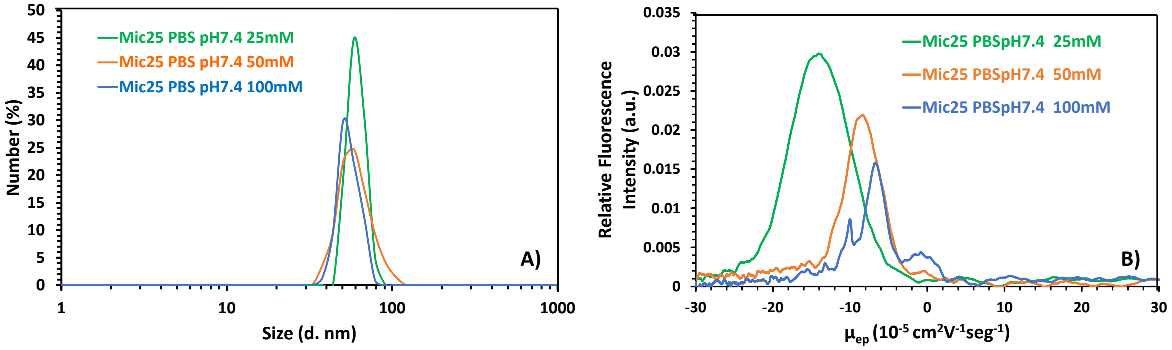

Figure 2.7 A) Ionic strength effect on the DLS hydrodynamic diameter (A) and electrophoretic profiles (B) of Mic25 in PBS (pH 7.4).

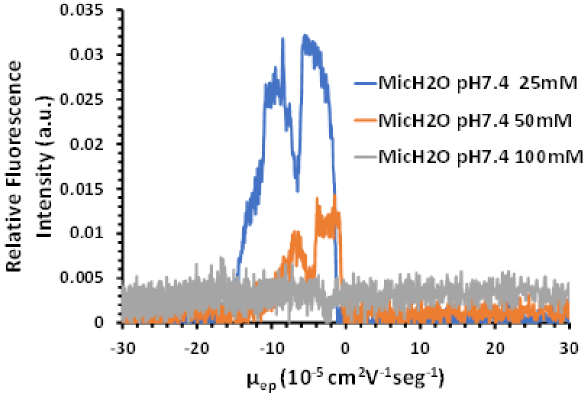

Figure 2.8 MicH2O C.E. micelle-like aggregates C.E. detection using a different I.S. BGE of PBS pH 7.4 (25mM, 50mM and 100mM).

2.3.3 UV-Light irradiation and pH effects on Mic25 micelle-like aggregates

The photo-sensitive spiropyran (SP) structure present in the micelles has hydrophobic characteristics. Its photoisomerization into its zwitterionic state merocyanine (MC) is reversible (Figure 2.9). Then, UV light irradiation leads to the formation of hydrophilic MC on the micelle backbone, and therefore to the disaggregation of the micelle. Spiropyran returns to its hydrophobic state (SP) under visible light, allowing for the re-formation of the micelle-like aggregates.[201,291,298–300] On the other hand, the micelles are known to be sensitive to pH, mainly due to the protonation of spiropyran (Figure 2.9).

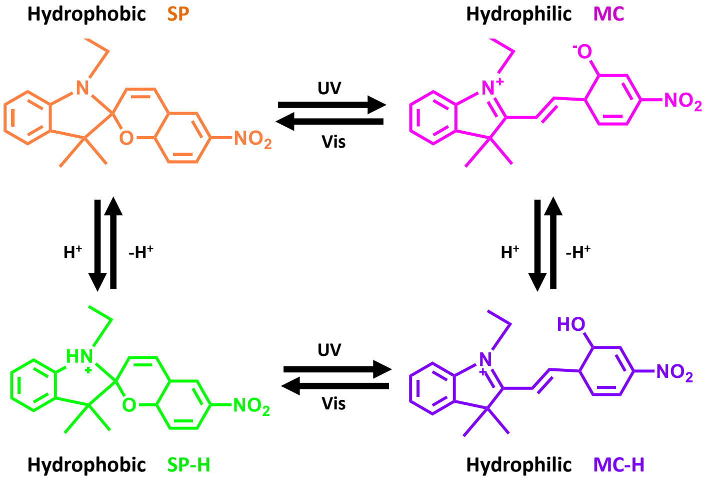

Figure 2.9 Schematic representation of reversible photo-induced isomerization of spiropyran (SP) and merocyanine (MC) and respective protonation equilibria.

In this context, a deep study was performed to evaluate the effect of both stimuli (either one by one or together) on the morphology and physicochemical properties of the Mic25 micelles. For this purpose, different methodologies were combined, including, DLS, LDE, TEM and CE. The samples were first dissolved in 25 mM PBS (pH 7.4), then irradiated with UV light (365 nm) for 15 minutes and stored under unlighted conditions for subsequent characterization.

First UV stimulation was studied. DLS measurements (Figure 2.10 A) showed an increase in the equivalent spherical diameters of micelle-like aggregates under UV irradiation (65 ± 2 nm (PDI 0.365) and 128 ± 3 nm (PDI 0.667) before and after 15 min UV light irradiation, respectively). On the other hand, LDE measurements (Figure 2.10 B) did not show a significant difference in the electrical charge of the compound without (one shouldered peak in the -1 to -20 mV domain) or with (one symmetrical peak at -7 mV) UV irradiation. It must be noted that DLS and LDE are good methods for spherical nano-objects, which is not the case if the micelles disaggregate. TEM micrography before UV irradiation (Figure 2.4 D) shows a spherical morphology with a small size distribution (60 nm ± 2) and apparent dispersion. In contrast, after 15 min of UV irradiation (Figure 2.10 C), the observed undefined geometry could be linked to a partial disaggregation of the Mic25. Therefore, the combined characterization by DLS, LDE and TEM highlights the impact of a 15 min UV light irradiation on the structure of the Mic25, with an evidenced on the increase of the equivalent spherical diameter of the structure in solution without significant modification of the measured zeta-potential and modification of the nanostructure by TEM. This evolution is schematized in Figure 2.12.

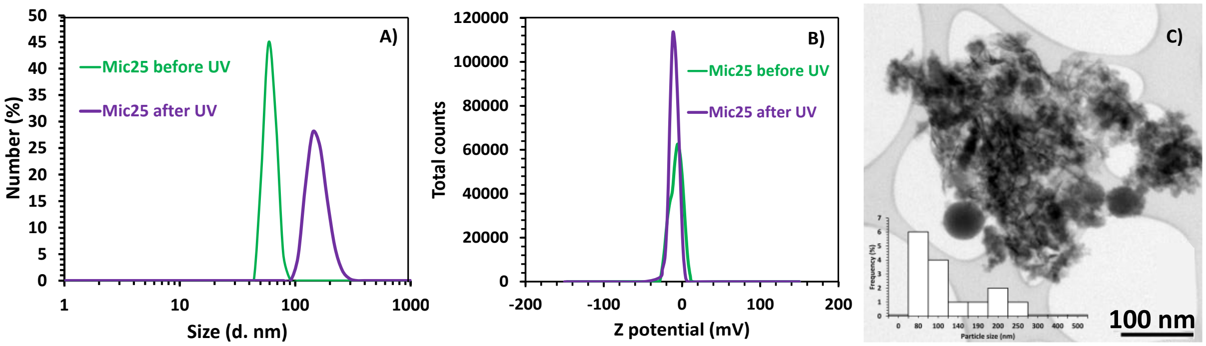

Figure 2.10 Light effect on the hydrodynamic diameter measured by DLS (A), the surface charge density measured by LDE superficial charge density (B) on Mic25. TEM image of Mic25 after 15 min 365 nm UV light irradiation (C).

For pH stimuli, Mic25 were analysed in PBS (pH 7.4), PBS (pH 6) and acetate buffer (ABS, pH 4), all at a 25 mM of ionic strength. Figure 2.11 A) presents the electropherograms at these 3 pH values: whereas a quite Gaussian electrokinetic profil was observed at pH 7.4, a structured electrokinetic profile showing unresolved peaks of diminished intensity and reduced mobility values was observed at pH 6 l. At pH 6, the evolution could be explained by (1) a possible quenching of the fluorescence when the pH decreases due to the protonation of the spiropyran structure (SP-H)[301], and/or (2) the swelling phenomenon for such micelles[293] leading to a polydispersity of the sample that starts disaggregating. At pH 4, no micelle signal could be detected, since the micelles at this pH should be disaggregated, showing the potential of this structure for the release of drugs in acidic environments.

Further studies were performed by combining pH and UV stimuli. After UV irradiation of Mic25 (Figure 2.11 B), the electrophoretic profile at pH 7.4 after irradiation shows a dissymmetric profile with small overlapping and slightly reduced mobility characteristic of a destabilization of the aggregated structure consistent with the to a partial disaggregation evidenced by TEM and increased equivalent spherical size measured in DLS. When the separation is performed at pH 6, irradiated samples characterized in CE show a more pronounced diminution of peak intensity with a shift toward lower electrophoretic mobilities in absolute value that prove that UV-light enhance the effect of pH with regards of micelle disaggregation. Again, at pH 4 no detection of the micelles could be obtained as expected either for irradiated or non-irradiated sample. The combined synergistic effects of pH (at pH 6) and UV stimuli were also analyzed by TEM. When dispersed in a pH 6 medium, Mic25 shows (Figure 2.11 C) a mix of spherical objects with larger diameter (120 to 250 nm) than for micelle-like aggregates characterized at pH 7.4 (60 nm), combined with apparently disaggregated structures. As explained before, micelles at a more acidic pH begin to swell. Indeed, the pH-sensitive SPMA chains tend to stretch after protonation towards the solvent[302], as schematized on Figure 2.12. After having irradiated the sample with UV light, Figure 2.11 D) shows a totally disaggregated amorphous structure with a polydisperse size distribution (150 – 400 nm). This result confirms that the two effects, swelling and disaggregation, can be controlled by the pH change and UV irradiation.

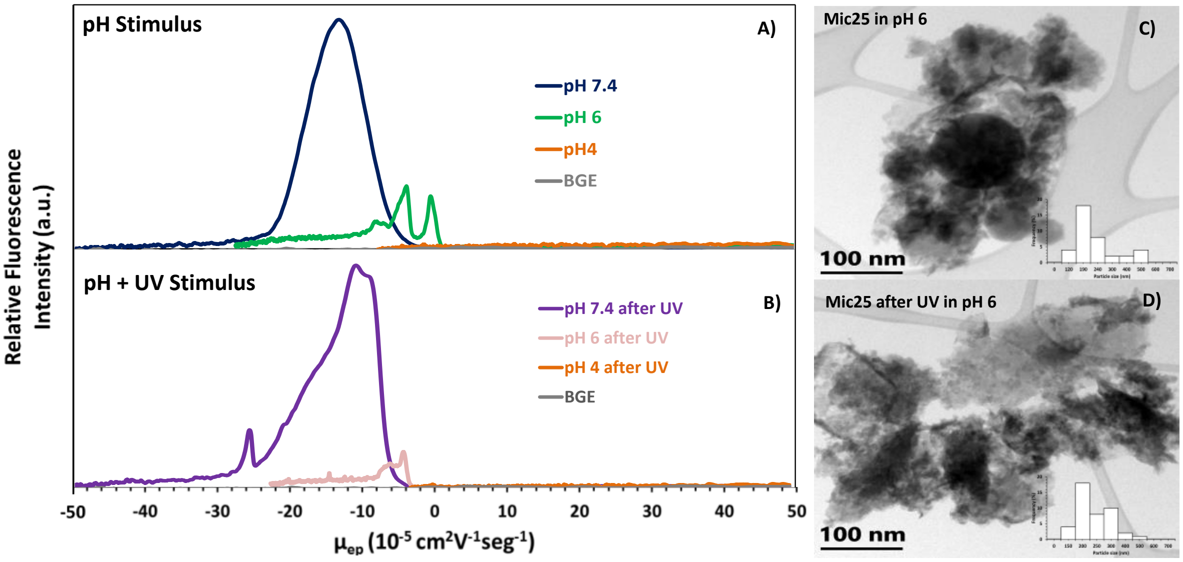

Figure 2.11 A) pH effect and B) dual pH – UV Light effect electrophoretic profiles of Mic25 (BGE PBS I.S. pH: 7.4 and 6 – BGE ABS pH 4 I.S. 25mM). C) pH effect and D) dual pH–Light effect TEM images (size distribution histograms insets) of Mic25 (15 min 365 nm UV light irradiation).

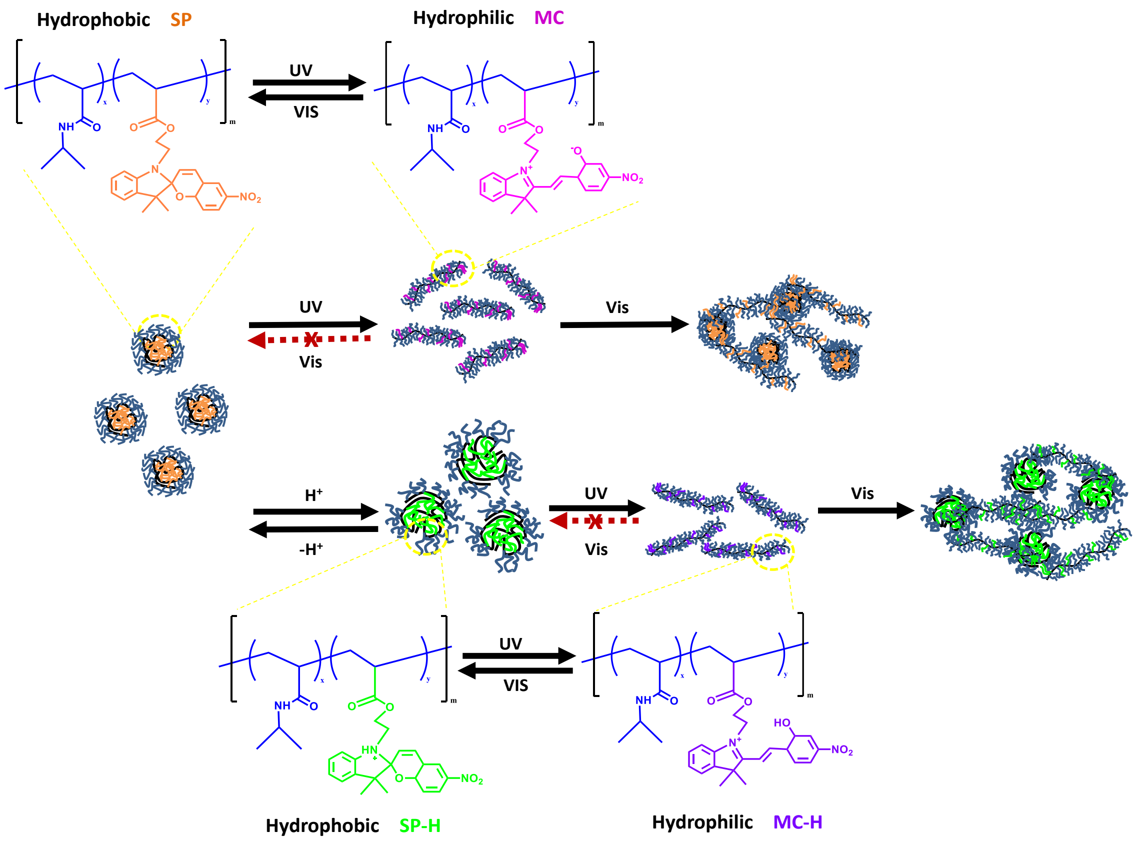

Figure 2.12 Schematic representation of the molecular and morphological variations of micelles under pH - UV light stimulus.

2.4 Preliminary conclusions

This work demonstrated for the first time that the self-assembly of micelle-like aggregates of the random Poly(NIPAM-co-Spiropyran) amphiphilic copolymer can be modulated not only by classic conditions such as the copolymer concentrations and the stirring time, but also by the ionic strength of the formation medium. In previously reported works, the formation of these structures was performed exclusively in deionized water, yielding micellar aggregates with uncontrolled morphologies and particle sizes ranging from 100 to 500 nm. Herein, phosphate-buffered solutions with controlled ionic strength were employed as reaction media at pH 7.4. Characterizations by DLS, LDE, TEM and CE demonstrated a hydrodynamic diameter value decrease using a saline medium formation in compared to classical water formation medium. Working in saline medium there is a slightly increase in hydrodynamic diameter while increasing ionic strength. Since the NIPAM blocks are electrostatically neutral, the ionic strength dependence cannot be related to electrostatic shielding in the outer layer shell but to electrostatic repulsions between the spiropyran monomer blocks, allowing a greater number of copolymers to aggregate into the core of larger micelles while the I.S. increases. In this work, optimized micelle-like aggregates with an average size of 60 nm and narrow size distribution were obtained in 25 mM PBS (pH 7.4).

Furthermore, a molecular mechanism of copolymer aggregation/disaggregation in response to both pH and light stimulus was elucidated through electrokinetic measurements, complemented with TEM observations, DLS and LDE analyses. Accordingly, the photo-sensitive spiropyran moieties in the micelle-like aggregates show a characteristic hydrophobic behavior at pH 7.4. Thereafter, the exposure of the micelle to UV-light leads to the photoisomerization into its hydrophobic zwitterionic state merocyanine, conducing to micelle disaggregation. Since the micelles are also sensitive to pH gradients mainly due to the protonation of spiropyran group at pH < 6.0, acidic environments trigger their swelling and consequent disaggregation, allowing to consider these nano-carriers for localized drug delivery at tumour sites. These findings make the basis to pursue the work towards the evaluation of the loading/release capabilities of this micelle-like aggregates, which is the main objective of the Chapter III.

To conclude, this work points out the delicate balance between copolymer concentration, pH and ionic strength in view of producing multi-responsive micelle-like aggregates for applications such as smart drug delivery. It furthermore highlights the need for a deep physico-chemical characterization by various methodologies, among which electrokinetic separations, to select the most effective nano-carriers for further biomedical applications.

CHAPTER III

Rational understanding of loading and release of doxorubicin by UV-light and pH responsive Poly(NIPAM-co-SPMA) micelle-like aggregates

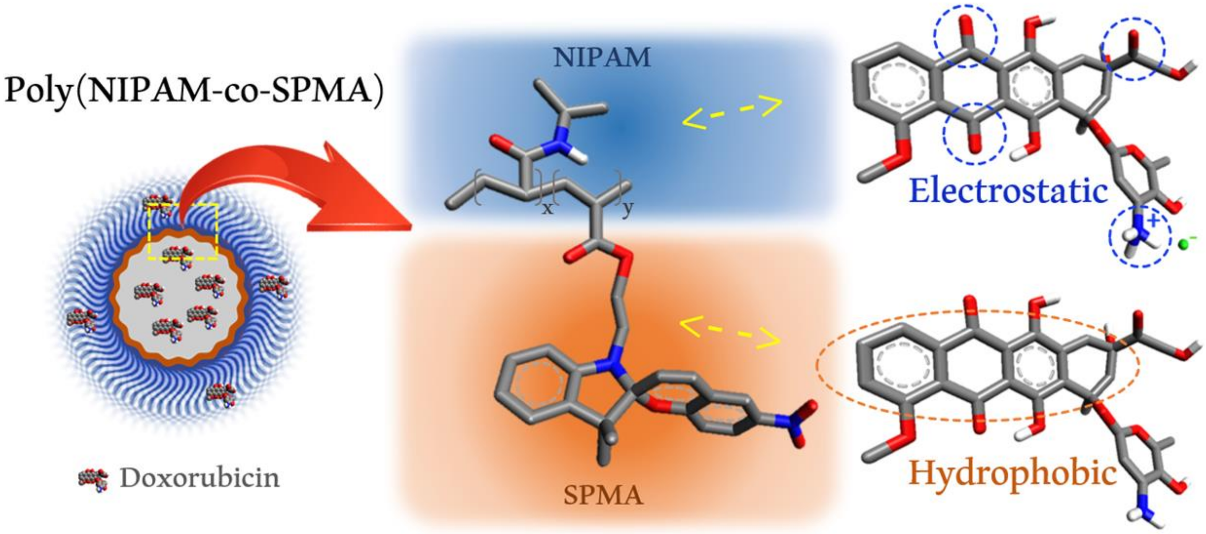

This work is being valorised by a scientific publication in a peer reviewed journal (Molecular Pharmaceutics, under revision)

3.1 Introduction

Once we have been able to well-control the formation of Poly(NIPAM-co-Spiropyran) micelle-like nanoaggregates (see Chapter II), the evaluation of their capability for the loading/release of drugs is essential for further translation into biomedical applications. In this way as mentioned in Chapter I section 1.2.1 different methodologies to produce micelle-like aggregates and capture drugs (section 1.2.1) has been described including oil-in-water emulsion, solvent evaporation, freeze-drying, and dialysis.[303,304] The latest is one of the most widely used methods, and it involves the solubilization of both, the amphiphilic copolymer and the drug, in a water-miscible organic solvent, followed by dialysis purification against water. There, the gradual replacement of the organic solvent with water triggers a self-association of the block copolymers and the incorporation of the model drugs within the assembled structures.[304] In those systems, it is well-accepted that poorly water-soluble active principles interact with the hydrophobic molecular segments at the inner part of the micelle-like aggregates, creating a hollow drug container. Moreover, different types of interactions could be expected according to the chemical nature of the polymeric components and the model drugs, such as hydrogen bonding, ionic, hydrophobic, π–π stacking, electrostatic, and stereocomplex interactions.[305–312] However, very scarce studies have been focused on studying these interactions. Notably, dissipative particle dynamics simulations were applied to model the interactions of Dox with polycaprolactone-b-polyethylene glycol methyl ether methacrylate and poly(ethylene glycol) methyl ether-b-poly(N,N-diethylamino ethyl methacrylate) micelles showing hydrophobic interactions in micelle core.[306] In another work, Dox-HCl was found to electrostatically interacts with the hydrophilic poly(ethylene oxide) units at the corona region of Pluronic micelles, thus affecting their size and photoluminescent response.[307] More studies in this field are highly demanded to better understand the behavior of this system. On the other hand, in drug-loading and release studies, till now, the evaluation has been achieved through classical methodologies based on UV-Vis, fluorescence spectroscopy, and HPLC.[313–321] Unfortunately, those analytical techniques did not reveal information about interactions between the model drugs and the structural components of the micelles under the releasing process.

Thereby, in this part of the work it is aimed to obtain a deep understanding of the interactions between micelle-like aggregates and the doxorubicin model-drug. For this purpose, stimuli-responsive poly[(N-isopropylacrylamide)-co-(1'-(2-methacryloxyethyl)-3',3'-dimethyl-6-nitrospiro(2H-1-benzo-pyran-2,2'-indoline)] (Poly(NIPAM-co-SPMA)) copolymer nanocarriers were synthesized[322], and the loading and release of poorly and highly water-soluble doxorubicin forms (Dox and Dox-HCl, respectively) were evaluated upon UV-light irradiation and/or pH decrease down to pH 6.0. Capillary zone electrophoresis coupled to a fluorescence detector (CE-LIF) allowed to specifically characterize the micelle-like aggregates, and free doxorubicin to quantify the loading and release capacity of the nanocarrier. Those results were complemented by TEM and DLS analysis, providing a full-panorama of the micelle-like aggregates formation, structure, and interactions with the antineoplastic model drug doxorubicin. Furthermore, the electrophoretic profiles were analyzed to evidence micelles and drug possible new structure intermediates or structures formations by the drug and the non-aggregated copolymer. Since all these parameters are involved on the global drug-delivery behavior, this work contributes to the development of more effective stimuli-responsive nanocarriers.

3.2 Materials and methods

3.2.1 Materials and reagents

Spiropyran (SP) was purchased from TCI (Paris, France); methacryloyl chloride, triethylamine (Et_3N), methylene chloride, tetrahydrofuran (THF), mono basic sodium phosphate, dibasic sodium phosphate, N-isopropylacrylamide (NIPAM), azobisisobutyronitrile (AIBN) and Doxorubicin Hydrochloride (Dox-HCl) were purchased from Sigma-Aldrich (Paris, France); Doxorubicin was obtained from Adooq Bioscience (Nanterre, France). Sodium bicarbonate ($NaHCO_3$), sodium hydroxide (NaOH), and magnesium sulfate ($MgSO_4$) were supplied by Karal (Guanajuato, Mexico). Solvents such as tert-butanol, diethyl ether, methyl alcohol, and ethyl alcohol were purchased from J.T. Baker (Mexico City, Mexico). Dialysis bags were obtained from Spectrum Labs (Breda, The Netherlands).

3.2.2 Formation of Poly(NIPAM-co-SPMA) micelle-like aggregates and doxorubicin loading

Poly(NIPAM-co-SPMA) was synthesized according to a previously reported methodology.[223] Then the micelle-like aggregates (Mic) formation was performed according to our previous work.[322] Briefly, 2 mg of poly(NIPAM-co-SPMA) were firstly dissolved in 1 mL of THF. A phosphate buffer solution (PBS) solution (pH 7.4 and I.S. 25 mM) was then added in two steps as follows: the first mL at a rate of 1 µL.s^{-1} under vigorous stirring (1100 rpm) followed by a quick addition of 9 mL ; the final solution was stirred at 1100 rpm for 7 hours. Finally, THF and reaction residuals were removed by dialysis (10 kDa cut-off) with PBS (pH 7.4 and I.S. 25 mM) at room temperature for 24 h. Samples were stored in amber vials at 8°C for further analysis.

Two chemical forms of the model drug doxorubicin were studied. They were incorporated during Mic formation at two different steps according to their corresponding solubility, as shown in Figure 3.1. For incorporation of the hydrophilic form, doxorubicin hydrochloride (Dox-HCl) (2.0, 3.5 or 5.0 µM concentrations) was dissolved in phosphate buffer solution (PBS) (pH 7.4 and I.S. 25 mM) and added to the poly(NIPAM-co-SPMA) solution in THF. For incorporation of the poorly water-soluble form doxorubicin (Dox) was dissolved in 1 mL of THF at similar concentrations and then mixed with poly(NIPAM-co-SPMA). In both cases, the other parameters were kept as for doxorubicin-free Mic synthesis.

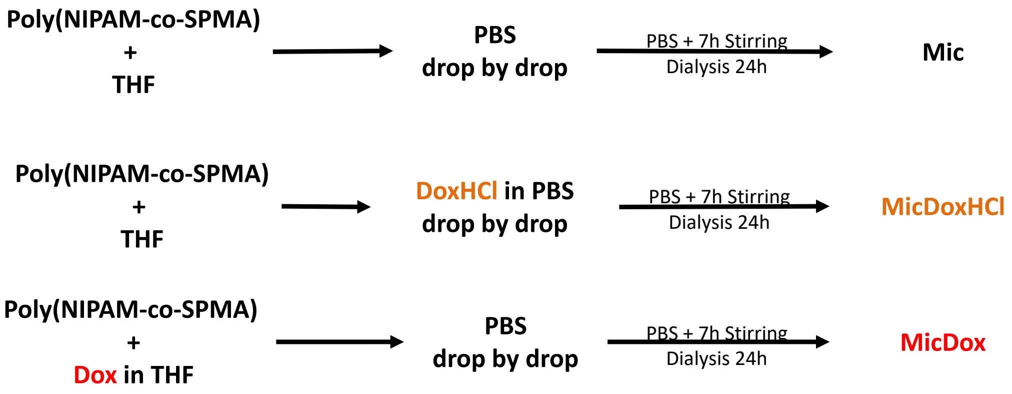

Figure 3.1 Workflow process for the formation of Micelle-like aggregates (Mic) and incorporation of DoxHCl (MicDoxHCl) or Dox (MicDox).

For further understanding of the mechanisms involved in the doxorubicin integration on the micelle-like aggregates, two additional experiments where performed mixing 5.0 µM DoxHCl with either the copolymer (CoPo) Poly(NIPAM-co-SPMA) or the micelle-like aggregates (Mic), named CoPo-DoxHCl and Mic+DoxHCl respectively, without further treatments (no dialysis). For CoPo-DoxHCl, DoxHCl 5.0 µM was dissolved in phosphate buffer 9 ml PBS solution (pH 7.4 and I.S. 25 mM) and added to the poly(NIPAM-co-SPMA) solution in 1 mL THF (No stirring and dialysis process). For Mic+DoxHCl after Mic formation, DoxHCl was added to achieve a final concentration of 5 µM in the sample solution (10 mL).

3.2.3 Structural and colloidal characterization

The hydrodynamic diameter of self-assembled micelle-like aggregates was measured at room temperature (25 °C) through dynamic light scattering (DLS) using a Malvern Zetasizer NanoMen3600 instrument. (Palaiseau, France). PBS was used as the medium for all measurements, controlling pH and ionic strength (I.S.), as specified in each experiment.

TEM images were obtained using a JEOL JEM-1010 microscope (Massachusetts, USA) equipped with an ORIUS digital camera by GATAN (Massachusetts, USA). Samples were prepared by immersion of 300 mesh lacey carbon-coated copper grids (provided by Ted Pella, Inc. CA, USA) into the micelle-like aggregate suspensions and allowed to dry at room temperature.

Capillary electrophoresis (CE) experiments were performed with an Agilent 7100 capillary electrophoresis instrument (Agilent Technologies, Waldbronn, Germany) coupled to a Zetalif LED-induced fluorescence detector (Adelis-Picometrics, Grabels, France), in this work CE-LIF. Fused silica capillaries of 75/363 µm I.D./O.D. with polyimide outer coating (cat. no. TSP075375) were purchased from Polymicro Technologies (Phoenix, AZ, USA). Capillary dimensions were 35 cm long, with 12 cm to fluorescence detection window. New capillaries were conditioned by successive washing under 950 mbar of 0.1 M NaOH (5 min), 0.01 M NaOH (5 min), water (5 min), and BGE (11 min). Analytical conditions are specified for each measurement. Samples were introduced hydrodynamically (20mbar for 3 s) from the inlet side of the capillaries. Separations were carried out by applying an

8.0 kV voltage, unless otherwise specified. The temperature of the capillary cartridge was set at 37 °C to emulate that of the human body.

3.2.4 Doxorubicin release under UV-light and pH stimuli

The effects of UV-light irradiation (15 min / 365 nm) or pH reduction (from pH 7.4 to 6.0) on the doxorubicin release were evaluated as well as the effects of combined stimuli. For UV-light stimuli, MicDoxHCl or MicDox aggregates samples (pH 7.4) were irradiated by 365 nm UV-light and then detected by CE using a PBS pH 7.4 I.S. 25mM solution as BGE. For pH stimuli, MicDoxHCl or MicDox aggregates samples (pH 7.4) were detected by CE using a PBS pH 6 I.S. 25mM solution as BGE. For both stimuli, MicDoxHCl or MicDox aggregates samples (pH 7.4) were irradiated by 365 nm UV-light and then detected by CE using a PBS pH 6 I.S. 25mM solution as BGE. Previously, an analytical strategy for specific and sensitive quantification of doxorubicin was developed herein using the CE-LIF technique. Calibrations curves (Figure 3.2) were prepared under similar analytical conditions, at pH 7.4 and 6.0 phosphate buffer solution. To obtain the amount in weight of doxorubicin released, the value of the concentration detected by CE-LIF was multiplied by the volume of the sample detected and then divided by the molecular weight of the compound.

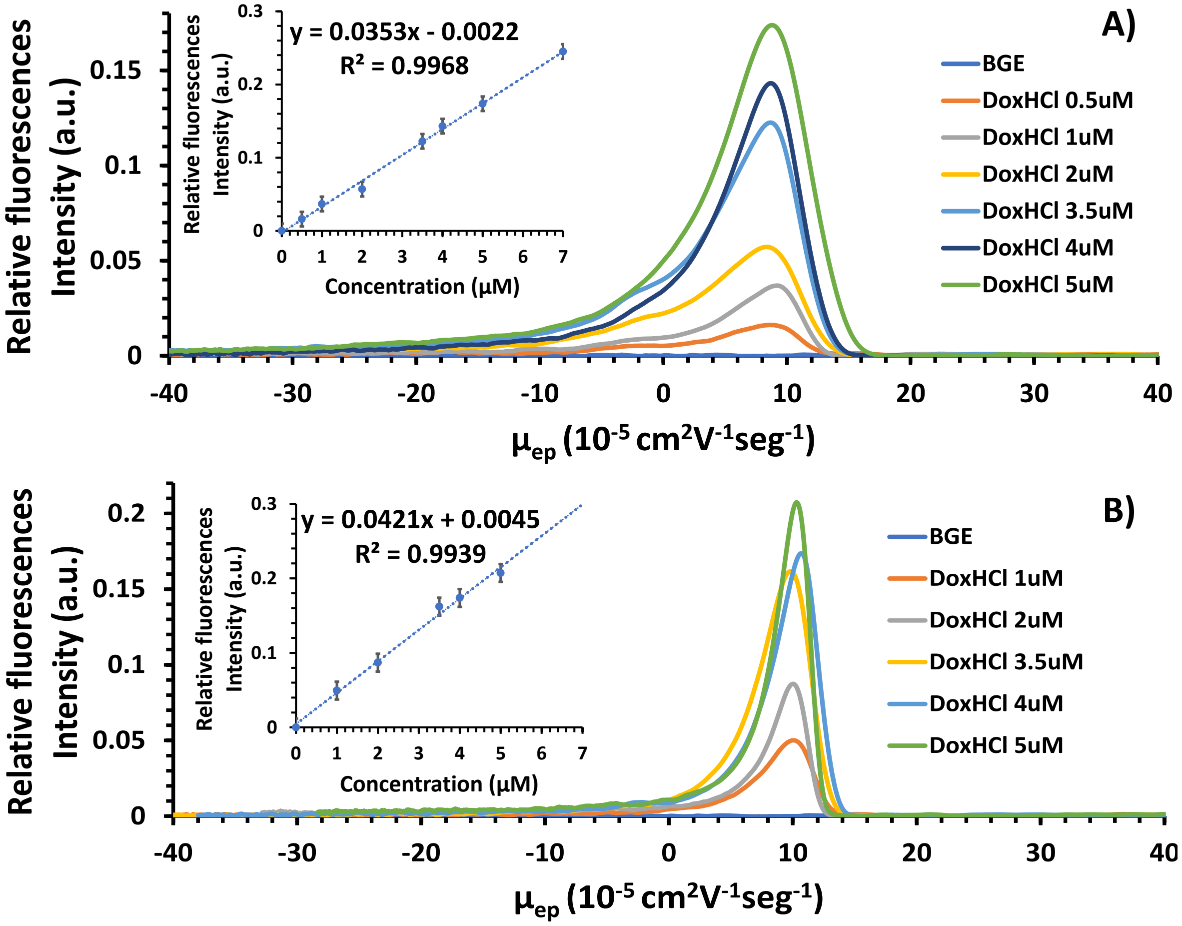

Figure 3.2 Electrophoretic profiles and calibration curve of A) DoxHCl in 25 mM PBS (pH 7.4), and B) DoxHCl in 25 mM PBS (pH 6.0).

3.3 RESULTS AND DISCUSSION

After Poly(NIPAM-co-SPMA) synthesis, formation of Mic was carried out with or without the two forms of the drug (DoxHCl – Dox) for TEM, DLS, and CE-LIF characterization. In MicDoxHCl/Dox, free drug (DoxHCL/Dox$_{equilibrium}$) could be detected by CE-LIF, with which it was possible to calculate drug encapsulated or not encapsulated (DoxHCL/Dox$_{loaded}$) by the nanosystem. DoxHCl/Dox was then detected by CE-LIF through UV and/or pH-change stimuli to MicDoxHCl/Dox for drug release quantification. Micelle-like aggregates formation, characterization and drug loading/release results are shown below.

3.3.1 Physicochemical characterization of micelle-like aggregates with and without doxorubicin loading

Figure 3.3 A) shows the hydrodynamic diameter distribution profiles determined by DLS of micelle-like aggregates formed in the absence (Mic) or the presence (MicDoxHCl) of DoxHCl at different loading concentrations (2, 3.5 and 5 µM) in PBS. It is shown a DoxHCl concentration-dependent increase in the aggregate size, ranging from 61 ± 2 nm (Peak width 28 nm) for Mic, to 122 ± 3 nm (Peak width 46 nm), 140 ± 9 nm (Peak width 45 nm) and 143 ± 1 nm (Peak width 58 nm) for MicDoxHCl at DoxHCl concentrations from 2.0, 3.5 and 5.0 µM, respectively. A clear increase of the micelle-like aggregates size was also demonstrated through TEM. Figures 3.3 B) and C) compare the TEM images of Mic and MicDoxHCl 5 µM respectively, showing spherical objects with modal solid diameters changing from 18 nm to 25 nm, respectively, logically lower than the hydrodynamic diameters. This variation in size observed with both DLS and TEM analysis corroborates the incorporation of the DoxHCl in the Mic. Additionally, it seems that at concentrations higher than 3.5 µM the size of the micelle-like aggregates tends to stabilize, meaning a possible saturation of the micelle with the drug (maximum loading capacity). This hypothesis will be evaluated in subsequent sections.

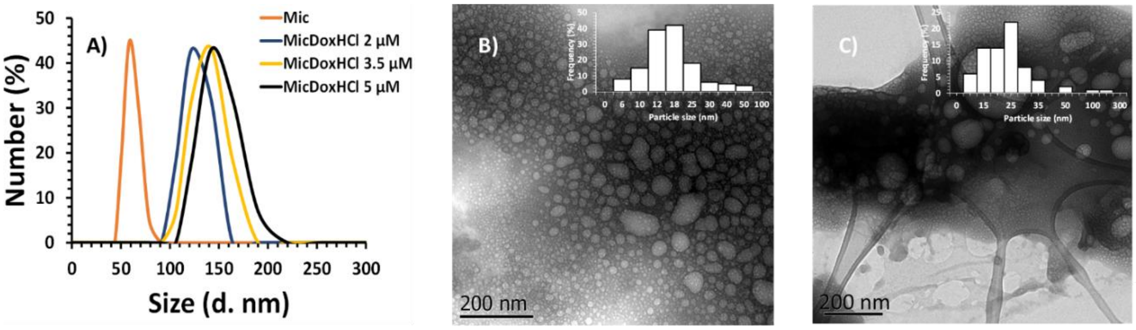

Figure 3.3 A) DoxHCl concentration effect on the hydrodynamic diameter of micelle-like aggregates (PBS pH 7.4; I.S. 25mM). TEM images of B) Mic and C) MicDoxHCl 5µM.

To go further, the electrokinetic separation of the samples was performed by CE-LIF, taking advantage of the inherent photoluminescent response of Doxorubicin and SP compounds. Indeed, compared to UV-visible detection, more selective and sensitive fluorescence signals could be detected, since the contribution of non-luminescent moieties of the samples were easily discarded. Figure 3.4 A) shows the electropherograms of Mic and DoxHCl 1 µM in 25 mM PBS pH 7.4, identifying a single peak for each sample. The electrophoretic mobility of Mic was calculated at -11 x 10^{-5} $cm^2V^{-1}s^{-1}$, which is coherent with previous reports[322], with a negative value due to the pKa (between 6 and 7) of SPMA molecule.[23] DoxHCl electrophoretic mobility, evaluated at +8 x 10^{-5} $cm^2V^{-1}s^{-1}$, is coherent with its first pKa at 8.2 [323], due to the amino group.

Figure 3.4 B) presents the electropherograms of the micelle-like aggregates formed in the presence of DoxHCl at 2 µM (MicDoxHCl 2.0 µM), 3.5 µM (MicDoxHCl 3.5 µM) and 5 µM (MicDoxHCl 5.0 µM) in PBS, along with the Mic electrophoretic profiles for a matter of comparison. For MicDoxHCl 2 µM (electropherogram c) only one peak is observed at -11 x 10^{-5} cm2$V^{-1}s^{-1}$, the same mobility as for Mic, but with an increase in the fluorescence signal intensity which could indicate the incorporation of the drug since the fluorescence signals are additive. From 3.5 µM and above, the increase in DoxHCl concentration, leads to a further the increase fluorescence signal for this peak at -11 x 10^{-5} cm2$V^{-1}s^{-1}$. Furthermore, the DoxHCl cationic peak signal at +8.0 x 10^{-5} $cm^2V^{-1}s^{-1}$appears, evidencing that the saturation of Mic is reached, along with the appearance of a third new peak at an electrophoretic mobility of -3.0 x 10^{-5} $cm^2V^{-1}s^{-1}$.

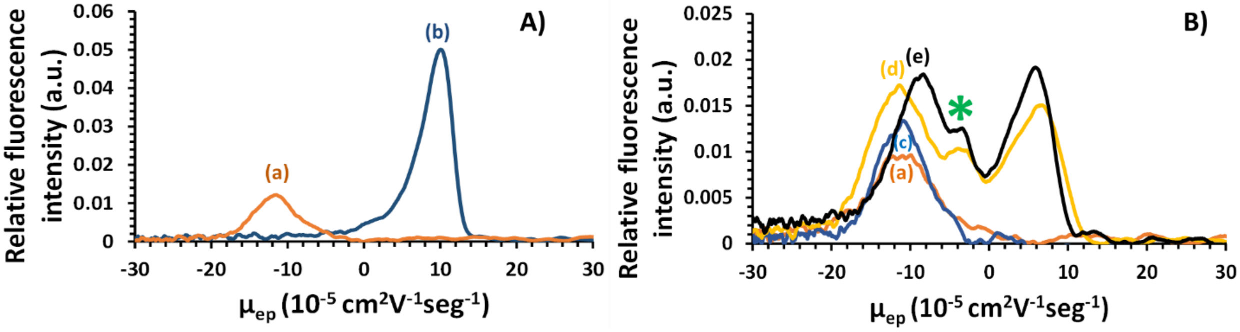

Figure 3.4 A) Electrophoretic profiles of a) Mic and b) DoxHCl 1 µM. B) MicDoxHCl formed in the presences of DoxHCl c) 2.0, d) 3.5 and e) 5.0 µM in PBS. BGE = PBS pH 7.4; I.S. 25mM.

This new peak could evidence the presence of a new structure (in equilibrium with MicDoxHCl and DoxHCl) in the loaded micelle-like aggregates separation. As the micelle is composed of a copolymer (CoPo), the hypothetic interaction of a non-aggregated CoPo with DoxHCl was therefore investigated. For this purpose, electrokinetic separations were performed on 5.0 µM DoxHCl solutions mixed with either CoPo or the micelle-like aggregates (Mic), named CoPo+DoxHCl and Mic+DoxHCl respectively, without further treatments (no dialysis). Figure 3.5 presents their separation just after synthesis (T_0) and one week later (T_{week}) and includes the electrophoretic profiles of Mic and MicDoxHCl 5 µM, for a matter of comparison. At T_0, CoPo+DoxHCl samples presented two predominant peaks at the electrophoretic mobilities of Mic and DoxHCl. After one week, these two peaks appear at a lower intensity, and an additional peak predominates in intensity at an electrophoretic mobility of -3.0 x 10^{-5} $cm^2V^{-1}s^{-1}$ (Figure 3.5 A). Figure 3.5 B) presents the evolution for Mic+DoxHCl, which presents the same tendency, but with a notable lower intensity for the third peak at -3.0 x 10^{-5} $cm^2V^{-1}s^{-1}$. The presence of free CoPo seems therefore to induce the appearance of this third peak, more pronounced when CoPo is directly mixed with DoxHCl, rather than when the micelles are pre-formed. The formation of a CoPo-DoxHCl complex is hence very likely. A dynamic equilibrium between the preformed micelle-like aggregate components and the doxorubicin allows the formation of the copolymer-doxorubicin complex only one week after the beginning of the interaction. This could be an important piece of information regarding the stability and employability of this drug delivery system. The DLS characterization of the CoPo-DoxHCl sample after one week (Figure 3.5 C) confirm the presence of structures of smaller size (20 ± 2 nm, peak width 11nm) compared to Mic (61 ± 2 nm, peak width 28 nm) which is coherent with a CoPo-DoxHCl complex. On the other hand, the Mic+DoxHCl (152 ± 2 nm, Peak with 60nm) sample presents a higher size than the MicDoxHCl (143 ± 1 nm, Peak width 58 nm), which should indicate different types of DoxHCl interaction with the micelle-like aggregate, whether it is introduced during the micelle formation (MicDoxHCl) or after the micelle formation (Mic+DoxHCl), i.e. internal or peripherical interaction of DoxHCl molecules with the aggregates.

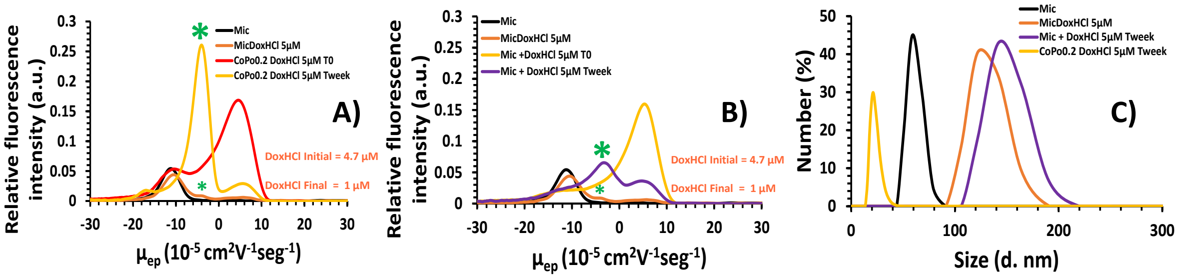

Figure 3.5 A) Electrophoretic profiles of CoPo+DoxHCl mixtures. B) Electrophoretic profiles of for Mic+DoxHCl mixtures. The samples were analyzed immediately after synthesis (T0) and one week later (T1week). C) DLS profiles of Mic, MicDoxHCl, CoPo+DoxHCl mixtures, Mic+DoxHCl mixtures, samples at T1week. (DoxHCL initial concentration 5 µM; BGE = PBS pH 7.4; I.S. 25mM).

The doxorubicin concentration effect on the structure of the micelle-like aggregates was also evaluated but using the poorly water-soluble Dox molecule (Figure 3.6). The same evolution was evidenced as for the hydrophilic DoxHCl (Figure 3.4 B). This indicates the formation of a similar CoPo-Dox complex disregarding the initial solubility of doxorubicin.

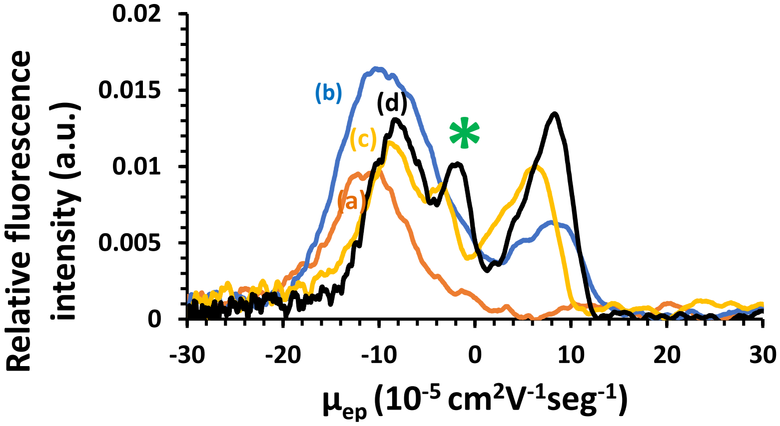

Figure 3.6 Electrophoretic profiles of a) Mic and MicDox formed with b) 2.0, c) 3.5 and d) 5.0 µM Dox. BGE = PBS pH 7.4; I.S. 25mM. Experimental conditions: see Figure 3.

3.3.2 Quantitation of doxorubicin loading by the micelle-like aggregates

To estimate the concentration of doxorubicin captured by the micelle-like aggregates, a calibration curve of doxorubicin was performed by CE-LIF. For DoxHCl in 25 mM PBS (pH 7,4), the limits of detection and quantification were calculated as 0.031 µM and 0.104 µM, respectively, with a linear range in the 0.5-5.0 µM range (Figure 3.2 A), compatible with the concentration of DoxHCl introduced for interaction with the micelle-like aggregates. These concentrations range was defined according to experimental results, and the loaded and released concentrations employed herein.

The estimation was performed thanks to the electropherograms of two solutions: the sample after dialysis, presenting an equilibrium between free and loaded doxorubicin (electropherograms in Figures 3B and S3 for captured DoxHCl or Dox respectively); and the dialysate containing free doxorubicin. Therefore, the total free doxorubicin concentration can be calculated form the peak height at +8 x 10^{-5} cm^{2}V^{-1}s^{-1} in both equilibrium sample and dialysate ($Dox_{equilibrium}$ and $Dox_{dialysate}$, respectively). The concentration of loaded doxorubicin was then calculated as $Dox_{loaded} = Dox_{initial} - Dox_{equilibrium} - Dox_{dialysate}$. Table 3.1 summarizes the estimated concentrations for both doxorubicin forms.

Table 3.1 Indirect quantitation of doxorubicin loading in the micelle-like aggregates.

	DoxHCl/Dox Initial		**DoxHCl/Dox Equilibrium**	**DoxHCl/Dox Dialysate**	**DoxHCl/Dox Loaded**
	μM	**μg**	**μg**	**μg**	**μg**
MicDoxHCl	**2**	11.6	0.9 ± 0.01	2.6 ± 0.06	8.1 ± 0.25
	3.5	20.2	0.9 ± 0.02	8.2 ± 0.30	**11.1 ± 0.30**
	5	28.9	1.2 ± 0.16	16.6 ± 0.25	**11.1 ± 0.21**
MicDox	**2**	11.6	1.2 ± 0.21	3.0 ± 0.02	7.4 ± 0.03
	3.5	20.3	0.6 ± 0.04	4.9 ± 0.16	14.8 ± 0.25
	5	28.9	0.8 ± 0.03	8.1 ± 0.25	**20.0 ± 0.30**

Average values ± standard deviations are presented. (n=3)

It was evidenced that both DoxHCl and Dox can interact with the micelle-like aggregates with larger amounts of the less soluble form of the drug being loaded in the micelles. For DoxHCl, a saturation of the micelle-like aggregates seems to occur at concentrations ≥ 3.5 µM, whereas Dox seems to be captured at a higher amount with no sign of saturation at least till 5 µM range.

Some hypotheses can arise concerning the capture process. Since DoxHCl is more soluble in polar media, its capture should be expected preferentially at the hydrophilic moiety of the PNIPAM with possible electrostatic interactions, which corresponds to the outer part of the micelle-like aggregates. These electrostatic interactions could be between the carbonyl of PNIPAM and the positively charged amino group of DoxHCl (pKa 8.2).[311] Similarly, interaction between the amino group of PNIPAM and the carbonyls groups of DoxHCl could be also expected. On the other hand, Dox, which dissolves in the less polar solvent THF, could interact preferentially through hydrophobic interactions such as dipole-dipole forces with spiropyran (SP) moieties located at the inner part of the micelle-like aggregates. This supports the higher loading capacity of the micelles towards Dox. A schematic representation of those possible interaction modes is depicted in Figure 3.7.

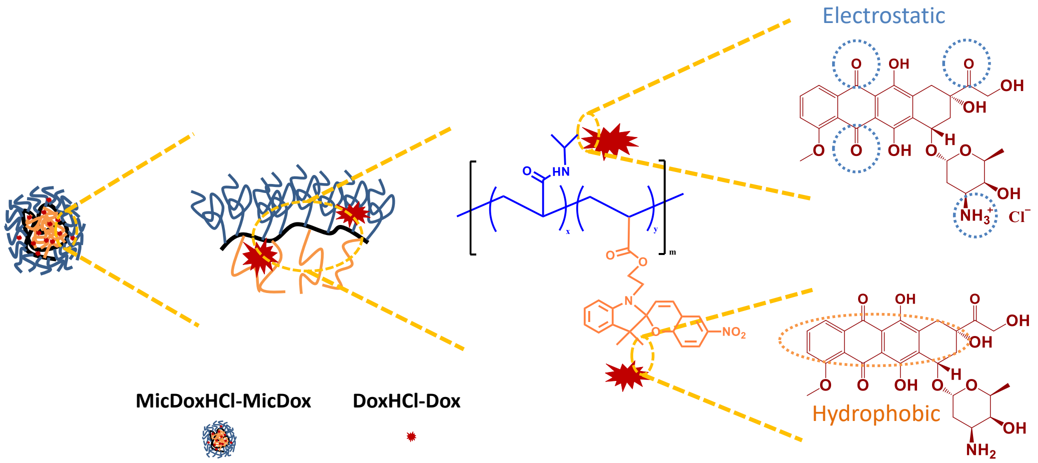

Figure 3.7 Schematic representation of DoxHCl and Dox interactions with the Poly(NIPAM-co-SPMA) random copolymer micelle-like aggregates.

3.3.3 pH and UV stimuli effects on micelle-like aggregates structure and doxorubicin release

The micelle-like aggregates were exposed to two stimuli: pH variation from 7.4 to 6.0, and UV-light irradiation (365 nm/15 min). DLS measurements (Figure 3.8 A for 25mM PBS pH 6) show an increase of Mic and MicDoxHCl size upon reduction of the pH value, with values for Mic of 295 ± 5 nm (Peak width 128nm), and for MicDoxHCl 5 µM of 340 ± 9 nm (Peak width 130nm). This increment in size at a more acidic pH may be due to the swelling of SP chains derived from their protonation (SP-H)[301] and the consequent solvent internalization. A further increase in the size of Mic and MicDoxHCl until 342 ± 5 nm (Peak width 130nm) and 360 ± 11 nm (Peak width 152nm), was respectively observed after irradiation with UV-light in PBS at pH 6.0. However, these measurements presented PDI values over 0.783, which means a high polydispersity or the formation of non-spherical structures which could be a proof of the disaggregation of the micelle facilitating drug liberation. These results also shows that the predominant stimulus for the release is the pH since it induces a more remarkable change in the micelle structure even if both could be necessary to complete release of the drug.

In addition, TEM images were obtained on the samples dissolved at pH 6.0 (Figures 3.8 B and 3.8 C). A remarkable increase in the size of spherical objects with larger diameter (Figure 3.8 B – 40 to 350nm) combined with apparently disaggregated structures was observed for micelle-like aggregates at pH 6.0 compared to pH 7.4 (Figure 3.3 B – 18nm). This confirms the results obtained through DLS measurements. When combining UV-light and pH 6.0 stimuli, the TEM image (Figure 3.8 C) clearly shows the micelle disaggregation with a polydisperse size distribution (200 – 400 nm). As reported before[322], this result confirms that the two effects, swelling and disaggregation, can be controlled by the pH change and UV irradiation.

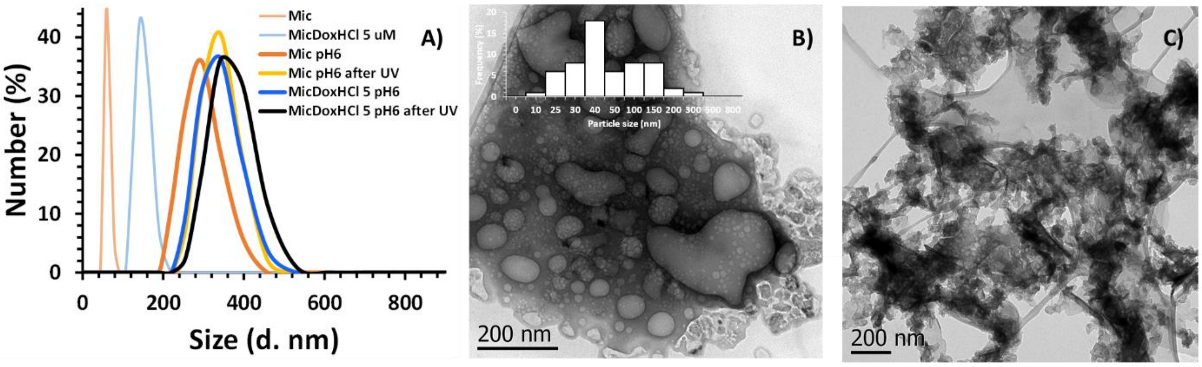

Figure 3.8. A) DLS profiles of Mic and MicDoxHCl 5 µM under pH 6 and UV light exposition (365 nm). TEM images of B) MicDoxHCl 5 µM in pH 6, and C) MicDoxHCl 5µM in pH 6 after UV light (365 nm) irradiation. Insets show the corresponding size distribution histograms.

So as to estimate the release rate, a calibration curve for doxorubicin was established with its separation by CE-LIF. In 25 mM PBS (pH 6), the limits of detection and quantification were calculated as 0.029 µM and 0.096 µM, respectively, with a linearity range between 0.5 to 5.0 µM (Figure 3.2 B).

Figure 3.9 shows a full electrokinetic panorama of Mic and MicDoxHCl exposed to the above-described stimuli. Figure 3.9 A) shows the electropherograms of Mic and MicDoxHCl (loaded with DoxHCl at concentrations ranging from 2 to 5 µM) upon excitation with UV-light. These electrophoretic profiles are similar to those observed for Mic without irradiation (Figure 3.4 B) confirming that this stimulus alone in not enough for the drug release. It is known that upon UV-light exposure, the SP molecules change from a nonpolar conformation to a planar and zwitterionic structure namely merocyanine with hydrophilic properties.[324] However, since this reaction is reversible, the molecule returns to its normal SP structure once the UV-light source is removed. As the analysis time in CE is around 2 minutes, this phenomenon cannot be visible.

To study the exposure of the micelle-like aggregates to a lower pH medium, they were formed at pH 7.4 and injected into a capillary filled with 25mM PBS pH 6.0 as the background electrolyte (Figure 3.9 B). Significant variations in the electrophoretic profiles were observed when compared with Figure 6A. First, the electrophoretic mobility of the DoxHCl signals shifted from 8.0 x 10^{-5} $cm^2V^{-1}s^{-1}$at pH 7.4 to 12 x 10^{-5} $cm^2V^{-1}s^{-1}$ at pH 6.0. Then, the intensities of DoxHCl signals were almost doubled at pH 6.0, which is expected due to the drug release under these conditions. It is noteworthy that the residence time of the analyzed samples inside the capillary before their detection is 2 minutes. This means that the changes in the micelle-like aggregates conformation occurs almost instantaneously upon exposure to a pH 6.0 environment (pKa of SP is in the 6.0 – 7.0 range[23]), which is very interesting for applications in drug delivery systems (release time < 2min). Furthermore, a novel peak seems to appear at -5.0 x 10^{-5} $cm^2V^{-1}s^{-1}$ that could derive from the SP protonation SP-H which induces inhomogeneous shapes-size and thus, the electrokinetic dispersion of the micelle profile.

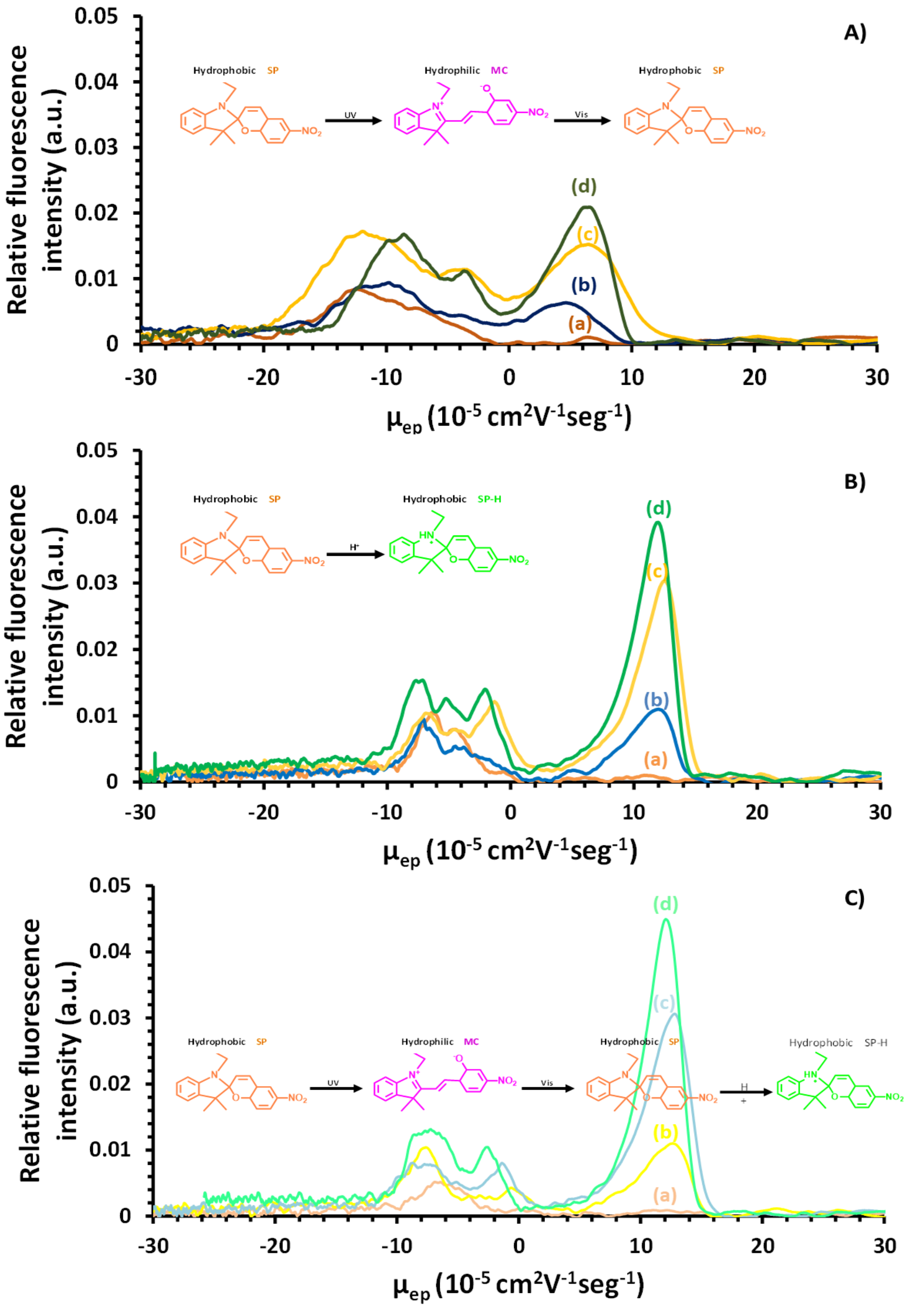

Figure 3.9 Capillary electrophoresis profiles of Mic and MicDoxHCl treated with different stimuli. A) UV-light (15 min / 365 nm) at pH 7.4, B) darkness at pH 6.0, and C) UV-light at pH 6.0. DoxHCl concentrations: a=0, b=2.0, c= 3.5 and d= 5.0 µM. All measurements were performed in PBS at a 25 mM ionic strength.

Figure 3.9 C) shows the electropherograms of MicDoxHCl formed at pH 7.4, exposed to UV-light irradiation and then detected in a capillary filled with PBS at pH 6.0. These electrophoretic profiles are similar to those presented in Figure 6B, except the absence of the fourth peak at -5.0 x 10^{-5} cm^{2}V^{-1}s^{-1}. However, a slight increase on the intensity of the signal of DoxHCl was observed when micelle-like aggregates interacted with 5.0 µM DoxHCl, showing a possible synergistic contribution of combined stimuli for the drug release, at this DoxHCl loading concentration. Similar profiles were observed upon analysis of micelle-like aggregates treated with varied Dox concentrations (Figure 3.10). However, less intense peaks associated to the doxorubicin were observed. This is an indication of a less efficient Dox release compared to DoxHCl from the corresponding micelle-like aggregates due to the lower water solubility. According to these observations the pH stimulus should mostly control the release.

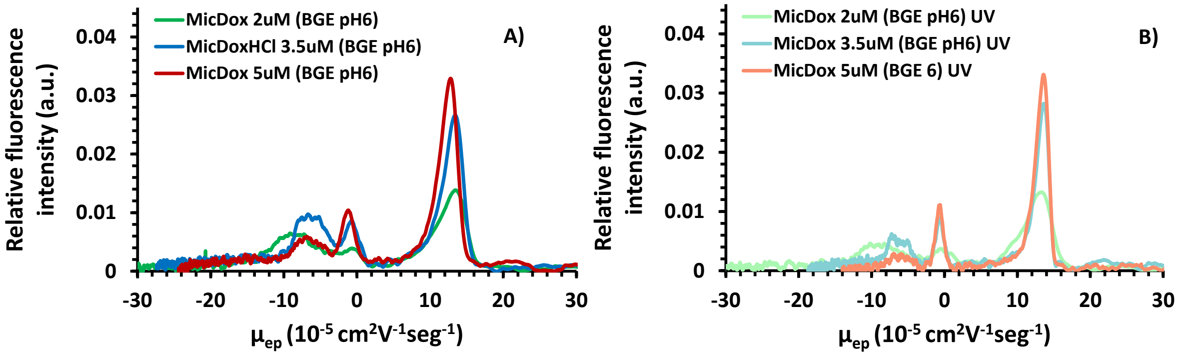

Figure 3.10 Electrophoretic profiles of a) Mic and MicDox formed with b) 2.0, c) 3.5 and d) 5.0 µM Dox. BGE = PBS pH 7.4; I.S. 25mM. Experimental conditions: see Figure 6.

To study the time effect on the release of doxorubicin from micelle like aggregates formed at pH 7.4 under pH stimuli, they were electrokinetically separated in the PBS pH 6.0 BGE under different voltages, namely 2, 4 or 8 kV (Figure 3.11), the latter one being the one applied for all previous studies. Other analytical conditions remained identical. A reduction of the applied separation voltage is inherently associated with a slower movement of the analyzed species inside the capillary, and thus, with increasing residence times before reaching the detection window. Under the applied analytical conditions, the migration times of DoxHCl resulted in 2, 6 and 12 min for 8, 4 and 2 kV, respectively. When transposing the electropherograms from migration time to electrophoretic mobility (in x-axis), the profiles presented similar ranges of mobilities whatever the voltage indicating good repeatability of the experimental conditions.

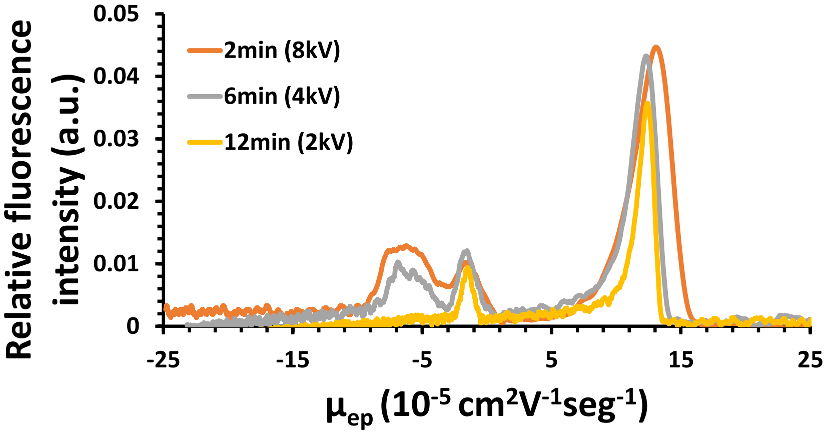

Figure 3.11 Impact of the separation voltage on the electrokinetic profiles of MicDoxHCl 5 µM in 25 mM PBS (pH 6.0). Experimental conditions: see Figure 3.6.

The peak areas (corrected by the time) for doxorubicin were identical when applying 4 and 8 kV, whereas a slight decrease was observed for separations under 2 kV. This could be due to intracapillary dispersion phenomenon due to diffusion. Therefore, it is confirmed that 2 minutes of micelle-like aggregates exposure at pH 6.0 are enough for the release of doxorubicin. However, the corresponding to the micelle-like aggregates slightly diminished at 4kV separation and was no more observed at 2 kV separation, which could indicate that swelling/disaggregation needs more time to be complete. This is important rewarding the translation of the micelle-like aggregates reported herein towards clinical applications. A fast release of the drug in acidic environments such as that of the cancer tumors could in turn allow a faster reaching of the therapeutic doses.

Thereby, the structure of micelle-like aggregates loaded with doxorubicin is affected at a different degree by UV-light or pH stimulus, but also by the concentration of loaded doxorubicin and its chemical form. To go deeper in this study, a quantitation of the doxorubicin loading and release (under either pH or combined pH and UV stimuli) was then undergone under CE-LIF separations.

Figure 3.12 summarizes the loaded and released amounts of DoxHCl and Dox as the effect of pH 6.0 and/or UV-light irradiation stimuli. Even if higher loading capacity of Dox was verified compared to DoxHCl (Table 1), it is noticeable that the amount of doxorubicin released from MicDoxHCl is higher than that from MicDox. This could be interpreted in terms of chemical form and solubility of the two doxorubicin forms, and their types of interaction with the micelle-like agregates. First, as Dox is poorly water soluble, this form is better loaded into the micelle (Table 1) and should logically be more difficult to be released. In addition, as described before, Dox was mainly located at the inner hydrophobic part of the micelles, whereas DoxHCl is supposed to mainly be located at the hydrophilic outer part. Moreover, the electrostatic interactions of DoxHCl with the PNIPAM moieties are expected to be less strong than the hydrophobic interactions of Dox with the SP molecules inside the micelle-like aggregates. This preferential outer location could boost the doxorubicin release, which reached up to 68 % of the captured DoxHCl (5 µM) in contrast to only 29 % of the captured Dox (5 µM). Furthermore, when both pH 6.0 and UV-light stimuli were combined, DoxHCl release from MicDoxHCl (5 µM) reached up to 74%, whereas the release from MicDox (5 µM) was not improved.

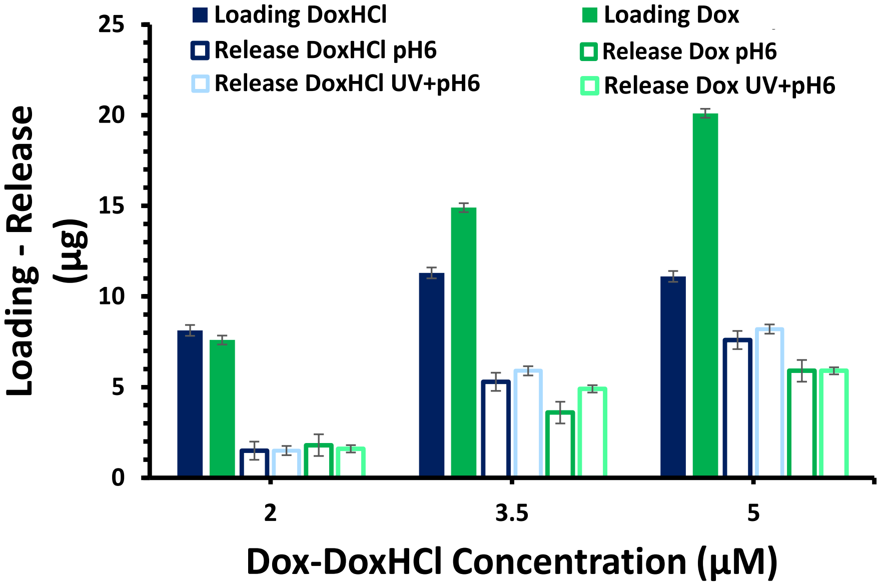

Figure 3.12 DoxHCl and Dox loading and release from micelle-likes aggregates exposed to pH and/or UV-light stimuli.

3.4 Preliminary conclusions

UV-light and pH responsive Poly(NIPAM-co-SPMA) micelle-like aggregates were formed and loaded with poorly (Dox) and highly water-soluble (Dox-HCl) forms of doxorubicin. A capillary zone electrophoresis methodology coupled to fluorescence detection revealed the presence of two species in equilibrium: the micelle-like aggregates with or without loaded doxorubicin and a complex formed between the non-aggregated copolymer and the doxorubicin molecules. This additional complex was observed with both Dox-HCl and Dox species, at doxorubicin concentrations higher than 3 µM. This complex was present in the suspensions even after exhaustive dialysis steps. The electrokinetic separation allowed to specifically quantify the loaded and released concentrations of doxorubicin at pH 7.4 and upon UV-irradiation and pH 6.0 stimuli. A most effective loading was observed when Dox was used compared to Dox-HCl (10 µg/mg vs 5.5 µg/mg, respectively). Drug release rates of 68 and 74 % were observed for Dox-HCl upon pH 6.0 and combined UV+ pH6.0 stimuli, while only 29% of the loaded Dox was released under these two stimuli. Those results are coherent with the strength of interactions and preferential locations of the highly and poorly water-soluble forms of doxorubicin with the micelle-like aggregates. Indeed, electrostatic interactions predominate between Dox-HCl and the poly-NIPAM section at the micellar shell, while hydrophobic interactions between Dox and the spiropyran moiety were expected at the inner section of the micelles. Since these kinds of interactions are directly implicated in the loading and release efficiency of drugs by nanocarriers, more studies are necessary to disclose their chemical interactions and thus to modulate their impact and potential affectation of pharmaceutical reactions with physiological targets. These results highlight the high performance of electrokinetic methodologies for such equilibrium studies between micelle-like aggregates and drugs. Finally, a fast drug release kinetics was demonstrated, with a maximal doxorubicin release achieved 2 minutes after micelle-like aggregates exposition to the combined stimuli which demonstrates this system very promising for developing drug delivery strategies.

CHAPTER IV

Near-Infrared Light-, and pH- responsive spiropyran micelle-like aggregate nanocarrier combined with magnetic-luminescent Janus nanoparticles for drug delivery

This work will be valorised by a scientific publication in a peer reviewed journal (manuscript in preparation)

4.1 Introduction

The polymeric micelle-like nanoaggregates constructed in this project have been proved to be UV light-sensitive (Chapters II & III). However, it is well-known the limitation of UV-light for direct *in vivo* applications (see Chapter I, section 1.1.3). To overcome these constraints and rends possible the use of the developed smart drug delivery system in the biomedical field, in this chapter we aim to describe an original alternative that implies the incorporation of up-converting NPs and/or Hybrid upconverting-magnetic NPs into the micelle-like aggregates. Those upconverting materials convert the NIR-light in the 980 nm wavelength into photoluminescent emissions in the UV-region, which are expected to be transferred to the photo-responsive moieties in the micelle-like aggregates, thus activating the drug delivery mechanism.

As described in Chapter I, section 1.3., Up-converting NPs (UCNPs) are lanthanides-dopped luminescent nanomaterials with the property of emitting higher energy light (UV-Vis) by absorbing lower energy light (near infrared – NIR) and they have been recently used as theranostic NPs for drug delivery systems and imaging probes [REF]. On the other hand, magnetic NPs (MNPs) are used for photo-thermal and photo-dynamic therapies as well as for in vivo magnetic guidance [REF]. In the past few years, multifunctional magnetic-luminescent hybrid nanoparticles (HNPs) have gathered large interest due to the combined functionalities of magnetic and luminescent properties giving them hight potential application in various fields.[325] With high chemical stability, penetration depth, detection sensitivity, and low cytotoxicity, several kinds of magnetic-luminescent HNPs have been explored as multimodal-imaging and therapy nanotheranostic tools in cell labelling, in vivo cancer targeting, and nanocarriers for photosensitizer-based photodynamic therapy.[325]

Three strategies based on the connection between individual functional components are commonly used to construct magnetic-luminescent HNPs: no-linkers, soft linkers, and hard linkers. The "No-linker strategy" refers to the process in which the two functional components directly grow without any connection mediators and by their difference in morphological structures. They can either include an isotropic structure (core/shell), the anisotropic structure (Janus-type), or a layered structure. The "soft-linker method" means that the functionals components have the capability to connect by binding sites or functional ligands and bring the individual components together to form a heterostructure connecting via specific recognition reaction, covalent bonding, electrostatic forces, or hydrophobic interactions. The "Hard-linker method" uses compounds like silica (SiO_2), Au, Fe oxide complexes, and TiO_2 as shells-linkers for inorganic NPs core structure (Au, Fe_2O_3, UCNPs, etc.). According to the connection process, three structure types arise, including embedding in hard linkers (core-shell-shell), hard shell linkers, and co-coating in hard linkers (Yolk-shell) structures types.[32] However, magnetic-luminescent HNPs core–shell structured[33–36] still face several challenges that limit their applications because the luminescent and magnetic properties can be highly reduced due to their combination. For example, magnetic shell could absorb and block the exciting light and up-conversion luminescence, so that the quantum yields of the UCNP core may considerably be reduced.[37] Inversely, up-conversion luminescence shell could interfere with the interaction between the magnetic core and an incident magnetic field. Even, soft linkers can reduce the restrictions on the selection of individual components as it does not require the lattice match or chemical similarity between them.

Consequently, the major challenge in this field is not only to develop reproducible and easy methods to obtain magnetic-luminescent nanostructures, but also to fabricate HNPs in an easy way with good either magnetic efficiency or/and high luminescence properties. Thus, owing to the combination of magnetic and luminescence property, Janus-like NPs (JNPs), having an asymmetric structure, will probably be a better structure applicable as theranostic tool. Janus nanoparticles are so named in reference to Janus, the Roman god of doorways, typically depicted as having two faces. Like the ancient deity, JNPs also have two faces, and these HNPs con me form from organic polymeric materials or/and inorganic materials (GNPs, MNPs, UCNPs, etc.), consisting each of them of different chemistry, size, morphology, material, etc.[38] A number of different synthetic strategies have been developed to synthesize them and can be categorised into three broad categories: masking, self-assembly, and phase separation strategies.[326] The "Masking method" is the simplest JNP synthetic strategy and involves blocking one side of the NP with a "blocking substrate", to chemically modify the free side, and then remove this blocking substrate. Several different "blocking" surfaces have been demonstrated, and they can be either solid (e.g., polymer crystal) or liquid (e.g., pickering emulsion).[327–329] For this method, the blocking substrate must be chemically inert but bounded to the NPs during the functionalisation process of the NP free face and also, the substrate must be easily removed after the process. The "self-assembly method" is normally used in the formation of Janus-like polymeric NPs with well-defined architecture, composition, and narrow molecular weight distribution block copolymers.[330,331] In the third general method, named "phase separation", and commonly used for inorganic HNPs, two or more incompatible components are mixed together to form HNPs via different preparation mechanisms such as: heterogeneous nucleation, non-epitaxial deposition followed by coalescence/crystallization, reactions at liquid—liquid interfaces, and homogeneous—heterogeneous nucleation.[39] In the "homogeneous—heterogeneous nucleation" process, the epitaxial growth of one NP fraction at the surface of another NP is produced. Such process can be controlled by tuning the conditions of nucleation and growth of the second NP.[40] Usually, the first NP works as a seed, but the lattice incompatibility makes it difficult for the second NP to form a stable core—shell structure, then being favoured the formation of a heterodimer, consisting of two different components joined together in a Janus-type NP structure.

On the other hand, in smart drug delivery applications, as previously shown in sections 1.2.2 and chapter II, due to their colloidal stability and modulable loading and release activity of different drugs, polymer-based amphiphilic nanocarriers are interesting[332]. Furthermore, the encapsulation of different types of inorganic nanoparticles such as golden NPs (GNPs), magnetic NPs (MNPs) or up-converting NPs (UCNPs), by polymeric micelles has been performed on several occasions.[333] The objective of these types of HNPs is to achieve the simultaneous diagnosis and therapy of the disease in a theranostic approach.[334] For example, *Maria-Teodora Popescu et al.*[335] describe the preparation and characterization of organic/inorganic hybrid polymer multifunctional core-shell nanocarrier (gold@pentablock nanoparticles) based on GNPs and poly(Ɛ-caprolactone)-b-poly(ethylene oxide)-b-poly(2-vinylpyridine)-b-poly(ethylene oxide)-b-poly("-caprolactone) pentablock terpolymers. These gold@pentablock nanoparticles could moderately encapsulate Tamoxifen as water-soluble drug, in their hydrophobic micellar cores showing prolonged release profiles, relative to the corresponding empty amphiphilic polymeric pentablock micelles. In another example, *Jaydev R. Upponi et al.*[336] prepared a platform-based nanosized combination agent suitable for the enhanced diagnosis and treatment of cancer using polymeric polyethylene glycolphosphatidylethanolamine-based (PEG-PE) micelles loaded with both, poorly soluble chemotherapeutic agent paclitaxel and hydrophobic superparamagnetic iron oxide nanoparticles (SPIONs) as Magnetic Resonance Imaging (MRI) contrast agent. In vivo, the resulting paclitaxel-SPION-co-loaded PEG-PE micelles retained their Magnetic Resonance contrast properties and cell death was observed in mouse models of breast tumours and melanoma in vivo.

Among polymer-based amphiphilic micelle-like aggregates, photo-sensible polymers are attractive candidates for smart drug-delivery due to their effective exogenous response, also incorporating poorly water-soluble active drugs in their core, which are released in a controlled way upon reaction of stimuli-responsive moieties. But most of these polymers are photosensitive to UV light, which is very harmful because of its side effects in generating skin burns. Hence, a strategy consists in coupling UCNPs to light-responsive micelle-like aggregates. Indeed, due to the up-conversion phenomenon generated by these UCNPs, their ability to absorb NIR light (which is not harmful to the body because it enters the skin's transparency window) and consequently UV light emission, which is absorbed by the photosensitive polymers, allows them to be used efficiently in theranostic applications. *Tzong-Liu Wang and co-workers*[337] for example synthesized an amphiphilic block copolymer (BCP) which contains both photoresponsive and thermoresponsive blocks, that allowed to encapsulat $\mathrm{LiY\text{-}F_4{:}Yb^{3+}_{0.25},Tm^{3+}_{0.01}@LiYF_4{:}Yb^{3+}_{0.2}}$ UCNPs and Nile red (NR) as a model drug. After exposing the UCNP-loaded micellar solution to near-infrared (NIR) light, it was found that the UV light emitted from UCNPs could disrupt the polymer micelles leading NR release.

Spiropyran (SP), as have been shown along this PhD manuscript, is one of these interesting responsive material (to multiple stimuli including light, temperature and pH) for the formation of micelle-like nanoaggregates,.[338] *Guojie Wang and co-workers*[223] reported a NIR light and pH responsive nanocomposite comprising spiropyran-functionalized amphiphilic polymers and UCNPs by their encapsulation through the self-assembly of the amphiphilic polymers. Upon near-infrared light irradiation, the upconversion fluorescence induced hydrophobic spiropyran isomerization to the hydrophilic merocyanine and disrupted the spherical morphology of the nanocomposites. Meanwhile, at low pH, the hydrophobic spiropyran could be also protonated, leading to the swelling of the self-assemblies. With this, hydrophobic Coumarin 102 and Doxorubicin were released from the nanocomposites triggered by the near-infrared light and acidic pH.

As shown above, HNPs combining inorganic nanoparticles with polymeric micelles have served as excellent theranostic tools through their synergistic properties for imaging, drug delivery, and phototherapies. There is however still a need to convert these nanocomposites into smart nanocarriers, so that they can be directed to the specific target.[5] For this purpose, adding magnetic fractions (MNPs) to the decoration of the nanocomposites, for external guidance has to be consider.[41] Hence, here smart nanocomposites consisting of JNPs (UCNPs with MNP fractions one part of their surface) with luminescent and magnetic properties were synthesized and characterized. They were then encapsulated into spiropyran micelle-like aggregates that react to pH and light stimuli, for their use in drug delivery and imaging via site-directed magnetic transport for cancer theranostic.

4.2 Materials and Methods

4.2.1 Materials and reagents

Spiropyran (SP) was purchased from TCI (Paris, France); yttrium oxide (Y_2O_3), ytterbium oxide (Yb_2O_3), thulium tetrachloride ($TmCl_3$), oleic acid, 1-octadecene, ammonium fluoride (NH_4F), iron acetylacetonate ($Fe(AcAc)_3$), oleylamine, methacryloyl chloride, triethylamine (Et3N), methylene chloride, 1,2 Dodecanediol, tetrahydrofuran (THF), mono basic sodium phosphate, dibasic sodium phosphate, N-isopropylacrylamide (NIPAM), azobisisobutyronitrile (AIBN) and Doxorubicin Hydrochloride (Dox-HCl) were purchased from Sigma-Aldrich (Paris, France); Sodium bicarbonate (NaHCO3), sodium hydroxide (NaOH), and magnesium sulfate (MgSO4) were supplied by Karal (Guanajuato, Mexico). Solvents such as tert-butanol, diethyl ether, acetone, methyl alcohol, and ethyl alcohol were purchased from J.T. Baker (Mexico City, Mexico). Dialysis bags were obtained from Spectrum Labs (Breda, The N_4etherlands).

4.2.2 Synthesis of Magnetic-luminescent Janus nanoparticles

The optimised $NaYF_4$:Yb,Tm UCNPs were synthesized following Gonzalo Ramírez-García's method.[339] Briefly, by vigorously stirring, a mixture of 2.0 mmol Y_2O_3, 0.5 mmol Yb_2O_3 and 18.1 μmol $TmCl_3$ with 40 mL of HCl (38%). After the solution became clear, the solution was evaporated to dryness, having as its product the mixture of chloride salts of each lanthanide. When it has cooled down, 5 mL deionized water was added into the chloride salt until dissolution. Then the solution was mixed with 30 mL oleic acid and 75 mL 1-octadecene, and stirred for 30 min. The mixture was then heated to 150 °C and maintained at this temperature for 30 min to form a clear yellow solution. After the solution cooled down to room temperature, a mixture composed of 20.3 mmol NH_4F and 12.8 mmol NaOH dissolved in 50 mL of methanol was added into the flask. After stirring for 30 min, the solution was heated to 110 °C and maintained at this temperature for 30 min to complete methanol evaporation. Then the solution was finally heated to 280 °C and maintained at this temperature for 30 min under N_2 flow. After the solution reached room temperature, the $NaYF_4$:Yb,Tm nanocrystals were precipitated from the solution with acetone and washed with ethanol/water (1 : 1 v/v) three times. The resulting nanocrystals (UCNPs) were easily dispersed in hexane.

To obtain iron oxide nanoparticles Fe_3O_4 (MNP), 3 mmol $Fe(AcAc)_3$, 15 mmol 1,2–Dodecanediol, 9 mmol of oleic acid, 9 mmol oleylamine and 30 of 1–Octadecene were introduced in a three–neck flask mounted in a reflux system under a nitrogen atmosphere. Subsequently, the mixture was heated to 100 °C and held for two hours. The temperature was further raised to 200 °C and kept for 2 hours, and finally to 315 °C and kept for 60 min. In all the cases, the heating rate was deliberately fixed at 5 ºC/min until it reaches 315 °C. The mixture was then left to cool down at room temperature. The synthesized MNPs were allowed to precipitate by adding an equal amount of ethanol and acetone (50:50% v:v) for their washing. The mixture was further decanted magnetically. This washing process was repeated for at least 7 times.

For the synthesis and optimization of Janus-type nanoparticles (JNPs), a fixed amount of previously synthesized UCNP was mixed with the MNP precursor $Fe(AcAc)_3$ in different amounts, performing an epitaxial growth of the magnetic fraction by thermal decomposition on the surface of the UCNP (luminescent fraction) as shown in Figure 4.1 A). The goal was to obtain hybrid materials with intense magnetic and upconverting properties simultaneously. Hence, three mass ratios between UCNP and iron precursor (UCNP: $Fe(AcAc)_3$) were used being 1:0.25, 1:0.5 and 1:1. These ratios were mixed with 15 mmol 1,2–Dodecanediol, 9 mmol oleic acid, 9 mmol oleylamine and 30 mL of 1–Octadecene in a three–neck flask with the reflux system under nitrogen atmosphere. Afterwards, temperature scale performance was carried out as magnetite synthesis process above, in accordance with the corresponding times. Precipitation was carried out after mixture cool down proceeding to washing.

4.2.3 DoxHCl & JNPs entrapment in Poly(NIPAM-co-SPMA) random copolymer micelle-like aggregates

The micelle-like aggregates were synthesized as previously reported[322] (Chapter II). Briefly, poly(NIPAM-co-SPMA) was dissolved in 1 mL THF. 1 mL of 25 mM phosphate buffer solution (PBS – pH 7.4) was then added under vigorous stirring (1100 rpm) at 1 $\mu L.s^{-1}$ rate followed by a quick addition of 9 mL of PBS, leaving the mixture 7 hours under stirring for micelle-like formation. Purification was performed by dialysis (10 kDa cut-off) with the same PBS buffer at room temperature for 24 h.

The hybrid nanoparticles and their loading with Doxorubicin (DoxHCl) were performed as follows: Poly(NIPAM-co-SPMA) (2 mg) was dissolved with a quick stirring rate (1100 r.p.m.) with 5 mg of JNPs previously well dispersed by ultrasonication in THF. Then, either 1 mL of 25 mM PBS (pH 7.4) (for the MicJNP), or 1 mL of 50 µM DoxHCl in 25 mM PBS (pH 7.4) (for the MicJNPDox) was added at a rate of 1 µL.s^{-1} followed by a quick addition of 9 mL of PBS. After the 7 hours of stirring step, the reagents and solvents that were not encapsulated into the micelle-like aggregates (THF and DoxHCl) were removed by dialysis (10 kDa cut-off) with PBS at room temperature for 24 h. Nanocomposite samples (MicJNP and MicJNPDox) were stored in amber vials at 8°C, and have a JNPs concentration of 0.5 mg/ml. A schematic representation of this loading process shown in Figure 4.1 B).

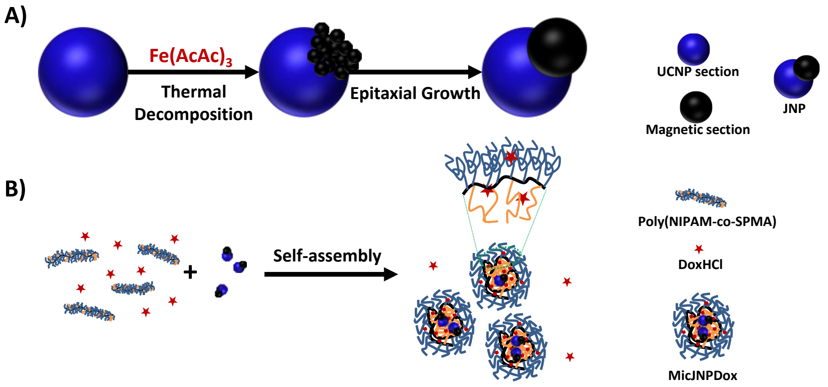

Figure 4.1. Schematic representation of A) magneto-luminescent JNPs synthesis by epitaxial growth of magnetite at the UCNPs surface; and B) JNP (MicJNP) and DoxHCl (MicJNPDox) encapsulation in micelle-like aggregates formation by the self-assembly of poly(NIPAM-co-SPMA) copolymer.

4.2.4 JNPs, micelle-like aggregates and hybrid nano systems structural and colloidal characterization

X-ray diffraction (XRD) analysis of UCNPs, MNPs, and JNPs were carried out using D2 PHASER X-Ray Diffraction System (Bruker). Photoluminescence characterization was performed upon excitation with 975 nm using a Roithner RLTMDL-975-3 W laser diode coupled to a PSU-LED power supply. The upconversion luminescence emission spectra were obtained with a Silver-Nova Spectrometer from StellarNet inc. The absorption spectra were recorded in the 300 to 800 nm region using the Agilent

Cary series UV-Vis-NIR spectrophotometer (Cary 5000) and a 1 cm thick quartz cuvette. By dynamic light scattering (DLS) the hydrodynamic diameter in 25 mM PBS (pH 7.4 and 6) of self-assembled micelle-like aggregates was measured at room temperature (25 °C) using a Malvern Zetasizer Nano Men3600 (ville, pays) in the same medium as for formation unless otherwise stated. TEM images, for the morphology of the micelle-like aggregates, were obtained using a JEOL JEM-1010 microscope equipped with an ORIUS digital camera, by GATAN. By immersing lacey carbon coated copper grids into the micelle-like aggregate suspensions and allowed to dry at room temperature, the samples were prepared. Lacey-carbon coated 300 mesh copper grids and were purchased from Ted Pella, Inc. (CA, USA).

Capillary electrophoresis experiments were performed on an Agilent 7100 capillary electrophoresis instrument coupled to a Zetalif LED induced fluorescence detector. Fused silica capillaries of 75/363 µm I.D./O.D. with polyimide outer coating (cat. no. TSP075375) were purchased from Polymicro Technologies (Phoenix, AZ, USA). Capillary dimensions were 35 cm long, with 12 cm to the fluorescence detection window. New capillaries were conditioned by performing successive washing under 950 mbar of 0.1 M NaOH (5 min), 0.01 M NaOH (5 min), water (5 min), and BGE (11 min). Unless otherwise specified, 25 mM PBS at pH 7.4 was used as BGE and for the pH response of the micelle-like aggregates 25 mM PBS pH 6 was used. Samples were introduced hydrodynamically (20mbar for 3 s) on the inlet side of the capillaries. Separations were carried out by applying a +8 kV voltage, otherwise specified. The temperature of the capillary cartridge was set at 37 °C to emulate that of the body

4.3 RESULTS AND DISCUSSION

4.3.1 Synthesis and characterization of magnetic-luminescent Janus nanoparticles

Structural and optical characterization of MNPs, UCNPs and the different JNPs samples (1:0.25, 1:0.5 and 1:1, (m/m) UCNP:Fe(AcAc)$_3$ is shown in Figure 4.2. All JNPs samples were magnetically separated, thus demonstrating their magnetic nature. Figure 4.2 A) presents the X-ray diffraction profiles of MNPs and UCNPs, which were indexed to cubic phase for magnetite, and hexagonal phase (β-$NaYF_4$) (according to the JCPDS files no. 19-0629 and 16-0334, respectively). Comparing the diffraction peaks of the JNPs with the MNPs and UCNPs, JNPs samples synthesised with ratios of 1:0.5 and 1:1 showed patterns more similar to those of magnetite at the 36° angle (3 1 1) than to those of UCNPs.[340] In contrast, the sample synthesized with a 1:0.25 sample showed patterns more similar to those of a UCNP, also finding very slight comparisons with the patterns of MNP, especially the one at the 57° angle (5 1 1).[341]

Figure 4.2 B) shows the TEM images of UCNPs and JNPs. UCNPs have a spherical morphology with a monodispersity and an average size of 30 nm in diameter. Finally, monodisperse JNPs are observed with a typical snowman morphology (40 nm) where the larger sphere (30 nm) would correspond to the luminescent fraction (UCNP) and the smaller sphere (8 nm) would correspond to the magnetic fraction. This demonstrates the epitaxial growth of the MNPs on the UCNP surface, and with an average size of janus-like nanoparticles of 40 nm, adequate size for NPs.[5]

Figure 4.2 C shows the up-conversion luminescence spectra of UCNPs and the different JNPs samples under 980 nm excitation (1 W cm^{-2}). It should be noted that there is no upconversion emission for MNPs. The upconversion spectra shows several band emissions extending from the near-ultraviolet to the near-infrared region. The two peaks at the UV region, 335 and 363 nm, are assigned to the $^1I_6 \rightarrow {}^3F_4$ and $^1D_2 \rightarrow {}^3H_6$ transitions of Tm^{3+}, respectively. The two peaks in the blue region at 450 and 478 nm, are assigned respectively to the $^1D_2 \rightarrow {}^3F_4$ and $^1G_4 \rightarrow {}^3H_6$ transitions from thulium. The peak within the red region, 655 nm, is attributed to the transition $^1G_4 \rightarrow {}^3F_4$ from thulium. Finally, in the near-infrared region the intense peak centred at 801 nm is ascribed to the $^3H_4 \rightarrow {}^3H_6$ transition of the Tm^{3+}. Similar transitions are observed for the JNPs sample with a mass ratio of 1:0.25 (UCNPs : $Fe(AcAc)_3$) for their synthesis, but with an important emission diminution decrease in 801 and 478 nm. For JNPs with mass ratios of 1:0.5 and 1:1 for their synthesis, the UV peaks were not observed, and the considerable reduction of emission intensity at the in Uv-Vis and near infrared regions was verified. These emissions reductions could be due to the energy transfer from the UCNPs fraction to the magnetic fraction (magnetite) epitaxially grown in the UCNPs surface. Magnetite has an absorption band between 375 and 650 nm.[342] The transfer energy absorption is dissipated, in a non-radiatively process called 'non-radiative de-excitation' by the release of thermal energy.[343] These processes result in the release of infinitesimal amounts of heat that cannot normally be measured experimentally, but the experimental evidence for non-radiative de-excitation processes is the quenching of luminescence, also observed in Figure 4.2 C). Preserving the emission in the UV region of the JNPs is important in the continuation of the project due to its used in this energy absorption by SP form the copolymer. Hence, when comparing the fluorescence results between the different JNPs samples, the one that showed magnetic properties and higher emission, especially in the UV region, was chosen for further experiments: the JNPs synthesized with a ratio of 1:0.25 (UCNPs:Fe(AcAc)$_3$). The observed radiative transitions in the NaYF$_4$: Yb,Tm UCNPs and the RET processes in the JNPs induced by 980 nm excitation are schematized in Figure 4.2 D). An additional RET process to the Spyropiran moiety (SP) will be described later in the manuscript.

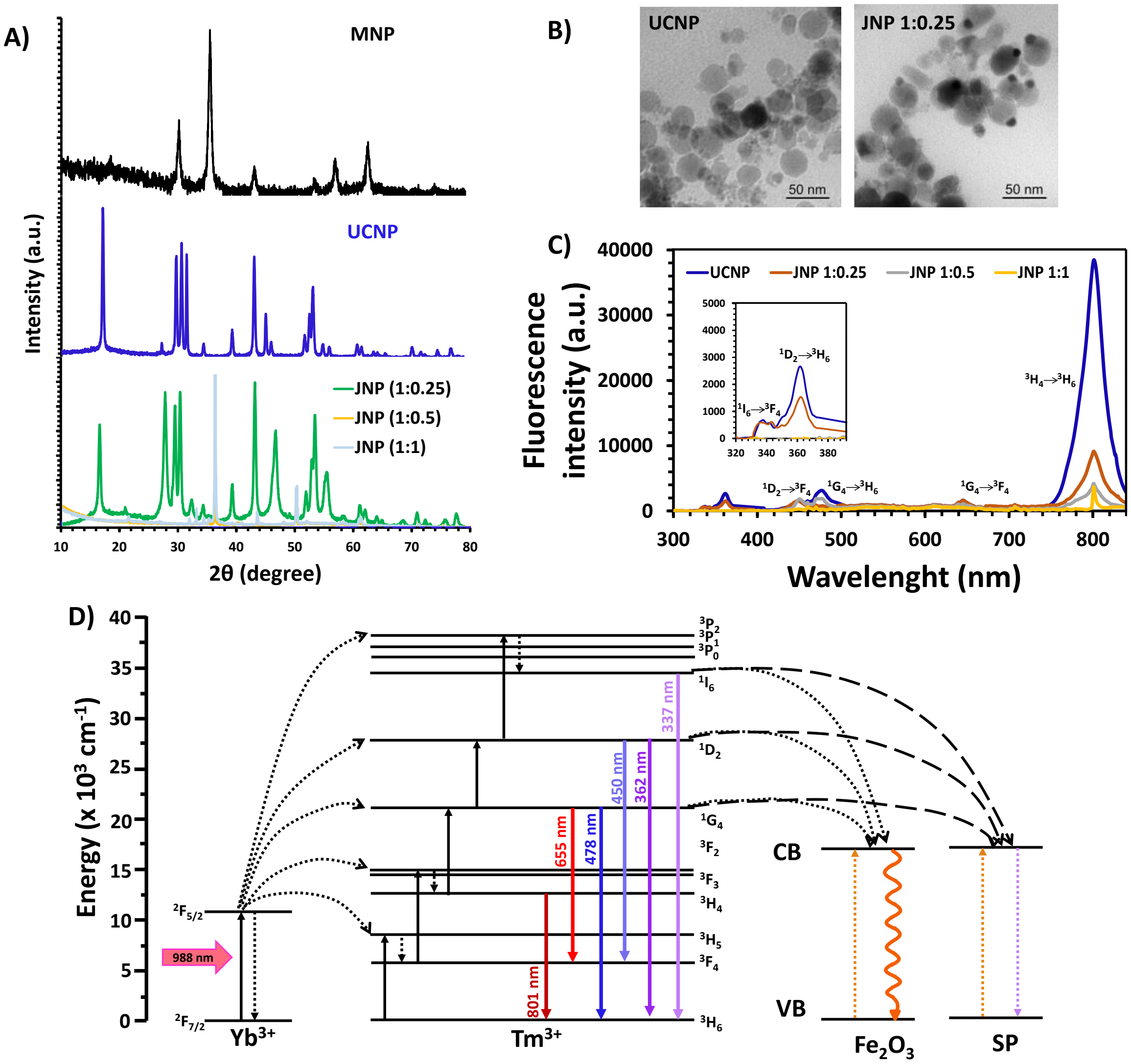

Figure 4.2 A) Powder XRD pattern, B) TEM micrography, and C) 980 nm NIR irradiation FS spectra of MNP, UCNP and JNP. D) Energy-level diagram of the up conversion and energy transfer process in the NaYF$_4$: Yb,Tm - Fe$_2$O$_3$ JNP and the energy transfer process in the MicJNP under 980 nm excitation

4.3.2 Doxorubicin loading of JNPs/micelle-like nanocomposite

The encapsulation of JNPs (1:0.25) by the micelle-like aggregates was then performed to generate the so-called MicJNPs nanocomposite. This encapsulation is possible through the hydrophobic interaction between the surface of the JNPs composed of oleylamine and 1-octadecene (surface compounds that give stability to the NPs in non-polar media) and the hydrophobic spiropyran of the copolymer Poly(NIPAM-co-SPMA). After purification by dialysis and magnetic separation, physicochemical characterisation was carried out using DLS, TEM, fluorescence spectroscopy and capillary electrophoresis (CE). Also, doxorubicin hydrochloride (DoxHCl) 5 µM was loaded together with JNPs into the nanocomposite (MicJNPDox) and its characterization was then performed.

DLS results are shown Figure 4.3 A). The size of Mic was increased 61 ± 2 nm (Peak width 28 nm) to 220 ± 2 nm (Peak width 100 nm) upon incorporation of JNPs (MicJNP). When DoxHCl was loaded into the nanosystem (MicJNPDox), the size increase to 295 ± 6 nm (Peak width 160 nm). The increase in the peak width may be due to two factors: i) possible entrapment of more than one JNPs in the micelle, or/and ii) as the JNPs are coloured NPs, the DLS values may not present quality criteria due to possible absorption of the incident light by the equipment.[344]

After micelle-like nanoaggregates synthesis in 25 mM PBS (pH 7.4), the sample pH was adjusted to pH 6 with HCl (38%). MicJNPs and MicJNPDox experimented an important increment in their size, up to 531 ± 5 nm (Peak width 140 nm) for MicJNP, and up to 396 ± 8 nm (Peak width 160 nm) for MicJNPDox. This increment in size at a more acidic pH may be due to the swelling of SP chains derived from their protonation (SP-H)[301] and the consequent solvent internalization. It seems from these results that swelling is greater fo MicJNPs, maybe due to differences in repulsive interactions, leading to a more stable structure when both JNPs and DoxHCl are loaded.

In addition, TEM images for MicJNP at physiological pH 7.4 (Figures 4.3 B) and acidic pH 6 (pH adjusted by adding HCl) are present in Figures 4.3 C). In physiological conditions, the micelle coating was on the JNPs conserving the spherical morphology with an average solid diameter of 48 nm. On the other hand, by changing the pH from 7.4 to 6, a slight increase in the size of spherical objects with apparently disaggregated structures was observed. This shows the effect of SP-H swelling and disaggregation under pH stimulus.

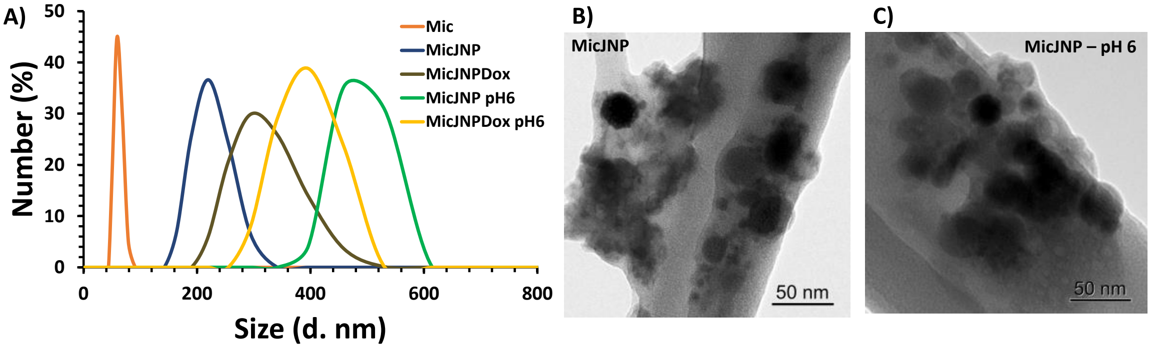

Figure 4.3. A) DLS profiles (under pH 7.4 and 6) and TEM micrographies of B) MicJNP and C) MicJNP DoxHCl 5 µM

Figure 4.4 A) shows the up-conversion luminescence spectra of JNPs (1:0.25) and the corresponding nanosystem MicJNPs under 980 nm excitation (1 W cm^{-2}). Comparing the intensity of the peaks at the near-infrared region (transition $^{3}H_{4}\rightarrow{}^{3}H_{6}$ at 801 nm), a slight difference is observed. On the contrary, peaks at 655 nm within the red region, attributed to the transition $^{1}G_{4}\rightarrow{}^{3}F_{4}$, remains unchanged. In the blue region, the peaks observed at 450 and 478 nm, assigned respectively to the $^{1}D_{2}\rightarrow{}^{3}F_{4}$ and $^{1}G_{4}\rightarrow{}^{3}H_{6}$ transitions, decrease in intensity for MicJNPs. Finally for the peaks at 335 and 363 nm in the UV region, assigned to the $^{1}I_{6}\rightarrow{}^{3}F_{4}$ and $^{1}D_{2}\rightarrow{}^{3}H_{6}$ respectively, there is a clear disappearance of the peaks for the MicJNPs nanosystem.

The spiropyran (SP) compound, that is part of the inner side of the micelle-like aggregates, absorb the energy transfer in the range between 200 and 400 nm wavelength. When this happen, the compound is photoexcited and undergoes a ring-opening intermediate that forms quickly a cis-trans isomerisation of the benzopyran double bond to give the merocyanine (MC) compound. This process is reversible, with the MC isomer reverting to the more stable SP isomer by irradiation with visible light. Hence, the energy in the UV wavelength region produced by the up conversion of JNPs in the irradiation of 980 nm near infrared light, could be transferred from the UCNPs fraction to the micelle-like aggregate Mic that encapsulate these NPs. This energy then could be absorbed by the phot-responsive SP changing to the stable zwitterionic isomer MC. Energy-level diagram of the up conversion and energy transfer process in the $NaYF_4$: Yb,Tm - Fe_2O_3 JNP under 980 nm excitation to SP in the micelle-like aggregate is presented in Figure 4.2 D).

These results indicate the very powerful combination between the JNPs and the micelle-like aggregates for theranostic. Indeed, the energy transfer from JNPs to Mic, would allow to activate the smart drug delivery system upon NIR-Light irradiation. In addition, the NIR emission band at 801 nm could be used for therapy monitoring by their easy penetration throw the epidermis.

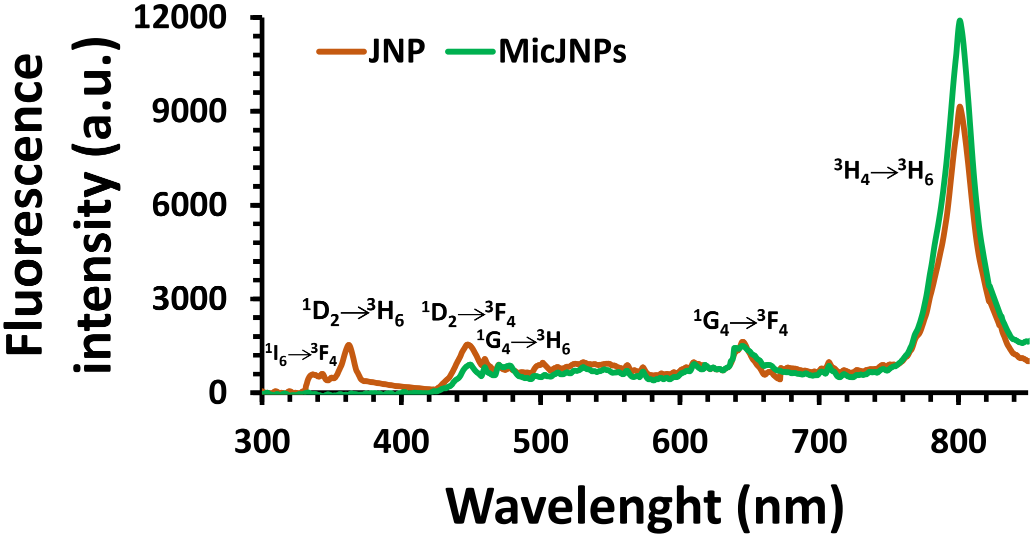

Figure 4.4. A) Up-conversion emission spectra of JNP and MicJNP upon 980 nm laser excitation (1 W cm^{-2}).

Figure 4.5 (A) shows the electrophoretic profiles of the nanosystem (MicJNP) corresponding to the entrapment of the JNPs trapped in the micelle-like aggregates (Mic) and the effect of pH and UV-light stimuli on the MicJNP nanocomposite. The samples synthesized in 25 mM PBS (pH 7.4) were electrokinetically separated and the electropherograms with separation time at the x-axis were converted to electrophoretic mobility thanks to the determination of the electrosmotic mobility thanks to a neutral marker. The detection was performed with a fluoresce detector, so as to increase selectivity of detection (such as in chapter II and III CE characterizations).[322] Mic and MicJNP present a similar electrophoretic profile, with a peak at a mobility around -11 x 10^{-5} cm^{2}V^{-1}s^{-1} ± 1, with a same intensity.

When the MicJNPs are irradiated by UV light two signals are observed: the peak at around -11 x 10^{-5} cm^{2}V^{-1}s^{-1} ± 1 previously identified for Mic and MicJNP; and a new peak at -18 x 10^{-5} cm^{2}V^{-1}s^{-1} ± 1, with a much thinner profile. In our previous study (chapter II and III) we evidenced that, when the polymeric micelles are irradiated by UV light, the spiropyran compound (hydrophobic) changes to its zwitterionic state called merocyanine (hydrophilic), from which the micelle disaggregates into unimers. When this irradiation is stopped, the unimers return to their spiropyran form and re-aggregate in an uncontrolled manner.[322] Therefore, one hypothesis for this new peak could be the formation of a new possible structure composed of copolymer unimers decorating the surface of JNPs called CoPo-JNPs which should form upon Mic disaggregation into unimers and release of JNPs.

pH-stimulus was studied by injecting the MicJNPs, synthesised in 25 mM PBS (pH 7.4), and separated electrokinetically in a BGE composed of 25 mM PBS (pH 6.0). An electrophoretic mobility shift from -11×10^{-5} $cm^2V^{-1}s^{-1} \pm 1$ to around -9×10^{-5} $cm^2V^{-1}s^{-1} \pm 2$. These could be due to the fact that the SP-H protonation induces the swelling of the micelles generating inhomogeneous sizes and shapes, also changing the electrokinetic dispersion of the micelle profile, comparable with our previous work.[322]

Finally, by combining the UV irradiation stimuli with the change of pH to 6, the electrophoretic profile of MicJNPs presents two peaks: the one identified when pH-stimulus was applied (two unresolved signals at -8×10^{-5} $cm^2V^{-1}s^{-1} \pm 1$ and -10×10^{-5} $cm^2V^{-1}s^{-1} \pm 1$) and a new peak at -18×10^{-5} $cm^2V^{-1}s^{-1} \pm 1$ which could again correspond to the possible CoPo-JNP structure. However, this second peak is at a lower intensity and seems to be composed of two unresolved peaks. Therefore, UV seems to form CoPo-JNPs nanosystems.

Figure 4.5 B) shows the electrophoretic profiles of the MicJNP nanocomposite loaded with the Doxorubicin (DoxHCl) drug (MicJNPDox) and the effect of pH and UV-light stimuli on MicJNPDox. Briefly, Dox loading was performed during the nanocomposite synthesis. After dispersion of JNPs and dissolution of the copolymer in THF, 1 mL of 25 mM PBS (pH 7.4) solution containing 50 µM DoxHCl, was added, and subsequent stirring and dialysis were performed in the same process as described for the MicJNPs. MicJNPDox presents three peaks: one at the same mobility of the one of MicJNP at around -11×10^{-5} $cm^2V^{-1}s^{-1} \pm 1$, but presenting a higher intensity; a second peak at -3×10^{-5} $cm^2V^{-1}s^{-1} \pm 0.5$; and a third peak at $+8 \times 10^{-5}$ $cm^2V^{-1}s^{-1} \pm 0.5$, corresponding to the electrophoretic mobility of DoxHCl. These results are in total accordance with what was proved when working on the loading of the Mic with DoxHCl (chapter III). Indeed, the first peak corresponding to the MicJNP presents a higher intensity due to the presence of DoxHCl in the MicJNP. In our previous study with MicDox, the second peak was proved to be CoPo-Dox, due to the interaction between the unimers of the copolymer and the drug at the time of MicJNP formation (chapter III). And the third peak corresponds to the free form of DoxHCl.

Upon irradiation by UV light, four peaks were observed for the MicJNpDox: that of the MicJNP (-11 x 10^{-5} $cm^2V^{-1}s^{-1}$ ± 1), that of CoPo-Dox (-3 x 10^{-5} $cm^2V^{-1}s^{-1}$ ± 0.5), that of DoxHCl (+8 x 10^{-5} $cm^2V^{-1}s^{-1}$ ± 0.5) and a new one at -18 x 10^{-5} $cm^2V^{-1}s^{-1}$ ± 1, which should correspond to CoPo-JNP, as previously explained, and at the same intensity as for MicJNPDOx without stimulus. The DoxHCl peak gained in intensity with UV light stimulus, which indicates a release of DoxHCl under this stimulus.

On the other hand, separating MicJNPDox (synthesized at pH 7.4) in a more acidic pH in BGE (25 mM PBS pH 6.0) presents three peaks. The first one corresponds to MicJNP with a small shift in electrophoretic mobility from -11 x 10^{-5} $cm^2V^{-1}s^{-1}$ ± 1 to -8 x 10^{-5} $cm^2V^{-1}s^{-1}$ ± 2, probably due to partial swelling of the micelles. The second peak corresponds to Copo-Dox (-2 x 10^{-5} $cm^2V^{-1}s^{-1}$ ± 0.5), at a higher intensity than with UV light stimulation, which could be due to the fact that the CoPo system under these conditions may be more stable. The third peak (+10 x 10^{-5} $cm^2V^{-1}s^{-1}$ ± 1) corresponds to free DoxHCl but does not present a significant increase in intensity compared to the MicJNPDox UV irradiated. Therefore, pH stimulus does not seem to provoke such an efficient DoxHCl release.

Finally, by combining the UV irradiation stimuli with the pH stimulus at pH 6, the signal intensity of the peak for free DoxHCl highly increased, showing that the synergic stimuli could release efficiently DoxHCl over 18 wt% (2 µg). The other broad peak seems to indicate an equilibrium state within the separation capillary between MicJNP and Copo-Dox, with a high decrease in the intensity of Copo-Dox. Furthermore, a thin peak appears in this broad signal at an electrophoretic mobility of -12 x 10^{-5} $cm^2V^{-1}s^{-1}$, which could correspond to CoPo-JNP structure but at a lower electrophoretic mobility due again to equilibrium state during separation.

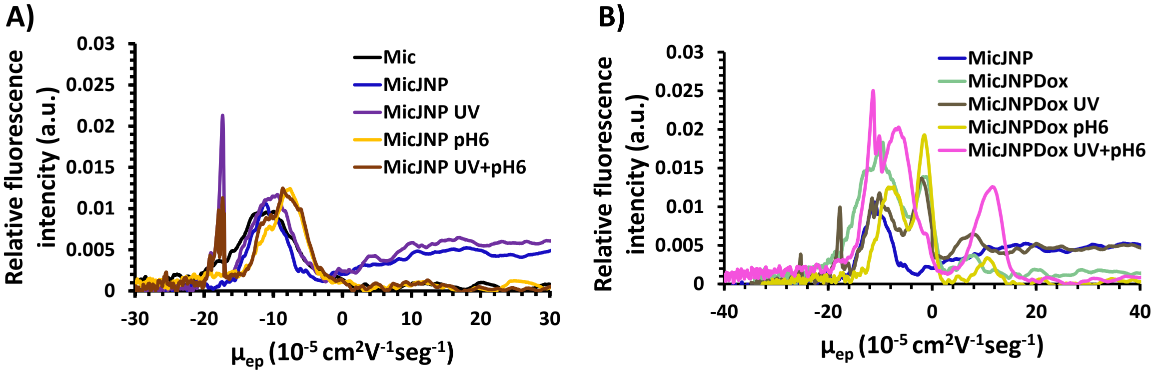

Figure 4.5. A) MicJNP and B) MicJNpDoxHCl 2uM electrophoretic profiles in response to UV (360nm) and pH 6 Stimuli. BGE 25 mM PBS (pH 7.4).

Hence, the electrophoretic profiles of the MicJNP and MicJNPDox without any stimulus prove the loading of DoxHCl in this original nanocomposite. Furthermore, the Dox release is mainly performed thanks to the UV light- pH simultaneous stimuli. The presence of Copo-Dox and Copo-JNP was also demonstrated, showing equivalent behaviors and equilibria as for the Mic alone.

4.4 Preliminary conclusions

Janus-like magneto-luminescent nanoparticles were synthesized by epitaxial growth of magnetite, having iron acetyl acetonate Fe(AcAc)$_3$ as precursor, on the surface of UCNPs made of NaYF$_4$:Yb,Tm. A study on the respective proportions was performed with (mass ratios of 1:0.25, 1:0.5 and 1:1 of UCNPs:Fe(AcAc)$_3$ and their respective physicochemical properties were determined. XDR measurements showed that the JNPs samples with 1:0.5 and 1:1 mass ratios have more pattern similarities with MNPs, in contrast with the sample with 1:0.25 ratio, indicating the combination of UCNPs and MNPs patterns, proving Janus nanomaterial formation in a structural way. TEM images evidenced the characteristic "snowman" geometry of these JNPs, with an adequate NP solid diameter size of 40 nm, which is convenient for *in vivo* applications. Using fluorescence spectroscopy under 980 nm near infrared irradiation, and by comparing the different spectra for UCNPs and the JNPs samples, it was shown that the one with the ratio of 1:0.25 (UCNPs:Fe(AcAc)$_3$) maintained the emission in the UV region (335 and 363 nm), in the blue region (450 and 478 nm) as well as in the red region (655 nm) and near-infrared light (801 nm), finding a decrease in the emission intensities for the other assayed NPs mass ratios . The latter is due to the resonant energy transfer from the UCNP to the magnetic section (Fe$_2$O$_3$) of the JNPs, inducing a thermally deactivated process and then a local heating. Thus, it was determined that the best formation ratio of the JNPs by an epitaxial growth procedure is 1:0.25.

Subsequently, the encapsulation of these JNPs in micelle-like aggregates (Mic) of the copolymer Poly(NIPMA-co-SPMA) was achieved for the formation of the MicJNPs nanosystem. The encapsulation of Doxorubicin hydrochloride (DoxHCl) was also performed creating the MicJNPDox nanosystem. This nanocomposite structure was demonstrated by DLS and TEM by observing an increase in both hydrodynamic and solid diameters. The response of the MicJNPs and MicJNPDox nanosystems to pH stimulus (pH 6) was also verified by DLS, observing a greater increase in their size due to the swelling of the micelle-like aggregates, due to the siporopyran modification under this stimulus.

A slight difference in fluorescence intensity of JNPs and MicJNPs samples was observed in the near-infrared (801 nm) and visible (655, 478 and 450 nm) regions. In contrast, in the UV region (362 and 337 nm), a complete disappearance of the signals was observed for MicJNPs. This is due to the UV energy transfer to the micelle-like aggregate (Mic), absorbed by the spiropyran (SP) compound. This is very important as, by this effect, SP changes to its zwitterionic merocyanine (MC) state where it allows the copolymer to be completely hydrophilic and thus the cargos (NPs, drugs, etc.) can be released.

The nanocomposite with (MicJNPDox) and without (MicJNPs) the drug DoxHCl was characterized by capillary electrophoresis. For MicJNPs after the influence of UV light irradiation to the sample a new signal appeared with an electrophoretic mobility of -18 x 10-5 $cm^2V^{-1}s^{-1}$, significantly different from that of the nanocomposite (-11 x 10^{-5} $cm^2V^{-1}s^{-1}$). This new structure should be a CoPo-JNP structure. Indeed, under UV light, the copolymer becomes completely hydrophilic thus JNPs can be released from the Mic; after stopping light irradiation, the copolymer becomes amphiphilic again, generating a possible interaction between the hydrophobic surface of the NPs and the SP compound of the copolymer. This phenomenon was also evidenced with the MicJNPDox nanocomposite. When stimulating with UV light, a slight increase in free Dox was shown, whereas this increase was negligible with pH stimulation. But a synergistic effect when combining UV and pH stimuli was proved to release significantly DoxHCl (18 wt%).

These results demonstrate the ability of these new nanocomposites to serve as magnetically steerable theranostic tools where, NIR light irradiation will allow the core of the JNPs to transfer the emitted energy towards the SP compound of the micelle for the controlled release of the DoxHCl drug, being of a higher release percentage; simultaneously having the ability to generate images. In addition, it could be envisaged that the increase of the surface temperature of the magnetic moiety by the energy transferred by the luminescent moiety could serve as a photothermal therapy.

General conclusions

The use of nanoparticles as simultaneous intelligent drug delivery systems and contrast agents for optical imaging(theranostics), is one powerful strategy for the future towards alleviating human diseases such as cancer. Nevertheless, the synthesis of new smart hybrid nanosystems with different properties, and the understanding of the related physicochemical interactions with drugs is still a great challenge.

In the first part of this PhD project, the synthesis of random poly(NIPAM-co-Spiropyran) amphiphilic copolymer and its self-assembly to micelle-like was performed, so as to generate a pH- and light-responsive nano-aggregate. They were classically synthesized in water, and we demonstrated for the first time that the self-aggregation can be modulated by the NPs concentration, the medium ionic strength, pH, and the stirring time. The different batches were characterized by classical methods for NPs, i.e. by DLS, LDE and TEM, combined with capillary electrophoretic methodologies. The measured hydrodynamic diameter values slightly decreased when increasing the ionic strength of the saline synthesis medium (PBS pH 7.4) in comparison to the classical synthesis medium containing pure water. Hence, optimized micelle-like aggregates (Mic) with an average size of 60 nm and narrow size distribution were obtained in 25 mM PBS (pH 7.4). Furthermore, the exposure of Mic to UV-light generated the SP photoisomerization into its hydrophilic zwitterionic state merocyanine (MC), conducing to micelle disaggregation; while a pH change (from pH 7;4 to 6), induced the self-aggregates to swell and disaggregate. These results proved the interest of these micelle-like nano-aggregates for localized drug delivery at tumor sites.

In the second part of the project, Mic were formed and loaded with poorly (Dox) and highly water-soluble (Dox-HCl) forms of doxorubicin. The study of the interactions involved in this process between the micelle-like aggregates and the drug was then performed. Capillary electrophoresis coupled to fluorescence detection results revealed the presence of two species in equilibrium: the micelle-like aggregates with or without loaded doxorubicin and a complex formed between the non-aggregated copolymer and the doxorubicin molecules, at doxorubicin concentrations higher than 3 µM. The electrokinetic separation allowed to quantify the loaded and released concentrations of doxorubicin at pH 7.4 and upon UV-irradiation and pH 6.0 stimuli. A most effective loading was observed when Dox was used compared to Dox-HCl (10 µg/mg vs 5.5 µg/mg, respectively). Drug release rates of 68 and 74 % were observed for Dox-HCl upon pH 6.0 and combined UV+ pH6.0 stimuli, while only 29% of the loaded Dox was released under these two stimuli. Hence, micelle-drug interactions could be explained by the possible predominant electrostatic interactions between Dox-HCl and the poly-NIPAM section at the micellar shell, while predominant hydrophobic interactions between Dox and the SP moiety arise at the inner section of the micelles. In addition, a fast drug release kinetics was demonstrated, with a maximal doxorubicin release achieved 2 minutes after micelle-like aggregates exposition to the combined stimuli.

In the last part of this project, Janus-type magneto-luminescent nanoparticles (JNPs) were synthesized in an epitaxial growth procedure of magnetite on the surface of upconverting nanoparticles UCNPs, using iron acetylacetonate ($Fe(AcAc)_3$) as the precursor. Different UCNPs:$Fe(AcAc)_3$ ratios (1:0.25, 1:0.5 and 1:1) were tested for the synthesis and XDR, TEM and fluorescence spectroscopy showed that the best formation ratio was 1:0.25, as it provides the highest emission intensity, as well as a response to a magnetic field between them. Thereafter, JNPs and DoxHCl were encapsulated together in the micelle-like nano-aggregates previously synthesized and characterized. A greater increase in diameter size was observed by DLS and TEM due to the swelling of the micelle-like aggregate upon acidification until pH 6. By fluorescence spectroscopy, the UV-energy transfer from JNPs to Mic was confirmed upon exposure to near-infrared light (980 nm) irradiation. The electrophoretic separation of the samples evidenced a possible CoPo-JNP structure formation after UV light irradiation, along with a release of the DoxHCl. Also, a synergistic effect was demonstrated by combining the effect of UV light irradiation with the change of pH to 6, thus boosting the drug release.

These results highlight the interest of such nanocarriers as multi-modal nano-objects for drug loading, vectorization under a magnetic field till the site of interest (cancerous area for example),and release of the drug under external and internal stimuli. These smart nanosystems should then be further studied as potential theranostic tools.

Perspectives

The first steps for further investigation concern a deeper characterization of the Janus-type hybrid NPs, such as magnetic hysteresis to ensure magnetic properties; Thermogravimetric analysis (TGA), Energy Dispersive X-Ray Analysis (EDX), and Nuclear magnetic resonance (NMR), for composition analysis, among others. This will provide more detailed information on the mass proportions of magnetic fractions in the JNPs together with the exact value of magnetization. Furthermore, photoluminescence decay analysis should be performed to verify the resonance energy transfer mechanism from the upconverting nanoparticle donors to the photo-responsive acceptors in the micelle-like aggregates.

It would be interesting to also determine the release of the drug doxorubicin hydrochloride deeper in conditions that should mimic the real medium, that means first under a pH change from physiological conditions to that of cancerous tumors (pH 6) and under the addition of the second stimulus of near-infrared light (980 nm).

The results presented in this manuscript could also be complemented with computational modeling techniques for analysis of interactions. It would help to verify the proposed interactions between the copolymer and the hydrochlorinated Doxorubicin drug for the formation of the CoPo-Dox structure, as well as the interactions between the copolymer and the Janus-type nanoparticle for the formation of the CoPo-JNP structure.

After these *ex-vitro* studies, a selection of performant smart nanocarriers will then undergo *in-vitro* toxicity tests, and finally *in-vivo* studies. Particularly, Janus-type nanoparticles should be tested for their use as a follow-up and cancer treatment through photothermal therapy, that is to elucidate whether it is possible to use them as a theranostic tool.

In a more general perspective, and so as to improve the design of the nanocarriers and explore all possible configurations, yolk-shell type nanoparticles combining the up-conversion NPs and magnetites could be synthesized and used to compare their light emission and magnetic properties with those observed with JNPs. They can be also implemented as components of the micelle-like aggregates.

Also, it would be interesting to study the use of JNPs for applications as photothermal agents because, when irradiated by light, they could induce a heat rise. The magnitude of the photothermal response should be verified.

References

1. Talevi, A. & Quiroga, P. A. M. *Introduction. Biopharmaceutics and Pharmacokinetics*. *ADME Processes in Pharmaceutical Sciences* (2018). doi:10.1007/978-3-319-99593-9_1.
2. Senapati, S., Mahanta, A. K., Kumar, S. & Maiti, P. Controlled drug delivery vehicles for cancer treatment and their performance. *Signal Transduct. Target. Ther.* **3**, 1–19 (2018).
3. Thostenson, E. T., Li, C. & Chou, T. W. Nanocomposites in context. *Compos. Sci. Technol.* **65**, 491–516 (2005).
4. Shen, Z., Nieh, M. P. & Li, Y. Decorating nanoparticle surface for targeted drug delivery: Opportunities and challenges. *Polymers (Basel).* **8**, 1–18 (2016).
5. Lombardo, D., Kiselev, M. A. & Caccamo, M. T. Smart Nanoparticles for Drug Delivery Application: Development of Versatile Nanocarrier Platforms in Biotechnology and Nanomedicine. *J. Nanomater.* **2019**, (2019).
6. Hossen, S. *et al.* Smart nanocarrier-based drug delivery systems for cancer therapy and toxicity studies: A review. *J. Adv. Res.* **15**, 1–18 (2019).
7. Ryu, J. H. *et al.* Theranostic nanoparticles for future personalized medicine. *J. Control. Release* **190**, 477–484 (2014).
8. Sailor, M. J. & Park, J. H. Hybrid nanoparticles for detection and treatment of cancer. *Adv. Mater.* **24**, 3779–3802 (2012).
9. Ghezzi, M. *et al.* Polymeric micelles in drug delivery: An insight of the techniques for their characterization and assessment in biorelevant conditions. *J. Control. Release* **332**, 312–336 (2021).
10. Terashima, T. Controlled self-assembly of amphiphilic random copolymers into folded micelles and nanostructure materials. *J. Oleo Sci.* **69**, 529–538 (2020).
11. Majumder, N., Das, N. G. & Das, S. K. Polymeric micelles for anticancer drug delivery. *Ther. Deliv.* **11**, 613–635 (2020).
12. Ding, H., Wang, X., Zhang, S. & Liu, X. Applications of polymeric micelles with tumor targeted in chemotherapy. *J. Nanoparticle Res.* **14**, (2012).
13. Yan, K. *et al.* Enzyme-responsive polymeric micelles with fluorescence fabricated through aggregation-induced copolymer self-assembly for anticancer drug delivery. *Polym. Chem.* **11**, 7704–7713 (2020).
14. Hu, J., Xu, Y. & Zhang, Y. Amphiphilic random polycarbonate self-assemble into GSH/pH dual responsive micelle-like aggregates in water. *Chinese Chem. Lett.* **30**, 2039–2042 (2019).
15. Li, Y. *et al.* Polymer-Assisted Magnetic Nanoparticle Assemblies for Biomedical Applications. *ACS Appl. Bio Mater.* **3**, 121–142 (2020).
16. Wang, J. *et al.* Ultrasonic responsive nanostructures prepared by self-assembly of polymeric single-chain nanoparticles. *Mater. Res. Innov.* **26**, 182–188 (2022).
17. Mihai, M., Stoica, I. & Schwarz, S. PH-sensitive nanostructured architectures based on synthetic and/or natural weak polyelectrolytes. *Colloid Polym. Sci.* **289**, 1387–1396 (2011).
18. Binauld, S. & Stenzel, M. H. Acid-degradable polymers for drug delivery: A decade of innovation. *Chem. Commun.* **49**, 2082–2102 (2013).
19. Deirram, N., Zhang, C., Kermaniyan, S. S., Johnston, A. P. R. & Such, G. K. pH-Responsive Polymer Nanoparticles for Drug Delivery. *Macromol. Rapid Commun.* **40**, 1–23 (2019).
20. Silva, J. M., Silva, E. & Reis, R. L. Light-triggered release of photocaged therapeutics - Where are we now? *J. Control. Release* **298**, 154–176 (2019).
21. Zhao, W. *et al.* Remote Light-Responsive Nanocarriers for Controlled Drug Delivery: Advances and Perspectives. *Small* **15**, 1–34 (2019).
22. Weis, P. & Wu, S. Light-Switchable Azobenzene-Containing Macromolecules: From UV to Near Infrared. *Macromol. Rapid Commun.* **39**, 1–12 (2018).
23. Klajn, R. Spiropyran-based dynamic materials. *Chem. Soc. Rev.* **43**, 148–184 (2014).
24. Kortekaas, L. & Browne, W. R. The evolution of spiropyran: Fundamentals and progress of an extraordinarily versatile photochrome. *Chem. Soc. Rev.* **48**, 3406–3424 (2019).
25. Chen, S., Jiang, F., Cao, Z., Wang, G. & Dang, Z. M. Photo, pH, and thermo triple-responsive spiropyran-based copolymer nanoparticles for controlled release. *Chem. Commun.* **51**, 12633–12636 (2015).
26. Auzel, F. Upconversion and Anti-Stokes Processes with f and d Ions in Solids. *Chem. Rev.* **104**, 139–173 (2004).
27. Wang, F. & Liu, X. Recent advances in the chemistry of lanthanide-doped upconversion nanocrystals. *Chem. Soc. Rev.* **38**, 976–989 (2009).
28. Qian, H. S. & Zhang, Y. Synthesis of hexagonal-phase core-shell NaYF4 nanocrystals with tunable upconversion fluorescence. *Langmuir* **24**, 12123–12125 (2008).
29. Bagheri, A., Arandiyan, H., Boyer, C. & Lim, M. Lanthanide-doped upconversion nanoparticles: Emerging intelligent light-activated drug delivery systems. *Adv. Sci.* **3**, (2016).
30. Lin, M. *et al.* Recent advances in synthesis and surface modification of lanthanide-doped upconversion nanoparticles for biomedical applications. *Biotechnol. Adv.* **30**, 1551–1561 (2012).
31. Wang, X. *et al.* Near infrared to ultraviolet upconversion nanocomposite for controlling the permittivity of polyspiropyran shell. *Polym. Test.* **94**, 107042 (2021).
32. Zhang, Y., Zhu, X. & Zhang, Y. Exploring Heterostructured Upconversion Nanoparticles: From Rational Engineering to Diverse Applications. *ACS Nano* **15**, 3709–3735 (2021).
33. Zhu, X. *et al.* Core-shell Fe 3O 4@NaLuF 4: Yb,Er/Tm nanostructure for MRI, CT and upconversion luminescence tri-modality imaging. *Biomaterials* **33**, 4618–4627 (2012).
34. Cheng, L. *et al.* Multifunctional nanoparticles for upconversion luminescence/MR multimodal imaging and magnetically

targeted photothermal therapy. *Biomaterials* **33**, 2215–2222 (2012).

35. Zhang, Y. *et al.* Multifunctional Microspheres Encoded with Upconverting Nanocrystals and Magnetic Nanoparticles for Rapid Separation and Immunoassays. *ACS Appl. Mater. Interfaces* **8**, 745–753 (2016).
36. Challenor, M. *et al.* The influence of NaYF4:Yb,Er size/phase on the multimodality of co-encapsulated magnetic photon-upconverting polymeric nanoparticles. *Dalt. Trans.* **43**, 16780–16787 (2014).
37. Liu, B. *et al.* Multifunctional NaYF4:Yb, Er@mSiO2@Fe3O4-PEG nanoparticles for UCL/MR bioimaging and magnetically targeted drug delivery. *Nanoscale* **7**, 1839–1848 (2015).
38. Rahiminezhad, Z., Tamaddon, A. M., Borandeh, S. & Abolmaali, S. S. Janus nanoparticles: New generation of multifunctional nanocarriers in drug delivery, bioimaiging and theranostics. *Appl. Mater. Today* **18**, 100513 (2020).
39. Carbone, L. & Cozzoli, P. D. Colloidal heterostructured nanocrystals: Synthesis and growth mechanisms. *Nano Today* **5**, 449–493 (2010).
40. Karthick, H. *et al.* Architectural fabrication of multifunctional janus nanostructures for biomedical applications Architectural fabrication of multifunctional janus nanostructures for biomedical applications. (2022) doi:10.22038/NMJ.2022.65101.1682.
41. Vasir, J., Reddy, M. & Labhasetwar, V. Nanosystems in Drug Targeting: Opportunities and Challenges. *Curr. Nanosci.* **1**, 47–64 (2006).
42. Hainaut, P. & Plymoth, A. Cancer as a metabolic disease. *Curr. Opin. Oncol.* **24**, 56–57 (2012).
43. Mattiuzzi, C. & Lippi, G. Current cancer epidemiology. *J. Epidemiol. Glob. Health* **9**, 217–222 (2019).
44. Brau-Figueroa, H., Alejandra Palafox-Parrilla, E. & Mohar-Betancourt, A. The national cancer registry in Mexico, a reality. *Gac. Mex. Oncol.* **19**, 1–5 (2020).
45. Defossez, G. *et al.* Estimations nationales de l’incidence et de la mortalité par cancer en France métropolitaine entre 1990 et 2018. *Vol. 1 – Tumeurs solides. Saint-Maurice Santé publique Fr.* **1**, 372 (2019).
46. Kalyane, D. *et al.* Employment of enhanced permeability and retention effect (EPR): Nanoparticle-based precision tools for targeting of therapeutic and diagnostic agent in cancer. *Mater. Sci. Eng. C* **98**, 1252–1276 (2019).
47. Kalyane, D. *et al.* Employment of enhanced permeability and retention effect (EPR): Nanoparticle-based precision tools for targeting of therapeutic and diagnostic agent in cancer. *Mater. Sci. Eng. C* **98**, 1252–1276 (2019).
48. Fang, F., Li, M., Zhang, J. & Lee, C. S. Different Strategies for Organic Nanoparticle Preparation in Biomedicine. *ACS Mater. Lett.* **2**, 531–549 (2020).
49. Paul, W. & Sharma, C. P. *Inorganic nanoparticles for targeted drug delivery*. *Biointegration of Medical Implant Materials* (Elsevier Ltd, 2019). doi:10.1016/B978-0-08-102680-9.00013-5.
50. Rommasi, F. & Esfandiari, N. Liposomal Nanomedicine: Applications for Drug Delivery in Cancer Therapy. *Nanoscale Res. Lett.* **16**, (2021).
51. Chauhan, A. S. Dendrimers for Drug Delivery. *Molecules* **23**, (2018).
52. Manzano, M. & Vallet-Regí, M. Mesoporous Silica Nanoparticles for Drug Delivery. *Adv. Funct. Mater.* **30**, 3–5 (2020).
53. Tashima, T. Smart strategies for therapeutic agent delivery into brain across the blood–brain barrier using receptor-mediated transcytosis. *Chem. Pharm. Bull.* **68**, 316–325 (2020).
54. Amina, S. J. & Guo, B. A review on the synthesis and functionalization of gold nanoparticles as a drug delivery vehicle. *Int. J. Nanomedicine* **15**, 9823–9857 (2020).
55. Zhi, D., Yang, T., Yang, J., Fu, S. & Zhang, S. Targeting strategies for superparamagnetic iron oxide nanoparticles in cancer therapy. *Acta Biomater.* **102**, 13–34 (2020).
56. Chou, I. C., Chen, S. I. & Chiu, W. Y. Surfactant-free dispersion polymerization as an efficient synthesis route to a successful encapsulation of nanoparticles. *RSC Adv.* **4**, 47436–47447 (2014).
57. Hamblin, M. R. Carbon Nanotubes : Smart Drug / Gene Delivery Carriers. 1681–1706 (2021).
58. He, C., Lu, J. & Lin, W. Hybrid nanoparticles for combination therapy of cancer. *J. Control. Release* **219**, 224–236 (2015).
59. Tang, C. *et al.* Large scale synthesis of janus submicrometer sized colloids by seeded emulsion polymerization. *Macromolecules* **43**, 5114–5120 (2010).
60. Chen, X. *et al.* Rational Design of Branched Au–Fe3O4 Janus Nanoparticles for Simultaneous Trimodal Imaging and Photothermal Therapy of Cancer Cells. *Chem. - A Eur. J.* **23**, 17204–17208 (2017).
61. Zhang, Y., Huang, K., Lin, J. & Huang, P. Janus nanoparticles in cancer diagnosis, therapy and theranostics. *Biomater. Sci.* **7**, 1262–1275 (2019).
62. Qiao, Y. *et al.* Stimuli-responsive nanotherapeutics for precision drug delivery and cancer therapy. *Wiley Interdiscip. Rev. Nanomedicine Nanobiotechnology* **11**, 1–20 (2019).
63. Pham, S. H., Choi, Y. & Choi, J. Stimuli-responsive nanomaterials for application in antitumor therapy and drug delivery. *Pharmaceutics* **12**, 1–19 (2020).
64. Das, S. S. *et al.* Stimuli-Responsive Polymeric Nanocarriers for Drug. *Polymers (Basel).* **12**, 1–45 (2020).
65. Logozzi, M. *et al.* Microenvironmental pH and exosome levels interplay in human cancer cell lines of different histotypes. *Cancers (Basel).* **10**, (2018).
66. Wan, M., Ding, Y., Li, Z., Wang, X. & Xu, M. Metabolic manipulation of the tumour immune microenvironment. *Immunology* **165**, 290–300 (2022).
67. Indermun, S., Govender, M., Kumar, P., Choonara, Y. E. & Pillay, V. *Stimuli-responsive polymers as smart drug delivery systems: Classifications based on carrier type and triggered-release mechanism*. *Stimuli Responsive Polymeric Nanocarriers for Drug Delivery Applications: Volume 1: Types and Triggers* (Elsevier Ltd., 2018). doi:10.1016/B978-0-08-101997-9.00002-3.
68. Cheng, Y. J. *et al.* Super-pH-Sensitive Mesoporous Silica Nanoparticle-Based Drug Delivery System for Effective Combination Cancer Therapy. *ACS Biomater. Sci. Eng.* **5**, 1878–1886 (2019).
69. Nezami, S., Sadeghi, M. & Mohajerani, H. A novel pH-sensitive and magnetic starch-based nanocomposite hydrogel as a controlled drug delivery system for wound healing. *Polym. Degrad. Stab.* **179**, (2020).
70. Mane, S. R., Sathyan, A. & Shunmugam, R. Biomedical applications of pH-responsive amphiphilic polymer nanoassemblies.

ACS Appl. Nano Mater. **3**, 2104–21117 (2020).

71. Zhou, Q., Zhang, L., Yang, T. H. & Wu, H. Stimuli-responsive polymeric micelles for drug delivery and cancer therapy. *Int. J. Nanomedicine* **13**, 2921–2942 (2018).
72. Abri Aghdam, M. *et al.* Recent advances on thermosensitive and pH-sensitive liposomes employed in controlled release. *J. Control. Release* **315**, 1–22 (2019).
73. Xu, F. *et al.* Development of a pH-responsive polymersome inducing endoplasmic reticulum stress and autophagy blockade. *Sci. Adv.* **6**, (2020).
74. Li, Z., Huang, J. & Wu, J. PH-Sensitive nanogels for drug delivery in cancer therapy. *Biomater. Sci.* **9**, 574–589 (2021).
75. Zhang, M. *et al.* Doxorubicin-conjugated PAMAM dendrimers for pH-responsive drug release and folic acid-targeted cancer therapy. *Pharmaceutics* **10**, 1–13 (2018).
76. Iyer, R. *et al.* Glutathione-responsive biodegradable polyurethane nanoparticles for lung cancer treatment. *J. Control. Release* **321**, 363–371 (2020).
77. Yao, Y. *et al.* Reactive oxygen species (ROS)-responsive biomaterials mediate tissue microenvironments and tissue regeneration. *J. Mater. Chem. B* **7**, 5019–5037 (2019).
78. Chen, B. *et al.* Glutathione-mediated formation of disulfide bonds modulates the properties of myofibrillar protein gels at different temperatures. *Food Chem.* **364**, 130356 (2021).
79. Li, J. *et al.* Self-sufficing H2O2-responsive nanocarriers through tumor-specific H2O2 production for synergistic oxidation-chemotherapy. *J. Control. Release* **225**, 64–74 (2016).
80. Xu, B., Xu, Y., Su, G., Zhu, H. & Zong, L. A multifunctional nanoparticle constructed with a detachable albumin outer shell and a redox-sensitive inner core for efficient siRNA delivery to hepatocellular carcinoma cells. *J. Drug Target.* **26**, 941–954 (2018).
81. Deng, S. *et al.* Dually cross-linked core-shell structure nanohydrogel with redox–responsive degradability for intracellular delivery. *Pharmaceutics* **13**, 1–32 (2021).
82. Tiwari, R. *et al.* Redox-Responsive Nanocapsules for the Spatiotemporal Release of Miltefosine in Lysosome: Protection against Leishmania. *Bioconjug. Chem.* **32**, 245–253 (2021).
83. Gisbert-Garzarán, M. & Vallet-Regí, M. Redox-responsive mesoporous silica nanoparticles for cancer treatment: Recent updates. *Nanomaterials* **11**, (2021).
84. Cao, J. *et al.* A new redox-active conjugated polymer containing anthraquinone pendants as anode material for aqueous all-organic hybrid-flow battery. *J. Power Sources* **423**, 316–322 (2019).
85. Nehate, C., Nayal, A. & Koul, V. Redox Responsive Polymersomes for Enhanced Doxorubicin Delivery. *ACS Biomater. Sci. Eng.* **5**, 70–80 (2019).
86. Sun, C. *et al.* Redox-sensitive polymeric micelles with aggregation-induced emission for bioimaging and delivery of anticancer drugs. *J. Nanobiotechnology* **19**, (2021).
87. Kumar, P., Liu, B. & Behl, G. A Comprehensive Outlook of Synthetic Strategies and Applications of Redox-Responsive Nanogels in Drug Delivery. *Macromol. Biosci.* **19**, 1–28 (2019).
88. Yan, X. *et al.* Redox-Responsive Multifunctional Polypeptides Conjugated with Au Nanoparticles for Tumor-Targeting Gene Therapy and Their 1 + 1 > 2 Synergistic Effects. *ACS Biomater. Sci. Eng.* **6**, 463–473 (2020).
89. Xu, P. *et al.* A DM1-doped porous gold nanoshell system for NIR accelerated redox-responsive release and triple modal imaging guided photothermal synergistic chemotherapy. *J. Nanobiotechnology* **19**, 1–19 (2021).
90. Peng, S. *et al.* Redox-responsive polyethyleneimine-coated magnetic iron oxide nanoparticles for controllable gene delivery and magnetic resonance imaging. *Polym. Int.* **69**, 206–214 (2020).
91. Zhang, Z. T., Huang-Fu, M. Y., Xu, W. H. & Han, M. Stimulus-responsive nanoscale delivery systems triggered by the enzymes in the tumor microenvironment. *Eur. J. Pharm. Biopharm.* **137**, 122–130 (2019).
92. Mi, P. Stimuli-responsive nanocarriers for drug delivery, tumor imaging, therapy and theranostics. *Theranostics* **10**, 4557–4588 (2020).
93. Zuo, Y. M. *et al.* Enzyme-Responsive Ag Nanoparticle Assemblies in Targeting Antibacterial against Methicillin-Resistant Staphylococcus Aureus. *ACS Appl. Mater. Interfaces* **12**, 4333–4342 (2020).
94. Wright, D. B., Thompson, M. P., Touve, M. A., Carlini, A. S. & Gianneschi, N. C. Enzyme-Responsive Polymer Nanoparticles via Ring-Opening Metathesis Polymerization-Induced Self-Assembly. *Macromol. Rapid Commun.* **40**, 1–5 (2019).
95. Bilalis, P. *et al.* Self-Healing pH- and Enzyme Stimuli-Responsive Hydrogels for Targeted Delivery of Gemcitabine to Treat Pancreatic Cancer. *Biomacromolecules* **19**, 3840–3852 (2018).
96. Naz, S. *et al.* Enzyme-responsive mesoporous silica nanoparticles for tumor cells and mitochondria multistage-targeted drug delivery. *Int. J. Nanomedicine* **14**, 2533–2542 (2019).
97. Zhang, Z. *et al.* Synthesis of enzyme-responsive phosphoramidate dendrimers for cancer drug delivery. *Polym. Chem.* **9**, 438–449 (2018).
98. Nosrati, H., Mojtahedi, A., Danafar, H. & Kheiri Manjili, H. Enzymatic stimuli-responsive methotrexate-conjugated magnetic nanoparticles for target delivery to breast cancer cells and release study in lysosomal condition. *J. Biomed. Mater. Res. - Part A* **106**, 1646–1654 (2018).
99. Barve, A., Jain, A., Liu, H., Zhao, Z. & Cheng, K. Enzyme-responsive polymeric micelles of cabazitaxel for prostate cancer targeted therapy. *Acta Biomater.* **113**, 501–511 (2020).
100. Lou, J. & Best, M. D. A General Approach to Enzyme-Responsive Liposomes. *Chem. - A Eur. J.* **26**, 8597–8607 (2020).
101. Li, Y. *et al.* Nitroimidazole derivative incorporated liposomes for hypoxia-triggered drug delivery and enhanced therapeutic efficacy in patient-derived tumor xenografts. *Acta Biomater.* **83**, 334–348 (2019).
102. Shen, X. & Gates, K. S. Enzyme-Activated Generation of Reactive Oxygen Species from Heterocyclic N-Oxides under Aerobic and Anaerobic Conditions and Its Relevance to Hypoxia-Selective Prodrugs. *Chem. Res. Toxicol.* **32**, 348–361 (2019).
103. Sahu, A., Choi, W. Il & Tae, G. Recent Progress in the Design of Hypoxia-Specific Nano Drug Delivery Systems for Cancer Therapy. *Adv. Ther.* **1**, 1–20 (2018).

104. Li, Y., Jeon, J. & Park, J. H. Hypoxia-responsive nanoparticles for tumor-targeted drug delivery. *Cancer Lett.* **490**, 31–43 (2020).
105. Long, M. *et al.* Azo-inserted responsive hybrid liposomes for hypoxia-specific drug delivery. *Acta Biomater.* **115**, 343–357 (2020).
106. Jang, E. H., Kim, G. L., Park, M. G., Shim, M. K. & Kim, J. H. Hypoxia-responsive, organic-inorganic hybrid mesoporous silica nanoparticles for triggered drug release. *J. Drug Deliv. Sci. Technol.* **56**, 101543 (2020).
107. Wang, P. *et al.* Fabrication of hypoxia-responsive and uperconversion nanoparticles-modified RBC micro-vehicles for oxygen delivery and chemotherapy enhancement. *Biomater. Sci.* **8**, 4595–4602 (2020).
108. Poon, Z., Chang, D., Zhao, X. & Hammond, P. T. Layer-by-layer nanoparticles with a pH-sheddable layer for in vivo targeting of tumor hypoxia. *ACS Nano* **5**, 4284–4292 (2011).
109. Chen, S. X. *et al.* A self-activating nanovesicle with oxygen-depleting capability for efficient hypoxia-responsive chemo-thermo cancer therapy. *Biomaterials* **269**, 120533 (2021).
110. Feng, H. *et al.* Hypoxia-Responsive Polymeric Micelles for Enhancing Cancer Treatment. *Front. Chem.* **8**, 1–8 (2020).
111. Kulkarni, P. *et al.* Tissue-Penetrating, Hypoxia-Responsive Echogenic Polymersomes For Drug Delivery To Solid Tumors. *Chem. - A Eur. J.* **24**, 12490–12494 (2018).
112. Yang, G. *et al.* A Hypoxia-Responsive Albumin-Based Nanosystem for Deep Tumor Penetration and Excellent Therapeutic Efficacy. *Adv. Mater.* **31**, 1–9 (2019).
113. Huang, C. *et al.* Azoreductase-Responsive Metal-Organic Framework-Based Nanodrug for Enhanced Cancer Therapy via Breaking Hypoxia-induced Chemoresistance. *ACS Appl. Mater. Interfaces* **11**, 25740–25749 (2019).
114. Luan, X., Pan, Y., Gao, Y. & Song, Y. Recent near-infrared light-activated nanomedicine toward precision cancer therapy. *J. Mater. Chem. B* **9**, 7076–7099 (2021).
115. Raza, A., Hayat, U., Rasheed, T., Bilal, M. & Iqbal, H. M. N. 'smart' materials-based near-infrared light-responsive drug delivery systems for cancer treatment: A review. *J. Mater. Res. Technol.* **8**, 1497–1509 (2019).
116. Golovynskyi, S. *et al.* Optical windows for head tissues in near-infrared and short-wave infrared regions: Approaching transcranial light applications. *J. Biophotonics* **11**, 1–12 (2018).
117. Chilakamarthi, U. & Giribabu, L. Photodynamic Therapy: Past, Present and Future. *Chem. Rec.* **17**, 775–802 (2017).
118. Zhi, D., Yang, T., O'Hagan, J., Zhang, S. & Donnelly, R. F. Photothermal therapy. *J. Control. Release* **325**, 52–71 (2020).
119. Jin, Q., Cai, T., Wang, Y., Wang, H. & Ji, J. Light-responsive polyion complex micelles with switchable surface charge for efficient protein delivery. *ACS Macro Lett.* **3**, 679–683 (2014).
120. Jiang, B. *et al.* Harmonizing the Intracellular Kinetics toward Effective Gene Delivery Using Cancer Cell-Targeted and Light-Degradable Polyplexes. *Biomacromolecules* **18**, 877–885 (2017).
121. Kim, K. N. *et al.* Light-responsive polymeric micellar nanoparticles with enhanced formulation stability. *Polymers (Basel).* **13**, 1–11 (2021).
122. Zhou, Y. *et al.* Light-responsive polymersomes with a charge-switch for targeted drug delivery. *J. Mater. Chem. B* **8**, 727–735 (2020).
123. Refaat, A. *et al.* Near-infrared light-responsive liposomes for protein delivery: Towards bleeding-free photothermally-assisted thrombolysis. *J. Control. Release* **337**, 212–223 (2021).
124. Augé, A., Camerel, F., Benoist, A. & Zhao, Y. Near-infrared light-responsive UCST-nanogels using an efficient nickel-bis(dithiolene) photothermal crosslinker. *Polym. Chem.* **11**, 3863–3875 (2020).
125. Li, X. *et al.* Red-light-responsive coordination polymers nanorods: New strategy for ultrasensitive photothermal detection of targeted cancer cells. *Biosens. Bioelectron.* **190**, 113417 (2021).
126. Li, C. *et al.* Light-Responsive Biodegradable Nanorattles for Cancer Theranostics. *Adv. Mater.* **30**, 1–8 (2018).
127. Sabri, T., Pawelek, P. D. & Capobianco, J. A. Dual Activity of Rose Bengal Functionalized to Albumin-Coated Lanthanide-Doped Upconverting Nanoparticles: Targeting and Photodynamic Therapy. *ACS Appl. Mater. Interfaces* **10**, 26947–26953 (2018).
128. Kim, H. S. & Lee, D. Y. Near-infrared-responsive cancer photothermal and photodynamic therapy using gold nanoparticles. *Polymers (Basel).* **10**, 1–14 (2018).
129. Gao, Y. Y. *et al.* Light-Responsive Actuators Based on Graphene. *Front. Chem.* **7**, 1–5 (2019).
130. Li, B. *et al.* Near infra-red light responsive carbon nanotubes@mesoporous silica for photothermia and drug delivery to cancer cells. *Mater. Today Chem.* **17**, (2020).
131. Dadfar, S. M. *et al.* Iron oxide nanoparticles: Diagnostic, therapeutic and theranostic applications. *Adv. Drug Deliv. Rev.* **138**, 302–325 (2019).
132. Sanchez, L. M. & Alvarez, V. A. Advances in magnetic noble metal/iron-based oxide hybrid nanoparticles as biomedical devices. *Bioengineering* **6**, (2019).
133. Manohar, A., Vijayakanth, V. & Kim, K. H. Influence of Ca doping on ZnFe2O4 nanoparticles magnetic hyperthermia and cytotoxicity study. *J. Alloys Compd.* **886**, (2021).
134. Avasthi, A., Caro, C., Pozo-Torres, E., Leal, M. P. & García-Martín, M. L. *Magnetic Nanoparticles as MRI Contrast Agents*. *Topics in Current Chemistry* vol. 378 (Springer International Publishing, 2020).
135. Shamsi, M. *et al.* Magnetically assisted intraperitoneal drug delivery for cancer chemotherapy. *Drug Deliv.* **25**, 846–861 (2018).
136. Fatima, H., Charinpanitkul, T. & Kim, K. S. Fundamentals to apply magnetic nanoparticles for hyperthermia therapy. *Nanomaterials* **11**, 1–20 (2021).
137. Sun, L. *et al.* Mechanistic study of nonivamide enhancement of hyperthermia-induced apoptosis in U937 cells. *Free Radic. Biol. Med.* **120**, 147–159 (2018).
138. Li, X., Li, W., Wang, M. & Liao, Z. Magnetic nanoparticles for cancer theranostics: Advances and prospects. *J. Control. Release* **335**, 437–448 (2021).
139. Farzin, A., Etesami, S. A., Quint, J., Memic, A. & Tamayol, A. Magnetic Nanoparticles in Cancer Therapy and Diagnosis. *Adv. Healthc. Mater.* **9**, 1–29 (2020).

140. Vlasova, K. Y. *et al.* Magnetic liposome design for drug release systems responsive to super-low frequency alternating current magnetic field (AC MF). *J. Colloid Interface Sci.* **552**, 689–700 (2019).
141. Dulińska-Litewka, J. *et al.* Superparamagnetic iron oxide nanoparticles-current and prospective medical applications. *Materials (Basel).* **12**, (2019).
142. Thorat, N. D. *et al.* Effective Cancer Theranostics with Polymer Encapsulated Superparamagnetic Nanoparticles: Combined Effects of Magnetic Hyperthermia and Controlled Drug Release. *ACS Biomater. Sci. Eng.* **3**, 1332–1340 (2017).
143. Mandal, P. *et al.* Magnetic particle ornamented dual stimuli responsive nanogel for controlled anticancer drug delivery. *New J. Chem.* **43**, 3026–3037 (2019).
144. Mura, S., Nicolas, J. & Couvreur, P. Stimuli-responsive nanocarriers for drug delivery. *Nat. Mater.* **12**, 991–1003 (2013).
145. Xu, X. *et al.* Thermoresponsive Composite Hydrogels for Biomedical Applications. *Polymers (Basel).* **12**, 1–22 (2020).
146. Rafael, D. *et al.* Thermo-responsive hydrogels for cancer local therapy: Challenges and state-of-art. *Int. J. Pharm.* **606**, (2021).
147. Haladjova, E., Rangelov, S. & Tsvetanov, C. Thermoresponsive polyoxazolines as vectors for transfection of nucleic acids. *Polymers (Basel).* **12**, 1–18 (2020).
148. Yang, J. *et al.* Temperature-tuned DNA condensation and gene transfection by PEI-g-(PMEO2MA-b-PHEMA) copolymer-based nonviral vectors. *Biomaterials* **31**, 144–155 (2010).
149. Chen, K. J. *et al.* A thermoresponsive bubble-generating liposomal system for triggering localized extracellular drug delivery. *ACS Nano* **7**, 438–446 (2013).
150. Zhang, X., Zheng, L., Suleiman, K. & Shu, C. Combined cryosurgery and cold-responsive drug-loaded nanoparticles to enhance deep-lying tumor therapy: A mathematical model. *Int. J. Heat Mass Transf.* **165**, (2021).
151. Naziris, N. *et al.* A thermal analysis and physicochemical study on thermoresponsive chimeric liposomal nanosystems. *J. Therm. Anal. Calorim.* **141**, 751–766 (2020).
152. Soltantabar, P., Calubaquib, E. L., Mostafavi, E., Biewer, M. C. & Stefan, M. C. Enhancement of Loading Efficiency by Coloading of Doxorubicin and Quercetin in Thermoresponsive Polymeric Micelles. *Biomacromolecules* **21**, 1427–1436 (2020).
153. Li, A. *et al.* NIR-laser switched ICG/DOX loaded thermo-responsive polymeric capsule for chemo-photothermal targeted therapy. *Eur. Polym. J.* **92**, 51–60 (2017).
154. Ghaeini-hesaroeiye, S., Bagtash, H. R. & Boddohi, S. gels Thermoresponsive Nanogels Based on Di ff erent. 1–32 (2020).
155. Mccoy, T. M. *et al.* Spontaneous Self-Assembly of Thermoresponsive Vesicles Using a Zwitterionic and an Anionic Surfactant. *Biomacromolecules* **21**, 4569–4576 (2020).
156. Sirsi, S. R. & Borden, M. A. State-of-the-art materials for ultrasound-triggered drug delivery. *Adv. Drug Deliv. Rev.* **72**, 3–14 (2014).
157. Halliwell, M. A tutorial on ultrasonic physics and imaging techniques. *Proc. Inst. Mech. Eng. Part H J. Eng. Med.* **224**, 127–142 (2010).
158. Coussios, C. C. & Roy, R. A. Applications of acoustics and cavitation to noninvasive therapy and drug delivery. *Annu. Rev. Fluid Mech.* **40**, 395–420 (2008).
159. Doinikov, A. A. & Bouakaz, A. Acoustic microstreaming around an encapsulated particle. *J. Acoust. Soc. Am.* **127**, 1218–1227 (2010).
160. Zhu, L. *et al.* Ultrasound Hyperthermia Technology for Radiosensitization. *Ultrasound Med. Biol.* **45**, 1025–1043 (2019).
161. Hamarat Şanlıer, Ş. *et al.* Development of Ultrasound-Triggered and Magnetic-Targeted Nanobubble System for Dual-Drug Delivery. *J. Pharm. Sci.* **108**, 1272–1283 (2019).
162. Fan, W. *et al.* Calcium carbonate-methylene blue nanohybrids for photodynamic therapy and ultrasound imaging. *Sci. China Life Sci.* **61**, 483–491 (2018).
163. Prabhakar, A. & Banerjee, R. Nanobubble Liposome Complexes for Diagnostic Imaging and Ultrasound-Triggered Drug Delivery in Cancers: A Theranostic Approach. *ACS Omega* **4**, 15567–15580 (2019).
164. Lea-Banks, H. & Hynynen, K. Sub-millimetre precision of drug delivery in the brain from ultrasound-triggered nanodroplets. *J. Control. Release* **338**, 731–741 (2021).
165. Jamburidze, A. *et al.* Nanoparticle-Coated Microbubbles for Combined Ultrasound Imaging and Drug Delivery. *Langmuir* **35**, 10087–10096 (2019).
166. Mahajan, A. & Aggarwal, G. Smart polymers: Innovations in novel drug delivery. *Int. J. Drug Dev. Res.* **3**, 16–30 (2011).
167. Reyes-Ortega, F. *pH-responsive polymers: Properties, synthesis and applications*. *Smart Polymers and their Applications* (Woodhead Publishing Limited, 2014). doi:10.1533/9780857097026.1.45.
168. Wadsworth, B. L., Nishiori, D., Nguyen, N. P., Reyes Cruz, E. A. & Moore, G. F. Electrochemistry of Polymeric Cobaloxime-Containing Assemblies in Organic and Aqueous Solvents. *ECS J. Solid State Sci. Technol.* **9**, 061018 (2020).
169. Nguyen, T. L., Ishihara, K. & Yusa, S. I. Separated Micelles Formation of pH-Responsive Random and Block Copolymers Containing Phosphorylcholine Groups. *Polymers (Basel).* **14**, 1–14 (2022).
170. Espinola-Portilla, F. *et al.* Superparamagnetic iron oxide nanoparticles functionalized with a binary alkoxysilane array and poly(4-vinylpyridine) for magnetic targeting and pH-responsive release of doxorubicin. *New J. Chem.* **45**, 3600–3609 (2021).
171. Wang, P. *et al.* pH-responsive nanomicelles of poly(ethylene glycol)-poly(ε-caprolactone)-poly(L-histidine) for targeted drug delivery. *J. Biomater. Sci. Polym. Ed.* **31**, 277–292 (2020).
172. Chytil, P., Koziolová, E., Etrych, T. & Ulbrich, K. HPMA Copolymer–Drug Conjugates with Controlled Tumor-Specific Drug Release. *Macromol. Biosci.* **18**, 1–15 (2018).
173. Bobde, Y., Biswas, S. & Ghosh, B. PEGylated N-(2 hydroxypropyl) methacrylamide-doxorubicin conjugate as pH-responsive polymeric nanoparticles for cancer therapy. *React. Funct. Polym.* **151**, (2020).
174. Chang, Z. *et al.* A PEGylated photosensitizer-core pH-responsive polymeric nanocarrier for imaging-guided combination chemotherapy and photodynamic therapy. *New J. Chem.* **45**, 6180–6185 (2021).
175. Li, G., Pei, M., Li, X. & Liu, P. Fluorescent traceable nanoparticles by co-self-assembly of carbon dot-drug conjugate and biodegradable hyperbranched polymer for diagnosis and therapy. *Particuology* **62**, 79–87 (2022).

176. Feng, X., Li, D., Han, J., Zhuang, X. & Ding, J. Schiff base bond-linked polysaccharide–doxorubicin conjugate for upregulated cancer therapy. *Mater. Sci. Eng. C* **76**, 1121–1128 (2017).
177. Zhu, J. *et al.* Multifunctional Dendrimer-Entrapped Gold Nanoparticles Conjugated with Doxorubicin for pH-Responsive Drug Delivery and Targeted Computed Tomography Imaging. *Langmuir* **34**, 12428–12435 (2018).
178. Graham, E. T. & Broaders, K. E. Spirocyclic Acetal-Modified Dextran as a Flexible pH-Sensitive Solubility-Switching Material. *Biomacromolecules* **20**, 2008–2014 (2019).
179. Xu, C. R., Qiu, L., Pan, C. Y., Hong, C. Y. & Hao, Z. Y. Efficient synthesis of polymer prodrug by thiol-acrylate michael addition reaction and fabrication of Ph-responsive prodrug nanoparticles. *Bioconjug. Chem.* **29**, 3203–3212 (2018).
180. Han, H. S. *et al.* Bioreducible shell-cross-linked hyaluronic acid nanoparticles for tumor-targeted drug delivery. *Biomacromolecules* **16**, 447–456 (2015).
181. Sim, T. *et al.* Development of pH-sensitive nanogels for cancer treatment using crosslinked poly(aspartic acid-graft-imidazole)-block-poly(ethylene glycol). *J. Appl. Polym. Sci.* **135**, 1–10 (2018).
182. Zarrintaj, P. *et al.* Thermo-sensitive polymers in medicine: A review. *Eur. Polym. J.* **117**, 402–423 (2019).
183. Tang, L. *et al.* Poly(N-isopropylacrylamide)-based smart hydrogels: Design, properties and applications. *Prog. Mater. Sci.* **115**, (2021).
184. Farjadian, F., Ghasemi, S., Andami, Z. & Tamami, B. Thermo-responsive nanocarrier based on poly(N-isopropylacrylamide) serving as a smart doxorubicin delivery system. *Iran. Polym. J. (English Ed.* **29**, 197–207 (2020).
185. Sponchioni, M., Capasso Palmiero, U. & Moscatelli, D. Thermo-responsive polymers: Applications of smart materials in drug delivery and tissue engineering. *Mater. Sci. Eng. C* **102**, 589–605 (2019).
186. Boustta, M. & Vert, M. A method to slow down the ionization-dependent release of risperidone loaded in a thermoresponsive poly(N-acryloyl glycinamide) hydrogel. *Drug Deliv. Transl. Res.* **7**, 460–464 (2017).
187. Le, M. *et al.* Upper critical solution temperature polymeric drug carriers. *Chem. Eng. J.* **432**, (2022).
188. Azzaroni, O., Brown, A. A. & Huck, W. T. S. UCST Wetting Transitions of Polyzwitterionic Brushes Driven by Self-Association. *Angew. Chemie* **118**, 1802–1806 (2006).
189. Lyons, S. K., Patrick, P. S. & Brindle, K. M. Imaging mouse cancer models in vivo using reporter transgenes. *Cold Spring Harb. Protoc.* **2013**, 685–699 (2013).
190. Romano, A., Roppolo, I., Rossegger, E., Schlögl, S. & Sangermano, M. Recent trends in applying ortho-nitrobenzyl esters for the design of photo-responsive polymer networks. *Materials (Basel).* **13**, 1–26 (2020).
191. Klán, P. *et al.* Photoremovable protecting groups in chemistry and biology: Reaction mechanisms and efficacy. *Chem. Rev.* **113**, 119–191 (2013).
192. Sun, J. *et al.* Use of Light-Degradable Aliphatic Polycarbonate Nanoparticles As Drug Carrier for Photosensitizer. *Biomacromolecules* **19**, 4677–4690 (2018).
193. Li, S., Ji, S., Zhou, Z., Chen, G. & Li, Q. Synthesis and self-assembly of o-nitrobenzyl-based amphiphilic hybrid polymer with light and pH dual response. *Macromol. Chem. Phys.* **216**, 1192–1200 (2015).
194. Ma, C. *et al.* Fragmentation of Fiber-like Micelles with a π-Conjugated Crystalline Oligo(p-phenylenevinylene) Core and a Photocleavable Corona in Water: A Matter of Density of Corona-Forming Chains. *Macromolecules* **53**, 8631–8641 (2020).
195. Zhou, Y., Ye, H., Chen, Y., Zhu, R. & Yin, L. Photoresponsive Drug/Gene Delivery Systems. *Biomacromolecules* **19**, 1840–1857 (2018).
196. Wang, C., Zhang, G., Liu, G., Hu, J. & Liu, S. Photo- and thermo-responsive multicompartment hydrogels for synergistic delivery of gemcitabine and doxorubicin. *J. Control. Release* **259**, 149–159 (2017).
197. Li, L., Wu, Y., Du, F. S. & Li, Z. C. Modular synthesis of photodegradable polymers with different sensitive wavelengths as UV/NIR responsive nanocarriers. *J. Polym. Sci. Part A Polym. Chem.* **57**, 334–341 (2019).
198. Fagan, A., Bartkowski, M. & Giordani, S. Spiropyran-Based Drug Delivery Systems. *Front. Chem.* **9**, 1–19 (2021).
199. Zhang, Y., Huang, Y. & Li, S. Polymeric micelles: Nanocarriers for cancer-targeted drug delivery. *AAPS PharmSciTech* **15**, 862–871 (2014).
200. Wang, D. *et al.* Reversibly Photoswitchable Dual-Color Fluorescence and Controlled Release Properties of Polymeric Nanoparticles. *Macromolecules* **52**, 7130–7136 (2019).
201. Razavi, B., Abdollahi, A., Roghani-Mamaqani, H. & Salami-Kalajahi, M. Light-, temperature-, and pH-responsive micellar assemblies of spiropyran-initiated amphiphilic block copolymers: Kinetics of photochromism, responsiveness, and smart drug delivery. *Mater. Sci. Eng. C* **109**, 110524 (2020).
202. Tong, R., Hemmati, H. D., Langer, R. & Kohane, D. S. Photoswitchable nanoparticles for triggered tissue penetration and drug delivery. *J. Am. Chem. Soc.* **134**, 8848–8855 (2012).
203. Xiao, P., Zhang, J., Zhao, J. & Stenzel, M. H. Light-induced release of molecules from polymers. *Prog. Polym. Sci.* **74**, 1–33 (2017).
204. Wang, H., Miao, W., Wang, F. & Cheng, Y. A Self-Assembled Coumarin-Anchored Dendrimer for Efficient Gene Delivery and Light-Responsive Drug Delivery. *Biomacromolecules* **19**, 2194–2201 (2018).
205. Barhoumi, A., Liu, Q. & Kohane, D. S. Ultraviolet light-mediated drug delivery: Principles, applications, and challenges. *J. Control. Release* **219**, 31–42 (2015).
206. Ash, C., Dubec, M., Donne, K. & Bashford, T. Effect of wavelength and beam width on penetration in light-tissue interaction using computational methods. *Lasers Med. Sci.* **32**, 1909–1918 (2017).
207. Cagel, M. *et al.* Polymeric mixed micelles as nanomedicines: Achievements and perspectives. *Eur. J. Pharm. Biopharm.* **113**, 211–228 (2017).
208. Perumal, S. & Atchudan, R. A Review of Polymeric Micelles and Their Applications. 1–19 (2022).
209. Zakaria, H., El Kurdi, R. & Patra, D. A Novel Study on the Self-Assembly Behavior of Poly(lactic- co-glycolic acid) Polymer Probed by Curcumin Fluorescence. *ACS Omega* **7**, 9551–9558 (2022).
210. Gupta, A. *et al.* Formulation and characterization of curcumin loaded polymeric micelles produced via continuous processing.

Int. J. Pharm. **583**, 119340 (2020).

211. Liu, H. *et al.* Amphiphilic block copolymer poly (Acrylic Acid)-B-polycaprolactone as a novel ph-sensitive nanocarrier for anti-cancer drugs delivery: In-vitro and in-vivo evaluation. *Polymers (Basel).* **11**, (2019).
212. Feng, J., Wen, W., Jia, Y. G., Liu, S. & Guo, J. pH-responsive micelles assembled by three-armed degradable block copolymers with a cholic acid core for drug controlled-release. *Polymers (Basel).* **11**, (2019).
213. Hsu, C. W. *et al.* pH-responsive polymeric micelles self-assembled from benzoic-imine-containing alkyl-modified PEGylated chitosan for delivery of amphiphilic drugs. *Int. J. Biol. Macromol.* **163**, 1106–1116 (2020).
214. Yu, C. *et al.* Smart micelles self-assembled from four-arm star polymers as potential drug carriers for pH-triggered DOX release. *J. Polym. Res.* **27**, 2–11 (2020).
215. Ju, B., Yan, D. & Zhang, S. Micelles self-assembled from thermoresponsive 2-hydroxy-3-butoxypropyl starches for drug delivery. *Carbohydr. Polym.* **87**, 1404–1409 (2012).
216. Sun, X. L. *et al.* Thermoresponsive block copolymer micelles with tunable pyrrolidone-based polymer cores: Structure/property correlations and application as drug carriers. *J. Mater. Chem. B* **3**, 814–823 (2015).
217. Zhao, C., Dolmans, L. & Zhu, X. X. Thermoresponsive Behavior of Poly(acrylic acid- co-acrylonitrile) with a UCST. *Macromolecules* (2019) doi:10.1021/acs.macromol.9b00794.
218. Liang, X., Liu, F., Kozlovskaya, V., Palchak, Z. & Kharlampieva, E. Thermoresponsive Micelles from Double LCST-Poly(3-methyl-N-vinylcaprolactam) Block Copolymers for Cancer Therapy. *ACS Macro Lett.* **4**, 308–311 (2015).
219. Chen, J. *et al.* Light-Responsive Micelles Loaded With Doxorubicin for Osteosarcoma Suppression. *Front. Pharmacol.* **12**, 1–11 (2021).
220. Pearson, S. *et al.* Light-responsive azobenzene-based glycopolymer micelles for targeted drug delivery to melanoma cells. *Eur. Polym. J.* **69**, 616–627 (2015).
221. Shen, H., Zhou, M., Zhang, Q., Keller, A. & Shen, Y. Zwitterionic light-responsive polymeric micelles for controlled drug delivery. *Colloid Polym. Sci.* **293**, 1685–1694 (2015).
222. Yang, Z., Zou, H., Liu, H., Xu, W. & Zhang, L. Self-assembly and drug release control of dual-responsive copolymers based on oligo(ethylene glycol)methyl ether methacrylate and spiropyran. *Iran. Polym. J. (English Ed.* **28**, 39–49 (2019).
223. Chen, S. *et al.* Nanocomposites of Spiropyran-Functionalized Polymers and Upconversion Nanoparticles for Controlled Release Stimulated by Near-Infrared Light and pH. *Macromolecules* **49**, 7490–7496 (2016).
224. Chen, G., Qiu, H., Prasad, P. N. & Chen, X. Upconversion Nanoparticles_ Design, Nanochemistry, and.pdf. (2014).
225. Li, D., Ågren, H. & Chen, G. Near infrared harvesting dye-sensitized solar cells enabled by rare-earth upconversion materials. *Dalt. Trans.* **47**, 8526–8537 (2018).
226. Wu, S., Blinco, J. P. & Barner-Kowollik, C. Near-Infrared Photoinduced Reactions Assisted by Upconverting Nanoparticles. *Chem. - A Eur. J.* **23**, 8325–8332 (2017).
227. Yang, B., Chen, Y. & Shi, J. Exogenous/Endogenous-Triggered Mesoporous Silica Cancer Nanomedicine. *Adv. Healthc. Mater.* **7**, 1–19 (2018).
228. Watermann, A. & Brieger, J. Mesoporous silica nanoparticles as drug delivery vehicles in cancer. *Nanomaterials* **7**, (2017).
229. Liu, J. N., Bu, W. B. & Shi, J. L. Silica Coated Upconversion Nanoparticles: A Versatile Platform for the Development of Efficient Theranostics. *Acc. Chem. Res.* **48**, 1797–1805 (2015).
230. Ghimire, P. P. & Jaroniec, M. Renaissance of Stöber method for synthesis of colloidal particles: New developments and opportunities. *J. Colloid Interface Sci.* **584**, 838–865 (2021).
231. Shirshahi, V. & Soltani, M. Solid silica nanoparticles: Applications in molecular imaging. *Contrast Media Mol. Imaging* **10**, 1–17 (2015).
232. Liu, J., Bu, W., Pan, L. & Shi, J. NIR-Triggered Anticancer Drug Delivery by Upconverting Nanoparticles with Integrated Azobenzene-Modified Mesoporous Silica. *Angew. Chemie* **125**, 4471–4475 (2013).
233. Mahalingam, V., Vetrone, F., Naccache, R., Speghini, A. & Capobianco, J. A. Colloidal Tm3+/Yb3+-Doped LiYF4 nanocrystals: Multiple luminescence spanning the UV to NIR regions via low-energy excitation. *Adv. Mater.* **21**, 4025–4028 (2009).
234. Himmelstoß, S. F. & Hirsch, T. Long-Term Colloidal and Chemical Stability in Aqueous Media of NaYF4-Type Upconversion Nanoparticles Modified by Ligand-Exchange. *Part. Part. Syst. Charact.* **36**, (2019).
235. Andresen, E., Resch-Genger, U. & Schäferling, M. Surface Modifications for Photon-Upconversion-Based Energy-Transfer Nanoprobes. *Langmuir* **35**, 5093–5113 (2019).
236. Jiang, S. *et al.* Surface-functionalized nanoparticles for biosensing and imaging-guided therapeutics. *Nanoscale* **5**, 3127–3148 (2013).
237. Wang, C., Cheng, L. & Liu, Z. Drug delivery with upconversion nanoparticles for multi-functional targeted cancer cell imaging and therapy. *Biomaterials* **32**, 1110–1120 (2011).
238. Yan, B., Boyer, J. C., Branda, N. R. & Zhao, Y. Near-infrared light-triggered dissociation of block copolymer micelles using upconverting nanoparticles. *J. Am. Chem. Soc.* **133**, 19714–19717 (2011).
239. Cheng, R. *et al.* Light-Triggered Disruption of PAG-Based Amphiphilic Random Copolymer Micelles. *Langmuir* **31**, 7758–7763 (2015).
240. Xiang, J. *et al.* Near-infrared light-triggered drug release from UV-responsive diblock copolymer-coated upconversion nanoparticles with high monodispersity. *J. Mater. Chem. B* **6**, 3531–3540 (2018).
241. Wang, X. *et al.* Synthesis of Yolk-Shell Polymeric Nanocapsules Encapsulated with Monodispersed Upconversion Nanoparticle for Dual-Responsive Controlled Drug Release. *Macromolecules* **51**, 10074–10082 (2018).
242. Yan, K., Chen, M., Zhou, S. & Wu, L. Self-assembly of upconversion nanoclusters with an amphiphilic copolymer for near-infrared- and temperature-triggered drug release. *RSC Adv.* **6**, 85293–85302 (2016).
243. Xing, Q. *et al.* Near-infrared light-controlled drug release and cancer therapy with polymer-caged upconversion nanoparticles. *RSC Adv.* **5**, 5269–5276 (2015).
244. Mourdikoudis, S., Pallares, R. M. & Thanh, N. T. K. Characterization techniques for nanoparticles: Comparison and

complementarity upon studying nanoparticle properties. *Nanoscale* **10**, 12871–12934 (2018).
245. Moraes, D. da S., Biz, H. M. & Rocha, T. L. A. de C. Gold Nanoparticles Synthesis With Different Reducing Agents Characterized By Uv-Visible Espectroscopy and Ftir. 72–80 (2022) doi:10.5151/siintec2021-209032.
246. Marbella, L. E. & Millstone, J. E. NMR techniques for noble metal nanoparticles. *Chem. Mater.* **27**, 2721–2739 (2015).
247. Hwang, N. & Barron, A. R. BET Surface Area Analysis of Nanoparticles, The Connexions Project. 1–11 (2011).
248. Kunc, F. *et al.* Surface chemistry of metal oxide nanoparticles: NMR and TGA quantification. *Anal. Bioanal. Chem.* **414**, 4409–4425 (2022).
249. Zhu, Y. L., Lian, Y. M., Wang, J. K., Chen, Z. P. & Yu, R. Q. Highly Sensitive and Specific Mass Spectrometric Platform for miRNA Detection Based on the Multiple-Metal-Nanoparticle Tagging Strategy. *Anal. Chem.* **93**, 5839–5848 (2021).
250. Turiel-Fernández, D., Gutiérrez-Romero, L., Corte-Rodriguez, M., Bettmer, J. & Montes-Bayón, M. Ultrasmall iron oxide nanoparticles cisplatin (IV) prodrug nanoconjugate: ICP-MS based strategies to evaluate the formation and drug delivery capabilities in single cells. *Anal. Chim. Acta* **1159**, (2021).
251. Mineo, P. G. *et al.* Salinomycin-loaded PLA nanoparticles: drug quantification by GPC and wave voltammetry and biological studies on osteosarcoma cancer stem cells. *Anal. Bioanal. Chem.* **412**, 4681–4690 (2020).
252. Bhattacharjee, S. DLS and zeta potential - What they are and what they are not? *J. Control. Release* **235**, 337–351 (2016).
253. Reimer & Kohl. 9780387347585_Toc. *Springer Ser. Opt. Sci.* **5**, (2008).
254. Kuntsche, J., Horst, J. C. & Bunjes, H. Cryogenic transmission electron microscopy (cryo-TEM) for studying the morphology of colloidal drug delivery systems. *Int. J. Pharm.* **417**, 120–137 (2011).
255. Crouzier, L. *et al.* Development of a new hybrid approach combining AFM and SEM for the nanoparticle dimensional metrology. *Beilstein J. Nanotechnol.* **10**, 1523–1536 (2019).
256. Slater, T. J. A. *et al.* STEM-EDX tomography of bimetallic nanoparticles: A methodological investigation. *Ultramicroscopy* **162**, 61–73 (2016).
257. Girardot, M., D'Orlyé, F. & Varenne, A. Electrokinetic characterization of superparamagnetic nanoparticle-aptamer conjugates: Design of new highly specific probes for miniaturized molecular diagnostics. *Anal. Bioanal. Chem.* **406**, 1089–1098 (2014).
258. Ramírez-García, G., Trapiella-Alfonso, L., D'Orlyé, F. & D'Orlyé, A. Electrophoretic methods for characterizing nanoparticles and evaluating their bio-interactions for their further use as diagnostic, imaging, or therapeutic tools. *Capill. Electromigr. Sep. Methods* 397–421 (2018) doi:10.1016/B978-0-12-809375-7.00019-8.
259. Ramírez-García, G. *et al.* Functionalization and characterization of persistent luminescence nanoparticles by dynamic light scattering, laser Doppler and capillary electrophoresis. *Colloids Surfaces B Biointerfaces* **136**, 272–281 (2015).
260. d'Orlyé, F. & Reiller, P. E. Contribution of capillary electrophoresis to an integrated vision of humic substances size and charge characterizations. *J. Colloid Interface Sci.* **368**, 231–240 (2012).
261. Ewing, A. G., Ross, A. & Teresa, M. o. **61**, (1989).
262. Tagliaro, F., Manetto, G., Crivellente, F. & Smith, F. P. A brief introduction to capillary electrophoresis. *Forensic Sci. Int.* **92**, 75–88 (1998).
263. Voeten, R. L. C., Ventouri, I. K., Haselberg, R. & Somsen, G. W. Capillary Electrophoresis: Trends and Recent Advances. *Anal. Chem.* **90**, 1464–1481 (2018).
264. Kizilkaya, F. Investigation of Electroosmotic Flow Dynamics and Reproducibility in Capillary Electrophoresis. (2012).
265. Harstad, R. K., Johnson, A. C., Weisenberger, M. M. & Bowser, M. T. Capillary Electrophoresis. *Anal. Chem.* **88**, 299–319 (2016).
266. Ban, E., Yoo, Y. S. & Song, E. J. Analysis and applications of nanoparticles in capillary electrophoresis. *Talanta* **141**, 15–20 (2015).
267. Trapiella-Alfonso, L., Ramírez-García, G., d'Orlyé, F. & Varenne, A. Electromigration separation methodologies for the characterization of nanoparticles and the evaluation of their behaviour in biological systems. *TrAC - Trends Anal. Chem.* **84**, 121–130 (2016).
268. Ramírez-García, G. *et al.* Characterization of phthalocyanine functionalized quantum dots by dynamic light scattering, laser Doppler, and capillary electrophoresis. *Anal. Bioanal. Chem.* **409**, 1707–1715 (2017).
269. Trapiella-Alfonso, L., D'Orlyé, F. & Varenne, A. Recent advances in the development of capillary electrophoresis methodologies for optimizing, controlling, and characterizing the synthesis, functionalization, and physicochemical, properties of nanoparticles Young Investigators in Analytical and Bioanaly. *Anal. Bioanal. Chem.* **408**, 2669–2675 (2016).
270. Li, L., Yu, H., Liu, D. & You, T. A novel dark-field microscopy technique coupled with capillary electrophoresis for visual analysis of single nanoparticles. *Analyst* **138**, 3705–3710 (2013).
271. Davis, T. A., Patberg, S. M., Sargent, L. M., Stefaniak, A. B. & Holland, L. A. Capillary electrophoresis analysis of affinity to assess carboxylation of multi-walled carbon nanotubes. *Anal. Chim. Acta* **1027**, 149–157 (2018).
272. Liu, T. *et al.* Monitoring surface functionalization of dendrigraft poly-l-lysines via click chemistry by capillary electrophoresis and Taylor dispersion analysis. *J. Chromatogr. A* **1273**, 111–116 (2013).
273. Helle, A., Hirsjärvi, S., Peltonen, L., Hirvonen, J. & Wiedmer, S. K. Quantitative determination of drug encapsulation in poly(lactic acid) nanoparticles by capillary electrophoresis. *J. Chromatogr. A* **1178**, 248–255 (2008).
274. Franzen, U., Nguyen, T. T. T. N., Vermehren, C., Gammelgaard, B. & Østergaard, J. Journal of Pharmaceutical and Biomedical Analysis Characterization of a liposome-based formulation of oxaliplatin using capillary electrophoresis : Encapsulation and leakage. *J. Pharm. Biomed. Anal.* **55**, 16–22 (2011).
275. Nguyen, T. T. T. N., Østergaard, J., Stürup, S. & Gammelgaard, B. Determination of platinum drug release and liposome stability in human plasma by CE-ICP-MS. *Int. J. Pharm.* **449**, 95–102 (2013).
276. Otarola, J., Lista, A. G., Fernández Band, B. & Garrido, M. Capillary electrophoresis to determine entrapment efficiency of a nanostructured lipid carrier loaded with piroxicam. *J. Pharm. Anal.* **5**, 70–73 (2015).
277. Kepinska, M., Kizek, R. & Milnerowicz, H. Fullerene as a doxorubicin nanotransporter for targeted breast cancer therapy:

Capillary electrophoresis analysis. *Electrophoresis* **39**, 2370–2379 (2018).
278. Ansar, S. M., Jiang, W. & Mudalige, T. Direct quantification of unencapsulated doxorubicin in liposomal doxorubicin formulations using capillary electrophoresis. *Int. J. Pharm.* **549**, 109–114 (2018).
279. Ansar, S. M. & Mudalige, T. Direct and simultaneous determination of intra-liposomal and external sulfate in liposomal doxorubicin formulations by capillary electrophoresis/inductively coupled plasma-tandem mass spectrometry (CE/ICP-MS/MS). *Int. J. Pharm.* **561**, 283–288 (2019).
280. Chen, S., Jiang, F., Cao, Z., Wang, G. & Dang, Z. M. Photo, pH, and thermo triple-responsive spiropyran-based copolymer nanoparticles for controlled release. *Chem. Commun.* **51**, 12633–12636 (2015).
281. Zou, H. & Liu, H. Synthesis of thermal and photo dual-responsive amphiphilic random copolymer via atom transfer radical polymerization and its control release of doxorubicin. *Int. J. Polym. Mater. Polym. Biomater.* **66**, 955–962 (2017).
282. Chen, S., Liu, H., Hu, J., Zou, H. & He, Y. Self-assembly and morphology transition of amphipathic spiropyran-based random copolymers to control drug release. *Des. Monomers Polym.* **19**, 730–739 (2016).
283. Jacquin, M. *et al.* Characterization of amphiphilic diblock copolymers synthesized by MADIX polymerization process. *Macromolecules* **40**, 2672–2682 (2007).
284. Phimphachanh, A. *et al.* Characterization of Diblock Copolymers by Capillary Electrophoresis: From Electrophoretic Mobility Distribution to Distribution of Composition. *Macromolecules* **53**, 334–345 (2020).
285. Morel, A., Cottet, H., In, M., Deroo, S. & Destarac, M. Electrophoretic behavior of amphiphilic diblock copolymer micelles. *Macromolecules* **38**, 6620–6628 (2005).
286. Oukacine, F., Bernard, S., Bobe, I. & Cottet, H. Physico-chemical characterization of polymeric micelles loaded with platinum derivatives by capillary electrophoresis and related methods. *J. Control. Release* **196**, 139–145 (2014).
287. Buwalda, S. *et al.* Stabilization of poly(ethylene glycol)-poly(ε-caprolactone) star block copolymer micelles via aromatic groups for improved drug delivery properties. *J. Colloid Interface Sci.* **514**, 468–478 (2018).
288. Li, P. Y. *et al.* Self-assembly behavior of amphiphilic linear-block-dendritic copolymers with long subchains: Dependences on dendron generation and mixing dynamics. *J. Polym. Sci. Part A Polym. Chem.* **56**, 1446–1456 (2018).
289. Smart, T. *et al.* Block copolymer nanostructures One of the most important classes of synthetic systems for creating. *Nanotoday* **3**, 38–46 (2008).
290. Owen, S. C., Chan, D. P. Y. & Shoichet, M. S. Polymeric micelle stability. *Nano Today* **7**, 53–65 (2012).
291. Klajn, R. Spiropyran-based dynamic materials. *Chem. Soc. Rev.* **43**, 148–184 (2014).
292. Zirino, A. & Healy, M. L. w. **6**, 243–249 (1972).
293. Wang, Z. *et al.* Mechanisms of drug release in pH-sensitive micelles for tumour targeted drug delivery system: A review. *Int. J. Pharm.* **535**, 253–260 (2018).
294. Honda, S., Yamamoto, T. & Tezuka, Y. Tuneable enhancement of the salt and thermal stability of polymeric micelles by cyclized amphiphiles. *Nat. Commun.* **4**, 1574–1579 (2013).
295. Lee, A. S. *et al.* Structure of pH-dependent block copolymer micelles: Charge and ionic strength dependence. *Macromolecules* **35**, 8540–8551 (2002).
296. Annaka, M., Morishita, K. & Okabe, S. Electrostatic self-assembly of neutral and polyelectrolyte block copolymers and oppositely charged surfactant. *J. Phys. Chem. B* **111**, 11700–11707 (2007).
297. Chen, Y., Lu, Y., Lee, R. J. & Xiang, G. Nano encapsulated curcumin: And its potential for biomedical applications. *Int. J. Nanomedicine* **15**, 3099–3120 (2020).
298. Yu, L. X., Liu, Y., Chen, S. C., Guan, Y. & Wang, Y. Z. Reversible photoswitching aggregation and dissolution of spiropyran-functionalized copolymer and light-responsive FRET process. *Chinese Chem. Lett.* **25**, 389–396 (2014).
299. Niskanen, J. & Vapaavuori, J. Photobreathing Zwitterionic Micelles. *ChemSystemsChem* **1**, (2019).
300. Jochum, F. D. & Theato, P. Temperature- and light-responsive smart polymer materials. *Chem. Soc. Rev.* **42**, 7468–7483 (2013).
301. Yang, L. *et al.* A highly sensitive probe based on spiropyran for colorimetric and fluorescent detection of thiophenol in aqueous media. *Dye. Pigment.* **175**, 108154 (2020).
302. Nie, S. Y., Lin, W. J., Yao, N., Guo, X. D. & Zhang, L. J. Drug release from pH-sensitive polymeric micelles with different drug distributions: Insight from coarse-grained simulations. *ACS Appl. Mater. Interfaces* **6**, 17668–17678 (2014).
303. Letchford, K. & Burt, H. A review of the formation and classification of amphiphilic block copolymer nanoparticulate structures: micelles, nanospheres, nanocapsules and polymersomes. *Eur. J. Pharm. Biopharm.* **65**, 259–269 (2007).
304. Feng, Y. H., Zhang, X. P., Li, J. Y. & Guo, X. D. How is a micelle formed from amphiphilic polymers in a dialysis process: Insight from mesoscopic studies. *Chem. Phys. Lett.* **754**, 1–7 (2020).
305. Lu, Y., Zhang, E., Yang, J. & Cao, Z. Strategies to improve micelle stability for drug delivery. *Nano Res.* **11**, 4985–4998 (2018).
306. Yang, Z. *et al.* DPD simulations on mixed polymeric DOX-loaded micelles assembled from PCL-SS-PPEGMA/PDEA-PPEGMA and their dual pH/reduction-responsive release. *Phys. Chem. Chem. Phys.* **23**, 19011–19021 (2021).
307. Behera, S. K., Mohanty, M. E. & Mohapatra, M. A Fluorescence Study of the Interaction of Anticancer Drug Molecule Doxorubicin Hydrochloride in Pluronic P123 and F127 Micelles. *J. Fluoresc.* **31**, 17–27 (2021).
308. Washington, K. E., Kularatne, R. N., Biewer, M. C. & Stefan, M. C. Combination Loading of Doxorubicin and Resveratrol in Polymeric Micelles for Increased Loading Efficiency and Efficacy. *ACS Biomater. Sci. Eng.* **4**, 997–1004 (2018).
309. Huang, Y. *et al.* pH/reduction dual-stimuli-responsive cross-linked micelles based on multi-functional amphiphilic star copolymer: Synthesis and controlled anti-cancer drug release. *Polymers (Basel).* **12**, (2020).
310. Wang, J. *et al.* Polylactide-cholesterol stereocomplex micelle encapsulating chemotherapeutic agent for improved antitumor efficacy and safety. *J. Biomed. Nanotechnol.* **14**, 2102–2113 (2018).
311. Yar, Y. *et al.* Development of tailored SPION-PNIPAM nanoparticles by ATRP for dually responsive doxorubicin delivery and MR imaging. *J. Mater. Chem. B* **6**, 289–300 (2018).
312. Liang, K., Chung, J. E., Gao, S. J., Yongvongsoontorn, N. & Kurisawa, M. Highly Augmented Drug Loading and Stability of

Micellar Nanocomplexes Composed of Doxorubicin and Poly(ethylene glycol)–Green Tea Catechin Conjugate for Cancer Therapy. *Adv. Mater.* **30**, 1–8 (2018).
313. Zhang, G. *et al.* Doxorubicin-loaded folate-mediated pH-responsive micelle based on Bletilla striata polysaccharide: Release mechanism, cellular uptake mechanism, distribution, pharmacokinetics, and antitumor effects. *Int. J. Biol. Macromol.* **164**, 566–577 (2020).
314. Ordanini, S. & Cellesi, F. Complex polymeric architectures self-assembling in unimolecular micelles: Preparation, characterization and drug nanoencapsulation. *Pharmaceutics* **10**, (2018).
315. Yuan, X. *et al.* Novel fluorescent amphiphilic copolymer probes containing azo-tetraphenylethylene bridges for azoreductase-triggered release. *Mater. Chem. Front.* **3**, 1097–1104 (2019).
316. Lo, C. L., Huang, C. K., Lin, K. M. & Hsiue, G. H. Mixed micelles formed from graft and diblock copolymers for application in intracellular drug delivery. *Biomaterials* **28**, 1225–1235 (2007).
317. Kalva, N. *et al.* Degradable pH-responsive polymer prodrug micelles with aggregation-induced emission for cellular imaging and cancer therapy. *React. Funct. Polym.* **166**, (2021).
318. Zhao, C. *et al.* Synthesis and characterization of photo-responsive flower-like copolymer micelles with o-nitrobenzyl as the junction point. *Mater. Lett.* **261**, (2020).
319. Li, Y. *et al.* Polymeric micelles with aggregation-induced emission based on microbial ε-polylysine for doxorubicin delivery. *Eur. Polym. J.* **122**, (2020).
320. Karmegam, V., Kuruppu, S. S., Udamulle Gedara, C. M., Biewer, M. C. & Stefan, M. C. Enhanced DOX loading in star-like benzyl functionalized polycaprolactone micelles. *J. Polym. Sci.* **59**, 3040–3052 (2021).
321. Feng, W. *et al.* Self-Assembled Nanosized Vehicles from Amino Acid-Based Amphiphilic Polymers with Pendent Carboxyl Groups for Efficient Drug Delivery. *Biomacromolecules* **22**, 4871–4882 (2021).
322. Espinola-portilla, F., Orly, F., Trapiella-alfonso, L. & Guti, S. A deep understanding of the self-assembly and colloidal stability of light and pH dual-responsive spiropyran random copolymer micelle-like. **31**, (2022).
323. Galhano, J., Marcelo, G. A., Duarte, M. P. & Oliveira, E. Ofloxacin@Doxorubicin-Epirubicin functionalized MCM-41 mesoporous silica–based nanocarriers as synergistic drug delivery tools for cancer related bacterial infections. *Bioorg. Chem.* **118**, 105470 (2022).
324. Wang, S., Liu, Q., Li, L. & Urban, M. W. Recent Advances in Stimuli-Responsive Commodity Polymers. *Macromol. Rapid Commun.* **42**, 1–20 (2021).
325. Li, X., Zhao, D. & Zhang, F. Multifunctional upconversion-magnetic hybrid nanostructured materials: Synthesis and bioapplications. *Theranostics* **3**, 292–305 (2013).
326. Safaie, N. & Ferrier, R. C. Janus nanoparticle synthesis: Overview, recent developments, and applications. *J. Appl. Phys.* **127**, (2020).
327. Niu, X. *et al.* Thermoswitchable Janus Gold Nanoparticles with Stimuli-Responsive Hydrophilic Polymer Brushes. *Langmuir* **32**, 4297–4304 (2016).
328. Shaghaghi, B., Khoee, S. & Bonakdar, S. Preparation of multifunctional Janus nanoparticles on the basis of SPIONs as targeted drug delivery system. *Int. J. Pharm.* **559**, 1–12 (2019).
329. Yao, X., Jing, J., Liang, F. & Yang, Z. Polymer-Fe3O4 Composite Janus Nanoparticles. *Macromolecules* **49**, 9618–9625 (2016).
330. Lattuada, M. & Hatton, T. A. Synthesis, properties and applications of Janus nanoparticles. *Nano Today* **6**, 286–308 (2011).
331. Vilain, C., Goettmann, F., Moores, A., Le Floch, P. & Sanchez, C. Study of metal nanoparticles stabilised by mixed ligand shell: A striking blue shift of the surface-plasmon band evidencing the formation of Janus nanoparticles. *J. Mater. Chem.* **17**, 3509–3514 (2007).
332. Pottanam Chali, S. & Ravoo, B. J. Polymer Nanocontainers for Intracellular Delivery. *Angew. Chemie - Int. Ed.* **59**, 2962–2972 (2020).
333. Hpone Myint, K., Brown, J. R., Shim, A. R., Wyslouzil, B. E. & Hall, L. M. Encapsulation of nanoparticles during polymer micelle formation: A dissipative particle dynamics study. *J. Phys. Chem. B* **120**, 11582–11594 (2016).
334. Zavaleta, C., Ho, D. & Chung, E. J. Theranostic Nanoparticles for Tracking and Monitoring Disease State. *SLAS Technol.* **23**, 281–293 (2018).
335. Popescu, M.-T. & Tsitsilianis, C. Gold/Pentablock Terpolymer Hybrid Multifunctional Nanocarriers for Controlled Delivery of Tamoxifen: Effect of Nanostructure on Release Kinetics. *Molecules* **27**, 3764 (2022).
336. Upponi, J. R. *et al.* Polymeric micelles: Theranostic co-delivery system for poorly water-soluble drugs and contrast agents. *Biomaterials* **170**, 26–36 (2018).
337. Chung, Y. C., Yang, C. H., Lee, R. H. & Wang, T. L. Dual Stimuli-Responsive Block Copolymers for Controlled Release Triggered by Upconversion Luminescence or Temperature Variation. *ACS Omega* **4**, 3322–3328 (2019).
338. Li, M., Zhang, Q., Zhou, Y. N. & Zhu, S. Let spiropyran help polymers feel force! *Prog. Polym. Sci.* **79**, 26–39 (2018).
339. Ramírez-García, G., De La Rosa, E., López-Luke, T., Panikar, S. S. & Salas, P. Controlling trapping states on selective theranostic core@shell (NaYF4:Yb,Tm@TiO2-ZrO2) nanocomplexes for enhanced NIR-activated photodynamic therapy against breast cancer cells. *Dalt. Trans.* **48**, 9962–9973 (2019).
340. He, H. *et al.* Natural magnetite: An efficient catalyst for the degradation of organic contaminant. *Sci. Rep.* **5**, 1–10 (2015).
341. Karami, A. *et al.* Facile Multistep Synthesis of ZnO-Coated β-NaYF4:Yb/Tm Upconversion Nanoparticles as an Antimicrobial Photodynamic Therapy for Persistent Staphylococcus aureus Small Colony Variants. *ACS Appl. Bio Mater.* **4**, 6125–6136 (2021).
342. Chaki, S. H., Malek, T. J., Chaudhary, M. D., Tailor, J. P. & Deshpande, M. P. Magnetite Fe3O4 nanoparticles synthesis by wet chemical reduction and their characterization. *Adv. Nat. Sci. Nanosci. Nanotechnol.* **6**, (2015).
343. Omary, M. A. & Patterson, H. H. Luminescence, theory. *Encycl. Spectrosc. Spectrom.* 636–653 (2016) doi:10.1016/B978-0-12-803224-4.00193-X.
344. Ramírez-García, G. *et al.* Characterization of phthalocyanine functionalized quantum dots by dynamic light scattering, laser Doppler, and capillary electrophoresis. *Anal. Bioanal. Chem.* **409**, 1707–1715 (2017).

ANNEXE I. RÉSUMÉ GÉNÉRAL EN FRANÇAIS

Synthèse et caractérisation de nanomatériaux pour la délivrance contrôlée de médicaments en réponse à des stimuli externes

A1. Introduction

La chimiothérapie, qui est le traitement le plus utilisé pour guérir les maladies cancéreuses, provoque divers effets secondaires dus à la réaction incontrôlée des médicaments qui agissent sans distinction sur les cellules normales et cancéreuses. Pour éviter ces problèmes, des systèmes d'administration de médicaments (SAM) ont été mis au point. Avec l'aide des nanotechnologies, de nouvelles stratégies thérapeutiques permettent une libération contrôlée des médicaments, ce qui permet de surmonter les inconvénients des thérapies classiques.[1,2]

Pour cela, il existe différentes configurations de nanostructures comme les nanoparticules (NPs) qui ont été employées pour transporter des agents comme les vaccins, les médicaments, les gènes, les protéines et les enzymes.[3] Ces nanovecteurs sont des nanoparticules colloïdales dont la taille se situe entre 1 et 100 nanomètres (nm) de diamètre, qui peuvent être conçus à partir d'une variété de matériaux de différentes formes et tailles. Ils doivent offrir une bonne biocompatibilité, une longue période de circulation sanguine et surmonter le mécanisme endosome-lysosome, afin de leur conférer des caractéristiques uniques telles que l'amélioration de la biodistribution, de la pharmacocinétique, de la stabilité, de la solubilité et de la réduction de la toxicité.[4,5] Ces nanoparticules (NPs) peuvent être de nature organique, inorganique et hybride (combinaison de matériaux). Les nanovecteurs organiques, notamment les liposomes, les dendrimères, les nano-agrégats polymériques de type micelle et les polymères de nanotubes de carbone (CNT), peuvent vectoriser une variété de médicaments et de ligands pour une administration appropriée. Les nanovecteurs inorganiques, formés de métaux nobles, de semi-conducteurs, d'oxydes métalliques ou de lanthanides, tels que les nanoparticules d'or (GNP), les points quantiques (QD), les nanoparticules magnétiques (SPION), la silice mésoporeuse (MSNP) et les nanoparticules à conversion ascendante (UCNP), possèdent, selon leur nature, des effets thérapeutiques synergiques aux SAM classiques, comme les thérapies photodynamiques ou photothermiques. Les nanoparticules hybrides (HNP) combinent deux ou plusieurs parties organiques et inorganiques avec une activité additive ou synergique, ayant des configurations comme organique-inorganique, inorganique-inorganique, ou multi-composants. Parmi les exemples de ces nanosystèmes, citons les micelles lipidiques-polymères, céramiques-polymères, magnétiques-polymères, luminescentes UCNPs-polymères, etc.[6]

En outre, la formation de ces HNP intégrées dans un nanosystème unique pourrait fournir des fonctions diagnostiques et thérapeutiques simultanées en une seule dose, appelées "outils de theragnostique".[7] il est possible de suivre leur bio-distribution, de surveiller la progression et l'efficacité d'une thérapie, par une imagerie in vivo. En général, il existe deux approches pour former ces outils de diagnostic, soit en liant la surface d'une NP solide à une autre NP, soit en encapsulant une nanostructure dans une autre.[8] Puisqu'il est vital d'éviter les effets secondaires, les outils nanotheranostic doivent être spécifiques du site d’intérêt et donc intelligents. Pour ce faire, deux éléments doivent être pris en compte : (i) des nanomatériaux intelligents et sensibles aux stimuli qui permettent un transport efficace des médicaments anticancéreux afin de contrôler leur chargement et leur libération, et (ii) des propriétés de ciblage pour une arrivée efficace sur le site cancéreux en vue d'une action thérapeutique.[6] Certaines méthodes de conversion en nanoparticules intelligentes incluent la fonctionnalisation pour un ciblage spécifique des cellules cancéreuses, l'incorporation de parties sensibles aux stimuli et l'incorporation d'autres substances à co-délivrer[5]

Les nanoagrégats de type micelle sont des NPs à base de polymères qui peuvent fournir de bonnes propriétés stimuli-réactives pour leur conférer cette intelligence. Ils sont formés par un auto-assemblage de structure cœur-coquille d'un bloc amphiphile ou d'un copolymère de structure aléatoire en présence d'un milieu aqueux avec un cœur hydrophobe interne et une coquille hydrophile externe. Les copolymères aléatoires sont constitués de monomères liés de manière aléatoire dans une chaîne polymère donnée. Lorsqu'elles sont diluées dans une solution aqueuse, les molécules amphiphiles existent séparément en tant qu'unimères (chaîne polymère unique) tels les tensioactifs. Par augmentation de leur concentration, les unimères interagissent jusqu'à ce que leur agrégation se produise, en raison de leur saturation dans la solution aqueuse, à la concentration d'agrégation critique (CAC), où l'auto-pliage ou l'assemblage est réalisé à partir de pendants hydrophobes dans la chaîne polymère, stabilisés par les pendants hydrophiles.[9,10] Pour leur processus de formation, la dialyse est la méthode la plus couramment employée sur le mélange réactionnel, consistant en la dissolution du copolymère dans un solvant organique tel que le N,N-diméthyl-formamide (DMF), le diméthylsulfoxyde (DMSO) ou le tétrahydrofurane (THF), suivi de l'ajout goutte à goutte de solutions aqueuses, par exemple l'eau désionisée. Par le processus de purification par dialyse, le solvant organique sera progressivement déplacé. Pour le chargement des médicaments peu solubles au cœur de la micelle hydrophobe, le médicament et le copolymère sont dissous dans le solvant organique, et le processus est ensuite appliqué comme précédemment.[11,12]

Certains problèmes subsistent dans l'emploi d'agrégats de type micelle, comme par exemple la libération prématurée ou inadéquate de médicaments dans la circulation ou le tissu cible. ne manière très efficace d'obtenir une libération appropriée des médicaments chargés dans les nanostructures consiste utiliser des polymères intelligents sensibles aux stimuli comme précurseurs d'agrégats de type micelle.[13–16] L'exploitation des caractéristiques internes associées aux tumeurs cancéreuses (pH, enzymes, hypoxie, etc.) ainsi que des stimuli externes (lumière, magnétisme, température, etc.) permettrait de déstabiliser les agrégats de type micelle en réponse à ces stimuli et d'obtenir une libération contrôlée dans le temps et dans l'espace.[6] La différence de pH dans le milieu acide de la plupart des tumeurs solides (pH 6,5-7,2) a été largement exploitée pour activer les agrégats de type micelle sensibles au pH sur le site de la tumeur ou dans un organe spécifique et libérer le médicament. Dans ce processus, les groupes acides ou basiques pendants tels que les groupes carboxylate, sulfonate et amino dans les chaînes polymériques, lorsqu'ils sont protonés (en fonction du pKa), modifient la polarité du polymère de la chaîne (d'hydrophobe à hydrophile), ou/et ressentent la répulsion électrostatique de la chaîne pour provoquer le gonflement des nanoagrégats de type micelle.[17,18] Certains exemples de micelles polymères sensibles au pH sont le poly(2-(diisopropylamino)éthyl méthacrylate) (PDPAEMA), le poly(4-vinylpyridine) (P4VP), le poly(histidine) (PHis) et le poly(β-amino ester).[19] Dans les polymères sensibles à la lumière, la source d'irradiation de lumière UV est la plus utilisée en raison du grand nombre de polymères qui répondent à cette longueur d'onde.[20] Les processus de réaction photochimique des polymères sont les suivants : i) les polymères photoclivés d'unités photosensibles, ii) les polymères de photo-isomérisation, et iii) les polymères de photoréticulation/déréticulation.[21] Les composés photo-isomérisés réversibles comme l'azobenzène (AZO) et le spiropyrane (SP), sont généralement utilisés comme parties hydrophobes dans la synthèse de copolymères amphiphiles photosensibles. Ils s'auto-assemblent en agrégats de type micelle dans un milieu aqueux, et , sous l'effet de l'irradiation par la lumière UV, s'isomérisent dans leur forme de structure polaire, provoquant le désassemblage des nano-agregats et, par la suite, une libération efficace et contrôlée du médicament.[22]

Le spiropyrane (SP) est un composé organique non polaire photoréactif qui, lorsqu'il est exposé à la lumière UV (200-400 nm), subit une isomérisation cis-trans via l'ouverture du cycle sur le carbone spiro, formant un composé polaire stable appelé mérocyanine (MC). Ce composé zwitterionique MC, après le clivage de la liaison C-O au niveau de l'ouverture SP, contient un anion phénolate et un indolium chargé positivement, qui fournit un moment dipolaire beaucoup plus grand, ce qui lui confère un caractère hydrophile, contrairement à la forme hydrophobe non polaire SP.[23] Dans le spectre visible (500-600 nm), en raison d'un décalage significatif du spectre d'absorption de MC, il retourne à l'isomère SP dans un processus réversible. En outre, l'isomérisation SP de MC peut également présenter un acido-chromisme par rapport à un changement de pH, un thermo-chromisme et un solvato-chromisme, par complexation avec des cations métalliques qui peuvent stabiliser MC.[24] En ce qui concerne l'utilisation d'agrégats de type micelle sensibles aux stimuli, par exemple, *Zhi-Min Dang et ses collègues* ont rapporté une forme de micelle dans l'eau à partir d'un copolymère aléatoire amphiphile qui comprend un noyau de spiropyrane (SP) photosensible au pH et une enveloppe de N-isopropyl acrylamide (NIPAM) thermosensible. Sous irradiation UV, les nanoparticules auto-assemblées se sont dissociées par photo-isomérisation, libérant ainsi les molécules chargées. Dans des conditions acides, les NPs gonflent et libèrent également le médicament.[25]

Bien que les nanoagrégats de type micelle sensibles à la lumière UV présentent de nombreux avantages, des défis se posent, notamment i) une faible profondeur de pénétration qui rend inefficace la libération des médicaments dans les régions profondes du corps, et ii) des dommages tissulaires élevés dus à la phototoxicité. Cependant, les longueurs d'onde NIR et Vis (600-1000 nm) permettent à l'inverse une plus grande profondeur de pénétration dans les tissus car une fenêtre tissulaire optiquement transparente est définie dans cette région en raison d'une très faible absorption par les molécules de sang, d'eau et de mélanine.[20] Par conséquent, pour procéder à ce processus de photo-réaction UV vers les nanoagrégats de type micelle, les nanomatériaux ayant la capacité de convertir la lumière NIR en lumière UV-Vis, tels que les NPs à conversion ascendante (UCNPs) sont des candidats prometteurs pour les applications biomédicales.

Les UCNP ont la propriété de convertir un rayonnement NIR de faible énergie en un rayonnement de haute énergie, dans la gamme spectrale UV-Vis-NIR, par un phénomène connu sous le nom d'e conversion ascendante de photons.[26] Constituées d'une matrice hôte, d'un activateur et d'ions sensibilisateurs, dans le processus de conversion ascendante, le sensibilisateur et l'activateur, en tant qu'ions voisins, absorbent un photon d'énergie identique de son état fondamental à un état E1 métastable. Ensuite, le sensibilisateur transfère son énergie non radiative à l'activateur, qui passe à son niveau d'émission E2, suivi d'une relaxation du sensibilisateur à l'état fondamental. Enfin, l'ion activateur se relaxe et émet sa lumière de plus haute énergie.[27] Avec une phase hexagonale $NaYF_4$ comme matrice hôte, un ion sensibilisateur Yb^{3+} stimulé par la lumière NIR de (980 - 800 nm) et Tm^{3+} utilisé comme ion activateur,[28,29] les UCNP excitées par la lumière NIR, émettant une lumière UV-Vis, sont synthétisées par décomposition thermique ou hydrothermale/solvothermique.[30] Par exemple, dans l'étude qui a inspiré ce projet de doctorat, *Xin Zhao et ses collaborateurs* ont préparé un nanosystème à conversion ascendante composé d'un UCNP encapsulé au cœur d'un nanoagrégat de type micelle de polyspiropyrane à pH 4. 5 et/ou une irradiation NIR pour fournir un processus de déplacement hydrophobe-hydrophile du spiropyrane grâce aux phénomènes de conversion ascendante des UCNP. Par irradiation de la lumière NIR, celle-ci est absorbée par l'UCNP émettant de la lumière UV pour son absorption ultérieure par le composé SP pour commencer la photo-isomérisation.[31]

D'autre part, les outils de nanotheranostic pour le marquage simultané des cellules, le ciblage *in-vivo* du cancer ont suscité un grand intérêt grâce à la combinaison de nanostructures magnétiques et luminescentes formant des NPs hybrides à l'aide de SiO_2, Au, Fe_2O_3, TiO_2 et de UCNP.[32] Dans la plupart des cas, des NPs magnétiques-luminescentes à structure Core-Shell[33–36] sont synthétisées, mais elles sont confrontées à plusieurs défis qui limitent leurs applications car les propriétés luminescentes et magnétiques peuvent être fortement réduites. Par exemple, la coquille magnétique pourrait absorber et bloquer la lumière d'excitation et la luminescence à conversion ascendante, ce qui réduirait les rendements quantiques des UCNPs[37], et inversement, la coquille de luminescence à conversion ascendante pourrait interférer avec l'interaction entre le noyau magnétique et un champ magnétique incident.

Par conséquent, le principal défi dans ce domaine est non seulement de développer des méthodes reproductibles et faciles pour obtenir des nanostructures magnéto-luminescentes, mais aussi de fabriquer facilement des échantillons de nanoparticules asymétriques présentant une luminescence par conversion ascendante ou des propriétés magnétiques élevées. Ainsi, grâce à la combinaison des propriétés magnétiques et de luminescence, les NPs de type Janus (JNPs) seront probablement une meilleure structure applicable comme outil de nanotheranostic. Les nanoparticules de Janus sont ainsi nommées en référence à Janus, le dieu romain des portes, typiquement représenté comme ayant deux visages. Comme la divinité antique, les JNP ont également deux visages, chacun d'entre eux ayant une chimie, une taille, une morphologie, un matériau, etc. différents.[38] Une méthode générale pour leur préparation est la séparation de phase avec des mécanismes de nucléation homogènes-hétérogènes[39] qui consistent en la croissance épitaxiale d'une particule à partir de la surface d'une autre, généralement la première NP fonctionnant comme une graine dans laquelle l'incompatibilité de réseau rend difficile pour le second matériau de former une structure stable cœur-coquille, favorisant alors la formation d'un hétérodimère.[40]

Par conséquent, les HNP combinant des nanoparticules inorganiques avec des nanoagrégats de type micelle sont potentiellement d'excellents outils de délivrance de médicaments et de sondes d'imagerie, qui combinent aussi la possibilité de générer des thérapies telles que la photothermie ou la photodynamique. Pour convertir ces nanocomposites en nanovecteurs intelligents, ils doivent être dirigés vers la cible spécifique target.[5] À cette fin, l'ajout de fractions magnétiques (MNP) pour un guidage externe à la décoration des nanocomposites doit être envisagé.[41]

Par conséquent, afin de développer des nanovecteurs theranostic pour une administration intelligente de médicaments via un transport magnétique et un diagnostic par imagerie, de nouveaux nanosystèmes hybrides intelligents doivent être conçus. Au vu de la littérature, nous souhaitons combiner les propriétés de luminescence et de magnétisme des JNPs,, par leur encapsulation dans des nanoagrégats de type micelle composés d'un copolymère rando amphiphile Poly(NIPAM-co-SPMA , qui réagissent à des stimuli tels que le pH et la lumière.

De plus, une bonne compréhension des interactions physico-chimiques du chargement et de la délivrance contrôlée de médicaments par ces nanosystèmes, est nécessaire pour optimiser leur leur composition, taille, géométrie et fonctionnalisation. A ce jour, la capacité de chargement et de libération de médicaments des nanovecteurs a été évaluée par des méthodologies classiques basées sur la spectroscopie UV-Vis, la spectroscopie de fluorescence et la HPLC. Cependant, l'électrophorèse capillaire (EC) peut être une excellente méthode analytique pour mieux comprendre les interactions entre les médicaments modèles et les nanoparticules, y compris les agrégats de type micelle et les nanovecteurs hybrides.

L'objectif de ce projet de doctorat est de synthétiser et de caractériser des nanomatériaux hybrides inorganiques magnéto-luminescents de type Janus recouverts d'un copolymère sensible à la lumière et au pH pour le suivi des maladies ainsi que pour l'administration intelligente et la libération contrôlée de principes actifs de manière ciblée. Pour cela, nous avons dans un premier temps effectué et optimisé la synthèse d'agrégats de type micelle composés d'un copolymère amphiphile sensible à la lumière et au pH. Puis nous avons développé une stratégie de caractérisation de ces nano-objets par différentes méthodes analytiques. Ensuite, la capacité de chargement de médicaments modèles par ces nano-agrégats et leur libération contrôlée par irradiation lumineuse et/ou changement de pH, ont été étudiées avec la combinaison de ces méthodes analytiques. Enfin, la synthèse et la caractérisation de nanoparticules inorganiques hybrides de type Janus avec des fractions magnétiques et de conversion ascendante ont été réalisées. Elles ont ensuite été encapsulées conjointement à un médicament modèle dans l'agrégat de type micelle et une caractérisation fine de leur capacité de chargement de ce médicament ainsi que sa libération sous stimuli d'irradiation de lumière et/ou de changement de pH a été effectuée.

A2. Résultats et discussion

Les travaux ont été menés par une construction étape par étape des différents éléments du nanovecteur final : la synthèse et l'optimisation de l'auto-assemblage de copolymères aléatoires en agrégats de type micelle en milieu physiologique a d'abord été effectuée ; en parallèle, des méthodologies électrocinétiques pour la détermination des propriétés physicochimiques des agrégats de type micelle, ainsi que l'effet de deux stimuli sur leur structure, ont été développées ; les nanostructures agrégées ont ensuite été évaluées pour leur propriété de vectorisation d'agents cancérigènes (dans notre cas la doxorubicine) avec une quantification des phénomènes de chargement maximum du médicament et sa libération contrôlée par les stimuli de changement de pH et d'irradiation; la synthèse et la caractérisation de nouvelles nanoparticules hybrides de type Janus avec des fractions magnétiques à conversion ascendante pour le guidage in-vivo du nanosystème et la génération d'un stimulus interne; enfin, les nanosystèmes finaux ont été conçus par l'encapsulation de ces nanoparticules hybrides dans les agrégats de type micelle et leur capacité de chargement du médicament et de la libération contrôlée du médicament en réponse au pH et à l'irradiation lumineuse ont été quantifiées.

A2.1. Formation de nanoagrégats de type micelle de copolymère aléatoire de spiropyranne à double réponse à la lumière et au pH

Les agrégats de type micelle (Mic) ont été réalisés en dissolvant tout d'abord 2 mg de poly(NIPAM-co-SPMA) dans 1 mL de THF. Une solution tampon phosphate (PBS) (pH 7,4 et F.I. 25 mM) a ensuite été ajoutée en deux étapes comme suit : le premier mL à un taux de 1 µL.s-1 sous agitation vigoureuse (1100 rpm) suivi d'une addition rapide de 9 mL ; la solution finale a été agitée à 1100 rpm pendant 7 heures. Enfin, le THF et les résidus de la réaction ont été éliminés par dialyse (seuil de coupure de 10 kDa) avec du PBS (pH 7,4 et F.I. 25 mM) à température ambiante pendant 24 h. Les échantillons ont été conservés dans des flacons ambrés à 8°C pour les analyses ultérieures.

Après la synthèse du copolymère statistique Poly(NIPAM-co-SPMA), pour contrôler la taille et la stabilité des agrégats de type micelle, leur formation a d'abord été réalisée dans l'eau en faisant varier le temps d'agitation dans la gamme de 2 à 15 h, et la concentration en copolymère dans la gamme de 0,1 à 0,5 g.L^{-1}. Pour le copolymère employé dans cette étude, il est connu que la formation de micelles doit être réalisée à une vitesse d'agitation rapide (supérieure à 800 r.p.m.) [288] et à une température inférieure à 40°C (inférieure à la température de solution critique inférieure du copolymère 38°C[280]). Par conséquent, l'agitation et la température ont été fixées à 1000 r.p.m. et 36°C, respectivement, pour toutes les expériences. Les différents lots ont été caractérisés par analyse DLS dans le même milieu de solubilisation pour estimer la taille moyenne des agrégats de type micelle. Le diamètre hydrodynamique, l'indice de polydispersité (PDI), la largeur du pic et la déviation standard sont présentés dans le tableau A2.1.

Table A2.1 Résultats DLS pour l'optimisation de la formation d'agrégats de type micelle en fonction de la concentration en polymère (à un temps d'agitation de 7h) et du temps d'agitation (à une concentration de 0,2 mg.mL^{-1}).

Concentration (mg.mL-1)	D_H [a] (nm)	PDI [b]	Std Dev (n=3) [c]	Peak with (nm)
0.1	125	0.302	3	20
0.2	**124**	**0.361**	**3**	**20**
0.3	193	0.547	8	6.2
	25		5	92

Temps d'agitation (h)	D_H[a] (nm)	PDI [b]	Std Dev (n=3) [c]	Peak with (nm)
2	36 294	0.557	3 4	5 141
5	358	0.598	33	236
7	**126**	**0.361**	**2**	**78**
15	110 718	0.552	28 14	111 884

[a] Diamètre hydrodynamique

[b] Indice de polydispersité

[c] Déviation standard (3 répétitions)

L'étude a été menée dans une gamme de concentration en copolymère de 0,1 à 0,5 g.L^{-1}, avec un temps d'agitation de 7h. Une membrane polymère a été visuellement observée uniquement à une concentration en copolymère de 0,5 g.L^{-1}, phénomène attendu compte tenu que cette concentration est supérieure à la concentration d'agrégation critique (CAC) .[289] Pour des concentrations de polymère de 0,1 et 0,2 g.L^{-1}, une seule population d'agrégats a été mise en évidence (diamètre hydrodynamique de 125 ± 3 et 124 ± 2 nm, respectivement) avec une distribution de taille étroite, ce qui est cohérent pour une concentration inférieure au CAC. D'autre part, en travaillant à 0,3 g.L^{-1}, deux populations ont été mises en évidence (193 ± 8 nm et 25 ± 5 nm) probablement en raison d'une restructuration des structures agrégées à cette concentration avec une transition vers des structures membranaires observées à et 0,5 g.L^{-1}. Ainsi, pour les expériences ultérieures, la concentration a été fixée à 0,2 g.L^{-1}. En ce qui concerne le paramètre temps d'agitation, les analyses par DLS ont montré la présence d'une ou deux populations, avec des diamètres hydrodynamiques allant de 36 ± 3 nm à 718 ± 14 nm, avec un PDI entre 0,3 et 0,6. Pour des temps d'agitation de 2h et 15h, deux populations ont été mises en évidence lors de la mesure de l'intensité des pics (diamètres hydrodynamiques de 36/294 nm et 110/718 nm, respectivement). Une seule population (la plus petite) a été mise en évidence lors de la mesure du nombre de particules alors que deux populations sont visibles par mesure de l'intensité, en cohérence avec le fait que la mesure en intensité donne un poids plus élevé aux plus gros objets. Ce résultat indique la formation de deux structures de taille différente. Pour des temps d'agitation de 5 et 7 heures, un seul signal a été mis en évidence (358 ± 33 et 126 ± 2 nm respectivement). Un temps d'agitation de 7 heures a permis d'obtenir la taille modale et la PDI de la population d'agrégats la plus petite. Ce temps d'agitation a été sélectionné pour des études ultérieures.

L'influence de la force ionique sur l'auto-assemblage du copolymère amphiphile aléatoire Poly(NIPAM-co-SPMA) a été étudiée en utilisant des tampons de phosphate de sodium de pH 7,4 à différentes forces ioniques : 100mM (Mic100), 50mM (Mic50), et 25mM (Mic25), comme milieu de formation. Des caractérisations de ces objets par électrophorèse de zone capillaire, DLS et TEM ont été effectuées en parallèle afin de comprendre en profondeur leurs propriétés physico-chimiques et d'optimiser la formation de ces structures (Figure A2.1.1).

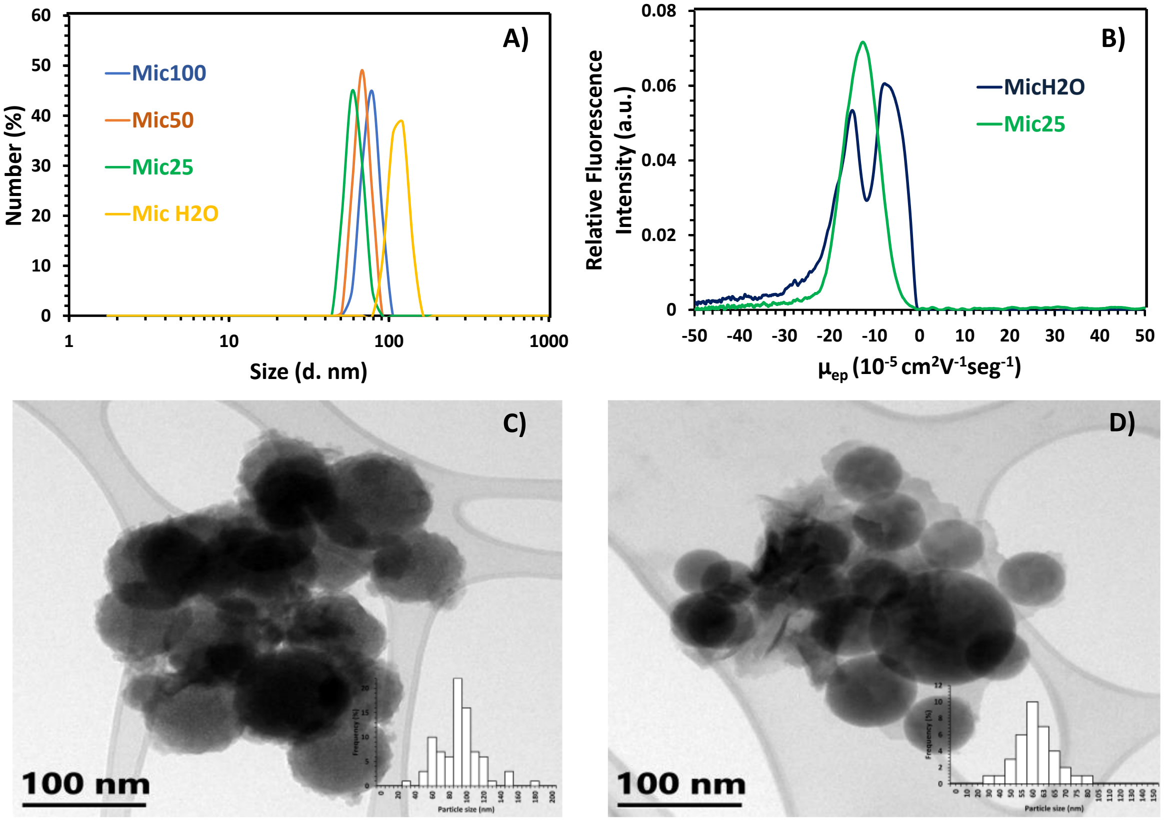

Figure A2.1.1 Effet de la force ionique sur le diamètre hydrodynamique DLS (A) et les profils électrophorétiques (B) des agrégats de type micelle, dans du PBS 25 mM (pH 7.4). Images TEM (histogrammes de distribution de taille en médaillon) de MicH2O (C) et Mic25 (D).

Le diamètre hydrodynamique de MicH$_2$O est plus élevé (126 nm ± 2, PDI 0,361) que ceux de Mic100 (91 ± 9 nm, PDI 0,565), Mic50 (67 ± 1 nm, PDI 0,414) et Mic25 (61 ± 2 nm, PDI 0,365) obtenus dans un tampon PBS de pH 7,4 (figure A2.1.1 A). Notons que le pH de la solution eau utilisée pour la synthèse de MicH$_2$0 est d'environ 5,6.[292] Les agrégats de type micelle synthétisés dans l'eau sont donc soumis à une force ionique très faible et un pH plus acide que dans le tampon PBS. Des travaux ont montré qu'à ce pH, leur gonflement apparait[293] car les blocs SPMA sensibles au pH (pKa 6-7)[291] ont tendance à s'étirer vers le solvant après protonation.[294] L'augmentation de la force ionique du

PBS génère une augmentation du diamètre hydrodynamique lié à une diminution de la solubilité du polymère précurseur, ce qui favorise les structures agrégées intégrant un plus grand nombre de copolymères au noyau, ce qui donne des objets plus grands.[295,296] La taille de population modale la plus faible (61 nm) et la valeur PDI (0,365) sont trouvées pour Mic25, ce qui indique un équilibre de formation de structures agrégées mieux contrôlé. La caractérisation par électrophorèse capillaire (CE) a été réalisée sur MicH2O et Mic25 (Figure A2.1.1 B) en utilisant un électrolyte de séparation (BGE) 25 mM PBS (pH 7,4), avec détection UV-visible et fluorescence. MicH2O présente un profil électrophorétique avec deux pics non résolus à une mobilité électrophorétique de -16x10-5 ± 2 et -7x10-5 ± 3 $cm^2V^{-1}s^{-1}$ alors que Mic25 (synthétisé dans le même tampon que l'électrolyte de séparation) présente un pic à -13x10-5 $cm^2V^{-1}s^{-1}$± 0,5. Les deux pics de MicH_2O pourraient être dus au transfert d'agrégats de type micelle de l'eau (milieu de synthèse) vers le PBS 25 mM (milieu de séparation), lié à une différence de conductivité entre la zone de l'échantillon (eau) et le milieu de séparation PBS 25 mM. Les mobilités électrophorétiques de MicH_2O et Mic25 sont similaires, alors que le diamètre hydrodynamique de MiCH_2O (mesuré par DLS dans leur milieu de formation) est deux fois supérieur à celui de Mic25, ce qui devrait indiquer des structures différentes selon le milieu de solubilisation, comme décrit précédemment. De plus, la morphologie et la taille des agrégats formés MicH2O (80 - 100 nm) et Mic25 (55 - 60 nm) déterminés par TEM dans la Figure A2.1.1 C) et la Figure A2.1.1 D) respectivement, montrent des morphologies sphériques ainsi qu'une tendance à la diminution du diamètre lorsque la formation des agrégats a lieu dans du PBS. Par conséquent, Mic25 a démontré un meilleur contrôle des structures agrégées en termes de taille, de polydispersité et de stabilité thermodynamique.

L'influence des conditions d'analyse de la Mic25 a ensuite été étudiée par DLS et CE dans du PBS pH 7.4 avec différentes forces ioniques (25, 50, et 100 mM). Les diamètres de la Mic25 mesurés par DLS sont de 64 ± 2 nm (PDI 0,365), 60 ± 3 nm (PDI 0,536) et 58 ± 5 nm (PDI 0,475) pour des forces ioniques de 25 mM, 50 mM et 100 mM respectivement, ce qui révèle de légères différences dans les diamètres hydrodynamiques. D'autre part, les mobilités électrophorétiques diminuent en valeur absolue lorsque la F.I. du BGE augmente ($-13x10^{-5}$ $cm^2V^{-1}s^{-1}$, $-8x10^{-5}$ $cm^2V^{-1}s^{-1}$ and $-6.5x10^{-5}$ $cm^2V^{-1}s^{-1}$ pour des F.I. de 25, 50 et 100 mM, respectivement). Cette évolution en conjonction avec la diminution de l'intensité de fluorescence est probablement liée à une modification de la structure auto-assemblée du noyau, montrant l'influence de la force ionique sur l'auto-assemblage de Mic25.

L'influence de l'irradiation sur la structure agrégée de type micelle a été effectuée par DLS, en irradiant Mic25 (Figure A2.1.2 A) montrant une augmentation des diamètres sphériques équivalents des agrégats de type micelle sous irradiation UV de 65 ± 2 nm (PDI 0,365) à 128 ± 3 nm (PDI 0,667), respectivement. D'autre part, les mesures de potentiel zeta par LDE (Figure A2.1.2 B) n'ont pas montré de différence significative dans la charge électrique du composé avant (un pic déformé dans le domaine de -1 à -20 mV) ou après (un pic symétrique à -7 mV) irradiation UV. La micrographie TEM avant irradiation UV (Figure A2.1.1 D) montre une morphologie sphérique avec une petite distribution de taille (rayon solide : 60 nm ± 2) et une dispersion apparente. En revanche, après 15 min d'irradiation UV (Figure A2.1.2 C), la géométrie observée pourrait être liée à une désagrégation partielle des Mic25. Ainsi, la caractérisation combinée par DLS, LDE et TEM met en évidence l'impact d'une irradiation UV de 15 min sur la structure de la Mic25, avec une mise en évidence de l'augmentation du diamètre sphérique équivalent de la structure en solution sans modification significative du potentiel zêta mesuré et d'une modification de la nanostructure par TEM.

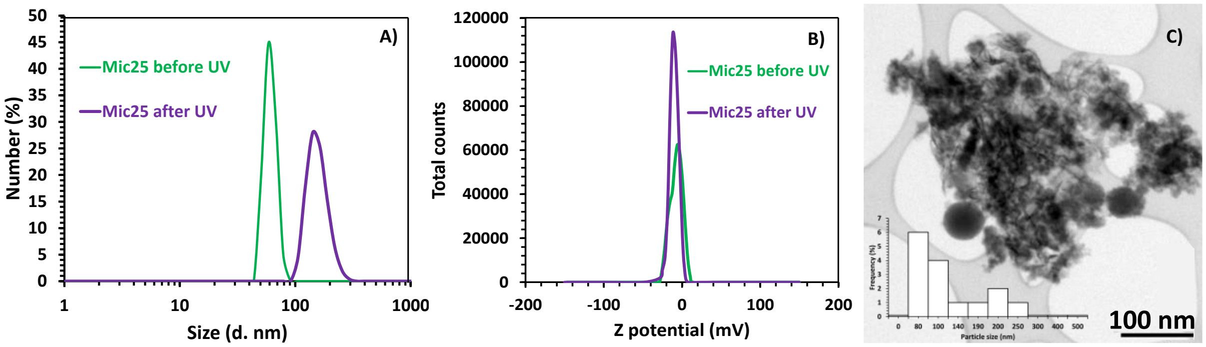

Figure A2.1.2 Effet de la lumière sur le diamètre hydrodynamique mesuré par DLS (A), la densité de charge superficielle mesurée par LDE (B) sur Mic25. Image TEM de Mic25 après 15 min d'irradiation par lumière UV 365 nm (C).

Pour l'étude des stimuli de pH, les Mic25 ont été analysés dans du PBS (pH 7.4), du PBS (pH 6) et du tampon acétate (ABS, pH 4), tous à une force ionique de 25 mM. La figure A2.1.3 A) présente les électrophérogrammes à ces 3 valeurs de pH : alors qu'un profil électrocinétique assez gaussien a été observé à pH 7,4, un profil présentant des pics non résolus d'intensité diminuée et des valeurs de mobilité réduites a été observé à pH 6. A pH 6, l'évolution pourrait être expliquée par (1) une possible extinction de la fluorescence lorsque le pH diminue en raison de la protonation de la structure spiropyrane (SP-H) [301], et/ou (2) le phénomène de gonflement de ces micelles[293] conduisant à une polydispersité de l'échantillon qui commence à se désagréger. À pH 4, aucun signal de micelle n'a pu être détecté, puisque les micelles à ce pH devraient être désagrégées, ce qui montre le potentiel de cette structure pour la libération de médicaments dans des environnements acides. D'autres études ont été réalisées en combinant les stimuli de pH et UV. Après irradiation UV de Mic25 (Figure A2.1.3 B), le profil électrophorétique à pH 7,4 montre un profil dissymétrique avec un petit chevauchement et une mobilité légèrement réduite caractéristique d'une déstabilisation de la structure agrégée, cohérente avec une désagrégation partielle mise en évidence par TEM et une augmentation de la taille sphérique équivalente mesurée en DLS. Lorsque la séparation est effectuée à pH 6, les échantillons irradiés caractérisés montrent une diminution plus prononcée de l'intensité du pic électrophorétique avec un déplacement vers des mobilités électrophorétiques plus faibles en valeur absolue qui prouvent que la lumière UV renforce l'effet du pH en ce qui concerne la désagrégation des micelles. Encore une fois, à pH 4, aucune détection des micelles n'a pu être obtenue comme prévu, que ce soit pour les échantillons irradiés ou non irradiés. Les effets synergiques combinés des stimuli pH (à pH 6) et UV ont également été analysés par TEM. Lorsqu'il est dispersé dans un milieu à pH 6, Mic25 présente (Figure A2.1.3 C) un mélange d'objets sphériques de plus grand diamètre (120 à 250 nm) que pour les agrégats de type micelle caractérisés à pH 7,4 (60 nm), combiné à des structures apparemment désagrégées. Comme expliqué précédemment, les micelles à un pH plus acide commencent à gonfler. En effet, les chaînes de SPMA, sensibles au pH, ont tendance à s'étirer après protonation vers le solvant. [302] Après avoir irradié l'échantillon avec de la lumière UV, la figure A2.1.3 D) montre une structure amorphe totalement désagrégée avec une distribution de taille polydispersée (150 - 400 nm). Ce résultat confirme que les deux effets, gonflement et désagrégation, peuvent être contrôlés par le changement de pH et l'irradiation UV.

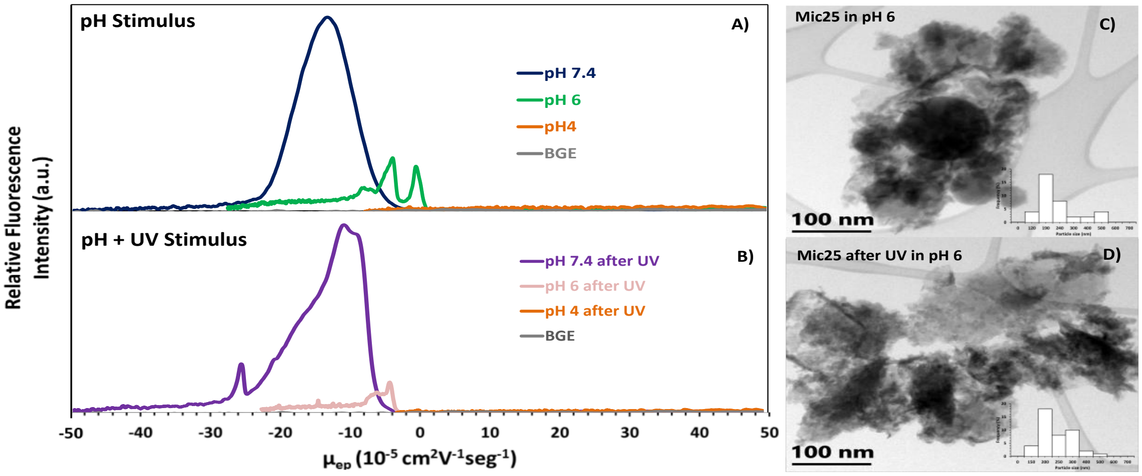

Figure A2.1.3 A) Effet pH et B) double effet pH - lumière UV profils électrophorétiques de Mic25 (BGE PBS F.I. pH : 7,4 et 6 - BGE ABS pH 4 I.S. 25mM). C) Effet pH et D) double effet pH-Lumière images TEM (histogrammes de distribution de taille en médaillon) de Mic25 (15 min 365 nm d'irradiation UV).

La figure A2.1.4 montre la variation morphologique des micelles sous différents stimuli. En bref, après avoir optimisé la formation des micelles dans un milieu PBS 25 mM pH 7,4, en obtenant des micelles de plus petite taille, lorsqu'elles sont irradiées par la lumière UV, bien qu'il soit connu qu'il y a une réversibilité dans l'isomérisation du composé spiro d'hydrophobe (SP) à hydrophobe (MC) et vice versa lorsqu'il est irradié par la lumière Vis, les micelles ne subissent pas de réversibilité structurelle. L'irradiation UV permet la désagrégation, mais lorsque l'irradiation est arrêtée, la tentative de ré-agrégation micellaire est incontrôlée, générant des amas d'agrégats. Lorsque le pH passe à un pH plus acide (pH 6), le composé SP est protoné, ce qui provoque un gonflement micellaire réversible. D'autre part, à ce pH, lorsqu'on irradie de la lumière UV, la désagrégation est visible et lorsque l'irradiation est arrêtée, la réagrégation redevient incontrôlée, formant des amas micellaires.

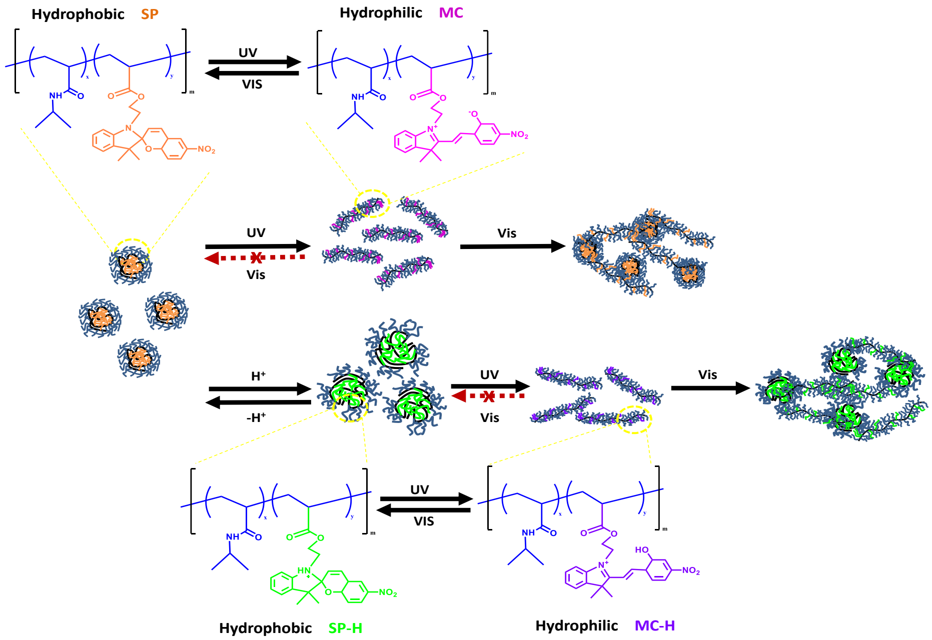

Figure A2.1.4 Représentation schématique des variations moléculaires et morphologiques des micelles sous stimulus pH - lumière UV.

A2.2. Études sur le chargement et la libération de la doxorubicine par des nanoagrégats de type micelle sensibles à la lumière et au pH.

Deux formes chimiques du médicament modèle doxorubicine ont été étudiées pour être incorporées pendant la formation du Mic à deux étapes différentes en fonction de leur solubilité correspondante, comme le montre la figure A2.2.1. Pour l'incorporation de la forme hydrophile, le chlorhydrate de doxorubicine (Dox-HCl) (concentrations de 2,0, 3,5 ou 5,0 µM) a été dissous dans une solution tampon phosphate (PBS) (pH 7,4 et F.I. 25 mM) et ajouté à la solution de poly(NIPAM-co-SPMA) dans le THF. Pour l'incorporation de la forme peu soluble dans l'eau, la doxorubicine (Dox) a été dissoute dans 1 mL de THF à des concentrations similaires, puis mélangée au poly(NIPAM-co-SPMA). Dans les deux cas, les autres paramètres ont été conservés comme pour la synthèse sans doxorubicine.

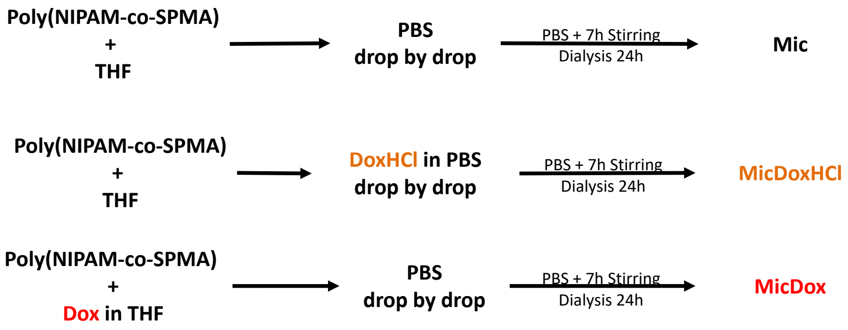

Figure A2.2.1 Processuspour la formation d'agrégats de type micelle (Mic) et l'incorporation de DoxHCl (MicDoxHCl) ou de Dox (MicDox).

La figure 2.2.2 A) montre les profils de distribution des diamètres hydrodynamiques déterminés par DLS des agrégats de type micelle formés en l'absence (Mic) ou en présence (MicDoxHCl) de DoxHCl à différentes concentrations de charge (2, 3,5 et 5 µM) dans du PBS. Il est montré une augmentation de la taille des agrégats en fonction de la concentration de DoxHCl, allant de 61 ± 2 nm (largeur de pic 28 nm) pour Mic, à 122 ± 3 nm (largeur de pic 46 nm), 140 ± 9 nm (largeur de pic 45 nm) et 143 ± 1 nm (largeur de pic 58 nm) pour MicDoxHCl à des concentrations de DoxHCl de 2,0, 3,5 et 5,0 µM, respectivement. Une nette augmentation de la taille des agrégats de type micelle a également été démontrée par TEM. Les figures 2.2.2 B) et C) comparent les images TEM de Mic et MicDoxHCl 5 µM respectivement, montrant des objets sphériques avec des diamètres solides modaux changeant de 18 nm à 25 nm, respectivement, logiquement inférieurs aux diamètres hydrodynamiques. Cette variation de taille observée à la fois avec l'analyse DLS et TEM corrobore l'incorporation du DoxHCl dans Mic. De plus, il semble qu'à des concentrations supérieures à 3,5 µM, la taille des agrégats de type micelle tend à se stabiliser, ce qui signifie une possible saturation de la micelle avec le médicament (capacité de charge maximale).

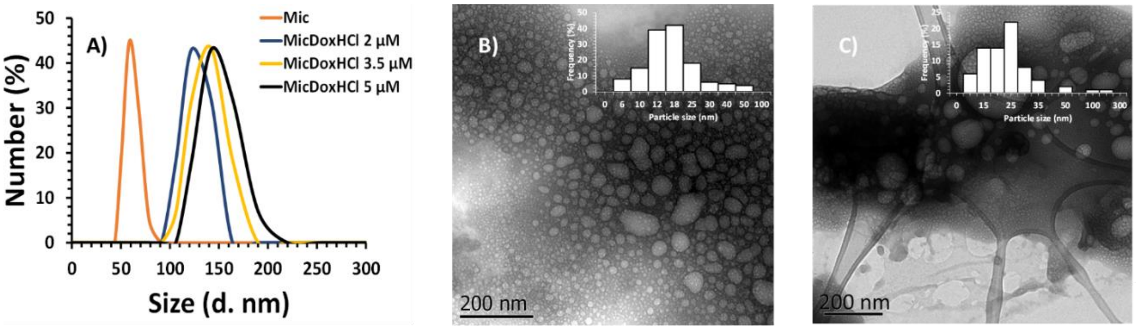

Figure A2.2.2 A) Effet de la concentration de DoxHCl sur le diamètre hydrodynamique des agrégats de type micelle (PBS pH 7,4 ; I.S. 25mM). Images TEM de B) Mic et C) MicDoxHCl 5µM.

La figure A2.2.3 A) montre les électrophérogrammes de Mic et de DoxHCl 1 µM dans du PBS 25 mM pH 7,4, identifiant un seul pic pour chaque échantillon. La mobilité électrophorétique de Mic a été calculée à -11 x 10-5 $cm^2V^{-1}s^{-1}$, ce qui est cohérent avec les résultats précédents[322], avec une valeur négative due au pKa (entre 6 et 7) de la molécule de SPMA.[23] La mobilité électrophorétique de DoxHCl, évaluée à +8 x 10-5 $cm^2V^{-1}s^{-1}$, est cohérente avec son premier pKa à 8,2[323], dû au groupe amino.

La figure A2.2.3 B) présente les électrophérogrammes des agrégats de type micelle formés en présence de DoxHCl à 2 µM (MicDoxHCl 2,0 µM), 3,5 µM (MicDoxHCl 3,5 µM) et 5 µM (MicDoxHCl 5,0 µM) dans du PBS, ainsi que les profils électrophorétiques de Mic à titre de comparaison. Pour MicDoxHCl 2 µM (électrophérogramme c), un seul pic est observé à -11 x 10-5 $cm^2V^{-1}s^{-1}$, à la même mobilité que Mic, mais avec une augmentation de l'intensité du signal de fluorescence qui pourrait indiquer l'incorporation du médicament puisque les signaux de fluorescence sont additifs. A partir de 3,5 µM et plus, l'augmentation de la concentration en DoxHCl, conduit à une augmentation supplémentaire du signal de fluorescence pour ce pic à -11 x 10-5 $cm^2V^{-1}s^{-1}$. De plus, le signal du pic cationique du DoxHCl à +8,0 x 10-5 $cm^2V^{-1}s^{-1}$ apparaît, ce qui prouve que la saturation de Mic est atteinte, ainsi que l'apparition d'un troisième nouveau pic à une mobilité électrophorétique de -3,0 x 10-5 $cm^2V^{-1}s^{-1}$. Ce nouveau pic pourrait prouver la présence d'une nouvelle structure (en équilibre avec MicDoxHCl et DoxHCl) dans l'échantillon des agrégats de type micelle chargés. Comme la micelle est composée d'un copolymère (CoPo), l'interaction hypothétique d'un CoPo non agrégé avec le DoxHCl a donc été étudiée par des solutions de 5,0 µM de DoxHCl mélangées soit à du CoPo, soit à aux agrégats de type micelle (Mic), nommés respectivement CoPo+DoxHCl et Mic+DoxHCl, sans autre traitement (pas de dialyse) et analysées par DLS et CE après leur formation (T_0) et une semaine plus tard (T_{week}). Les résultats montrent que la présence de CoPo libre semble donc induire l'apparition de ce troisième pic, plus prononcé lorsque le CoPo est directement mélangé au DoxHCl, plutôt que lorsque les micelles sont préformées. La formation d'un complexe CoPo-DoxHCl est donc très probable.

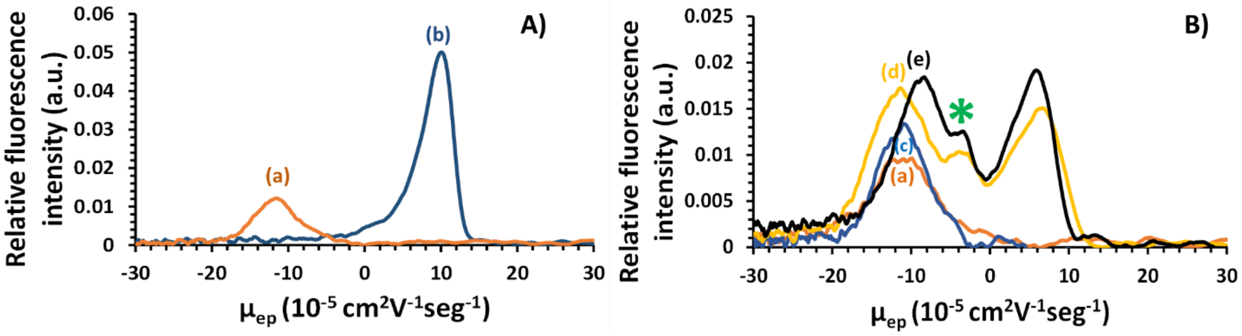

Figure A2.2.3 A) Profils électrophorétiques de a) Mic et b) DoxHCl 1 µM. B) MicDoxHCl formé en présence de DoxHCl c) 2,0, d) 3,5 et e) 5,0 µM dans du PBS. BGE = PBS pH 7,4 ; F.I. 25mM.

L'estimation de la capacité maximale de charge de doxorubicine dans ces nanostructures a été réalisée grâce à l'établissement d'une courbe d'étalonnage de doxorubicine libre à partir de son pic électrophorétique et des électrophérogrammes de deux solutions: l'échantillon après dialyse, présentant un équilibre entre la doxorubicine libre et la doxorubicine chargée (électrophérogrammes des Figures A2.2.3 B); et le dialysat contenant la doxorubicine libre. Par conséquent, la concentration totale de doxorubicine libre peut être calculée à partir de la hauteur du pic à +8 x 10-5 $cm^2V^{-1}s^{-1}$ dans l'échantillon à l'équilibre et le dialysat ($\text{Dox}_{\text{equilibrium}}$ et $\text{Dox}_{\text{dialysate}}$, respectivement). La concentration de doxorubicine chargée a ensuite été calculée comme suit : $\text{Dox}_{\text{loaded}} = \text{Dox}_{\text{initial}} - \text{Dox}_{\text{equilibrium}} - \text{Dox}_{\text{dialysate}}$. Le tableau A2.2 résume les concentrations estimées pour les deux formes de doxorubicine.

Table A2.2 Quantification indirecte de la charge de doxorubicine dans les agrégats de type micelle.

	DoxHCl/Dox Initial		**DoxHCl/Dox Equilibrium**	**DoxHCl/Dox Dialysate**	**DoxHCl/Dox Loaded**
	µM	**µg**	**µg**	**µg**	**Mg**
MicDoxHCl	**2**	11.6	0.9 ± 0.01	2.6 ± 0.06	8.1 ± 0.25
	3.5	20.2	0.9 ± 0.02	8.2 ± 0.30	**11.1 ± 0.30**
	5	28.9	1.2 ± 0.16	16.6 ± 0.25	**11.1 ± 0.21**
MicDox	**2**	11.6	1.2 ± 0.21	3.0 ± 0.02	7.4 ± 0.03
	3.5	20.3	0.6 ± 0.04	4.9 ± 0.16	14.8 ± 0.25
	5	28.9	0.8 ± 0.03	8.1 ± 0.25	**20.0 ± 0.30**

Les valeurs moyennes ± écarts types sont présentées. (n=3)

Le DoxHCl et le Dox peuvent tous deux être incorporés dans les agrégats de type micelle, et les résultats indiquent de plus grandes quantités de la forme moins soluble du médicament peuvent être chargées dans les micelles. Pour le DoxHCl, une saturation des agrégats de type micelle semble se produire à des concentrations ≥ 3,5 µM, tandis que le Dox semble être capturé à une quantité plus élevée, sans signe de saturation au moins jusqu'à la concentration de 5 µM. Le DoxHCl étant plus soluble dans les milieux polaires, il faut s'attendre à ce que sa capture se fasse préférentiellement au niveau de la partie hydrophile du PNIPAM avec de possibles interactions électrostatiques, ce qui correspond à la partie externe des agrégats de type micelle. Ces interactions électrostatiques pourraient être entre le carbonyle du PNIPAM et le groupe amino chargé positivement du DoxHCl (pKa 8,2).[311] De même, une interaction entre le groupe amino du PNIPAM et les groupes carbonyles du DoxHCl pourrait être attendue. D'autre part, le Dox, qui se dissout dans le solvant moins polaire THF, pourrait interagir préférentiellement par des interactions hydrophobes telles que les forces dipôle-dipôle avec les fragments de spiropyrane (SP) situés à l'intérieur des agrégats de type micelle. Cela pourrait expliquer la capacité de charge plus élevée des micelles vis-à-vis du Dox. Une représentation schématique de ces modes de chargement possibles est illustrée à la figure A.2.2.4.

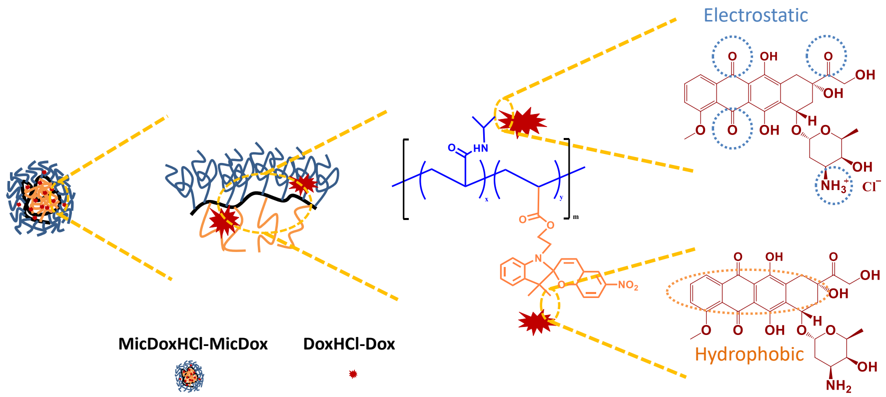

Figure A2.2.4 Représentation schématique des interactions du DoxHCl et du Dox avec les agrégats de type micelle du copolymère aléatoire Poly(NIPAM-co-SPMA).

Dans les agrégats de type micelle, des stimuli de variation du pH de 7,4 à 6,0, et d'irradiation par lumière UV (365 nm/15 min) ont été réalisés. Les mesures de DLS (Figure A2.2.5 A pour 25mM PBS pH 6) montrent une augmentation de la taille de Mic (295 ± 5 nm - largeur de pic 128nm) et MicDoxHCl (340 ± 9 nm - largeur de pic 130nm) lors de la réduction de la valeur du pH en raison du gonflement des chaînes SP dérivées de leur protonation (SP-H)[301] et de l'internalisation du solvant qui en résulte. Après irradiation avec des rayons UV dans du PBS à pH 6,0, une nouvelle augmentation de la taille de Mic (342 ± 5 nm - largeur de pic 130nm) et de MicDoxHCl (360 ± 11 nm - largeur de pic 152nm), avec des valeurs de PDI supérieures à 0,783, ce qui signifie une polydispersité élevée ou la formation de structures non sphériques qui pourraient être une preuve de la désagrégation montrée par les images TEM. Avec cette méthode, une augmentation remarquable de la taille des objets sphériques de plus grand diamètre (Figure A2.2.5 B - 40 à 350nm) combinée à des structures apparemment désagrégées a été observée pour les agrégats de type micelle à pH 6,0 par rapport à pH 7,4 (Figure A2.2.5 B - 18nm). En combinant les stimuli de la lumière UV et du pH 6,0, l'image TEM (Figure A2.2.5 C) montre clairement la désagrégation des micelles avec une distribution de taille polydispersée (200 - 400 nm).

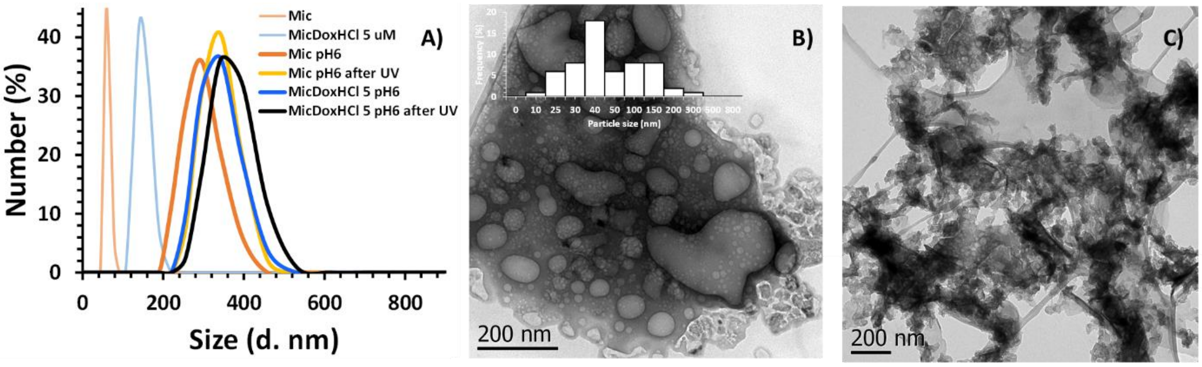

Figure A2.2.5. A) Profils DLS de Mic et MicDoxHCl 5 µM sous pH 6 et exposition à la lumière UV (365 nm). Images TEM de B) MicDoxHCl 5 µM à pH 6, et C) MicDoxHCl 5 µM à pH 6 après irradiation à la lumière UV (365 nm). Les encarts montrent les histogrammes de distribution de taille correspondants.

La figure A2.2.6 A) montre les électrophérogrammes de Mic et de MicDoxHCl (chargé de DoxHCl à des concentrations allant de 2 à 5 µM) lors de l'excitation par la lumière UV. Ces profils électrophorétiques sont semblables à ceux observés pour Mic sans irradiation (Figure A2.2.3 B) confirmant que ce stimulus seul n'est pas suffisant pour la libération du médicament. A la diminution du pH (pH 6) (Figure A2.2.6 B), un déplacement de la mobilité électrophorétique du DoxHCl a été observé. De plus, les signaux d'intensité ont presque doublé à pH 6,0, en raison de la libération du médicament dans ces conditions. Un pic à -5,0 x 10-5 cm^{2}V^{-1}s^{-1} pourrait provenir de la protonation SP-H qui induit des formes-tailles inhomogènes et donc la dispersion électrocinétique du profil des micelles. Les micelles exposées à une irradiation aux UV et dans du PBS à pH 6,0 (Figure A2.2.6 C) présentent des électrophérogrammes de MicDoxHCl similaires à ceux présentés dans la Figure 6B. Cependant, une légère augmentation sur l'intensité du signal du DoxHCl a été observée lorsque les agrégats de type micelle ont interagi avec 5,0 µM de DoxHCl, montrant une possible contribution synergique des stimuli combinés pour la libération du médicament, à cette concentration de charge en DoxHCl. Des profils similaires ont été observés lors de l'analyse des agrégats de type micelle traités avec des concentrations variées de Dox, Cependant, des pics moins intenses associés à la doxorubicine ont été observés. Ceci est une indication d'une libération moins efficace de la Dox par rapport au DoxHCl à partir des agrégats micellaires correspondants, en raison de leur plus faible solubilité dans l'eau. D'après ces observations, le stimulus du pH devrait principalement contrôler la libération.

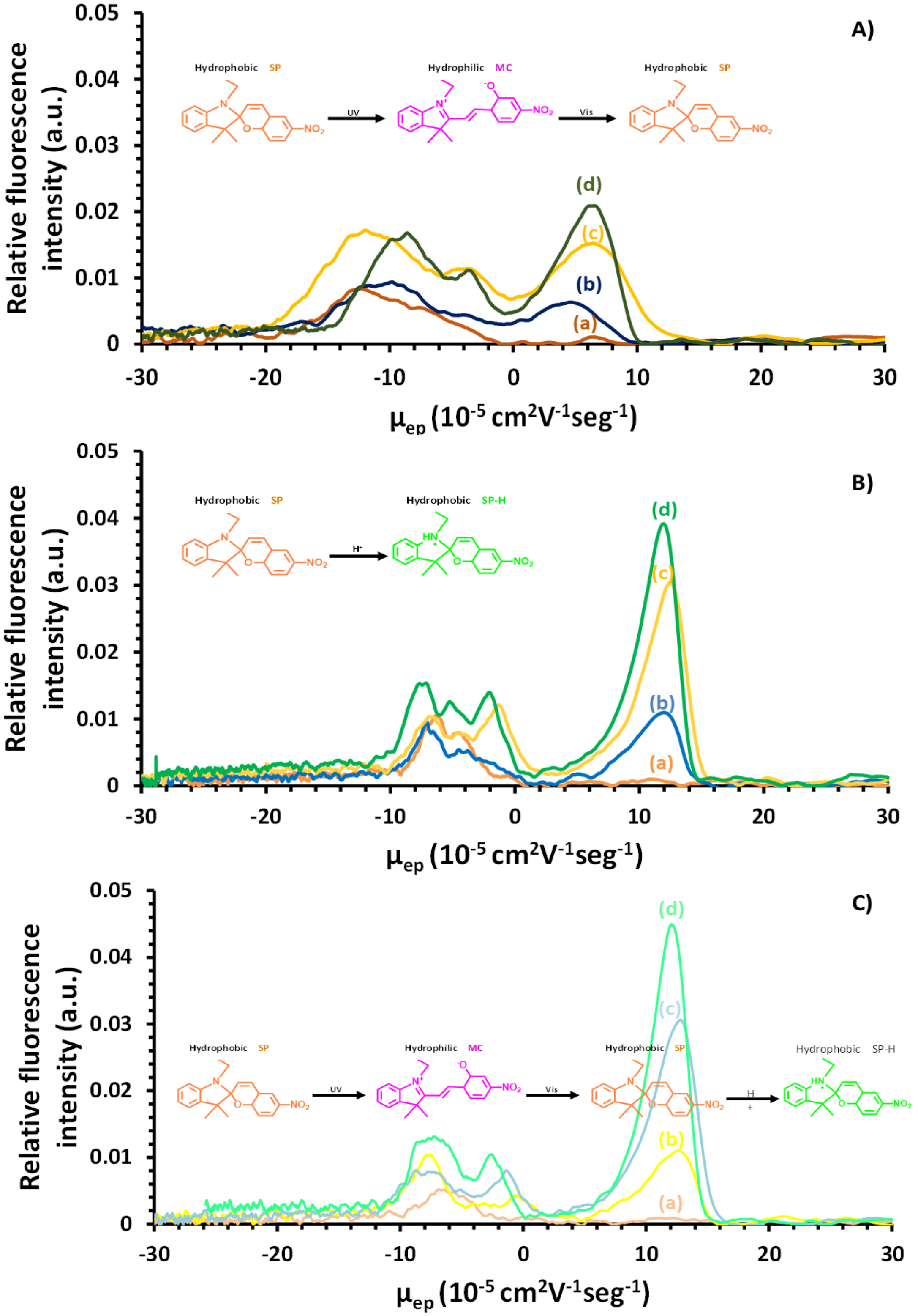

Figure A2.2.6 Profils CE de Mic et MicDoxHCl traités avec différents stimuli. A) Lumière UV (15 min / 365 nm) à pH 7,4, B) obscurité à pH 6,0, et C) lumière UV à pH 6,0. Concentrations de DoxHCl : a=0, b=2,0, c= 3,5 et d= 5,0 µM. Toutes les mesures ont été effectuées dans du PBS à une force ionique de 25 mM.

La figure A2.2.7 résume les quantités de DoxHCl et de Dox chargées et libérées en fonction des stimuli de pH 6,0 et/ou d'irradiation aux UV. Même si la capacité de charge du Dox est plus élevée que celle du DoxHCl, la quantité de doxorubicine libérée par le MicDoxHCl est supérieure à celle du MicDox. Cela peut être interprété en termes de forme chimique et de solubilité des deux formes de doxorubicine, et de leurs types d'interaction avec les agrégats de type micelle. Tout d'abord, le Dox étant peu soluble dans l'eau, cette forme est mieux chargée dans la micelle et devrait logiquement être plus difficile à libérer. De plus, le Dox devrait logiquement être localisé dans la partie hydrophobe interne des micelles, alors que le DoxHCl est censé être principalement localisé dans la partie hydrophile externe. De plus, les interactions électrostatiques du DoxHCl avec les fragments de PNIPAM devraient être moins fortes que les interactions hydrophobes du Dox avec les molécules de SP à l'intérieur des agrégats de type micelle. Cette localisation externe préférentielle pourrait stimuler la libération de la DoxHCl, qui a atteint jusqu'à 68 % du DoxHCl capturé (5 µM), contre seulement 29 % du Dox capturé (5 µM). En outre, lorsque les stimuli de pH 6,0 et de lumière UV sont combinés, la libération de DoxHCl à partir de MicDoxHCl (5 µM) atteint jusqu'à 74 %, alors que la libération de MicDox (5 µM) n'est pas améliorée.

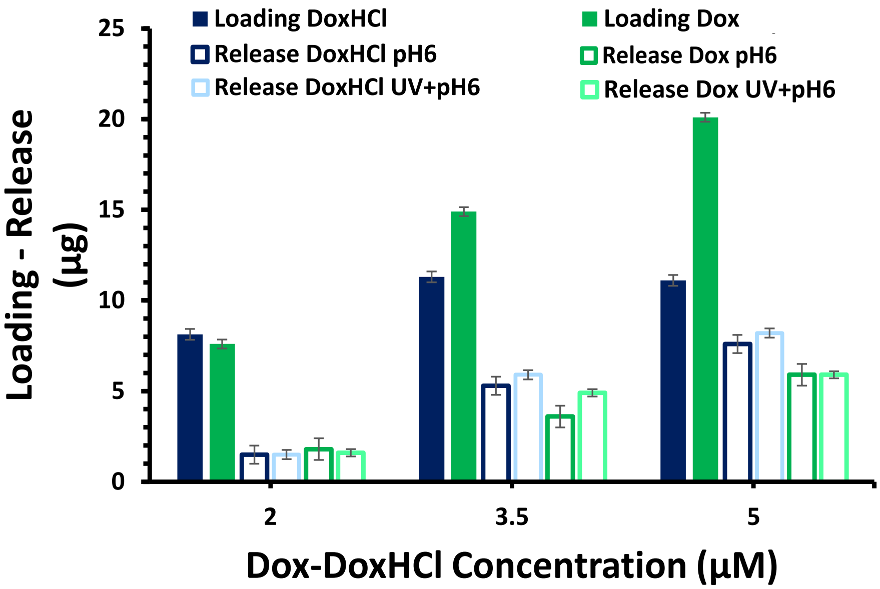

Figure A2.2.7 Chargement et libération de DoxHCl et de Dox à partir d'agrégats de type micelle exposés à des stimuli de pH et/ou de lumière UV.

A2.3. Nano-agrégat de type micelle, sensible à la lumière, au magnétisme et au pH, avec un cœur de Janus NP magnéto-luminescent.

Les nanoparticules à conversion ascendante (UCNPs) de $NaYF_4$:Yb,Tm ont été synthétisées [339], en agitant vigoureusement un mélange de 2,0 mmol de Y_2O_3, 0,5 mmol de Yb_2O_3et 18,1 mol de $TmCl_3$ dans 40 mL de HCl jusqu'à ce que la solution devienne claire, puis en poursuivant l'évaporation de la solution jusqu'à sec. Un volume de 5 mL d'eau désionisée a été ajouté aux cristaux de chlorure jusqu'à dissolution totale. Puis cette solution a été mélangée avec 30 mL d'acide oléique et 75 mL de 1-octadécène, et agitée pendant 30 min. Le mélange a ensuite été chauffé à 150 °C pendant 30 min pour former une solution jaune claire. Après refroidissement de la solution à température ambiante, un mélange composé de 20,3 mmol de NH4F et 12,8 mmol de NaOH dissous dans 50 mL de méthanol a été ajouté dans le ballon. Après avoir agité pendant 30 min, la solution a été chauffée à 110 °C et maintenue à cette température pendant 30 min supplémentaires pour compléter l'évaporation du méthanol. Puis la solution est finalement chauffée à 280 °C pendant 30 min sous la protection d'un flux de N_2. Après que la solution ait atteint la température ambiante, les nanocristaux de $NaYF_4$:Yb,Tm ont été précipités de la solution avec de l'acétone et lavés avec de l'éthanol/eau (1 : 1 v/v) trois fois. Les nanocristaux résultants (UCNPs) ont été facilement dispersés dans l'hexane.

Pour la synthèse et l'optimisation des nanoparticules de type Janus (JNP), une quantité fixe d'UCNP précédemment synthétisée a été mélangée au précurseur de NPs magnétiques (MNP), le Fe(AcAc)3 en différentes quantités, en réalisant une croissance épitaxiale de la fraction magnétique par décomposition thermique à la surface de l'UCNP (fraction luminescente) comme le montre la figure 2.3.1 A). L'objectif était d'obtenir des matériaux hybrides présentant simultanément des propriétés magnétiques et à conversion ascendante intenses. Ainsi, trois rapports de masse entre les UCNP et le précurseur de fer (UCNP : $Fe(AcAc)_3$) ont été étudiées, à savoir 1:0,25, 1:0,5 et 1:1. Ces rapports ont été mélangés avec 15 mmol de 1,2-Dodécanediol, 9 mmol d'acide oléique, 9 mmol d'oléylamine et 30 mL de 1-Octadécène dans un ballon à trois cols avec le système de reflux sous atmosphère d'azote. Ensuite, le mélange a été chauffé à 100 °C et maintenu pendant deux heures. La température a ensuite été portée à 200 °C et maintenue pendant 2 heures. Enfin, elle a été portée à 315 °C et maintenue pendant 60 minutes. Le mélange a ensuite été laissé refroidir à température ambiante. Les MNP synthétisées ont été précipitées en ajoutant une quantité égale d'éthanol et d'acétone (50:50% v:v) pour leur lavage. Le mélange a ensuite été décanté magnétiquement. Ce processus de lavage a été répété au moins 7 fois.

Pour l'incorporation de la doxorubicine (DoxHCl) et des JNP dans les agrégats de micelles, le Poly(NIPAM-co-SPMA) (2 mg) a été dissout dans 1 mL de THF contenant 50 µM de DoxHCl et 5 mg de JNP, prélablement dispersés par ultrasonication avec une vitesse d'agitation rapide (1100 r.p.m.). Ensuite, 1 mL de PBS (pH 7,4 et F.I. 25 mM) a été ajouté à un débit de 1 µL.s^{-1} suivi à nouveau des 9 mL restants de PBS (pH 7,4 et F.I. 25 mM). Après l'étape d'agitation de 7 heures, les réactifs et solvants qui n'ont pas été encapsulés dans les agrégats de type micelle (THF et DoxHCl) ont été éliminés par dialyse (seuil de coupure de 10 kDa) avec de l'eau à température ambiante pendant 24 h. Les échantillons nanocomposites (MicJNPDox) ont été conservés dans des flacons ambrés à 8°C, et ont une concentration en JNPs de 0,5 mg/ml. Une représentation schématique de ce processus de chargement est présentée dans la figure 2.3.1 B).

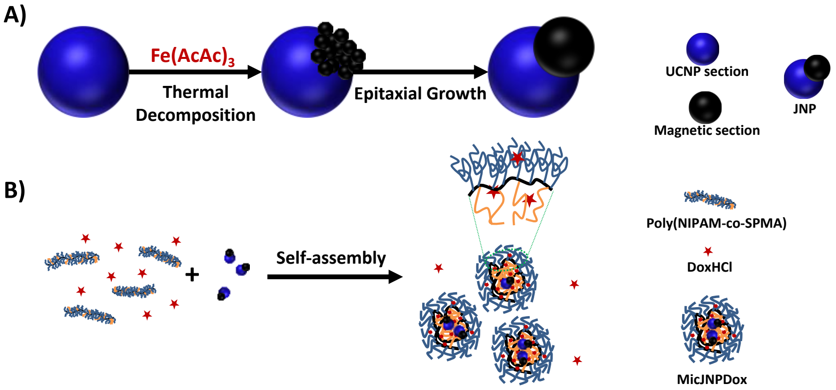

Figure A2.3.1 Représentation schématique de A) la synthèse de JNP magnéto-luminescents et B) l'encapsulation de JNP (MicJNP) et de DoxHCl (MicJNPDox) dans des agrégats de type micelle auto-assemblés.

La caractérisation structurelle et optique des MNPs, des UCNPs et des différents échantillons de JNPs (1:0.25, 1:0.5 et 1:1, UCNP: Fe(AcAc)$_3$) est présentée dans la figure A2.3.1. Tous les échantillons de JNPs ont été séparés magnétiquement, démontrant ainsi leur nature magnétique. La figure A2.3.2 A) présente les profils de diffraction des rayons X des MNPs et des UCNPs, qui ont été indexés à la phase cubique pour la magnétite, et à la phase hexagonale (β-NaYF4) (selon les fichiers JCPDS n° 85-1436 et 28-1192, respectivement). En comparant les pics de diffraction des JNPs avec leurs deux précurseurs précédents, les échantillons de JNPs 1:0.5 et 1:1 ont montré des motifs plus proches de ceux de la magnétite que de ceux des UCNPs. En revanche, l'échantillon 1:0,25 montre des motifs plus proches de ceux d'une UCNP, trouvant également de très légères comparaisons avec les motifs de MNP. La figure A2.3.2 B) montre les images TEM des UCNP et des JNP. Les UCNP ont une morphologie sphérique avec une monodispersité et une taille moyenne de 30 nm de diamètre.

Enfin, on observe des JNP monodispersées avec une morphologie typique de « bonhomme de neige » (40 nm) où la plus grande sphère (30 nm) correspondrait à la fraction luminescente (UCNP) et la plus petite sphère (8 nm) correspondrait à la fraction magnétique. Ceci démontre la croissance épitaxiale des MNP sur la surface de l'UCNP, et avec une taille moyenne des nanoparticules de type Janus de 40 nm.

La figure A2.3.2 C montre les spectres de luminescence par conversion ascendante des UCNPs et des différents échantillons de JNPs sous une excitation de 980 nm (1 W cm^{-2}). Les UCNPs présentent deux pics dans la région UV, à 335 ($^1I_6 \rightarrow {}^3F_4$), età 363 nm ($^1D_2 \rightarrow {}^3H_6$), deux pics dans la région bleue à 450 ($^1D_2 \rightarrow {}^3F_4$) et 478 nm ($^1G_4 \rightarrow {}^3H_6$), un pic dans la région rouge à 655 nm ($^1G_4 \rightarrow {}^3F_4$) et un pic dans la région proche infrarouge à 801 nm ($^3H_4 \rightarrow {}^3H_6$), toutes des transitions de Tm^{3+}. Des transitions similaires sont observées pour l'échantillon de JNPs avec une concentration fractionnée de précurseur de Fe 1:0,25 (UCNPs : $Fe(AcAc)_3$), mais avec une diminution importante de l'émission pour les pics à 801 et 478 nm. Pour les échantillons de JNPs 1:0.5 et 1:1, les pics UV n'ont pas été observés, et la réduction considérable de l'intensité d'émission dans les régions du visible et du proche infrarouge a été vérifiée. Ces réductions d'émissions pourraient être dues au transfert d'énergie de la fraction UCNPs à la fraction magnétique (magnétite) épitaxiée dans la surface des UCNPs en raison de la bande d'absorption de la magnétite entre 375 et 650 nm.[342] L'absorption de l'énergie de transfert est dissipée dans un processus non radiatif appelé " désexcitation non radiative " par la libération d'énergie thermique et est mise en évidence expérimentalement par l'extinction de la luminescence.[343] L'échantillon qui a montré des propriétés magnétiques et une émission plus élevée, en particulier dans la région UV, était l'échantillon JNPs 1:0,25 (UCNPs: $Fe(AcAc)_3$), choisi pour les expériences suivantes. Les transitions radiatives observées dans les UCNPS $NaYF_4$: Yb,Tm et les processus RET dans les JNP induits par une excitation à 980 nm sont schématisés dans la figure A2.3.2 D). Un processus RET supplémentaire pour la fraction de spyropirane (SP) sera décrit plus loin.

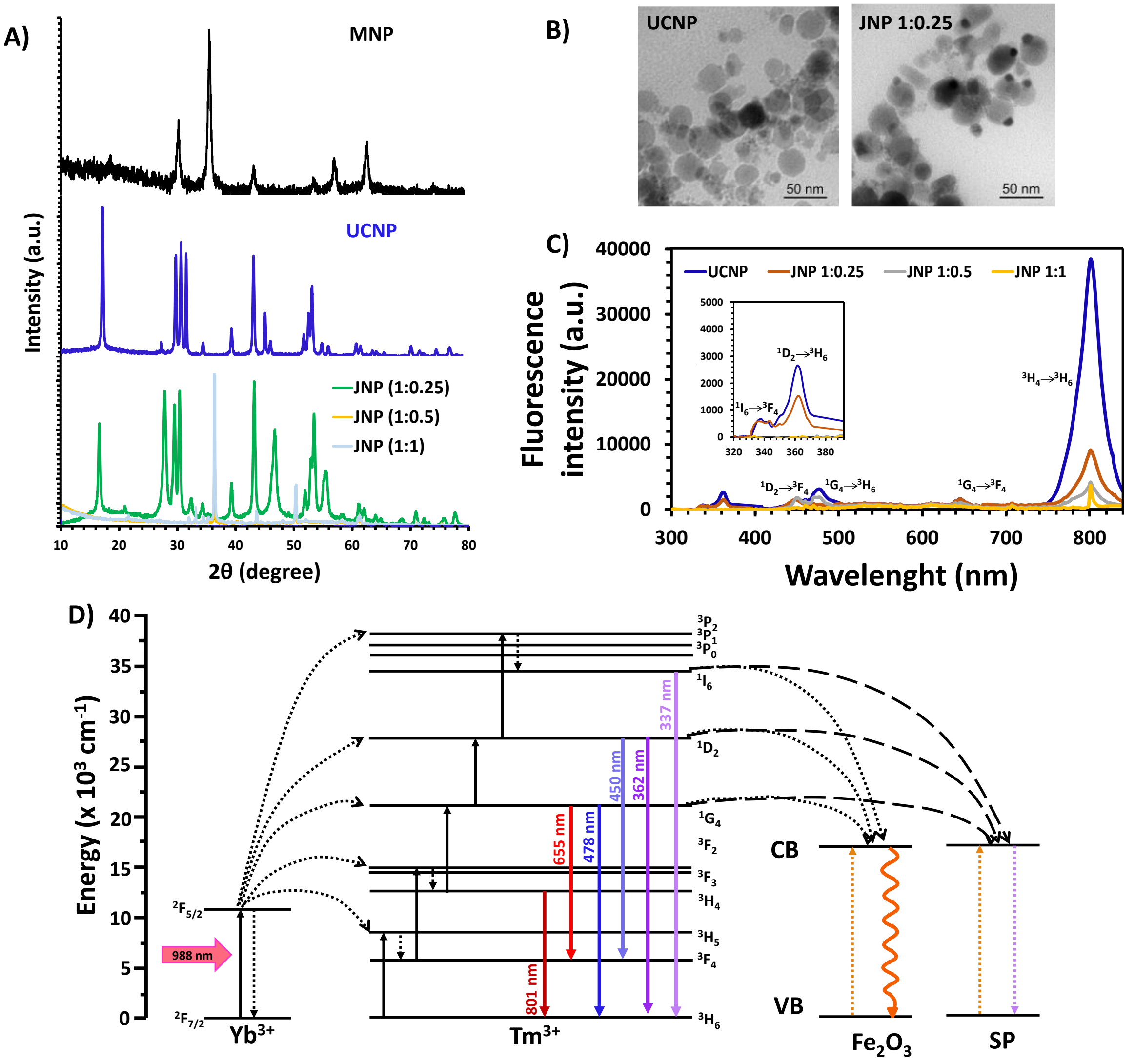

Figure A2.3.2 A) diagramme XRD de la poudre, B) micrographie TEM, et C) spectres FS de MNP, UCNP et JNP sous irradiation NIR 980 nm. D) Diagramme de niveau d'énergie de la conversion ascendante et du processus de transfert d'énergie dans le $NaYF_4$: Yb,Tm - Fe_2O_3 JNP et le processus de transfert d'énergie dans le MicJNP sous une excitation de 980 nm.

L'encapsulation des JNPs (1:0.25) par les agrégats de type micelle a été testée pour la formation du nanocomposite MicJNPs. Cette encapsulation est possible grâce à l'interaction hydrophobe entre la surface des JNPs et le spiropyrane hydrophobe du copolymère Poly(NIPAM-co-SPMA). Les résultats de la DLS (figure 2.3.3 A) montrent une augmentation de la taille de la Mic de 61 ± 2 nm (largeur de pic 28 nm) à 220 ± 2 nm (largeur de pic 100 nm) après incorporation des JNP (MicJNP). Lorsque le DoxHCl est chargé dans le nanosystème (MicJNPDox), la taille augmente à 295 ± 6 nm (largeur de pic 160 nm). Lors du changement de pH de 7,4 à 6, les MicJNP et MicJNPDox subissent une augmentation importante de leur taille, jusqu'à 531 ± 5 nm (largeur de pic 140 nm) pour les MicJNP, et jusqu'à 396 ± 8 nm (largeur de pic 160 nm) pour les MicJNPDox. Cette augmentation de la taille à un pH plus acide peut être due au gonflement des chaînes SP dérivées de leur protonation (SP-H) [301] et à l'internalisation du solvant qui en résulte. En outre, des images TEM pour les MicJNP à pH physiologique 7,4 (Figures 4.3 B) et à pH acide 6 (Figures 4.3 C) ont été obtenues, montrant dans les MicJNP (pH 7,4) le revêtement de micelles sur les JNP conservant la morphologie sphérique avec une taille moyenne de 48 nm. D'autre part, en changeant le pH de 7,4 à 6, une légère augmentation de la taille des objets sphériques avec des structures apparemment désagrégées a été observée. Cela montre encore l'effet du gonflement et de la désagrégation des SP-H sous l'effet du pH.

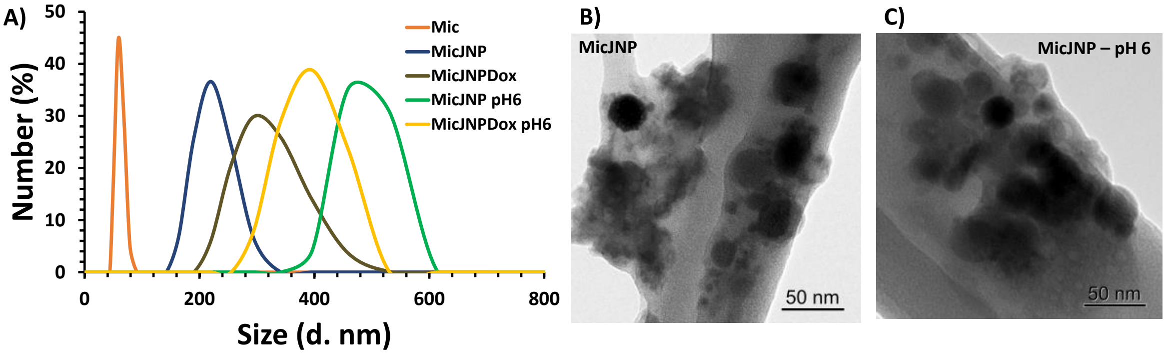

Figure A2.3.3 A) Profils DLS (à pH 7,4 et 6) et micrographies TEM de B) MicJNP et C) MicJNP DoxHCl 5 µM

La figure A2.3.4 montre les spectres de luminescence par conversion ascendante des JNPs (1:0,25) et du nanosystème MicJNPs sous une excitation de 980 nm (1 W cm^{-2}). En comparant l'intensité des pics dans la région NIR (transition $^3H_4 \rightarrow {}^3H_6$ à 801 nm), une légère différence est observée. Au contraire, les pics à 655 nm ($^1G_4 \rightarrow {}^3F_4$) dans la région rouge, restent inchangés. Dans la région bleue, les pics observés à 450 ($^1D_2 \rightarrow {}^3F_4$) et 478 nm ($^1G_4 \rightarrow {}^3H_6$), présentent une diminution d'intensité pour les MicJNP presque négligeable. Mais dans la région UV pour les pics à 335 ($^1I_6 \rightarrow {}^3F_4$) et 363 nm ($^1D_2 \rightarrow {}^3H_6$), il y a une nette disparition de l'intensité de fluorescence pour le nanosystème MicJNPs. Ceci est dû à l'absorption UV du composé spiropyrane (SP) entre 200 et 400 nm qui conduit à la photo-isomérisation pour donner le composé hautement stable merocyanine (MC). Ainsi, l'énergie UV produite par la conversion ascendante des JNPs sous l'irradiation d'une lumière infrarouge proche à 980, pourrait être transférée de la fraction UCNPs vers l'agrégat micellaire Mic qui encapsule ces NPs. Cette énergie pourrait ensuite être absorbée par le composé SP photosensible qui se transforme en l'isomère zwitterionique stable MC. Le diagramme du niveau d'énergie de la conversion ascendante et du processus de transfert d'énergie dans la JNP $NaYF_4$: Yb,Tm - Fe_2O_3 sous excitation à 980 nm vers le SP dans l'agrégat de type micelle est présenté à la figure A2.3.2 D).

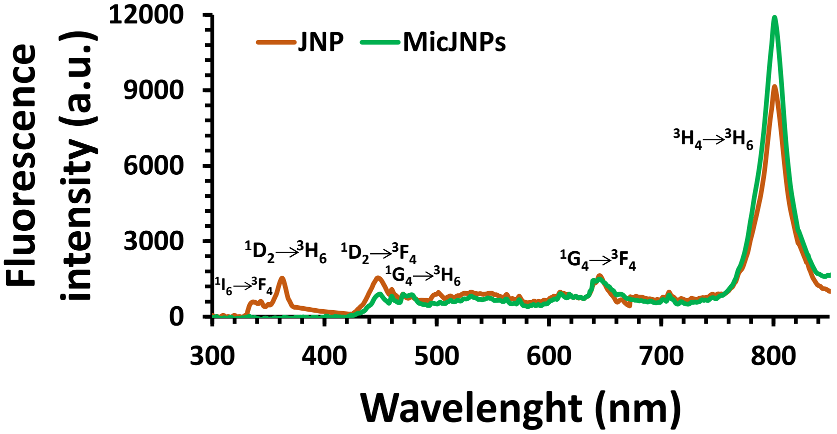

Figure A2.3.4 Spectres d'émission par conversion ascendante de la JNP et de la MicJNP après excitation par un laser de 980 nm (1 W cm^{-2}).

La figure A2.3.5 A) montre les profils électrophorétiques du nanosystème (MicJNP) des JNP piégées dans les agrégats de type micelle (Mic). Mic et MicJNP, ont la même valeur de mobilité électrophorétique (-11 x 10^{-5} $cm^2V^{-1}s^{-1}$) ayant la même intensité et un comportement gaussien. Lorsque les MicJNP sont irradiés par la lumière UV, deux signaux sont observés, celui de la micelle et un nouveau à -18 x 10^{-5} $cm^2V^{-1}s^{-1}$. Lorsque Mic est irradié par la lumière UV, il est connu que la micelle se désagrège (SP en isomères MC) et lorsque l'irradiation s'arrête, une ré-agrégation de manière incontrôlée se produit. Par conséquent, ce dernier signal pourrait être attribué à une nouvelle structure possible composée d'unimères de copolymères décorant la surface des JNPs, appelée CoPo-JNPs, qui se forme lors de la désagrégation des micelles en unimères et de la libération des JNPs. Dans le cas des MicJNP à un pH de 6, un changement de mobilité électrophorétique (-11 x 10^{-5} $cm^2V^{-1}s^{-1}$ à -8 x 10^{-5} $cm^2V^{-1}s^{-1}$) est observé, probablement dû à la protonation du SP. Enfin, en combinant les stimuli d'irradiation UV avec le changement de pH à 6, la mobilité des MicJNP reste identique et le pic de structure CoPo-JNP possible est également observé (-18 x 10^{-5} $cm^2V^{-1}s^{-1}$).

La figure A2.3.5 B) montre les profils électrophorétiques de MicJNPDox. En comparant MicJNP avec MicJNPDox, le signal à -11 x 10^{-5} $cm^2V^{-1}s^{-1}$ reste identique. Le pic du DoxHCl est observé à +8 10^{-5} $cm^2V^{-1}s^{-1}$ avec le pic du composé CoPo-Dox observé à -3 x 10^{-5} $cm^2V^{-1}s^{-1}$. Quatre signaux ont été observés pour l'échantillon MicJNpDox lors de l'irradiation par la lumière UV : celui de la micelle (-11 x 10^{-5} $cm^2V^{-1}s^{-1}$), celui du CoPo-Dox (-3 x 10^{-5} $cm^2V^{-1}s^{-1}$), celui du DoxHCl (+8 x 10^{-5} $cm^2V^{-1}s^{-1}$) et un nouveau signal à -18 x 10^{-5} $cm^2V^{-1}s^{-1}$. Le signal à -18 x 10^{-5} $cm^2V^{-1}s^{-1}$ pourrait à nouveau être dû au composé CoPo-JNP formé par les unimères du copolymère décorant la surface des JNP. D'autre part, la stimulation des MicJNPDox dans un pH plus acide (6) montre un déplacement de la mobilité électrophorétique probablement dû au gonflement des micelles. De plus, l'intensité du signal pour le Copo-Dox est augmentée par rapport au DoxHCl. Cela pourrait être dû au fait que le système CoPo dans ces conditions est plus stable. Enfin, en combinant les stimuli d'irradiation UV avec le changement de pH à 6, la mobilité du MicJNPDox reste à nouveau à -8 x 10^{-5} $cm^2V^{-1}s^{-1}$, mais le signal du CoPo diminue très considérablement. En revanche, l'intensité du signal du DoxHCl augmente fortement, ce qui montre que les stimuli combinés peuvent libérer davantage de DoxHCl. De plus, un nouveau pic est observé à -12 x 10^{-5} $cm^2V^{-1}s^{-1}$qui pourrait à nouveau correspondre à la possible structure CoPo-JNP en équilibre dans l'échantillon.

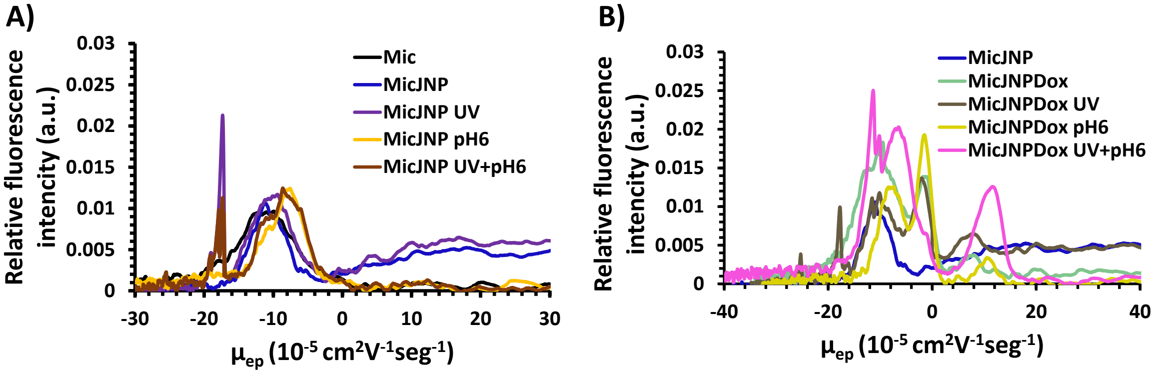

Figure A2.3.5. A) MicJNP et B) Profils électrophorétiques de MicJNpDoxHCl 2uM en réponse aux stimuli UV (360nm) et pH 6. BGE 25 mM PBS (pH 7,4).

A3. Conclusions

L'utilisation des NPs comme nanovecteurs intelligents, ainsi que pour la détection de maladies (theranostic), est l'avenir de la lutte contre les maladies et, plus particulièrement, contre le cancer. Néanmoins, la synthèse de nouveaux nanosystèmes hybrides intelligents aux propriétés différentes et la compréhension des interactions physico-chimiques entre les médicaments et les nanosystèmes doivent être étudiées.

Dans la première partie de ce projet, il a été démontré que l'auto-assemblage d'agrégats de type micelle du copolymère amphiphile aléatoire poly(NIPAM-co-SPMA) peut être modulé par la force ionique. La dépendance à la force ionique est due aux répulsions électrostatiques entre les blocs monomères de spiropyrane, permettant à un plus grand nombre de copolymères de s'agréger au cœur de micelles plus grandes lorsque la force ionique augmente. Ainsi, des agrégats optimisés de type micelle (Mic) avec une taille moyenne de 60 nm et une distribution de taille étroite ont été obtenus dans du PBS 25 mM (pH 7,4). Il a également été vérifié que par l'exposition des Mic à la lumière UV et au changement de pH (d'un milieu neutre à un milieu de pH 6), les fragments de spiropyrane (SP) subissent une photoisomérisation vers leur état zwitterionique hydrophile, la mérocyanine (MC), et/ou une protonation (SP-H) générant un gonflement des micelles .

Grâce à ces résultats, dans la deuxième partie du projet, des micelles ont été formées et chargées avec des formes peu (Dox) et très solubles dans l'eau (Dox-HCl) de doxorubicine pour étudier les interactions "agrégats de type micelle - médicaments". Les séparations et caractérisation par électrophorèse capillaire ont révélé la présence de plusieurs espèces en équilibre : les agrégats de type micelle avec ou sans doxorubicine chargée et un complexe formé entre le copolymère non agrégé et les molécules de doxorubicine, à des concentrations de doxorubicine supérieures à 3 µM. La séparation électrocinétique a permis de quantifier les concentrations de doxorubicine chargée et libérée à pH 7,4 et lors de stimulations par irradiation UV et pH 6,0. Un chargement plus efficace a été observé lors de l'utilisation du Dox par rapport au Dox-HCl (10 µg/mg vs 5,5 µg/mg, respectivement). Des taux de libération du médicament de 68 et 74 % ont été observés pour le Dox-HCl lors des stimuli pH 6,0 et combinés UV+ pH6,0, respectivement, alors que seulement 29 % du Dox chargé a été libéré sous ces deux stimuli. Les interactions "Mic - médicament" ont été expliquées par les possibles interactions électrostatiques prédominantes entre le Dox-HCl et la section poly-NIPAM de l'enveloppe micellaire, tandis que les interactions hydrophobes prédominantes entre le Dox et la fraction SP se situent dans la section interne des micelles.

Dans la dernière partie de ce projet, des nanoparticules magnéto-luminescentes de type Janus (JNP) ont été synthétisées dans une procédure de croissance épitaxiale de magnétite sur la surface de nanoparticules à conversion ascendante UCNPs, en utilisant l'acétylacétonate de fer $Fe(AcAc)_3$ comme précurseur. En testant différents rapports UCNPs: $Fe(AcAc)_3$ (1:0.25, 1:0.5 et 1:1), les analyses par XDR, TEM et spectroscopie de fluorescence, ont montré que la plus grande intensité d'émission et une réponse à un champ magnétique entre eux ont été obtenues pour un rapport massique de formation était 1:0.25,. Par la suite, les JNP et le DoxHCl ont été encapsulés durant l'auto-assemblage de Mic. Là encore, une augmentation plus importante de la taille du diamètre due au gonflement de l'agrégat de type micelle a été observée par DLS et TEM ; l'effet de changement de pH vers un milieu plus acide (pH 6) a été étudié,par spectroscopie de fluorescence ; avec une irradiation de lumière proche infrarouge (980 nm), le transfert d'énergie UV des JNPs vers Mic a été confirmé. Les séparations électrocinétiques ont montré une possible formation de la structure CoPo-JNP après irradiation par la lumière UV. De plus, une synergie est démontrée en combinant l'effet de l'irradiation par la lumière UV avec le changement du pH à 6, avec une augmentation du signal DoxHCl, prouvant ainsi la libération du médicament par les stimuli.

Ainsi, les objectifs fixés dans ce projet doctoral ont été atteints par la création d'un nanosystème capable de répondre à un champ magnétique, pouvant profiter de cette propriété pour sa possible vectorisation vers une zone cancéreuse, qui pourrait également être surveillée par l'émission de lumière générée par le nanosystème. Parallèlement, le développement de ce nanosystème MicJNPDox final, formé par les nanoparticules hybrides de type Janus et les agrégats de type micelle du copolymère amphiphile, ainsi que tous les résultats obtenus en termes de charge et de libération du médicament par le stimulus externe de l'irradiation dans le proche infrarouge, ainsi que par une diminution de la valeur de pH, permettent à ce nanosystème théranostique d'être éventuellement fonctionnel dans le suivi et le traitement des maladies cancéreuses.

RÉSUMÉ

Dans le domaine de la nanomédecine, de nouveaux outils nanotheranostiques sont développés pour la détection, le suivi et le traitement simultanés des maladies. Par conséquent, ce travail explore la synthèse de nanomatériaux théranostiques composés de nanoagrégats polymères de type micelle (Mic) sensibles au pH et à la lumière, capables de charger et de libérer des médicaments, et de nanoparticules hybrides de type Janus (JNPs) avec des propriétés magnétiques et luminescentes, à des fins de guidage spécifique, thérapeutiques et d'imagerie. L'optimisation de l'auto-assemblage des Mic a été réalisée à l'aide de méthodologies complémentaires, telles que la DLS, la TEM et l'électrophorèse capillaire (EC). L'EC a également été utilisée pour quantifier la charge de doxorubicine (DOX) dans le Mic et sa libération par stimulation. En outre, la synthèse et l'optimisation de JNPs présentant une luminescence à conversion ascendante et des propriétés magnétiques ont été réalisées. Ensuite, les JNPs ont été encapsulées avec la DOX dans le Mic, et la capacité de chargement et de libération de ce nanosystème a de nouveau été évaluée par EC. De plus, sous irradiation proche infra-rouge, ces JNPs émettent de la lumière UV. Ceci implique la modification de la structure moléculaire des Mic permettant la libération de médicaments. Ces résultats soulignent l'intérêt de tels nanosystèmes hybrides pour des applications théranostiques in vivo.

MOTS CLÉS

Théranostic, nanoagrégats de type micelle, stimuli-réceptif, nanoparticules hybrides de type Janus, électrophorèse capillaire.

ABSTRACT

In the domain of nanomedicine, new nanotheranostic tools are being developed for simultaneous detection, monitoring, and treatment of diseases. Therefore, this work explores the synthesis of theranostic nanomaterials composed by pH and light-responsive poly(NIPAM-co-SPMA) polymeric micelle-like nanoaggregates (Mic) being able to load and release drugs, and Janus-type hybrid nanoparticles (JNPs) with magnetic and luminescent properties, for specific guidance, therapeutic and imaging purposes. Optimisation of Mic self-assembly was carried out with complementary methodologies, such as DLS, TEM and capillary electrophoresis (CE). CE was further used for the quantitation of doxorubicin (DOX) loading in the MIc and its stimuli-responsive release. Moreover, synthesis and optimisation of JNPs with up-converting luminescence and magnetic properties was performed. Then, JNPs were encapsulated together with DOX into the Mic, and the loading and release capacity of this nanosystem was again evaluated by CE. Furthermore, under NIR irradiation, the JNPS emited UV light. This implies the modification of the Mic molecular structure enabling drug release. These results highlight the interest of such hybrid nanosystems for in vivo theranostic applications.

KEYWORDS

Theranostic, micelle-like nanoaggregates, stimuli-responsive, Janus-type hybrid nanoparticles, capillary electrophoresis